Sede Amministrativa: Università degli Studi di Padova

Dipartimento di Ingegneria Industriale

SCUOLA DI DOTTORATO DI RICERCA IN: INGEGNERIA INDUSTRIALE
INDIRIZZO: INGEGNERIA DELL'ENERGIA
CICLO XXVIII

EXPERIMENTAL STUDY OF PHASE CHANGE HEAT TRANSFER IN MINICHANNELS FOR GROUND AND SPACE APPLICATIONS

Direttore della Scuola: Prof. Paolo Colombo
Coordinatore d'indirizzo: Prof.ssa Luisa Rossetto
Supervisore: Prof. Davide Del Col

Dottorando: Marco Azzolin

ABSTRACT

Two-phase heat transfer is widely encountered in minichannels heat exchangers such as air-cooled condensers and evaporators for automotive, compact devices for electronic cooling, aluminum condenser for air-conditioning applications, loop heat pipes and capillary pumped loops for space applications. Nowadays there is also an increasing interest on new refrigerants, pure and blended, with a low-GWP.

This thesis aims at studying the physical phenomena of condensation by investigating the effect of gravity inside small channels, presenting an experimental analysis during normal gravity and microgravity conditions. Another objective of this thesis is to analyze the two-phase heat transfer performance of non-azeotropic mixtures, with low-GWP, in minichannels. Regarding mixtures the work focused not only on condensation heat transfer but also on flow boiling and two phase pressure drop.

In the first part of this thesis the design and the realization of a new test section to study the effect of gravity during convective condensation is presented. The new test section has an internal diameter of 3.38 mm and it allows to measure quasi-local heat transfer coefficients and to visualize the flow pattern. Quasi-local heat transfer coefficients measured on ground during condensation of R134a at 40°C and mass velocities between 50 and 200 kg m^{-2} s^{-1} are presented. The flow patterns visualized are compared with flow pattern maps available in the literature and the experimental heat transfer coefficients with different models for condensation. The new test section has been also used to study convective condensation in microgravity conditions during the 62nd ESA Parabolic Flight Campaign. This has been one of the first attempts to perform heat transfer coefficients measurements and flow pattern visualizations on normal gravity and microgravity conditions during convective condensation inside tubes. The deep connection between gravity effect and flow pattern are shown in the images.

Regarding on-ground applications, in the recent years much attention has been paid to the possible use of fluorinated propene isomers for the substitution of HFC fluids being in most cases high-GWP refrigerants. However, the available HFOs (hydrofluoroolefins) cannot cover all the air-conditioning, heat pump, and refrigeration systems when used as pure fluids because their thermodynamic properties are not suitable for all operating conditions; therefore some solutions may be found using blends of refrigerants, to satisfy the demand for a wide range of working conditions.

The second part of this thesis presents an experimental study of the two-phase heat transfer for a R32/R1234ze(E) non-azeotropic mixture, at different mass compositions, inside a 0.96 mm inner diameter minichannel. As first step, frictional pressure gradient during adiabatic two-phase flow has been investigated. The experimental data are also compared with several models available in the literature. Local heat transfer coefficients have been then measured during condensation of the R32/R1234ze(E) mixture at three different mass compositions (23/77%, 46/54 and 75/25% by mass). The new experimental data are compared to those of pure R1234ze(E) and R32. This allows to analyze the heat transfer

penalization due to the mass transfer resistance occurring during condensation of this zeotropic mixture and to assess about suitable predicting models. The present work reports also the local heat transfer coefficient measured during flow boiling of the R32/R1234ze(E) mixture (50/50% by mass) at a pressure of 14 bar, which corresponds to a bubble temperature of 26.2 °C. The flow boiling data, taken in the 0.96 mm minichannel, are discussed with particular regard to the mass transfer mechanism. The new experimental data are also compared to flow boiling data of pure R1234ze(E) and pure R32. This flow boiling database, encompassing more than 300 experimental points at different values of mass velocity, heat flux and vapor quality, is compared with available correlations in the literature. The introduction of a correction to account for the additional mass transfer resistance is discussed and such correction is found to be necessary and proper to provide a correct sizing of the evaporator.

RIASSUNTO

Lo scambio termico bifase in minicanali è utilizzato in diverse applicazioni come ad esempio, condensatori ed evaporatori ad aria nel settore automobilistico, sistemi compatti per il raffreddamento di elettronica, condensatori in alluminio per applicazioni di climatizzazione, tubi di calore per applicazioni spaziali. In più oggi c'è un crescente interesse verso i nuovi fluidi, puri e in miscela, con basso GWP.

Questo lavoro di tesi si propone di studiare i fenomeni fisici dello scambio termico in condensazione indagando l'effetto della gravità all'interno di canali con piccolo diametro, presentando un'analisi sperimentale in condizioni di gravità normale e di microgravità. Un altro obiettivo di questa tesi è quello di analizzare le prestazioni di miscele non azeotropiche, a basso GWP, durante lo scambio termico bifase in minicanali. Per quanto riguarda le miscele si analizzerà sperimentalmente non solo lo scambio termico durante la condensazione ma anche la vaporizzazione e le cadute di pressione bifase.

Nella prima parte di questa tesi viene presentata la progettazione e la realizzazione di una nuova sezione sperimentale per studiare l'effetto della gravità durante lo scambio termico in condensazione. La nuova sezione di prova ha un diametro interno di 3.38 mm e permette di misurare i coefficienti di scambio termico quasi-locali e di visualizzare il regime di deflusso. I coefficienti di scambio termico in condensazione sono stati misurati con R134a alla temperatura di saturazione di 40 °C e per portate specifiche tra 50 e 200 kg m^{-2} s^{-1}. I regimi di deflusso visualizzati sono stati confrontati con quelli predetti dalle mappe di deflusso disponibili in letteratura e i coefficienti di scambio termico sperimentali con modelli sviluppati per la condensazione. La nuova sezione sperimentale è stata utilizzata anche durante la 62° Campagna di Volo Parabolico di ESA per studiare lo scambio termico in condensazione in condizioni di microgravità. Questo studio è uno dei primi tentativi di effettuare misure dei coefficienti di scambio termico e visualizzazioni dei regimi di flusso in condizioni di gravità normale e di microgravità durante la condensazione all'interno di tubi. Il legame profondo tra effetto della gravità e regime di flusso è analizzato servendosi delle immagini acquisite.

Per quanto riguarda le applicazioni terrestri, negli ultimi anni molto interesse si è sviluppato intorno al possibile utilizzo di isomeri fluorurati del propene per la sostituzione di fluidi HFC (idrofluorocarburi) che nella maggior parte dei casi sono ad alto GWP. Tuttavia gli HFO (idrofluoroolefine) disponibili non possono coprire tutte le applicazioni di climatizzazione, pompe di calore e sistemi di refrigerazione quando vengono utilizzati come fluidi puri perché le loro proprietà termodinamiche non sono adatte a tutte le condizioni operative; quindi una soluzione è quella di utilizzarli in miscela con altri refrigeranti.

La seconda parte di questa tesi presenta uno studio sperimentale dello scambio termico bifase per una miscela non azeotropica di R32/R1234ze(E), a diverse composizioni di massa, all'interno di un minicanale con diametro interno di 0.96 mm. Come primo passo si sono studiate le cadute di pressione durante il deflusso adiabatico bifase. I dati sperimentali sono stati confrontati con diversi modelli disponibili in letteratura. Successivamente i

coefficienti locali di scambio termico in condensazione sono stati misurati per la miscela R32/R1234ze(E) a tre diverse composizioni di massa (23/77%, 46/54 e 75/25%). I nuovi dati sperimentali sono confrontati con quelli dei componenti puri R1234ze(E) e R32. Questo ha permesso di analizzare la penalizzazione introdotta dalla resistenza al trasporto di massa e di valutare i modelli teorici in grado di predirla. In seguito vengono anche presentati i coefficienti di scambio termico misurati durante la vaporizzazione convettiva della miscela R32/R1234ze(E) (composizione 50/50%) ad una pressione di 14 bar, corrispondente ad una temperatura di bolla di 26.2 °C. I risultati sperimentali, ricavati nel minicanale di diametro 0.96 mm, sono stati discussi con particolare riguardo al meccanismo di trasporto di massa e successivamente confrontati con quelli dei fluidi puri R1234ze(E) e R32. I nuovi dati, più di 300 punti sperimentali a differenti valori di portata specifica, flusso termico e titolo di vapore, sono stati confrontati con le correlazioni disponibili in letteratura. L'introduzione di una correzione per tenere conto dell'ulteriore resistenza al trasporto di massa è stata discussa e risulta essere necessaria per un corretto dimensionamento degli evaporatori.

Contents

1 INTRODUCTION

Nowadays, new heat transfer systems with enhanced characteristics are demanded for various applications in industries. Condensers and evaporators should have not only high performance but also a small size and weight. Micro-scale heat transfer finds application in compact heat exchangers, heat pipes for electronic equipment and in many other refrigeration applications including aeronautical and space applications. For example, in a reduced gravity environment, the applications of condensation process include the life support systems, the thermal management systems for satellites, the energy production and power managements systems for long time missions or manned space platforms, waste water treatment for long duration space exploration missions and fluid management from the storage tanks through the lines to the engine. Considering that future space missions are expected to be longer, more challenging and complex, two-phase thermal management systems should be more reliable and able to meet the demand for higher efficiencies and higher thermal loads. While evaporation has received more interest, convective condensation has been less studied in microgravity conditions. Anyway, in order to increase the performance of condensers and to develop reliable tools for heat exchanger design both in ground and space environments, a proper understanding of condensation phenomenon is necessary. In this thesis an attempt to study the effect of gravity during convective condensation inside small channels is presented. A new test section with an inner diameter of 3.38 mm has been designed and realized. Heat transfer coefficients have been measured and flow patterns have been visualized not only in Earth's gravity but also in microgravity conditions on a parabolic flight aircraft. Microgravity experiments allow to better understand convective condensation inside channels during reduced gravity, to study the influence of shear stress and surface tension effect on flow structures, heat transfer coefficient and flow pattern. If the experimental study of convective condensation inside tubes in microgravity conditions is at the beginning, the study of condensation on ground in minichannel has received an increasing interest and more and more research laboratories deal with it. From some of these works [1-6] it is clear as, at low mass velocity, a difference between micro-scale and macro-scale heat transfer, as well as an effect of cross sectional shape may exist. Therefore, such conditions are of great interest but unfortunately the low mass flux conditions are also the least investigated, mainly because it is a real challenge to perform measurements of heat transfer coefficient with low experimental uncertainty when the heat flow rate is in the order of few watts. An attempt to account for the relative influence of shear, gravity and surface tension forces was recently made by Garimella et al. [7] and they developed a model for the prediction of the heat transfer coefficient divided in two zones: shear/gravity dominated and shear/surface tension dominated.

Another open task in the refrigeration and air conditioning is the development of new HVAC technologies with low environmental impact. The introduction of minichannels heat exchangers in this field is one attempt to tackle this issue. Minichannels allow to develop compact elements, to reach high heat transfer performance and to work with reduced refrigerant charge, minimizing the problems of release of potentially hazardous fluids in the

atmosphere. Beside achieving high heat transfer rates in compact heat exchangers, there is an increasing interest in refrigerants possessing low global warming potential (GWP). In the Fourth Assessment Report of the Intergovernmental Panel on Climate Change of the United Nations Framework Convention on Climate Change it is stated that, on the basis of existing scientific data, developed countries would need to reduce greenhouse gas emissions by 80% to 95% below 1990 levels by 2050 to limit global climate change to a temperature increase of 2°C and thus prevent undesirable climate effects. In the Resolution of the 15 March 2012, the European Parliament endorsed a roadmap for moving to a competitive low carbon economy in 2050. In the Resolution is stated that, non-CO_2 emissions, including fluorinated greenhouse gases, should be reduced by 72% to 73% by 2030 and by 70% to 78% by 2050, compared to 1990 levels. If based on the reference year 2005, a reduction in non-CO_2 emissions of 60% to 61% by 2030 is required. Afterwards, with the Regulation No 517/2014 of 16 April 2014 [8], the European Parliament imposes conditions on specific uses of fluorinated greenhouse gases and for specific products and equipment that contain fluorinated greenhouse gases. For example it is prohibited to place in the market:

- from the 1st January 2015, domestic refrigerators and freezers that contain HFCs with GWP of 150 or more
- from the 1st January 2020,
  1. refrigerators and freezers for commercial use (hermetically sealed equipment) that contain HFCs with GWP of 2500 or more;
  2. stationary refrigeration equipment, that contains, or whose functioning relies upon, HFCs with GWP of 2500 or more except equipment intended for application designed to cool products to temperatures below −50 °C;
  3. movable room air-conditioning equipment (hermetically sealed equipment which is movable between rooms by the end user) that contain HFCs with GWP of 150 or more;
- from the 1st January 2022, refrigerators and freezers for commercial use (hermetically sealed equipment) that contain HFCs with GWP of 150 or more;
- from the 1st January 2025, single split air-conditioning systems (systems for room air conditioning that consist of one outdoor unit and one indoor unit linked by refrigerant piping) containing less than 3 kg of fluorinated greenhouse gases, that contain, or whose functioning relies upon, fluorinated greenhouse gases with GWP of 750 or more.

The search for alternatives primarily focuses on the use of natural refrigerants (hydrocarbons, ammonia, carbon dioxide) and new synthetic refrigerants having low GWP (hydrofluoroolefins). However, natural refrigerants are often flammable or toxic so they can be used only in apparatuses with reduced charge and the currently available HFOs (hydrofluoroolefins) cannot replace all the high GWP hydrofluorocarbons employed in cooling, heat pump and refrigeration systems because their thermodynamic properties are not suitable for the wide range of working conditions. Hence, an alternative to high GWP synthetic refrigerants might rely on refrigerants blends, obtained mixing the new HFOs

with available HFC refrigerants. In this thesis the two-phase heat transfer performance of a R32/R1234ze(E) mixture at different mass composition have been studied in a single minichannel with an inner diameter of 0.96 mm. Experimental heat transfer coefficient during condensation and flow boiling and pressure drop data are presented and compare against different correlations.

This manuscript is organized as follows:
- Section 2: description of the available test facility and test sections with an inner diameter of 0.96 mm used for heat transfer and two-phase frictional pressure drop measurements;
- Section 3: design and construction of a new test section for heat transfer experiments on normal gravity and microgravity conditions;
- Section 4: condensation test with HFE-7000 in the 0.96 mm inner diameter test section and condensation tests with R134a in the new test section on ground;
- Section 5: condensation heat transfer in microgravity conditions with HFE-7000 in the new test section;
- Section 6: two-phase frictional pressure drop for the mixture R32/R1234ze(E) and pure R1234ze(E) in the 0.96 mm inner diameter minichannel;
- Section 7: condensation heat transfer of R32/R1234ze(E) non-azeotropic mixtures inside the minichannel with 0.96 mm diameter;
- Section 8: flow boiling of R32/R1234ze(E) mixture inside the 0.96 mm inner diameter minichannel.

2   EXPERIMENTAL APPARATUS

2.1   Introduction

The experimental apparatus available at the Two Phase Heat Transfer Lab at the University of Padova is hereafter described. The test rig allows to perform heat transfer and pressure drop measurements during condensation and vaporization of refrigerant inside channels.

2.2   Available test facility

A schematic layout of the test facility is reported in Figure 2.1. The facility consists of a primary refrigerant loop and three auxiliary water loops. The refrigerant loop underwent several washing cycles before filling it with the refrigerant, to remove all possible contaminants. During test runs, in the primary loop, the subcooled refrigerant exiting the post-condenser is sent through a filter dryer by an independently controlled gear pump that is magnetically coupled to a variable-speed electric motor. The gear pump is an oil-free system, thus no oil separator is required in the refrigerant loop. The refrigerant mass flow rate is measured by a Coriolis-effect mass flow meter. Hence, the fluid passes through a mechanical filter, and using the hot water of the secondary loop, it can be vaporized and superheated in a tube-in-tube heat exchanger. Then the working fluid can be sent in different test sections for heat transfer or pressure drop measurements. Of the available test section installed before the realization of the new one, two will be used in this thesis:
- the heat transfer test section with an inner diameter of 0.96 mm;
- the pressure drop test section with an inner diameter of 0.96 mm.
In the heat transfer test section (described in 2.2.1) the fluid can be condensed or vaporized. Both the sectors are served by the same thermal bath, using distilled water as secondary fluid. Each hydraulic loop is provided with a flow regulating valve and a Coriolis effect mass flow meter to set and measure the mass flow rate. When necessary the inlet water temperature in the pre-conditioning sector and in the measuring sector can be maintained at different values by using electrical heaters installed downstream of the thermal bath in each loop. In each sector the inlet and outlet water temperature is measured with a T-type thermocouple and the temperature difference is checked using a triple junction thermopile. On the refrigerant side the refrigerant temperature is measured at the inlet of the pre-conditioning sector and of the measuring sector with two T-type thermocouples and along the measuring sector with a three junctions thermopile soldered at the two ends.

The experimental test section for pressure drop measurements consists of two parts: a counter-current heat exchanger (pre-conditioning sector) and an adiabatic channel (measuring sector, described in 2.2.2). The pre-conditioning sector is a mini shell-and-tube counter-current heat exchanger and its purpose is to achieve the desired saturated thermodynamic state of the refrigerant at the inlet of the measuring sector by setting the inlet temperature and the mass flow rate of a secondary flow of distilled water. The

secondary fluid is supplied by the dedicated thermal bath through an hydraulic loop provided with a flow regulating valve and a Coriolis effect mass flow meter. The water outlet temperature in the pre-conditioning sector is measured by a thermocouple and the water temperature difference between inlet and outlet is measured by a copper constantan triple-junction thermopile. Static mixers have been positioned upstream of the water temperature sensors and therefore the measured temperatures can be considered as the mean effective temperatures. On the refrigerant side the temperature at the inlet of the pre-conditioning sector is measured by a T-type thermocouple; other two thermocouples are located upstream and downstream of the measuring sector.

In both the test sections (pressure drop and heat transfer test section), the operative pressure is measured at the inlet and outlet of the pre-conditioning sectors by means of two relative pressure transducers, whereas two differential pressure transducers with different full scale (1 kPa and 100 kPa) are employed to measure pressure drop along the measuring sectors.

At the exits of the test sections the fluid is collected and sent to the post-condenser in which is subcooled using another thermal bath serving brine at 5°C. During the test runs, when the apparatus is working in steady-state conditions, measurements of pressure, temperature, and mass flow rate are recorded for 50 s and averaged.
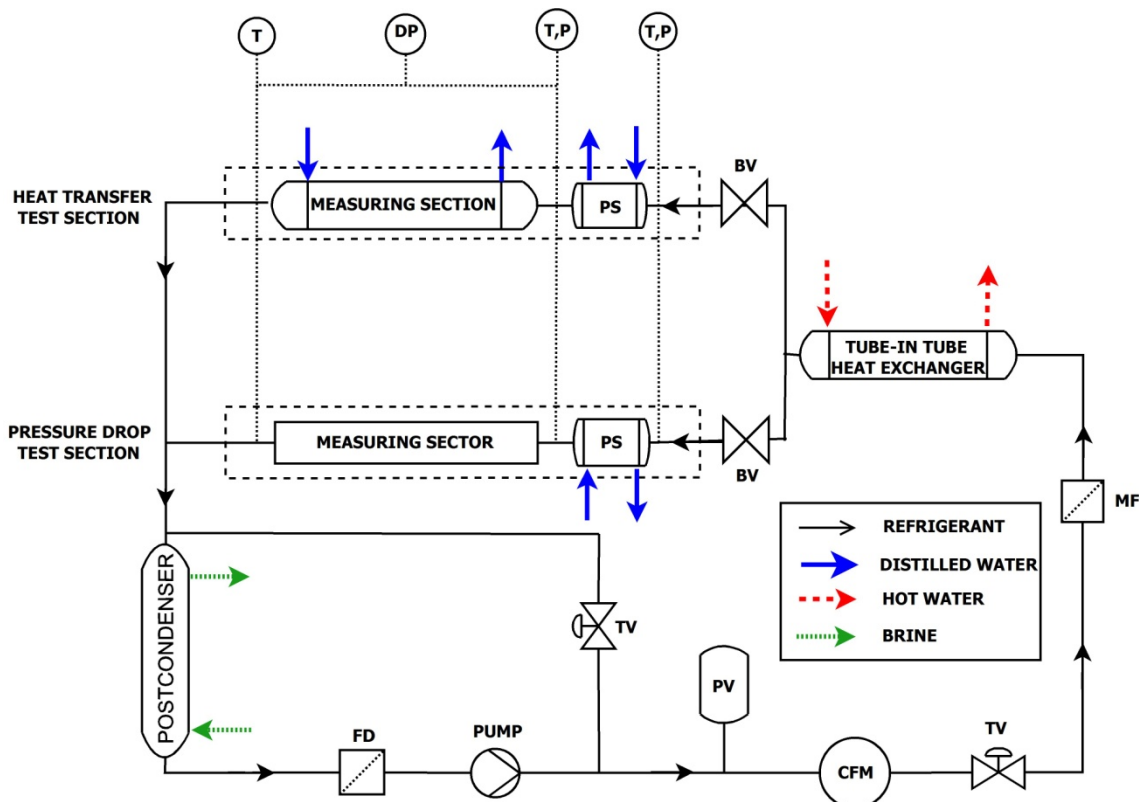

Figure 2.1. Experimental test rig: MF (mechanical filter); FD (filter dryer); PV (pressure vessel); CFM (Coriolis-effect mass flow meter); TV (valve); BV (ball valve); P (pressure transducer); DP (differential pressure transducer); T (thermocouple).

2.2.1 Description of the available heat transfer test section

The heat transfer test section (Figure 2.2) consists of two parts that work as counter-current heat exchangers: the pre-conditioning sector which is 55 mm long and the measuring sector that is 227.5 mm long. They are both obtained from an 8 mm external diameter copper rod having a 0.96 mm internal bore and an arithmetic mean roughness of the inner surface Ra of 1.3 μm. The uncertainty associated to the diameter is determined from an enlarged image of the minichannel obtained by a microscope and it is equal to ±0.02 mm including dimensional and geometric tolerances. The roughness measurement has been performed following the EN ISO 4287 standard [9] with the digital surface roughness machine ZEISS-TSK Surfcom 1400A.

The test section is connected to the test rig by means of two stainless steel capillaries, with an internal diameter of 0.762 mm and an inner surface roughness $Ra=2$ μm; because of the low thermal conductivity they guarantee thermal separation and allow the insertion of two pressure ports, 23 mm far from the inlet and outlet of the measuring sector, connected to the pressure transducers. The presence of both temperature and pressure transducers at the inlet of the measuring section allows a check of the saturation temperature during two-phase heat transfer tests.

The external surface of the copper rod was machined to embed the secondary fluid channel (Figure 2.3), which is closed externally using an epoxy resin sheath that allows also the insertion of the thermocouples. Such channel geometry for the water enables good water mixing for a precise local coolant temperature measurement, and, at the same time, it reduces the coolant-side heat transfer resistance, leading to low measurement uncertainty. The inlet and outlet water temperatures are measured by thermocouples at the ends of each part of the test section, while the water temperature differences across both parts are measured by multi-junction copper-constantan thermopiles. Moreover, in the measuring section, the local water temperature profile is calculated from the measurements of fifteen thermocouples placed in the secondary fluid channel. The local wall temperatures are gauged by thirteen thermocouples embedded into 0.6 mm diameter cylindrical holes in the wall which were realized 0.5 mm far from the internal tube surface along the measuring section (Figure 2.4). The accommodation of the wall thermocouples is made in such a way as the thermocouple wires do not cross the coolant path, therefore the error of the temperature measurements due to axial conduction along the thermocouple wire and the spurious electromotive force build up for the presence of high temperature gradients is minimized.

After the construction, the test section was accurately insulated to minimize heat dissipation. More details on the test section design and building are given in Matkovic [10].
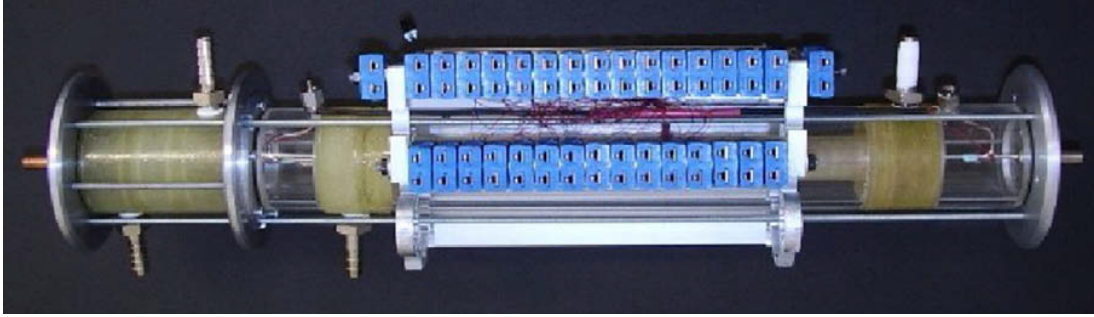
Figure 2.2. Heat transfer test section, d_h=0.96 mm
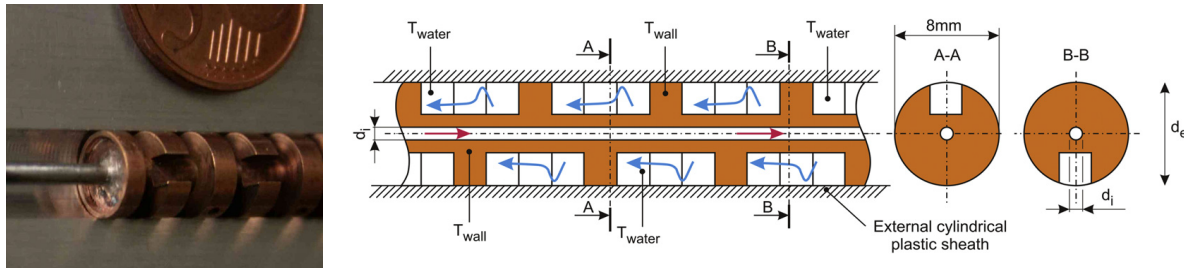
Figure 2.3. Details of the external coolant path
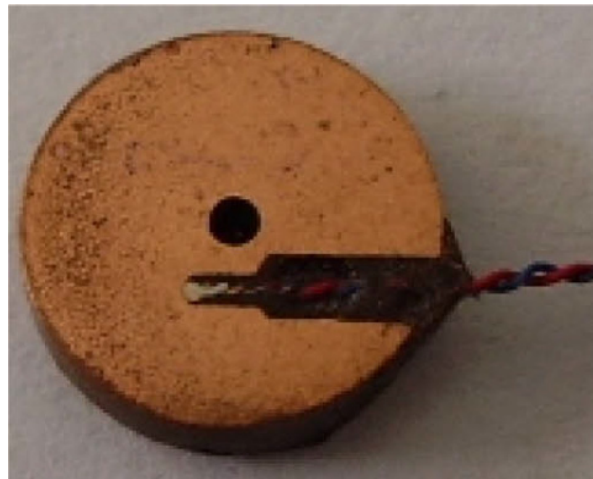
Figure 2.4. Detail of the thermocouple emended in the wall

2.2.2 Description of the available pressure drop test section

The test section used for pressure drop measurements is installed in the experimental apparatus described in Section 2.2 and depicted in Figure 2.1. The experimental test section consists of two parts: a counter-current heat exchanger (pre-conditioning sector) and an adiabatic channel (measuring sector).

The measuring sector was made from an 8 mm external diameter copper rod having a 0.96 mm internal bore and an inner surface roughness Ra is equal to 1.3 µm, as defined by the EN ISO 4287 standard [9]. The inner surface roughness has been measured with the digital surface roughness machine ZEISS-TSK Surfcom 1400A.

The measuring sector is connected to the rest of the test rig through two adiabatic stainless steel tubes. Two pressure ports have been machined at the inlet and at the outlet of the 0.96 mm copper minichannel: the distance between the two ports is equal to 220 mm.

The design of the stainless steel pressure ports was carefully realized in order to avoid any geometry change in the cross section of the minichannel and any variation of the refrigerant flow. Thus, the copper channel was predrilled with holes of 0.5 mm for the pressure ports accommodation. To avoid melted material from obstructing the flow passage and to reduce oxidation of the tube, soldering was performed at constant nitrogen flow within the minichannel and on the external side. Furthermore, the two pressure ports were located at a distance equal to 50 times the hydraulic diameter from the inlet and the outlet of the minichannel, in order to be out of the developing flow length. Other details on the realization of the measuring section can be found in [11]. All the pressure transducers are connected to the pressure ports by stainless steel pressure lines provided with wire electrical heaters. On the refrigerant side one thermocouple is placed at the inlet of the pre-conditioning sector and two thermocouples are located upstream and downstream of the measuring sector on the two stainless steel tubes.

3 DESIGN AND CONSTRUCTION OF A NEW TEST SECTION FOR GROUND AND MICROGRAVITY HEAT TRANSFER EXPERIMENTS

3.1 Introduction

Evaporation and condensation processes are used in many engineering fields (e.g. energy conversion, chemical, pharmaceutical and food industries) and, particularly, in space applications. For example, Loop Heat Pipes and Capillary Pumped Loops are used on satellites to ensure the heat transfer from core a module to a radiator. The main components of Loop Heat Pipes and Capillary Pumped Loops are evaporators and condensers, using latent heat of vaporization of the fluid to transfer heat efficiently at a nearly constant temperature.

While evaporation is already studied in microgravity conditions, much less investigation has been performed on the effect of microgravity during convective condensation. In order to reduce the size of the equipment and at the same time to increase their performance, in a wide range of applications and especially in the aerospace industry, requires a better knowledge of convective condensation inside tubes, in particular since there are operating conditions when the condensing heat transfer is strongly affected by gravity.

In the following chapters a new experimental test section to study the convective condensation inside channels will be presented and tested both in normal and microgravity conditions; heat transfer coefficient data and flow visualizations will be presented during convective condensation, when the two mechanisms of surface tension and shear stress at the liquid-vapour interface compete to control the heat transfer.

In a recent paper, Lips and Meyer [12] presented an experimental research on convective condensation of R134a at 40 °C saturation temperature in a smooth tube (8.38 mm inner diameter) for the whole range of inclination angles, from vertical downward to vertical upward, and for mass velocities ranging from 200 kg m^{-2} s^{-1} to 600 kg m^{-2} s^{-1}. It was highlighted that at high mass velocities, the shear stress is the dominant force and there is no effect of inclination on the heat transfer but for low mass velocities and low vapour qualities flow pattern is strongly dependent on the inclination angle. On ground gravity conditions Del Col et al. [5] measured the heat transfer coefficient during condensation of R134a in a square minichannel with 1.23 mm internal hydraulic diameter with different orientation both upflow and downflow. They found that, when varying the inclination angle, at high mass flux the heat transfer coefficients display a trend that one would expect for condensation inside conventional tubes, but at low mass flux (G<200 kg m^{-2} s^{-1}) the shear stress may not be the dominant force and a gravity effect appears. This implies that gravity has a role in the distribution of the liquid film on the wall. The authors developed also a criterion to determine a gravity dependent zone, where gravity has a relevant effect, as a function of fluid properties, channel diameter, mass velocity and vapour quality.

Some studies aim also to analyze condensation in the condition of low gravity effect by considering condensation in capillaries. In that case, it is expected that the surface tension

effects, as well as the viscous effects, are great compared to the gravity effect [13, 14]. Such studies are complementary as the range of surface tension force, viscous force and inertial effect in a conventional channel or a minichannel with microgravity shall be different as compared to the range of these forces in a capillary tube. This modification of surface tension effect implies that viscous and inertia are also greatly modified.

In particular, in this Section will be presented:

- the design steps of a new test section for the measurement of the quasi-local heat transfer coefficients both in normal and reduced gravity conditions;

- the realization process of the new test section included the material selection and the technological solutions adopted.

3.2 Design of the new test section

3.2.1 Test section diameter

The new test section will be developed to investigate the effect of gravity during condensation, thus it should be designed keeping in mind this goal.

In the work of Del Col et al. [5], published in 2014, the authors investigated the effect of inclination during condensation of R134a and R32 in a minichannel with an inner hydraulic diameter of 1.23 mm and square cross section. They found that the effect of the channel inclination on the condensation heat transfer coefficient becomes noteworthy in downflow, at vapor qualities less than about 0.6 and mass velocities lower than a critical value G = 150 kg m^{-2} s^{-1} for R134a and G = 200 kg m^{-2} s^{-1} for R32. What is more interesting is that, they have developed a dimensionless correlation with the aim of predicting the critical mass velocity at which, in vertical downflow configuration, the effect of inclination starts to appear. The dimensionless inclination parameter Y^* (Eq. 3.1) calculated using, the Eötvös number Eo, the thermodynamic vapor quality x and the density ratio $\Delta\rho/\rho_G$, allows to predict a gravity dependent region as a function of the working conditions during condensation.

$$Y^* = 0.185 \cdot Eo^{0.35} \left(\frac{\Delta\rho}{\rho_G} \right)^{0.65} x^{-1.748} \qquad \textbf{3.1}$$

The Y^* parameter should be compared with the dimensionless inclination parameter Y as reported in Eq. 3.2 and firstly defined by Taitel and Duckler in [15]:

$$Y = \frac{\Delta\rho \cdot g \cdot \sin(\beta)}{\left(\dfrac{dp}{dz} \right)_{f,G}} \qquad \textbf{3.2}$$

where, β is the inclination angle which is equal to 0° in horizontal configuration and 90° in vertical downflow and $(dp/dz)_{f,G}$ represents the single-phase pressure gradient for the vapor phase and it is calculated from Eq. 3.3:

$$\left(\frac{dp}{dz}\right)_{f,G} = \frac{2f\,G_G^2}{d_h\rho_G}$$

3.3

the Fanning friction factor f is computed for the present channel using the proper friction factor – Reynolds number product in the laminar region equal to 16 and the Churchill [16] equation in the turbulent region.

If this criterion, to define a gravity dependent region, is applied to a round tube of 1 mm for R134a and HFE-7000 the critical mass velocity is about 150 and 50 kg m⁻² s⁻¹. If a tube of 3 mm is considered the critical mass velocity moves to 200 and 70 kg m⁻² s⁻¹; increasing the internal diameter the minimum mass velocity to appreciate an effect of gravity is increased. For the new test section the choice of a tube with an internal diameter of 3 mm seems also to be good from the point of view of the measurement of the heat transfer coefficient, because in this way a higher heat flow rate is exchange, reducing the uncertainty in the evaluation of the heat flux and consequently the uncertainty on the heat transfer coefficient. After a market survey a tube with an internal diameter of 3.4 mm was found as a good compromise between costs and realization constrains of the test section.

In Figure 3.1 the gravity dependent region for a round tube with a inner diameter of 3.4 mm is presented for R134a (left) and HFE-7000 (right).

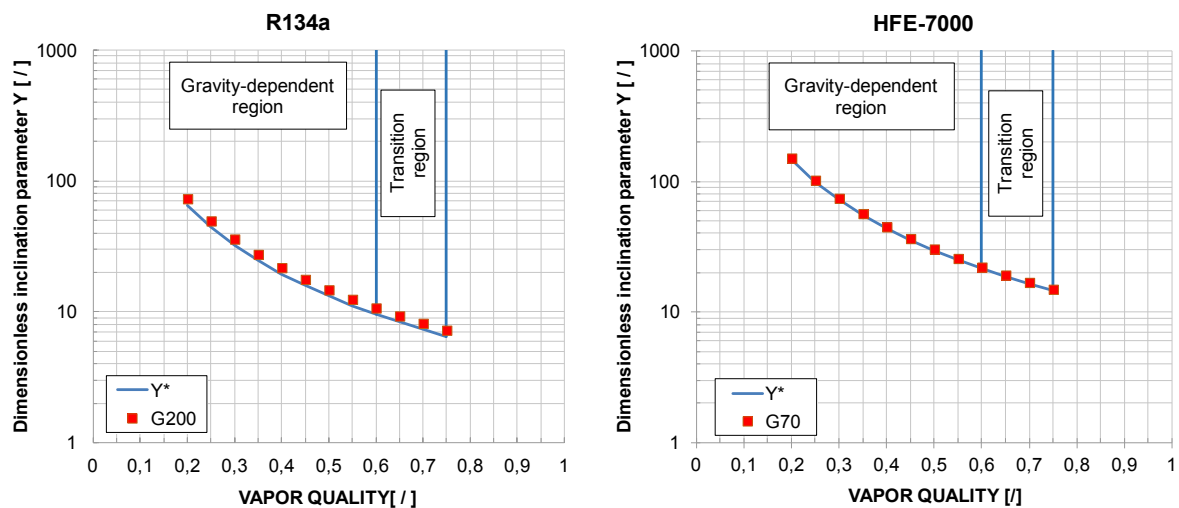**Figure 3.1. Dimensionless inclination parameter versus vapor quality. Each plot is related to a mass velocity _G_. Left: _G_ = 200 kg m⁻² s⁻¹ and R134a; right: _G_ = 70 kg m⁻² s⁻¹ and HFE-7000. The curve of _Y*_ bounds the gravity-dependent region and determines at which _G*_ the inclination starts to affect the condensation heat transfer coefficients taking the horizontal configuration as reference case.**

3.2.2 Test section tube length

The first step of the design process is the calculation of the tube length. The basic idea is to realize a test section similar to a tube in tube heat exchanger in which the quasi-local heat transfer coefficient can be measured with a low uncertainty and some visualization of the flow pattern can be performed. Thus the idea is to realize a test section with two heat exchangers divided by an adiabatic glass tube with the same internal diameters. This kind of layout will help for sure the realization of the test section because it will avoid to machine a long copper tube.

In general as reported in Matkovic et al. [17] some good tips for the design process of an heat transfer test section are the following:

1) High heat transfer coefficient and enhanced surface area on the external path: since the test tube is a condenser, its length will depend severely on the single-phase heat transfer on the coolant side, thus increasing the heat transfer coefficient on the coolant side will lead to a tube length mainly dependent only on the refrigerant heat transfer coefficient. According with this tip the leading thermal resistance will move on the refrigerant side so the wall to refrigerant temperature difference will rise at given heat flow rate resulting in an evaluation of the heat transfer coefficient with a lower uncertainty.

2) Homogenous wall temperature distribution: the enhance surface area will help in reducing systematic errors in the wall temperature measurements.

3) Low thermal resistance of the channel wall and low axial heat conduction: these seem to be two opposite features because a high thermal conductivity of the test tube will increase the axial heat flux. A high thermal conductivity of the wall will lead to a lower error due to deviation in temperature sensor positioning, but to avoid a high axial heat flux the wall thickness should be keep as small as possible.

4) Good coolant mixing: for a precise measurement of the water temperature a good mixing of the water is necessary to avoid temperature gradient on the water profile.

The optimum tube length is assumed to be the one required for complete condensation of superheated vapor of HFE-7000 at G=150 kg m^{-2} s^{-1}. With a superheating of about 15 K the total heat flow rate is approximately of 160 W. HFE-7000 is the working fluid that will be used for the condensation tests in microgravity conditions.

The following assumptions have been considered:

- the higher heat transfer resistance is on the refrigerant side, so the external heat transfer resistance can be neglected for the evaluation of the heat transfer length;

- on the refrigerant side the Cavallini et al. [18] model has been used for the evaluation of the heat transfer coefficient and the outlet vapor quality at the exits of the test section is 0.05, to avoid computational problems;

- heat is transferred from refrigerant to coolant only and no axial heat conduction is present;

- saturation temperature depends on saturation pressure only and the Del Col et al. [19] model has been used to evaluate the frictional pressure drop;

- fixed temperature difference between the wall and the fluid.

According with these assumptions the necessary heat transfer length to condense HFE-7000, is about 700 mm or 600 mm respectively with temperature differences of 8 and 10 K. If the wall temperature is not considered constant but it increases following the water temperature profile due to heat transfer and thus a mean wall to refrigerant temperature difference value equal to 6 K is considered, the necessary heat transfer length is about 900 mm. These values are the active heat transfer lengths so connection lengths and water distributors spaces are not considered. A test section with an active heat transfer length of 800 or 900 mm can be used on ground but for microgravity measurements during parabolic flight it is too long; moreover technological constrains due to the lathe available in the workshop should be considered. This means that a compromise should be found.

In the end, the first heat exchanger has been divided in three parts call sub-sectors, each sub-sector with an active heat transfer length of 100 mm; the second heat exchanger has been divided in two sub-sectors with an active heat transfer length of 128 mm. The sub-sectors of the second heat exchanger are longer because, proceeding the condensation process, the heat transfer coefficient decreases and so if the length is the same the heat flux will be lower. At some working conditions this can lead to a low water temperature difference resulting in a higher uncertainty on the evaluation of the heat flow rate. Thus the sub-sectors in the second heat exchanger are about the 30% longer.

3.2.3 Design of the coolant path

Before starting with the choice of the various materials and the construction of the test section some simulations have been run to assess the best coolant geometry.
The crucial points on the coolant side design are the following:
- inlets and outlets of the coolant path;
- external path geometry to obtain high heat transfer coefficient and enhanced surface area;
- position of the thermocouples on the wall.
Inlets and outlets of the coolant paths have been firstly studied by means of 1 jet perpendicular to the z-axis of the section. This solution led to very high temperature gradient at the inlet and outlet of the test section because part of the channel was hit by a water flow with high velocity and part was in contact with backwater. Additional studies with 4 and 5 jets reveal better solutions for the intake and outtake. Thus the final design of the inlet and outlet water path has been done with 5 jets as is reported in Section 3.3.4.
During the design step different materials for the refrigerant side have been considered. The initial idea was to use sapphire tubes for the refrigerant side but this idea was mainly discarded due to the problems in machining sapphire to realize the secondary fluid path; thus copper was found as a good solution and the results hereafter reported regards only the simulations done with copper.
Simulations have been run considering only a sub-sector and with the following assumption:
- heat is exchanged only between the water and the copper;
- influence of the gravity is not considered;

- imposed constant heat transfer coefficient on the refrigerant side.

Regarding the geometry of the coolant path the idea is to start from a copper tube and machined it to obtained fins and groves. The fins have different objectives:

- increase the heat transfer area;

- realize a good coolant mixing, preventing high temperature gradient;

- fixed temperature and velocity of the water at the inlet;

- allow to insert the wall thermocouples inside holes machined on the copper without having wires crossing the coolant path.

What is important is to decide the geometry of the fins and the position of the thermocouples to a correct evaluation of the refrigerant heat transfer coefficient.

The first geometry tested was the one depicted in Figure 3.2; with two fins on the water side. This can be considered as a first attempt to design the coolant path.
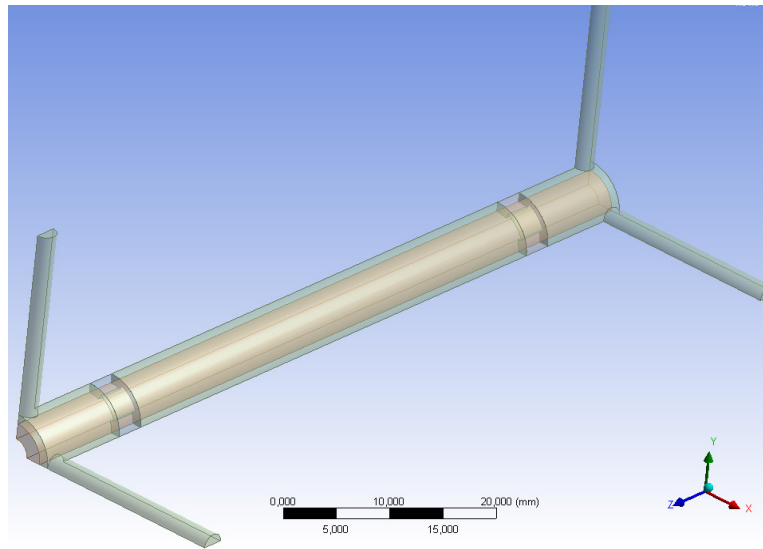
Figure 3.2. Sketch of the geometry used in the simulations

To verify the quality of the geometry the heat transfer coefficient imposed on the refrigerant side is compared with the one calculated using the temperature in the copper in the same position in which the thermocouple will be placed. Thus, as result of the simulation, the water temperature at the outlet is obtained and the heat flow rate can be evaluated; the temperature profiles on the copper are also known (Figure 3.3) and the heat transfer coefficient can be calculated using the local wall temperature at the same coordinates of the thermocouples. With this geometry the water flowing in the path is mixed only in correspondence of the two fins leading to a temperature profile which is modified in the presence of the fins. The calculated heat transfer coefficient is 1% different if compared with the imposed one.
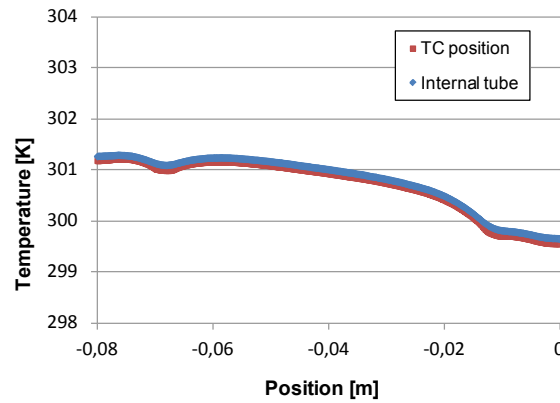
Figure 3.3. Profile of the wall temperature along a line on the copper tube.

As a result, the geometry of the coolant path has been changed adding some more fins rotated of 45° one after the others in the axial direction. Thus in the new geometry, there are 7 fins and each one has 4 grooves. The resulting geometry is depicted in Figure 3.4.
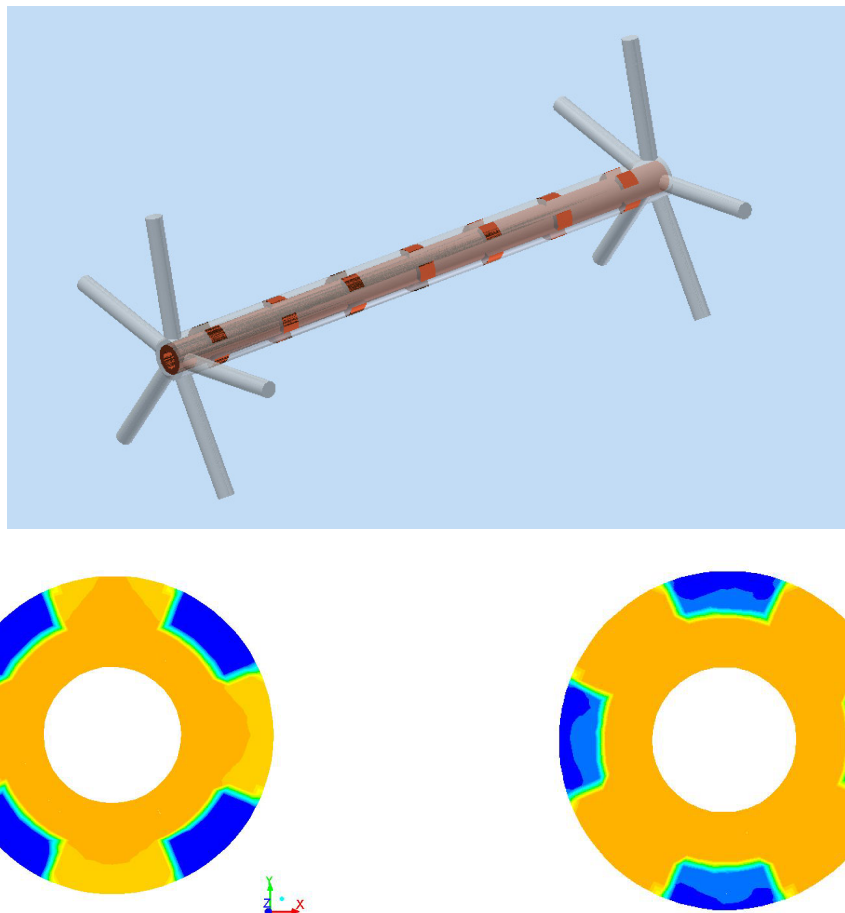
Figure 3.4. Top: Sketch of the new geometry used in the simulations. Bottom: temperature distribution on an axial cross section of the test section in two subsequent fins.

With this geometry the resulting temperature profile along the copper wall in the correspondence of the thermocouple positioning is reported in Figure 3.5 under the following boundary conditions:

- refrigerant heat transfer coefficient equal to 3000 W m^{-2} K^{-1};
- refrigerant temperature of 40°C;
- water mass flow rate of 20 kg h^{-1}
- inlet water temperature of 25 °C.
- laminar condition on the water side.
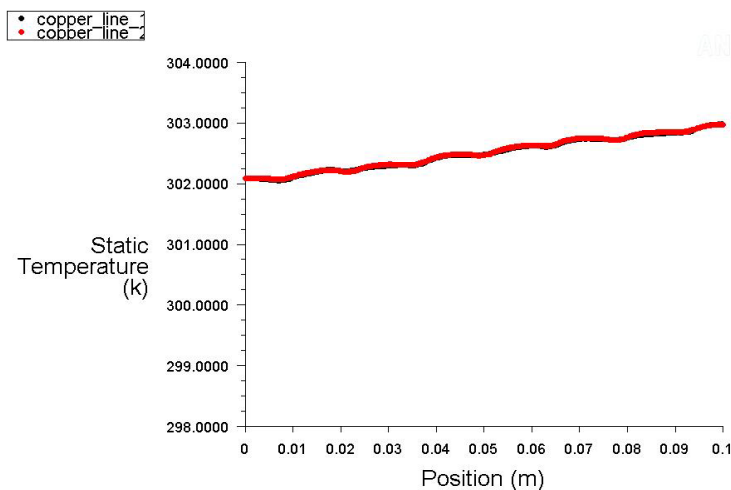
Figure 3.5. Profile of the wall temperature along a line on the copper tube.

Compare with the profile in Figure 3.3 there are no sharp increases after the fins and the profile results globally more linear.

Different calculation have been performed to evaluate the heat transfer coefficient, using the mean logarithmic temperature difference between the imposed temperature of the refrigerant and considering to evaluate the wall temperature in the 1st and 7th fin or in the 2nd and 6th fin or in the 3rd and 5th fin. The results are promising because with this geometry the error between the calculated and the imposed heat transfer coefficient is below 1% under these conditions. The same simulations have been repeated imposing an internal heat transfer coefficient of 1000 W m^{-2} K^{-1} and 5000 W m^{-2} K^{-1} obtaining an error of approximately 0.4% and 1.3% independently from the pair of fins used.

Some simulations have been performed under the same conditions but assuming a turbulent conditions on the water side and they gave quite similar results.

To conclude, this last geometry allows to evaluate with an high precision the internal heat transfer coefficient measuring the wall temperature in different positions, and thus it will be the one used to realize the new test section.

3.3   Construction of the new test section

After the design there has been a material selection process and a first prototype has been realized. Hereafter the complete process is described.

3.3.1   Starting materials

For the realization of the test section, copper tubes will be used for the refrigerant circuit and lexan tubes and sheets for the coolant path.

Using a polished piece of the copper tube the internal diameter has been measured with a numerical microscope (Figure 3.6). The internal diameter of the copper tube results to be 3.38 mm ± 0.02 mm. The external diameter of the copper tube is about 7 mm.
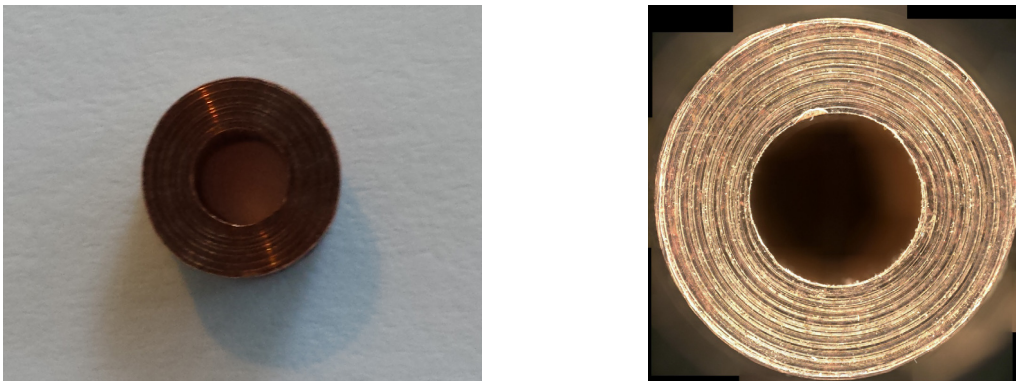
Figure 3.6. Cross section of the copper tube for the measurements of the internal diameter

The internal surface roughness of the tube (*Ra*), at different positions, has also been measured and is about 0.18 μm.

In Figure 3.7 the copper tube cut for the roughness measurements is depicted.
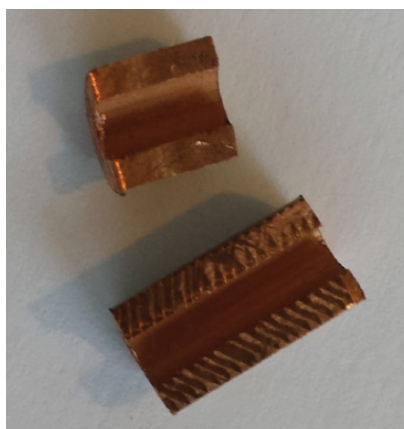
Figure 3.7. Pieces of the copper tube used for the roughness measurements.

The lexan tubes have an internal diameter of 7 mm and an external one of 10 mm.

The lexan sheet used for the realization of the water distributors has a thickness of 15 mm.

3.3.2 Test section prototype

A simple prototype has been made to verify the feasibility of the complete realization process. This prototype was used to test the machining process of the copper tube, the bonding process of the different parts and to understand the problems of embedding the thermocouples on the wall.

The starting copper tube has been machined to realize the coolant path Figure 3.8 (top). Compare to the final one a very simple coolant path has been realized, with only two fins and two groves. From the initial design the grooves should be 4 for each fin, but this was very difficult to realize due to small size of the external copper diameter.

Lexan tube and distributors were than glued on the copper tube and the holes for the thermocouples drilled Figure 3.8 (bottom).

Some leakage tests on the water side were performed. These tests proved the perfect sealing of all the bonding processes, a fundamental step to the construction of the final section.
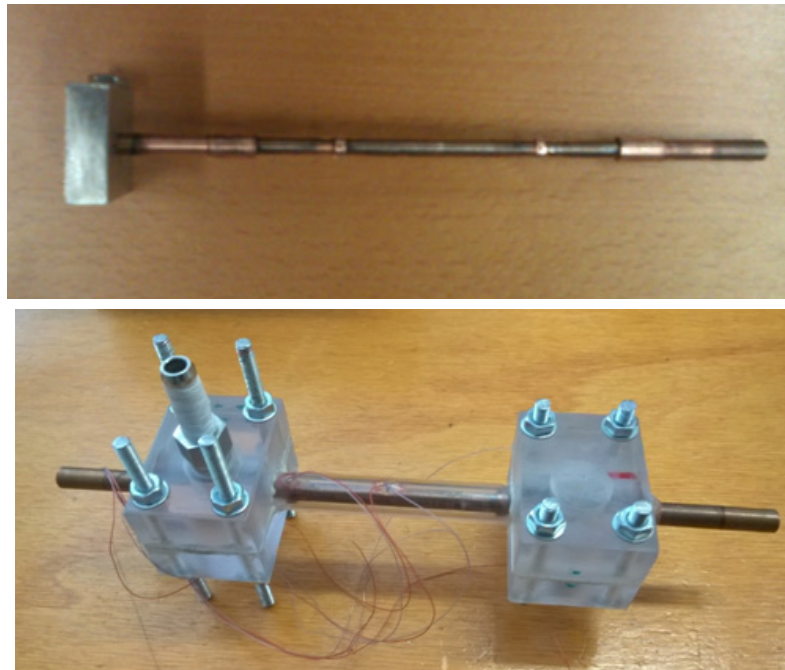
Figure 3.8. Top: copper tube machined for the prototype test section. Bottom: prototype test section after the thermocouples installation.

3.3.3 Machining of the copper tubes

As described in Section 3.2.2, the test section is composed of two counter-current heat exchangers. Each heat exchanger is composed of several sub-sectors for the measurements of the quasi-local heat transfer coefficient: the first heat exchanger has 3 sub-sectors and the second heat exchanger has 2 sub-sectors (Figure 3.9).
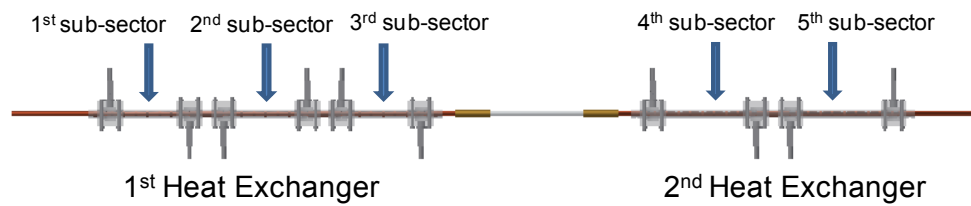
Figure 3.9. Simple layout of the test section

The cores of the heat exchangers are obtained from the copper tubes previously described, after a matching process to create the coolant path. The technical drawings of the heat exchangers are reported in the Annex 10. The particular geometry of the coolant path decreases the water side heat transfer resistance:

- increasing the external heat transfer area;
- disturbing the boundary liquid layer changing continuously the flow direction;
- mixing the coolant flow through the complex flow passages.

All these features allow to obtain a low heat transfer resistance on the water side, reducing the temperature difference between the copper wall and the coolant flow. This means that the higher temperature difference is on the refrigerant side, between the condensing fluid and the wall, which is favorable to a precise measurement of the heat transfer coefficient.

The first heat exchanger is 540 mm long (Figure 10.3) and is composed of 3 sub-sectors. Each one has an active heat transfer length of 100 mm. For active heat transfer length is considered the distance between the first and the last fin, in which the water is in contact with the copper tube. The geometry of the coolant path has been studied in Section 3.2.3 but due to problems encounter during the machining process of the prototype (Section 3.3.2) some few modification have been done. These sub-sectors (Figure 10.1) have 9 fins; on each fin there are only two grooves, to create the flow passage. Between one fin and the following the groves are rotated of 90°. Compare to the geometry studied in Section 3.2.3 the number of fin has been increased to have more fixing point along the tube to tighten it during the machining process on the lathe.

The second heat exchanger is 448 mm long (Figure 10.6) and is composed of 2 sub-sectors, with a heat transfer length of 128 mm, which is higher than the sub-sectors of the first heat exchanger. As explain in Section 3.2.2, to avoid some problems on the evaluation of the heat flow rate at low values of the heat transfer coefficient the heat transfer length has been increased. These sub-sectors (Figure 10.4) have 9 fins, with two grooves for each fin; compare with the sub-sectors of the first heat exchanger the distance between two subsequent fins (due to a feasible design) is changed. Between one fin and the following the groves are rotated of 90°.

A detail of one sub-sector and the first heat exchanger after the machining process are depicted in Figure 3.10 and Figure 3.11.
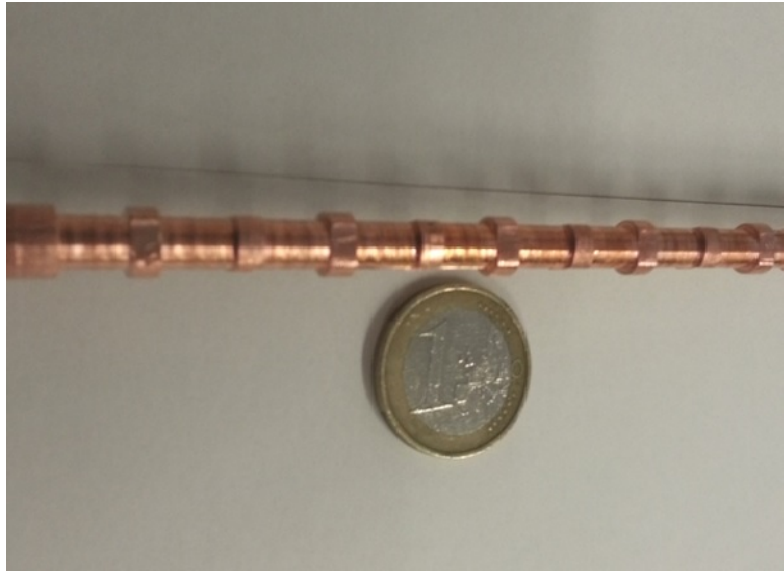
Figure 3.10. Detail of the copper tube in a sub-sector of the first heat exchanger. Fins and groves are visible.
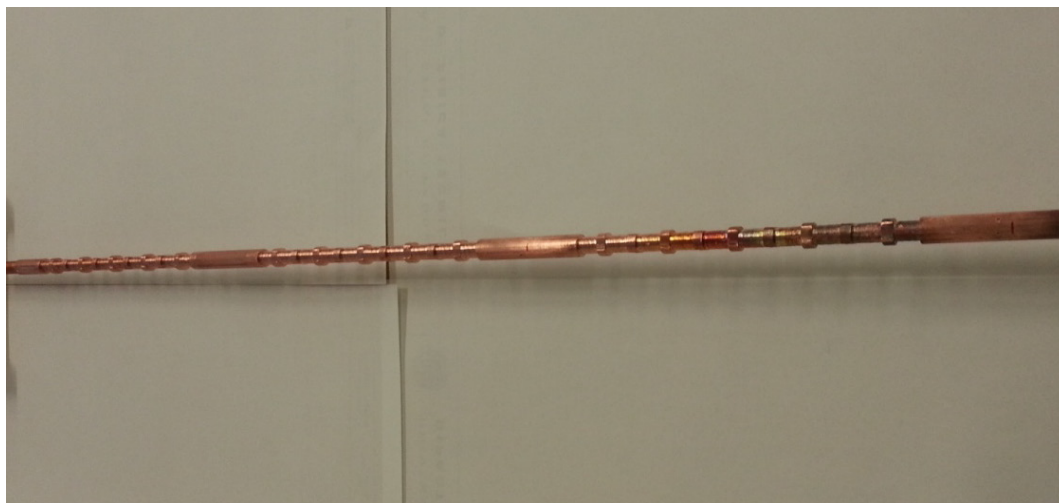
Figure 3.11. View of the first heat exchanger after the machining process

The test section has been designed for the measurements of the quasi-local two-phase heat transfer coefficient. On each sub-sectors the heat flow rate is evaluated on the water side and using the thermocouples embedded on the wall the quasi-local heat transfer coefficient can be evaluated.

Two pressure ports have been soldered at the inlet and outlet of the test section; one at the inlet of the first heat exchanger and one at the outlet of the second heat exchanger. The pressure ports have been soldered directly on the copper tubes, allowing a precise measurement of the pressure without any abrupt change in the geometry. The pressure ports are two stainless steel tubes with diameters of an eighth of an inch. Before soldering a pressure port a mark of 3.5 mm has been done in the copper tube and a 0.7 mm hole has been drilled to connect the port with the internal channel. An ad hoc copper ring has also

been used to solder the copper tube and the stainless steel tube in a robust way (Figure 3.12 - Left). The soldering process, which can appear very simple, has two different concerns.

The first one refers to possible obstruction to the fluid flow due to the entrance of melted materials in the minichannel. Therefore, the soldering took place while nitrogen was pressurized. Anyway the nitrogen flux should be controlled to not remove too much heat from the soldering point.

The second concern regarded the high heat flux from the hot spot. Thus the soldering of the pressure port should be done before any gluing of plastic pieces.

Taking into account these concerns the pressure ports have been soldered successfully (Figure 3.12 - Right).
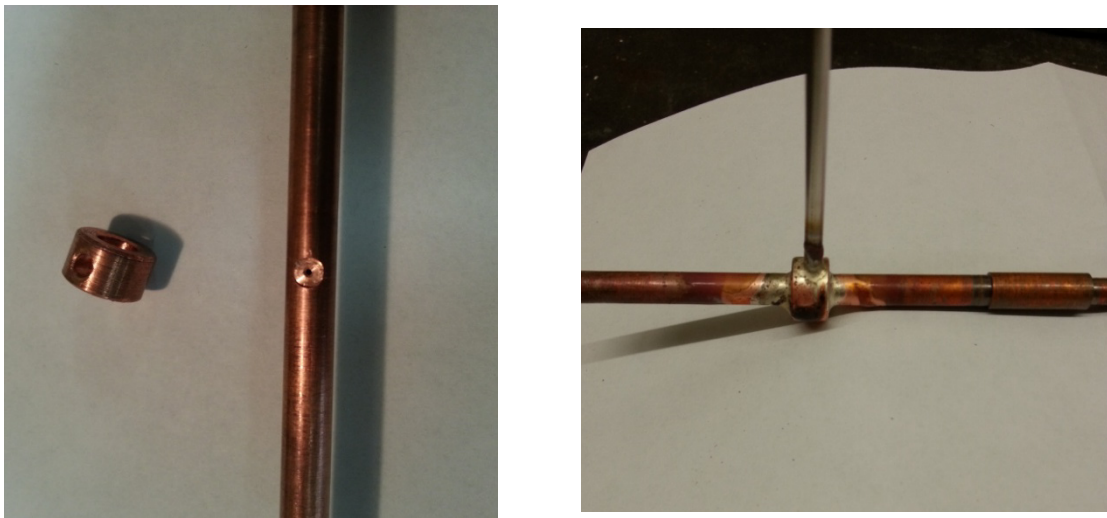
Figure 3.12. Left: copper tube with the hole and the copper bush for the soldering. Right: pressure port soldered on the heat exchanger

3.3.4 Machining of the lexan tubes and water distributors

The lexan tubes will be used as containment for the water side. Five tubes have been used, one for each sub-sector. On the lexan tubes, at both ends, 5 holes of 2 mm have been drilled every 60° along the circumference. Thinking about a circumference with 5 holes every 60° it means that only between two holes the radial distance is the double compare to the others. This has been specifically done to avoid that the water entering from the connection hoses goes directly, in perpendicular direction, inside the coolant path. In such a way the water is forced to fill the water distribution chamber before entering in the coolant path; this allows the water to enter with an uniform velocity and to avoid a water jet direct on the copper tube. This geometry has been analyzed through simulations reported in Section 3.2.3.

The water distributors have been realized, starting from a lexan sheet, with subsequent milling and drilling. Each distributor is realized in two parts which will be than glued together; the dimensions of each part are 30 x 40 x 15 mm. Inside each part a distribution chamber of 15 mm diameter and 8 mm depth is drilled; than the two part are temporarily

fixed together to drill a 10.25 mm hole in which the lexan tube will be inserted and glued. Lastly a 1/8" NPT connection has been attached. In Figure 3.13 one half of the distributor after the machining process is depicted.

To complete the water side, for each distributor, a mixer has been realized to mix the water and ensure a constant temperature in the direction of the flow.
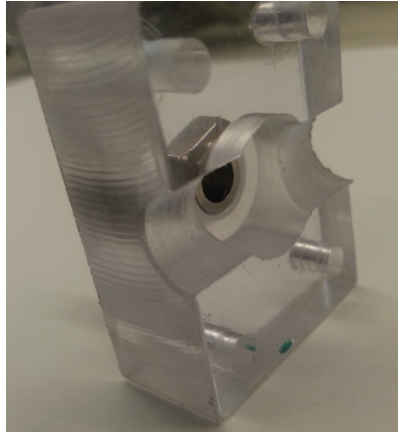
Figure 3.13. Piece of the water distributor obtained from the lexan sheet after the machining process

3.3.5 *Thermocouples and thermopiles*

All the T-type thermocouples and thermopiles used in the present test section are homemade from copper and constantan wires of 0.127 mm. One concern about the fabrication of thermocouples and thermopiles is that the tip should be as small and short as possible, to have a precise measurement and to avoid effect of heat conduction along the wires. All the thermocouples have been carefully fabricated to avoid these problems.

In each sub-sector six thermocouples are embedded in the copper wall. The holes for the thermocouples are 0.7 mm wide and 2.7 mm depth from the external surface of the lexan tube; so the thermocouple is place 0.6 mm far from the internal copper wall. On each sub-sector, six T-type thermocouples for the measurements of the wall temperatures have been distributed on the 2nd, 5th and 8th fin, on the two sides where the copper tube has not been machined (Figure 3.14). On the 2nd and 8th fin the thermocouples are placed one on the upper part and one on the lower part of the tube; on the 5th fin the two thermocouples are place in the middle of the tube. This distribution of thermocouples allows to evaluate the internal heat transfer coefficient with two different methods as reported in Section 4.2.2.

The accommodation of the wall thermocouples is made so that the thermocouple wires do not cross the coolant path; therefore the error of the temperature measurements due to axial conduction along the thermocouple wire and the spurious electromotive force build up for the presence of high temperature gradients is minimized.
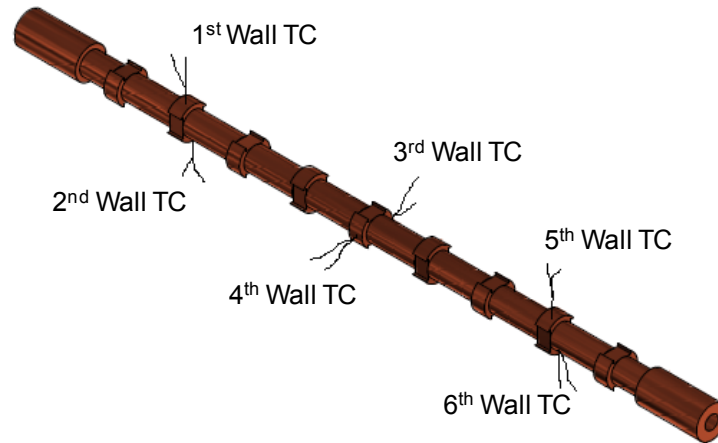
Figure 3.14. Position of the thermocouples on a sub-sector

Thermal conductive glue has been used to bond the thermocouple junction to the copper wall and then a bi-component glue is used to fix definitively the thermocouple wires on the lexan tube. For the present test section, of the 30 thermocouples installed, only two had some problems during the gluing process. One has been badly glued on the copper tube and one has been glued far from the internal wall because the tool of the drill broke inside the hole.

On the water side, for each sub-sector, two thermocouples and a triple junction thermopile are used to double check the temperature difference of the flowing water. In each distributor a thermocouple and one junction of a thermopile are glued inside a 1/8" stainless steel tube (Figure 3.15) which is then placed in contact with the water. Thermal conductive glue is used to isolate each junction of the thermopile and then to glue the sensors on the stainless steel tube.

The measurement of the water temperature at the inlet and outlet of a sub-sector is fundamental for a precise evaluation of the heat flow rate and then for the heat transfer coefficient. Thus it is important that before the temperature sensor the water is mixed and the boundary layer is broken to avoid possible temperature gradient. This is why some mixers have been placed on the water path before the water inlets and after the water outlets. The mixers are like the one depicted in Figure 3.16. They have been place inside a stainless steel tube of 6.5 mm and 30 mm long. The connections with the distributors are then realized with a stainless steel tube of 6 mm and 20 mm long.
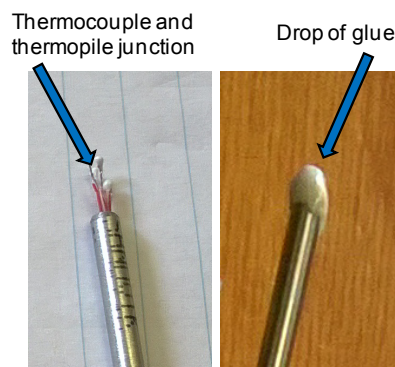
Figure 3.15. Water side thermocouple and thermopile inside the stainless steel tube

Figure 3.16. Mixer for the water side temperature measurements. Top: detail of the mixer. Bottom: stainless steel tubes for the connection of the mixer to the distributor and the temperature sensor

3.3.6 Glass tube

Between the two heat exchangers of the test section a borosilicate glass tube will be used for the visualization of the flow patterns. The glass tube is 200 mm long and has an internal diameter of 3.4 mm; in this way the flow disturbances due to possible steps between the copper tube and the glass tube will be minimized.

The glass tube and the fittings that will be used have been tested up to 20 bar (Figure 3.17).

Figure 3.17. Glass tube for visualization during the leakages test.

3.3.7 Assembling of the test section

Once all the components have been machined and prepared they have been assembled for the realization of the test section.

The steps were the following:

- the lexan tubes have been glued on the copper tube. This gluing process takes place in several times to give the right time for the lexan tube of each sub-sector to stick on the copper tube. Two picture of this process are reported in Figure 3.18. After the gluing process the cross section of a sub-sector appears as depicted in Figure 3.19;
- the holes for the wall thermocouples have been drilled on the lexan and copper tubes, the holes are 0.7 mm wide and 2.7 mm depth from the external surface of the

lexan tube, so the thermocouple is place 0.6 mm far from the internal copper wall (Figure 3.20);

- the distributors have been glued on the lexan tube. This step was quite difficult because the distributors should be placed just above the inlet holes of the lexan tube and between two subsequent distributors there should be enough space for the support of the test section;
- wall thermocouples have been embedded;
- the mixers have been attached at the inlet and outlet of each sub-sectors; water temperature sensors were also placed.

At this point a sub-sector of the test section appears as depicted in Figure 3.21.

Then the two heat exchangers have been positioned, with ad hoc supports, on an aluminum bar. The heat exchangers and the mixer have been insulated, to reduce the heat dissipation to the ambient. The glass tube have been connected using bore through fittings, in such a way there are no abrupt changes in the geometry between the copper and the glass.

In the end the total distance between the two pressure ports results to be 1080 mm.

Figure 3.18. Gluing process of the lexan tubes and the copper tubes
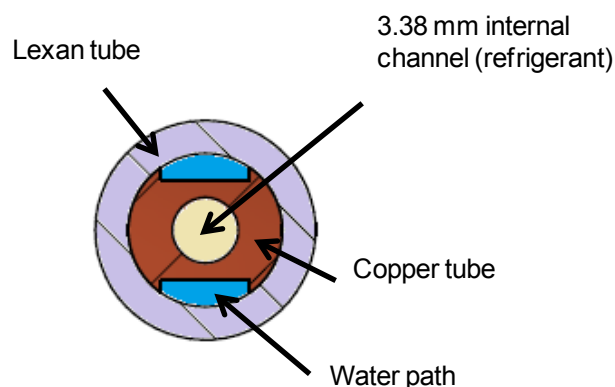
Figure 3.19. Cross section of a sub-sector. The copper tube is brown, the coolant water path is blue and the lexan is violet
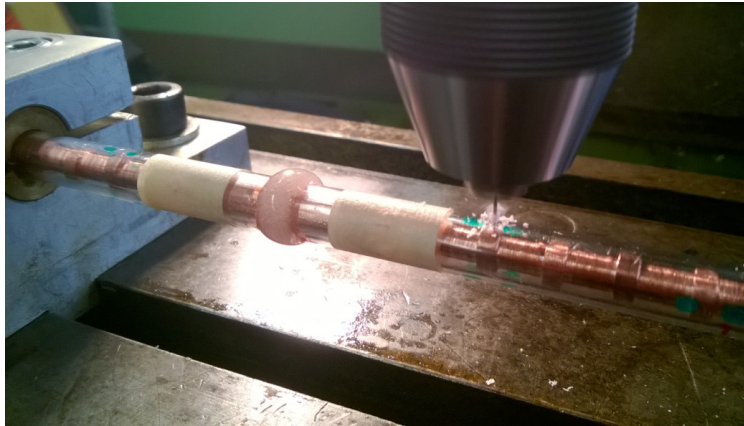
Figure 3.20. Drilling of the lexan and copper tubes for the realization of wall thermocouples holes.
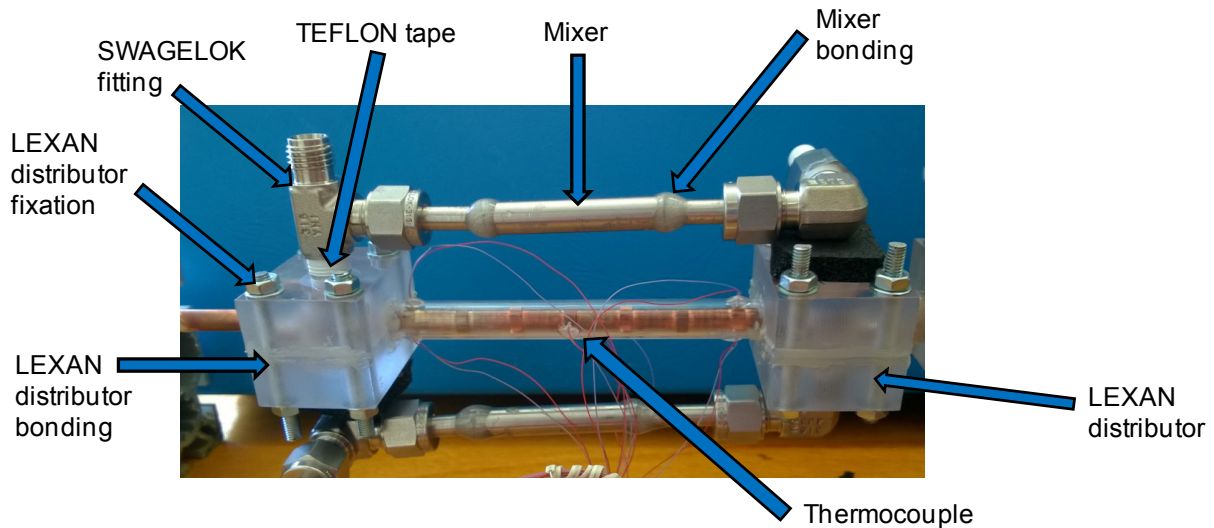
Figure 3.21. Sub-sector of the heat transfer test section with the distributors and the mixers installed.

3.4   Nomenclature

d	diameter	[m]
$(dp/dz)_{f,G}$	frictional pressure gradient for the vapor phase	[Pa m^{-1}]
f	friction factor	[/]
Eo	Eötvös number	[/]
x	vapor quality	[/]
Y, Y^*	dimensionless inclination parameter	[/]
β	inclination angle	[°]
$\Delta\rho$	density difference	[kg m^{-3}]
ρ_G	vapor density	[kg m^{-3}]

4 CONDENSATION TESTS WITH PURE FLUIDS ON GROUND

In parallel with the design of the 3.38 mm test section some condensation heat transfer tests with HFE-7000 in the 0.96 mm inner diameter test section have been performed and are hereafter presented. These tests have been done to become familiar with this fluid and to analyze its performance during condensation, with the aim of assessing the models used in the design steps.

4.1 Condensation heat transfer of HFE-7000 in a 0.96 mm inner diameter circular minichannel

Condensation heat transfer tests with HFE-7000, presented in this Section, have been performed in the circular minichannel described in Section 2.2.1 and installed in the experimental apparatus described in Section 2.2.

4.1.1 Degassing of HFE-7000 and preliminary tests

Before performing condensation heat transfer tests the HFE-7000 has been degassed. For the degassing procedure an apparatus has been expressly prepared.
The liquid has been stared inside a vessel and connected to:
- high precision pressure transducer Druck Calibrator with a full scale value of 20 bar and an accuracy of ±0.05% of the reading between 200 mbar and 20 bar and within ±0.1 mbar below 200 mbar;
- a high precision four wire thermistor connected to a Hart Scientific Super Thermometer II. This measurement chain has a global accuracy of ±0.002 °C;
- a sight glass followed by a vacuum pump.
With this configuration the temperature and the pressure in the chamber are measured and they can be compared with the fluid properties using REFPROP 9.1 (Lemmon et al. [20]).
The procedure starts with the fluid at ambient temperature and pressure. Then the vacuum pump is connected to the vessel, the pressure is lowered, some liquid boiled, ensuring that all the vapor/air present in the volume above the liquid is removed; when some drops of liquid are seen passing through the sight glass the connection with the vacuum pump is closed. Then the vessel is allowed to equilibrate and so the air contained in the liquid should come out to fill the free volume with the vapor above the liquid. This procedure has been repeated several times to ensure to remove the maximum possible quantity of air. After the degassing procedure the measured temperature inside the vessel was about 20.1°C and the pressure of about 0.577 bar corresponding to a saturation temperature of about 19.6°C; if the fluid were in saturated conditions the pressure should be 0.588 bar.

As a preliminary test the adiabatic single phase pressure drop has been evaluated in the test section described in Section 2.2.2, in order to gain a critical insight into the properties of the HFE-7000. The experimental liquid phase friction factor evaluated, as reported in Eq. 4.13, is depicted in Figure 4.1 function of the Reynolds number during the adiabatic flow of HFE-7000 at about 2.8 bar. For comparison in the figure the values calculated with the Churchill [16] correlation are also reported.
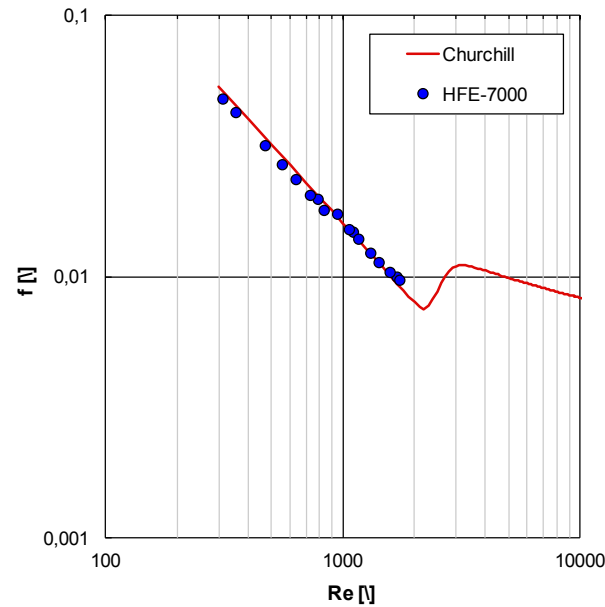
Figure 4.1. Experimental and predicted liquid single phase friction factor versus the Reynolds number for the HFE-7000

The fluid properties have been evaluated using REFPROP 9.1 (Lemmon et al. [20]) except for surface tension, which has been evaluated using Eq. 4.1, where *T* is the temperature in [K], as reported in [21].

In Table 4.1 the properties of the HFE-7000 are reported at different conditions. As per manufacturer specification the critical pressure of the HFE-7000 is 24.8 bar and so at 40°C saturation temperature the reduced pressure is about 0.05.

$$\sigma_l = 40.36 - 0.09343 \cdot T \quad \left[mN\,m^{-1} \right] \qquad\qquad \textbf{4.1}$$

Table 4.1. Properties of saturated HFE-7000 NIST Refprop v. 9.1 (Lemmon et al. [20]) except for the surface tension (Eq. 4.1).

p_{sat} [bar]	T_{sat} [°C]	ρ_l [kg m^{-3}]	ρ_g [kg m^{-3}]	μ_l [μPa s]	μ_l [μPa s]	λ_l [W m^{-1} K^{-1}]	σ_l [mN m^{-1}]
0,72	25,0	1405	6,1	479,1	11,0	0,0742	12,5
1,01	34,1	1379	8,4	424,5	11,3	0,0716	11,7
1,25	40,0	1362	10,2	392,7	11,5	0,0699	11,1
1,5	45,5	1346	12,2	365,4	11,7	0,0684	10,6

4.1.2 Data reduction and calibration tests

For the determination of the local heat transfer coefficient (Eq. 4.2) three parameters are used: the local heat flux, the local saturation temperature and the local wall temperature.

$$\alpha(z) = \frac{q'(z)}{T_{sat}(z) - T_W(z)} \qquad \textbf{4.2}$$

As the local wall temperatures are directly measured at a certain axial positions with the thermocouples embedded on the wall, the value of heat flux and saturation temperature should be defined.

The local heat flux is calculated from the slope of the water temperature profile along the test section, Eq. 4.3:

$$q' = \frac{\dot{m}_{water}\, c_{water}}{\pi d} \frac{\mathrm{d}T_{water}(z)}{\mathrm{d}z} \qquad \textbf{4.3}$$

where $dT_{water}(z)/dz$ is the derivative of the polynomial equation interpolating the measured water temperature along the channel. Thus a proper interpolating function of the measured water temperatures along the measuring sector is needed. Four possible interpolating equations are considered in the following order of preference to minimize the uncertainty of heat transfer coefficients: a second order polynomial, an exponential equation with three parameters, a third order polynomial and a four order polynomial. An example of the polynomial function and of the exponential function adopted is reported in Eqs. 4.4-4.5. The equation parameters are calculated by means of the least square method.

$$t_{water}(z) = a\,z^2 + b\,z + c \qquad \textbf{4.4}$$

$$t_{water}(z) = a + b\,e^{-z/c} \qquad \textbf{4.5}$$

Two different criteria are used to find the best fitting equation: the first criterion is physical and the second one is statistical.

The physical criterion is based on the experimental uncertainty of the temperature measurements. Specifically, all the values of the calculated water temperatures with the fitting equation have to be within the expanded experimental uncertainty of the corresponding thermocouple readings. If this check test fails, the next fitting equation in the order of preference will be considered, until the criterion is satisfied.

In the second criterion, the coefficients of determination R square (R^2) and adjusted R square (R_{adj}^2) are utilized to assess the fitting procedure (Rawlings [22]). Unlike R^2, R_{adj}^2 increases with the number of parameters of the fitting equation only if the new term improves significantly the model. Thus, let y_1 and y_2 be two functions that are one after the

other in the aforementioned order of preference: in the present data reduction, by convention, y_1 would be the chosen fitting if the following condition is satisfied:

$$\left| R^2_{adj}(y_1) - R^2_{adj}(y_2) \right| \leq 0.0035 \qquad \textbf{4.6}$$

The threshold value in Eq. 4.6 has been defined through experimental observations as it gives a fitting function that is in good agreement with the measured temperature values and leads to a low sensitiveness of the heat transfer coefficient to the interpolation method.

Finally, in order to assure the accuracy and repeatability of the results, the heat transfer coefficients has to result insensitive to the method of interpolation, that is to say that the variation in heat transfer coefficients using the fitting equation that meets the conditions of the statistical and uncertainty criteria and the next admissible equation in the order of preference should be within the experimental uncertainty.

Once the interpolating equation for the water temperature is established, the local heat flux can be determined along the channel. Actually, from the direct measurement of the local wall temperatures along the test section, the contribution of the axial conduction in the copper wall is calculated from an energy balance and the heat flux, calculated from Eq. 4.3, is corrected accordingly. The heat losses contribution due to the temperature difference between the water temperature and the ambient is also considered in the evaluation of the local heat flux. Its magnitude has been measured leading to the following expression for the total heat dissipated in the measuring sector:

$$q_{diss,MS} = 0.1772 \left(T_{amb} - \frac{T_{water,in,MS} + T_{water,out,MS}}{2} \right) + 0.1253 \qquad \textbf{4.7}$$

The local dissipated heat is given by:

$$q'_{diss(z)} = \frac{q_{diss,MS}}{\pi d} \frac{T_{water}(z) - T_{amb}}{\int_0^z (T_{water}(z) - T_{amb}) \, dz} \qquad \textbf{4.8}$$

When a second degree polynomial function is assumed, the local heat dissipation rate is calculated as reported in Eq. 4.9. Similarly Eq. 4.10 is used if exponential function is assumed.

$$q'_{diss}(z) \pi d = \frac{q_{diss,MS} \left(T_{water}(z) - T_{amb} \right)}{\frac{1}{3} \cdot a \cdot z^3 + \frac{1}{2} \cdot b \cdot z^2 + c \cdot z - T_{amb} \cdot z} \qquad \textbf{4.9}$$

$$q'_{diss}(z)\pi d = \frac{q_{diss,MS}\left(T_{water}(z)-T_{amb}\right)}{a\cdot z - b\cdot c\cdot\left(e^{-z/c}-1\right)-T_{amb}\cdot z} \qquad \textbf{4.10}$$

Once the local heat flux is known, for the determination of the heat transfer coefficient other two parameters are necessary:

- the wall temperature T_w, which is measured with the thermocouples embedded in the wall; anyway a small correction is introduced to account for the thermal conduction due to the wall thickness between the internal wall and the hole in which the thermocouple is placed. Even if the tube is made of copper, yielding rather small temperature gradients, this correction should be taken into account.
- The saturation temperature T_{sat} along the test section which is calculated from the local pressure.

The refrigerant pressure in the measuring sector is measured at the inlet and at the outlet. The local pressure could be obtained from a linear interpolation of these measured values, but in the present case, it is evaluated with a more precise iterative procedure. In fact, the pressure profile is not linear along the microchannel and the interpolation between inlet and outlet pressure must account for the physical phenomena, specifically for the frictional pressure drop in the stainless steel tubes and in the copper microchannel the pressure variations due to changes in the geometry, and the pressure recovery due to momentum variation during condensation. To clarify the effect of the geometry on the pressure losses a layout of the test section is reported in Figure 4.2.
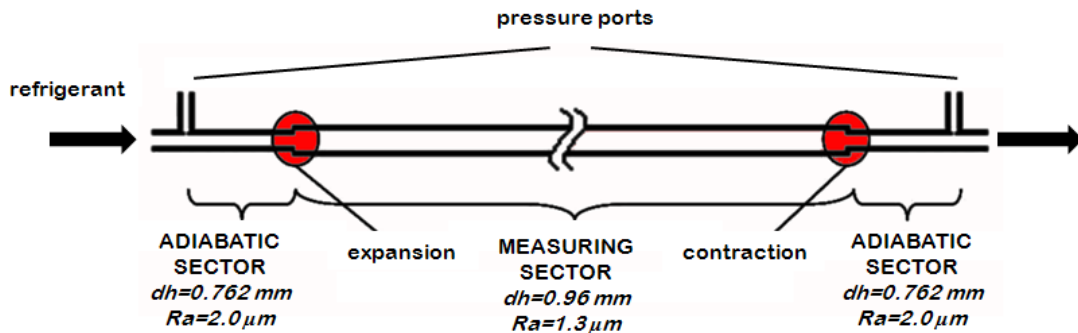
Figure 4.2. Layout of the geometry of the measuring sector between the two pressure ports installed. Dimensions of the copper microchannel and of the stainless steel adiabatic sector are reported. Abrupt geometry changes are highlighted in red. Image from Bortolato [23]

Different models have been implemented to get the pressure at the position z. The Del Col et al. [19] model is used for the frictional pressure gradient, the Paliwoda [24] equation is used when sudden changes in the geometry occurs under two-phase flow conditions, the Idelchik [25] correlation is used for a sudden contraction when subcooled refrigerant exits the measuring sector and the Cavallini et al. [26] model is used for the pressure recovery due to the momentum. Then the total calculated pressure drop is matched to the measured value by using a multiplying factor. In this procedure, the above models are used only to get

the correct shape of the pressure profile, but the overall pressure drop is equal to the measured value. Once the local pressure gradient is known the saturation temperature can be evaluated.

Along the measuring sector, the refrigerant enthalpy at the position z can be calculated as reported in Eq. 4.11:

$$h(z) = h_{in,MS} - \frac{\dot{m}_{water}}{\dot{m}_{ref}} c_{water} \left(T_{water,out} - T_{water,j} \right) \qquad \textbf{4.11}$$

During a condensation test run, the refrigerant can enter the measuring sector as superheated vapor or in saturated conditions. In the first case the enthalpy at the inlet of the measuring sector ($h_{in,MS}$) is evaluated with the measured temperature and pressure using the properties of the refrigerant; in the second case, when the refrigerant has been cooled down in the pre-conditioning sector, the refrigerant enthalpy at the inlet of the measuring sector is determined with a thermal balance on the water side, using Eq. 4.12.

$$h_{in,MS} = h_{in,PS} - \frac{\dot{m}_{water,PS}}{\dot{m}_{ref}} c_{water} \Delta T_{water,PS} \qquad \textbf{4.12}$$

At this point the local vapor quality can also be evaluated.

As a preliminary test the energy balance in the test section was controlled by comparing the water side heat transfer rate to the refrigerant side when superheated vapor enters the pre-conditioning sector and subcooled liquid exits the measuring sector. The agreement was found to be within 4%. The check between the measured refrigerant temperature and the saturation temperature obtained from the measured pressure in saturated conditions at the inlet of the measuring sector has been checked; the agreement between the two temperatures was about ±0.4 K.

4.1.3 Condensation test results

Experimental tests have been carried out at mass velocity ranging between 100 to 300 kg m^{-2} s^{-1} and at a saturation temperature of approximately 40°C. The refrigerant enters the test section has superheated vapor at a temperature ranging between 56°C and 63°C. The pre-conditioning sector can be used to set the thermodynamic quality at the inlet of the measuring sector. Different tests have been carried out controlling the heat flow rate in the pre-conditioning sector allowing the fluid to enter the measuring sector alternatively as superheated vapor or in saturated conditions, fixing the vapor quality in the pre-conditioning sector. The measured local heat transfer coefficients are reported versus vapor quality in Figure 4.3.

The heat transfer coefficient increases with vapor quality and mass velocity. In the graph the uncertainty bars are also reported, and the uncertainty analysis has been done has reported in Section 11, considering that the working fluid is pure. The mean experimental uncertainty on the heat transfer coefficient is about 10% and on the vapor quality is ±0.03.
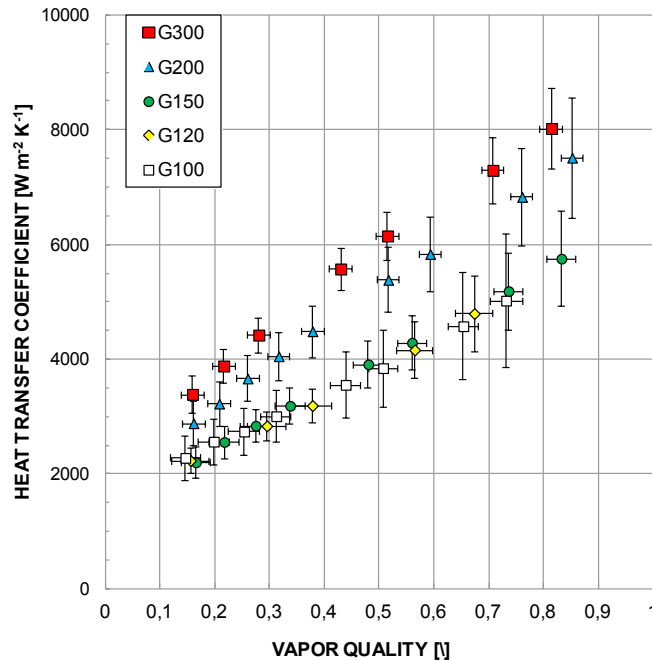
Figure 4.3. Local heat transfer coefficient versus vapor quality for HFE-7000 during condensation at varying mass velocity G [kg m^{-2} s^{-1}] and saturation temperature of about 40°C

In Figure 4.4 the present database is compared against the model by Cavallini et al [18]. This model was developed for condensation inside horizontal smooth tubes with an inner diameter greater than 3 mm. In the recent years it has been compared with experimental data of different fluids taken in circular and square minichannels with an inner diameter of about 1 mm giving, on the whole, good results with slightly higher deviation at lower mass flow rates or lower vapor qualities [5, 6, 17, 27]. From the comparison with the present database it can be seen that the collected data are generally underpredicted by the model, especially at the low mass flow rates: the mean absolute deviation between the experiments and predictions e_{AB} is about 26% with a standard deviation σ_N of approximately 6%. It should be also keep in mind that the model is outside his range of applicability.

Anyway, from the present analysis it can be concluded that the Cavallini et al. [18] model gives a general indication about the heat transfer coefficient during condensation for the HFE-7000 in a 1 mm diameter channel and it can be used for the evaluation of the internal heat transfer coefficient during the design steps of the new test section in Section 3.2.2.
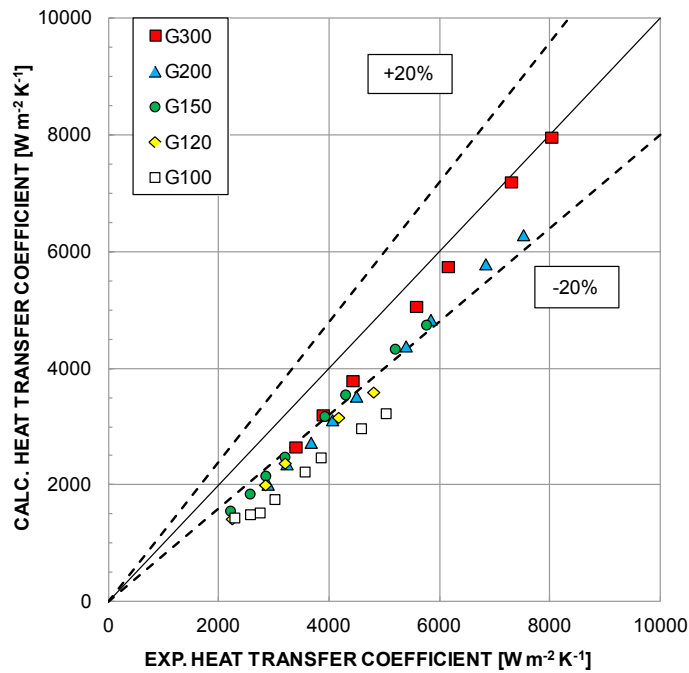
Figure 4.4. Calculated versus experimental HFE-7000 condensation heat transfer coefficients using the model by Cavallini et al. [18] at varying *G* [kg m⁻² s⁻¹]

4.2 Condensation heat transfer of R134a inside the new test section

The new test section for heat transfer investigations with 3.38 mm inner diameter has been accommodated in the experimental apparatus available and described in Section 2.2. The updated scheme of the test apparatus with the new test Section is depicted in Figure 4.5.

The 3.38 mm heat transfer test section is composed of two counter-current heat exchangers: the first one is divided in three sub-sectors and the second one is divided in two sub-sectors. The two heat exchangers are divided by a visualization glass tube.

During condensation tests the refrigerant enters the first heat exchanger as superheated vapor and then it can be partially or fully condensed along the test section. Both the heat exchangers are served by the same thermal bath, using distilled water as secondary fluid. Each hydraulic loop is provided with a flow regulating valve and a Coriolis effect mass flow meter to set and measure the mass flow rate. When necessary the inlet water temperature in the first heat exchanger and in the second one can be maintained at different values by using electrical heaters installed downstream of the thermal bath in each loop. In each sub-sector the inlet and outlet water temperatures are measured with a T-type thermocouple and the temperature difference is checked using a triple junction thermopile.
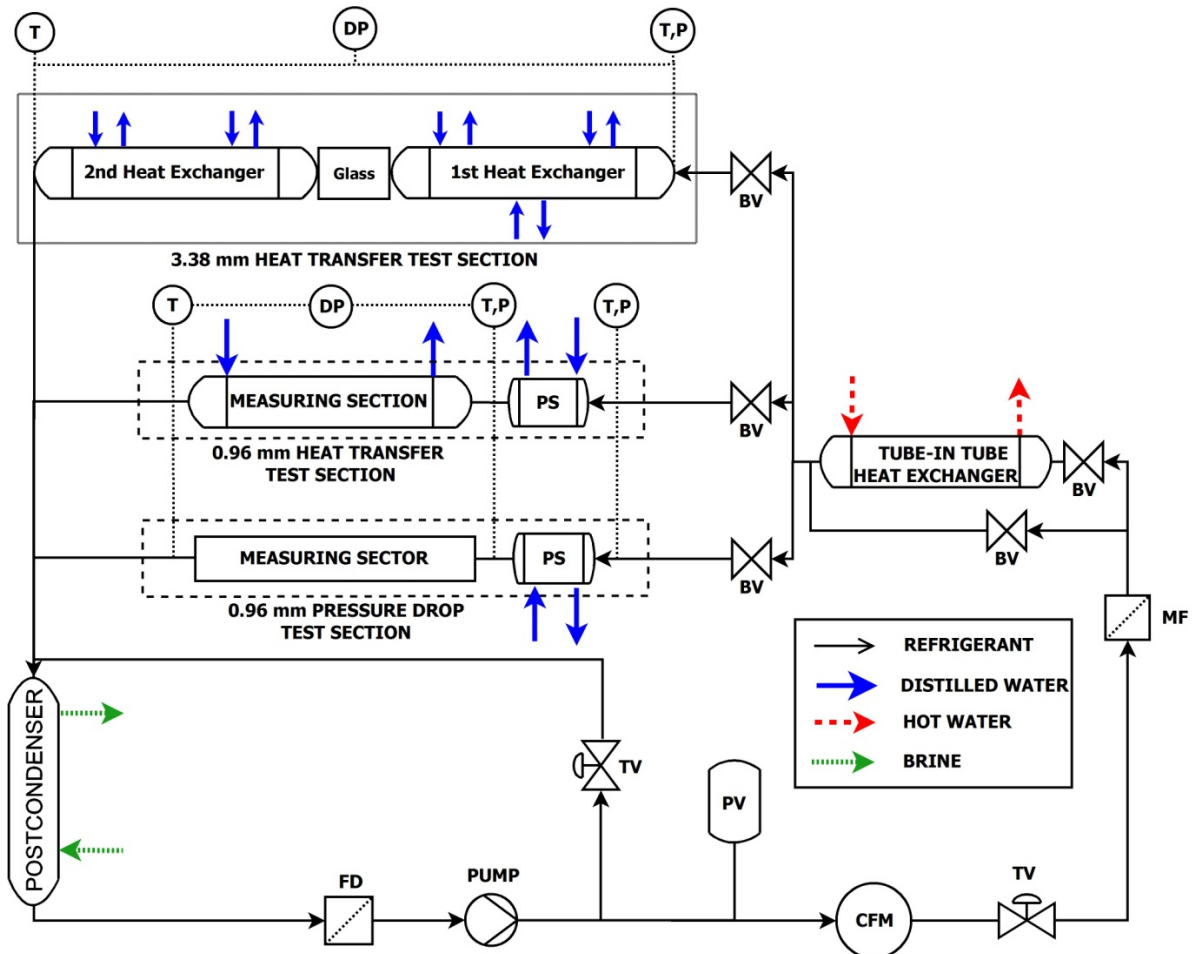
Figure 4.5. Experimental test rig: PS (pre-conditioning sector); MF (mechanical filter); FD (filter dryer); PV (pressure vessel); CFM (Coriolis-effect mass flow meter); TV (valve); BV (bulb valve); P (pressure transducer); DP (differential pressure transducer); T (thermocouple).

On the refrigerant side the operative pressure is measured at the inlet of each the test section by means of a relative pressure transducer whereas two differential pressure transducers with different operative ranges are employed to measure the pressure drop along the test section. The refrigerant temperature is measured at the inlet and outlet of the test section with two T-type thermocouples directly immersed on the fluid flow.

At the exit of the test section the fluid is collected and sent to the post-condenser in which is completely condensed and subcooled

4.2.1 Calibration and preliminary tests

After the realization and installation of the new test section with an inner diameter of 3.38 mm and before performing two-phase heat transfer tests, the calibration of the thermal sensors, thermopiles and thermocouples, has been done. Then some preliminary tests have been performed:

- single-phase frictional pressure drop;
- heat losses evaluation;

- single-phase and two-phase heat balance;
- check of the temperature and pressure under saturated conditions.
The following tests have been performed with R134a as working fluid.

4.2.1.1 *Calibration of thermal sensors*

The on-site calibration of thermopile and thermocouples is a fundamental step towards the analysis of the heat transfer performance of refrigerant in the test section.

The calibration of thermopiles has been done using as reference thermometers two calibrated thermistors Pt100 coupled with an Hart Scientific Super-Thermometer II 1590; this configuration achieves an uncertainty of 0.002 K on the measured temperatures. The two ends of the thermopiles have been inserted in two different calibration holes to realize the temperature differences desired. A correction function for each thermopile has been extract.

A separate calibration was done for the thermocouples installed in the thermopiles ends; this was done using only one calibration hole changing his temperature in the range 10°C to 60°C. With a similar procedure also the thermocouples on the refrigerant side have been calibrated.

Once the temperature sensors on the water side were calibrated they have been installed in the sub-sectors and used to calibrate the thermocouples on the wall. Water was circulated in the sub-sectors and in order to avoid heat losses on the refrigerant side, vacuum has been realized inside the minichannel. From the readings of the thermocouples and thermopiles installed in each sub-sector it was possible to get the mean temperature and to calibrate each wall thermocouple.

4.2.1.2 *Single-phase frictional pressure drop*

The single phase friction factor *f* has been experimentally determined according to Eq. 4.13 and its values are reported in Figure 4.6 against Reynolds number.

$$f = \frac{\rho \cdot D_h \cdot \Delta p}{2 \cdot G^2 \cdot L} \qquad\qquad \textbf{4.13}$$

As reported in Eq. 4.13, the evaluation of the friction factor requires the measurement of the pressure drop Δp along the channel length *L* and of the refrigerant mass velocity *G*.

Single-phase pressure drop tests are fundamental to have a critical insight into the test section hydraulic performance. In fact, if there were big discrepancies between the experimental friction factor and the expected values from literature, it means that the hydraulic diameter of the test section was not well known.

In the present case, the friction factor data are in good agreement with the Churchill [16] correlation (Eqs. 6.2-6.4) and the Blasius [28] correlation (Eq. 6.5) as shown in Figure 4.6.
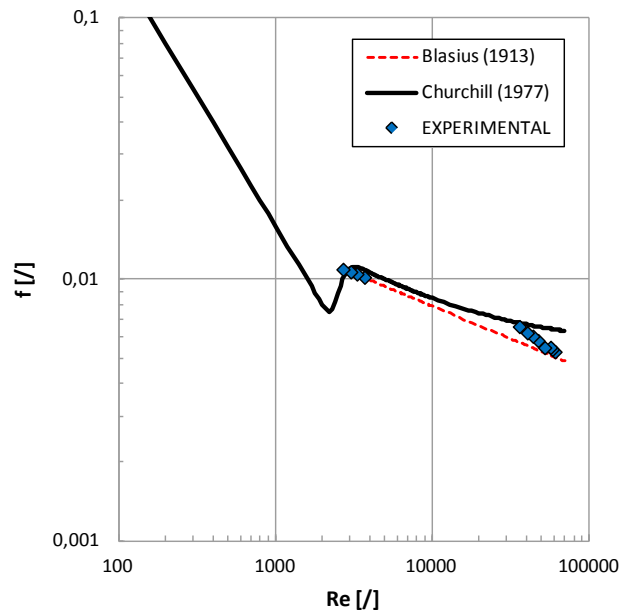
Figure 4.6: Experimental and calculated single phase friction factor versus Reynolds number

4.2.1.3 *Evaluation of the heat dissipations*

Even if the test section is insulated there can be an heat flow rate (a couple of watts for each sub-sector) towards the environment. In principle, this heat flux can be reduced keeping the water temperature close to the ambient, but obviously this implies restrictions on the test conditions that can be done.

Some tests have been performed to evaluate the dissipated heat flow rate for each sub-sector as a function of the water to ambient temperature difference. Tests have been done changing the water temperature while the refrigerant side of the test section was in vacuum, so the heat flow rate measured on the coolant side could not be attributed to the tested fluid. This approach considers that the heat dissipations are associated with the mean water temperature in a sub-sector and with the ambient temperature.

The dissipated heat flow for the first sub-sector is reported function of the mean water to ambient temperature difference in Figure 4.7.
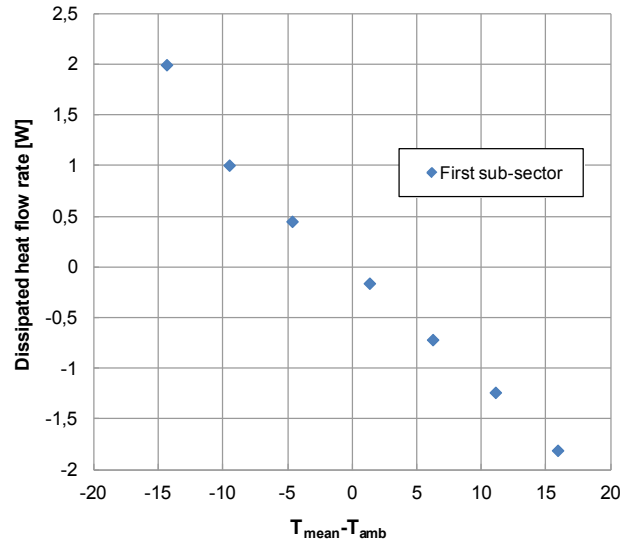
Figure 4.7. Experimentally measured heat dissipations rate for the first sub-sector versus water to ambient temperature difference

4.2.1.4 *Single-phase and two-phase heat balance*

Another check to verify the quality of the test section and the goodness of the calibration procedure is to compare the water side heat flow rate to the one calculated on the refrigerant side. The water side heat flow rate is calculated as the sum of the heat flow rate for each sub-sector:

$$q_{water} = \sum_{i=1}^{5} q_{water,i} \qquad\qquad \textbf{4.14}$$

where $q_{water,i}$ is the heat flow rate in a sub-sector evaluated as:

$$q_{water,i} = \dot{m}_{water,i}\, c_{water}\, \Delta T_{water,i} \qquad\qquad \textbf{4.15}$$

where $m_{water,i}$ is the mass flow rate of the *i-th* sub-sector and ΔT_i the water temperature difference of the *i-th* thermopile.

On the refrigerant side the heat flow rate is evaluated as:

$$q_{ref} = \dot{m}_{ref}\, \Delta h_{ref} \qquad\qquad \textbf{4.16}$$

where Δh_{ref} is the refrigerant enthalpy difference at the inlet and outlet of the test section where the pressure and temperature sensors are installed.

Considering single phase heat balance tests the difference between the heat flow rate measured on the water side and the heat flow rate measured on the refrigerant side is below 3.5 W for all mass velocities.

During two-phase heat balance tests the refrigerant enters the test section with a superheating of about 10 K and exits with a subcooling of about 10 K. The maximum percentage difference between the heat flow rate measured on the water side and the one evaluated on the refrigerant side is below ±3 % for mass velocities greater than 100 kg m^{-2} s^{-1}; at G=50 kg m^{-2} s^{-1} the heat balance is within ±5 %, corresponding to a difference of approximately 4 W.

4.2.1.5 *Check of temperature and pressure under saturated conditions*

As a later check of the experimental apparatus, the refrigerant temperature at the outlet of the test section has been measured during two-phase flow and compared with the saturation temperature obtained from the pressure. The disagreement is typically in the order of 0.2 K, which is within the uncertainty range of the two instruments. Some tests results are reported in Table 4.2.

Table 4.2. Agreement between the measured refrigerant temperature and the one obtained with the pressure during two-phase flow

Mass velocity [kg m^{-2} s^{-1}]	100	100	200	200
Experimental Temperature [°C]	39,24	40,70	40,27	41,16
Saturation Temperature [°C]	39,10	40,79	40,50	41,24
Difference [K]	0,14	-0,09	-0,23	-0,08

4.2.2 *Heat transfer coefficient: data reduction*

During heat transfer tests the quasi-local heat transfer coefficient for each sub-sector can be evaluated as:

$$\alpha_i = \frac{q_{water,i}}{A \cdot \left(T_{sat} - T_w\right)_i}$$

4.17

where A is the internal heat transfer area and $q_{water,i}$ is the heat flow rate measured on the water side Eq. 4.15.

On each sub-sector the wall temperatures are measured with 6 thermocouples in different positions as shown in Figure 3.14. The refrigerant saturation temperature at the same axial position of the wall thermocouples, is evaluated starting from the measured pressure at the inlet and outlet of the test section and considering a linear behaviour. Actually the pressure drop along a test section is not linear but in the present case, considering that the pressure gradient is small, this assumption can be assumed.

Thus, having in mind the Figure 3.14 and the Eq. 4.17, the heat transfer coefficient can be calculated with the mean wall temperature ($T_{wall,m}$) measured from the 3rd and 4th thermocouple:

$$\alpha_i = \frac{q_{water,i}}{A \cdot \left(T_{sat} - T_{w,m}\right)_i} \qquad \textbf{4.18}$$

or using the mean logarithmic temperature difference (ΔT_{ml}) between the wall and the refrigerant:

$$\alpha_i = \frac{q_{water,i}}{A \cdot \left(\Delta T_{ml}\right)_i} \qquad \textbf{4.19}$$

where:

$$\Delta T_{ml} = \frac{\left(T_{sat,out} - T_{w,in}\right) - \left(T_{sat,in} - T_{w,out}\right)}{\ln \dfrac{\left(T_{sat,out} - T_{w,in}\right)}{\left(T_{sat,in} - T_{w,out}\right)}} \qquad \textbf{4.20}$$

considering in this case $T_{w,in}$ as the mean temperature between the 1st and 2nd thermocouple and $T_{w,out}$ the mean temperature between the 5th and the 6th thermocouple.

The enthalpy at the outlet of each sub-sector can be found from the heat flow rate, the mass flow rate of the refrigerant and the inlet refrigerant enthalpy:

$$h_{out,i} = h_{in,i} - \frac{q_{water,i}}{\dot{m}_{ref}} \qquad \textbf{4.21}$$

where the enthalpy at the inlet of the test section is evaluated with the measured temperature and pressure using REFPROP 9.1 (Lemmon et al. [20]). Then the thermodynamic vapor quality can be calculated:

$$x_{out,i} = \frac{h_{out,i} - h_L}{h_{LG}} \qquad \textbf{4.22}$$

The mean vapor quality for each sub-sector is calculated from the inlet and outlet values.

Unlike two-phase heat transfer tests, when single phase heat transfer test are performed the saturation temperature is replace by the refrigerant temperature. Thus for each sub-sector with the outlet enthalpy evaluated using Eq. 4.21 and with the outlet pressure, the temperature is evaluated using REFPROP 9.1 (Lemmon et al. [20]). At this point the refrigerant temperature at the same position of the wall thermocouple is evaluated assuming a linear behavior from the values previously calculated.

To complete the data reduction some corrections should be applied:

1) Correction for dissipated heat flow rate.

The water heat flux is corrected to account of the heat dissipation rate of the water towards the external environment. The local dissipated heat flow rate for each sector has been evaluated as shown in Section 4.2.1.3.

2) Correction for the axial heat flux.

The contribution to the variation in axial heat flow rate should also be considered in the evaluation of the heat flux and consequently in the interpretation of the heat transfer coefficient. Anyway the axial conduction is minimize by the small tube wall thickness, which is also useful in reducing the thermal response of the test section.

3) Correction for the wall temperature measurements.

This correction is associated to the wall temperature correction. The effective wall temperature measurement is located around 0.6 mm from the internal minichannel surface. Even though the test tube is made of copper, that yields rather small temperature gradient, the effect of distant wall temperature measurement is accounted.

4.2.3 Single phase heat transfer tests

During single phase heat transfer tests the refrigerant enters the test section as subcooled liquid and then is heated up or cooled down with the secondary fluid that flows in counter-flow. The tests have been performed with R134a as working fluid and water as secondary fluid. In Figure 4.8 typical refrigerant and water temperature profiles are reported for single phase heat transfer tests in cooling and heating mode.
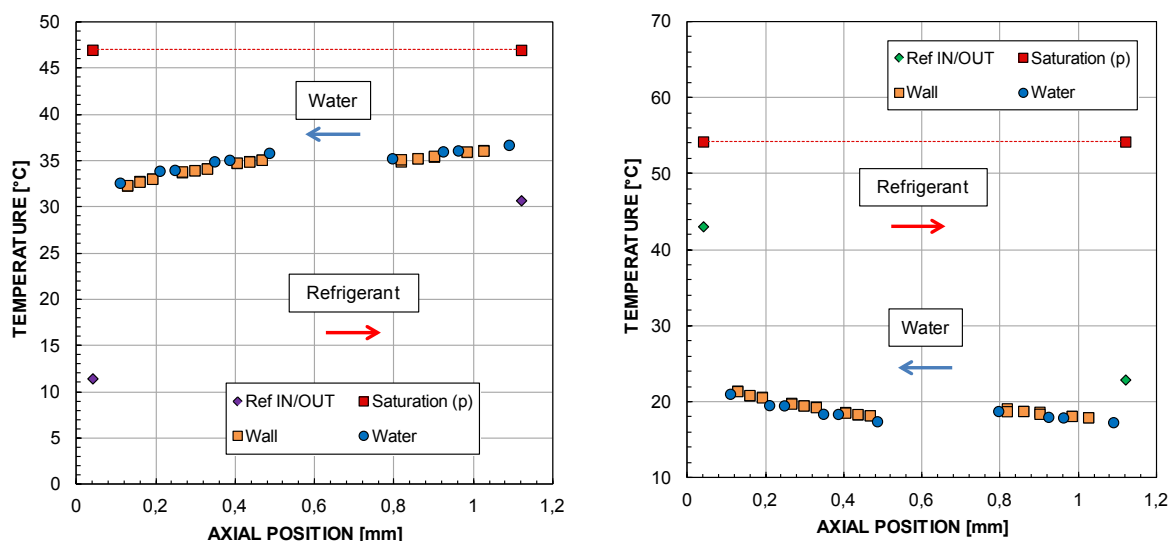
Figure 4.8. Temperature profile during R134a liquid flow at G=200 kg m^{-2} s^{-1}. Left: heating test; right: cooling test

The measured heat transfer coefficients have been compared in Figure 4.9 with the Gnielinski correlation for fully developed turbulent flow [29]. The Reynolds number varied from 2350 to 4800.
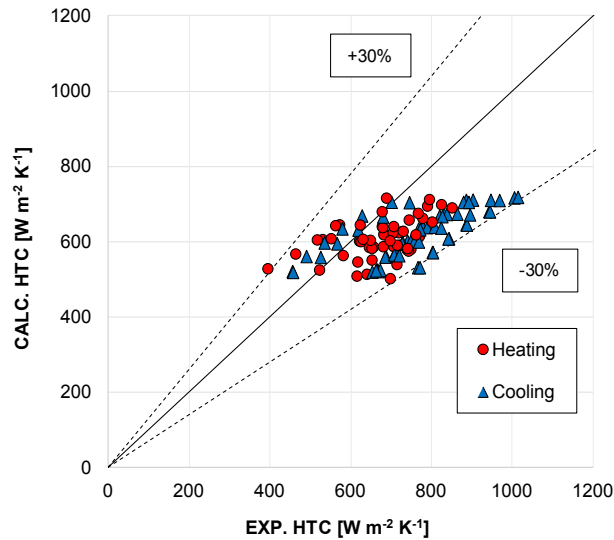
Figure 4.9. Experimental heat transfer coefficients measured during R134a single phase heat transfer and compared against Gnielinski correlation for fully developed turbulent flow [29]

The heat transfer coefficient calculated for the 1st and 2nd sub-sector using the mean wall temperature and the mean logarithmic temperature difference are reported in Figure 4.10 versus the Reynolds number. The disagreement between the two methods is about 0.8% for the 1st sub-sector and about 0.3% for the 2nd; so it can be concluded that the evaluation of the heat transfer coefficient is independent on the method chosen for the reduction.
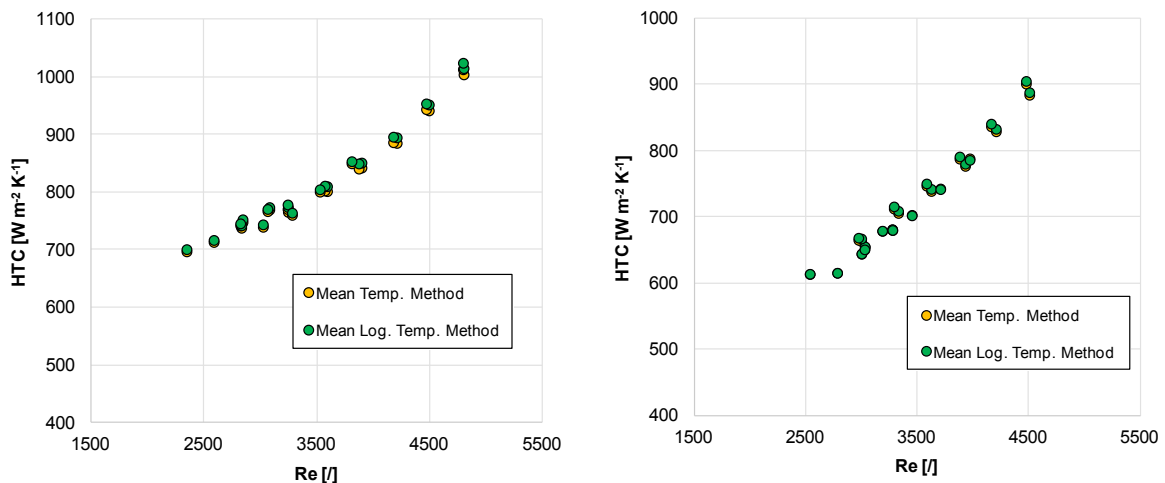
Figure 4.10. Experimental heat transfer coefficient for the 1st (left) and 2nd (right) sub-sector evaluated with the two different methods: mean temperature method and mean logarithmic temperature method.

4.2.4 Condensation heat transfer tests

The precise measurement of condensation heat transfer coefficient within a minichannel is still a difficult experimental task. In the past, most of the experiments have been performed with the Wilson plot technique, which does not require the measurement of the wall temperature but calculates the coefficient from the variation of the external thermal resistance. In the present test section the evaluation of the heat transfer coefficient is done with the precise measurements of the wall temperature with thermocouples embedded on the wall; in such a way the experimental error is reduced compare to Wilson plot technique.

4.2.4.1   *Tests performed*

Tests have been performed with the experimental apparatus described in Section 2.2.

Similarly to single phase heat transfer tests, the subcooled refrigerant from the post condenser is sent through a dehumidifier into a variable speed gear pump. The fluid is then pumped through the Coriolis effect mass flow meter in the evaporator, in which is heated up and exists as superheated vapor. The pressure and the temperature of the refrigerant are measured in order to get the thermodynamic state of the superheated vapor. The fluid then enters in the test section, which is composed of two sectors divided by an adiabatic glass tube for visualization purpose. In the two sectors the fluid can be partially or completely condensed using water as secondary fluid. Each sector is divided in several sub-sectors in which the heat flow rate can be measured and the heat transfer coefficient evaluated. The fluid than returns to the post-condenser in which is completely subcooled before coming back to the variable speed gear pump. During heat transfer tests to reduce the dissipation towards the environment the glass tube has been covered with an insulating material.

A typical profile of refrigerant, wall and water temperatures during a condensation test run at G=100 kg m^{-2} s^{-1} is reported in Figure 4.11. The refrigerant enters in the test section at about 56°C and it is cooled down to the saturation temperature, which is pretty constant at 41°C, and slightly sub-cooled to 40°C. The water flows in counter-current in the two heat exchanger, so in the 1st heat exchanger the water enters at about 26°C, flows in 3 sub-sectors and exits at approximately 33°C and similarly in the 2nd heat exchanger it enters at 26°C and exits at 30.5°C after crossing 2 sub-sectors. The measured wall temperature is between the water and the refrigerant temperature, but close to the water one, showing that the dominant thermal resistance is on the refrigerant side and thus allowing the evaluation of the heat transfer coefficients with low uncertainties. From Figure 4.11 it can be noticed that in the 4th sub-sector there is a big difference between the thermocouples place on the top and on the bottom in the first and last fin, and that in the 5th sub-sector there are 2 thermocouples less. This is due to the following reasons:

- in the 4th sub-sector one hole has not been realized because the drill broke inside the fin and one thermocouple has been badly placed. So in the first and last fin of the 4th sub-sector the thermocouples on the top are not measuring the real temperature of the internal wall ;

- the two thermocouples in the last fin of the 5th sub-sector have been damaged during the parabolic flight campaign, which has been performed in June 2015, before the reported condensation tests.

Anyway even if these thermocouples have been lost the heat transfer coefficients in the 4th and 5th sector can be measured using the mean wall temperature in the central fin and, as shown in Section 4.2.2, the agreement between the mean wall temperature method and the mean logarithmic wall temperature method is really good.

Before moving to the two-phase heat transfer results an analysis of sensitivity to coolant conditions is hereafter presented.
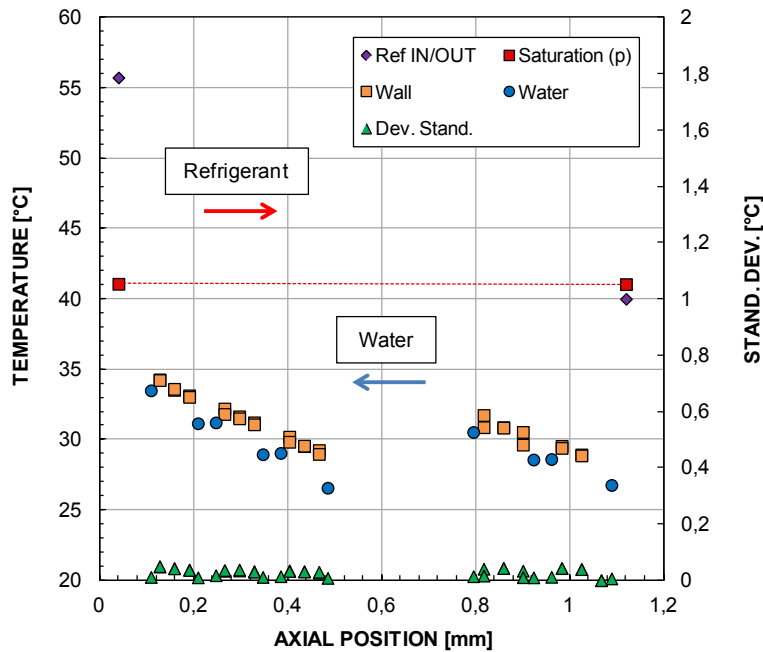
Figure 4.11. Temperature profiles during condensation tests of R134a at G=100 kg m^{-2} s^{-1}

4.2.4.2   *Sensitivity to coolant conditions*

On the water side, several conditions have been tested to assure that there are no effects on the measurements of the internal heat transfer coefficient.

As one can see from the data reduction, the technique for the evaluation of the heat transfer coefficient is highly dependent on the measurement of the water conditions, especially on the water temperature; for this reason on the water side there is a double check of the temperature in each sub-sector, using a triple-junctions thermopile and two thermocouples. After checking the thermal balance during single and two-phase heat transfer, as an indirect validation of the technique and to assure the goodness of the test section, it was checked that the coolant operating conditions does not affect the resultant internal heat transfer coefficient, at fixed refrigerant conditions.

Figure 4.12 shows the experimental heat transfer coefficient for R134a at 100 kg m^{-2} s^{-1} and 40°C saturation temperature. The coolant mass flow rate was varied between 17.6 kg h^{-1} and 6 kg h^{-1} and no effect on the internal heat transfer coefficient was detected.

Figure 4.13 shows the measured heat transfer coefficient at G=100 kg m^{-2} s^{-1} and 40°C saturation temperature in the channel. The mean coolant temperature was varied from 20.3°C to 33.1°C. The variation of the coolant temperature implies a change in the saturation to wall temperature difference. In this test conditions (100 kg m^{-2} s^{-1} and 40°C saturation temperature) no effect of the saturation to wall temperature difference on the heat transfer coefficient.

Changing the water mass flow rates and the temperatures at the inlet of the two heat exchangers it is possible to change the heat flow rate and thus to evaluate the heat transfer coefficient at the same vapor quality but at different axial positions. In Figure 4.14 the measured heat transfer is reported for each sub-sector. For example it can be seen that for x=0.7 the heat transfer coefficient has been measured in the 2nd and 3rd sub-sector or for x=0.5 the same heat transfer coefficient has been measured in the 3rd, 4th and 5th sector. It is clear that the heat transfer coefficient is independent from the axial position in which it has been measured. This may be looked at as an additional assessment of the present experimental technique. In the same way, in Figure 4.15, the experimental heat transfer coefficients have been plotted accounting for the condensation rate for each experimental point; it means that it is accounted for the condensing heat flow rate exchanged in each sub-sector or, in other words, of the change in vapor quality in a sub-sector. As one can see the heat transfer coefficient is independent from the variation of vapor quality.

Figure 4.12. Experimental quasi-local heat transfer coefficient versus vapor quality for R134a at G=100 kg m^{-2} s^{-1} for different mass flow rates

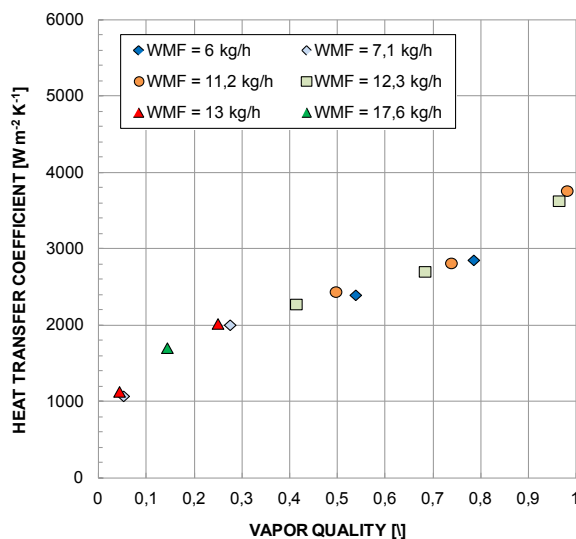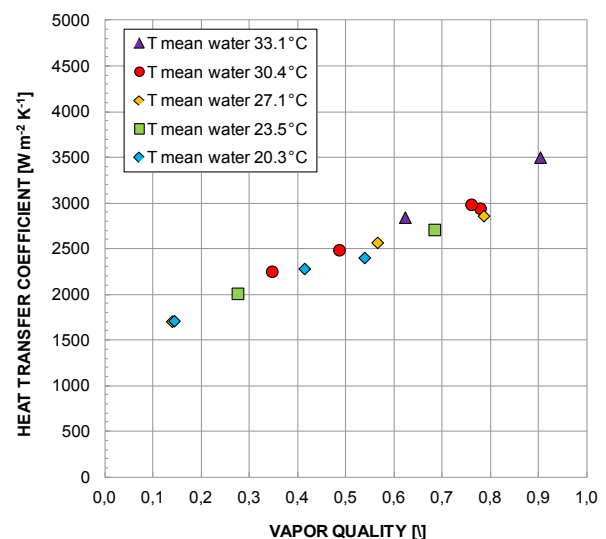**Figure 4.13. Experimental quasi-local heat transfer coefficient versus vapor quality for R134a at G=100 kg m^{-2} s^{-1} for different mean water temperature in the sub-sectors**
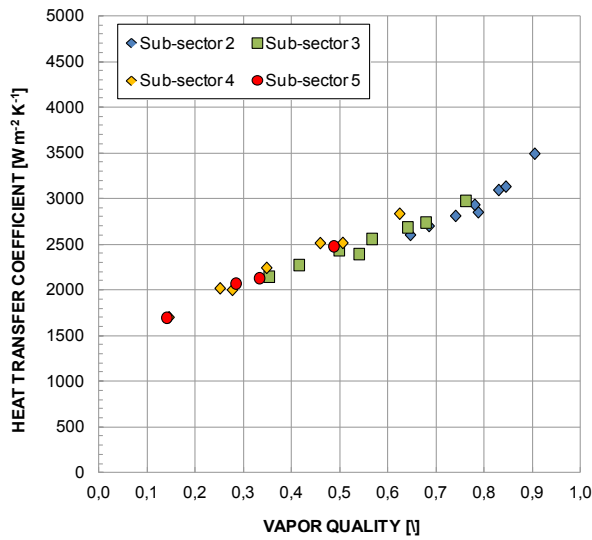
Figure 4.14. Experimental quasi-local heat transfer coefficient versus vapor quality for R134a at *G*=100 kg m⁻² s⁻¹ for different sub-sectors
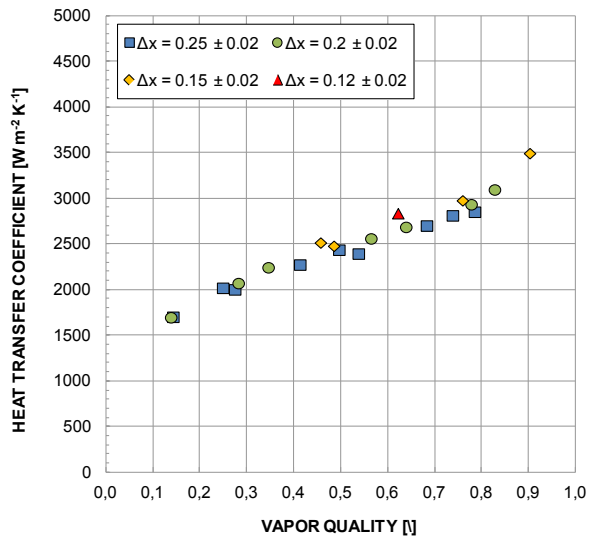
Figure 4.15. Experimental quasi-local heat transfer coefficient versus vapor quality for R134a at *G*=100 kg m⁻² s⁻¹ for different condensation rates

4.2.4.3   *Experimental results*

Condensation tests in the 3.38 mm test section have been performed with R134a at mass velocity of 200, 150, 100 and 50 kg m⁻² s⁻¹ and at a saturation temperature of about 40°C.

The experimental heat transfer coefficient measured during condensation of R134a for mass velocity ranging from 200 to 100 kg m⁻² s⁻¹ is plotted versus vapor quality in Figure 4.16. The measured heat transfer coefficient for 100 and 50 kg m⁻² s⁻¹ is reported in Figure 4.17. Every heat transfer coefficient is depicted with its uncertainty bars, evaluate with the procedure in Section 4.2.5.

As expected for forced convective condensation inside pipes, the heat transfer coefficient increases with vapor quality. The increase with the mass flow rate is evident between 200 and 150 but less clear below 150 kg m⁻² s⁻¹; it may indicate that for mass velocity higher than 150 kg m⁻² s⁻¹ the condensation process is dominated by shear stress at these operating conditions. It is also worth noting that for 50 kg m⁻² s⁻¹ the heat transfer coefficients depends on the saturation minus wall temperature difference showing that the gravity force is dominant and the flow regime is mainly stratified. In Figure 4.17 the heat transfer coefficients at *G*=50 kg m⁻² s⁻¹ are reported at four different mean temperature difference between the wall and the saturation: 14.7 K, 9.2 K, 5.4 K and 3.9 K.
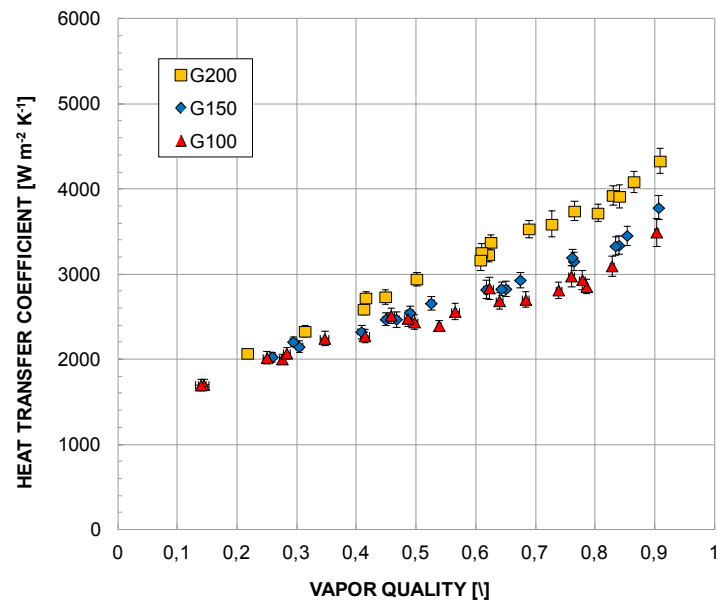
Figure 4.16. Experimental quasi-local heat transfer coefficients versus vapor quality during condensation of R134a at 200, 150 and 100 kg m⁻² s⁻¹ at 40°C saturation temperature
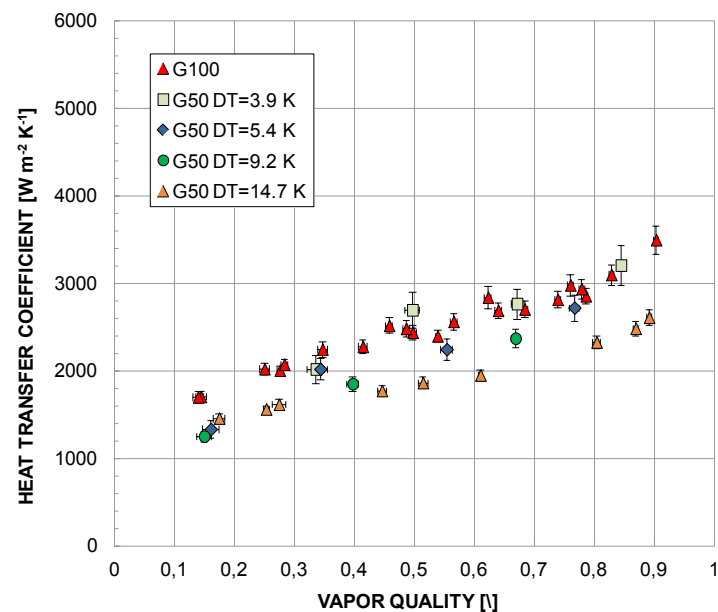
Figure 4.17. Experimental quasi-local heat transfer coefficients versus vapor quality during condensation of R134a at 100 and 50 kg m⁻² s⁻¹ at 40°C saturation temperature

4.2.5 Uncertainty analysis

The type B experimental uncertainties of the measured parameters are reported in Table 4.3. On site calibration of refrigerant, wall and water thermocouples was carried out to reduce their experimental uncertainty; thermopiles have also been calibrated to improve the accuracy on the measurements of the heat flow rate. The uncertainty on the channel diameter has been determined starting from an enlarged image of the minichannel

obtained at the microscope. The uncertainty of the diameter is about 0.02 mm. Considering the construction procedure the uncertainty in the length of each sub-sector is 1 mm.

As well known, the experimental uncertainty for each measured parameter during a test run is made of two parts: the first one is the type A uncertainty that derives from repeated observations, the second one is the type B uncertainty that comes from the instruments calibration and manufacturer's specifications.

According to the ISO Guide to Expression of Uncertainty in Measurements [30], the type A standard uncertainty is given by the experimental standard deviation of the mean as follows:

$$u(\theta) = s(\bar{\theta}) = \frac{s(\theta_k)}{\sqrt{n}} \qquad\qquad \textbf{4.23}$$

with

$$s(\theta_k) = \sqrt{\frac{1}{n-1} \sum_{k=1}^{n} (\theta_k - \bar{\theta})} \qquad\qquad \textbf{4.24}$$

where $\bar{\theta}$ is the mean values of the n readings of the parameter θ (all experimental measurements have been recorded during a period of 50 s with a time step of 1 s).

The heat transfer coefficient is obtained as:

$$\alpha_i = \frac{q_{water,i}}{A \cdot (T_{sat} - T_{w,m})_i} = f(m_{water}, \Delta T_{water}, T_{sat}, T_w, d, L_i) \qquad\qquad \textbf{4.25}$$

and the thermodynamic vapor quality at the outlet of each sub-sector is evaluated as:

$$x_{out,i} = \frac{h_{out,i} - h_L}{h_{LG}} \qquad\qquad \textbf{4.26}$$

where the enthalpy at the outlet of each sub-sector can be found from the heat flow rate, the mass flow rate of the refrigerant and the inlet refrigerant enthalpy:

$$h_{out,i} = h_{in,i} - \frac{q_{water,i}}{m_{ref}} \qquad\qquad \textbf{4.27}$$

where the enthalpy at the inlet of the test section is evaluated with the measured temperature and pressure using REFPROP 9.1 (Lemmon et al. [20]).

The mean vapor quality for each sub-sector is calculated from the inlet and outlet values.

The type A and type B uncertainties for the measured parameters are correlated as follows:

$$u_C(\theta) = \sqrt{u_A(\theta)^2 + u_B(\theta)^2}$$

4.28

and when a searched parameter ξ is not directly measured but it can be expressed as a function F of uncorrelated input quantities θ_1, θ_2, ..., θ_N, as in the case of heat transfer coefficient or thermodynamic vapor quality, its combined standard uncertainty is determined from Eq. 4.29.

$$u_C(\xi) = \sqrt{\sum_{i=1}^{N}\left(\frac{\delta F}{\delta \theta_i}\right)^2 u_C(\theta_i)^2}$$

4.29

The expanded uncertainty U is obtained by multiplying the combined standard uncertainty by a coverage factor $k=2$ with a level of confidence of approximately 95%.

Table 4.3. Type B experimental uncertainty of measured parameters

Temperature	$\pm$ 0.05 °C
Temperature difference (with thermopile)	$\pm$ 0.03 °C
Water flow rate in measuring sector	$\pm$ 0.14 % at 10 kg h^{-1}
Refrigerant flow rate	$\pm$ 0.2 % at 2 kg h^{-1}
Absolute pressure	$\pm$ 5 kPa (level of confidence: 99.7%)
Pressure difference (greater than 1 kPa)	$\pm$ 0.12 kPa (level of confidence: 99.7%)
Pressure difference (below 1 kPa)	$\pm$ 0.1% (level con confidence 99.7%)

The expanded percentage uncertainty, considering a coverage factor equal to 2 (level of confidence of 95.45%), for the heat transfer coefficient is reported in Table 4.4.

On average the percentage uncertainty is 3.7%; a maximum of 7,9% has been found at G=50 kg m^{-2} s^{-1}; the experimental uncertainty is higher by decreasing the mass velocity.

Regarding vapor quality, the maximum expanded uncertainty (coverage factor equal to 2 - level of confidence of 95.45%) is about ±0.015.

Table 4.4. Minimum, maximum and mean combined experimental uncertainty of the experimental heat transfer coefficient.

G [kg m^{-2} s^{-1}]	$U(\alpha)$ min [%]	$U(\alpha)$ max [%]	$U(\alpha)$ mean [%]
200	2,5	4,3	3,0
150	2,8	3,9	3,2
100	2,6	4,7	3,6
50	2,7	7,9	4,9

4.2.6 Flow visualizations during convective condensation

The visualization window between the 1st and 2nd heat exchanger allows to record the flow pattern using a Photron FASTCAM Mini UX100 high speed camera (CMOS sensor with Bayer color filter array). The high speed camera has been coupled with a 100 mm Tokina macro lens and a LED illumination system is used as light source. During a condensation test at the same mass velocity, different images have been recorded changing the vapor quality in the glass tube; the vapor quality at the inlet of the glass tube is settled changing the water conditions in the 1st heat exchanger. The images reported from Figure 4.19 to Figure 4.44 have been recorded at 2000 fps except for the visualization at mass velocity equal to 200 kg m^{-2} s^{-1} that have been recorded at 3200 or 4000 fps depending on the vapor quality. In the figures below for each mass velocity and vapor quality there are several images to better appreciate the flow pattern.

One of the most famous flow regimes definition is that reported in Nema et al. [31], which summarized the works of Coleman and Garimella [32-34]. They investigated flow regime during condensation of R134a in both circular channel, inner diameter of 4.91 mm, and rectangular channels with an hydraulic diameter between 1 and 4.8 mm. The four major flow regimes categories observed are: annular, wavy, intermittent and dispersed; each category is then divided in subcategories (Figure 4.18).

As known the annular flow regime is characterized by a liquid film at the tube wall and a vapor core in the channel. They subdivided the annular low regime in:

- mist flow: a very thin liquid film at the wall and a vapor core with significant liquid entrainment;

- annular ring: mist flow with periodic appearance of ring pattern;

- wave ring: similar to the annular ring pattern except that the liquid rings become noticeably thicker at the bottom compared to the top;

- wave packet: wave packets occurring periodically in the flow and waves confined to the bottom of the tube;

- annular film: noticeably thick and approximately uniform liquid film on the tube wall.

In the wavy flow regime there are liquid and vapor layers with liquid flowing on the bottom of the tube and vapor on the top. In this regime they considered only two sub-categories:

- discrete waves: the liquid-vapor interface is clearly distinguishable with the dominant wave pattern being of large wavelength and amplitude. Increasing the wave intensity this flow regime can be further classified;

- disperse waves: the liquid-vapor interface is indistinguishable and there are multiple waves typically with smaller wavelengths and amplitudes along the dominant waves.

In the intermittent flow pattern they considered:

- slug flow pattern: vapor slug move through the liquid often accompanied by discrete waves. The slug can be followed by trailing bubbles;

- plug flow pattern: solitary plug without trailing bubbles.

In the dispersed flow pattern they placed the bubbly flow, characterized by flow of small vapor bubbles in the liquid.

In the categorization above reported the stratified smooth flow is missing.
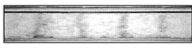
	FLOW REGIMES			
	Annular	**Wavy**	**Intermittent**	**Dispersed**
Flow Patterns	Mist Flow	Discrete Wave (0)	Slug Flow	Bubbly Flow
	Annular Ring	Discrete Wave (1)	Slug Flow	Bubbly Flow
	Wave Ring	Discrete Wave (2)	Plug Flow	Bubbly Flow
	Wave Packet	Disperse Wave (3)	Plug Flow	
	Annular Film	**Note:** Numbers above denote intensity of secondary waves		

Figure 4.18. Flow regime classification. Image from Nema et al. [31]

In the light of the foregoing, the flow pattern visualized during the convective condensation of R134a at a saturation temperature of about 40°C in the test section with an inner diameter of 3.38 mm, are the following:

- at G=200 kg m^{-2} s^{-1} and vapor quality ranging between 0.88 and 0.69 the flow seems to be annular, the liquid film on the bottom of the channel is recognizable and slightly thicker than the film on the top even at this vapor quality (Figure 4.19-Figure 4.21); it can also be supposed that for vapor qualities higher than 0.88 the flow is annular. If the vapor quality is in the range 0.6<x<0.44 (Figure 4.22-Figure 4.24) the flow pattern is in a transition between annular ring and discrete waves (stratified-wavy). So for this mass velocity the two macro-categories of annular flow and wavy flow are present;

- at G=150 kg m^{-2} s^{-1} the annular flow and wavy flow are still the two predominant flow regimes. For x=0.81 (Figure 4.25) or higher the flow is mainly annular ring with the liquid film that start to increase on the bottom of the channel; for 0.69<x<0.58 the flow is in the transition between annular and discrete waves (Figure 4.26 and Figure 4.27); for 0.52<x<0.41 the discrete waves flow pattern has been visualized (Figure 4.28 and Figure 4.29);

- at G=100 kg m^{-2} s^{-1} the discrete wave flow pattern can be recognized in a wide range of vapor qualities, from x=0.81 to x=0.27 (Figure 4.30-Figure 4.37). The wave intensity and amplitude is changing in the vapor quality range but the liquid-vapor interface is always clearly distinguishable. At x=0.21 waves at the interface are able to wash the upper part of the tube (Figure 4.37);

- at G=50 kg m^{-2} s^{-1} in the vapor quality range between 0.81 and 0.45 the flow is completely stratified and the interface between the liquid-vapor is completely smooth without waves (Figure 4.38-Figure 4.42). At x=0.37 and x=0.26 the there some liquid plug (Figure 4.43 and Figure 4.44).

Figure 4.45 summarizes in a plot mass velocity versus vapor quality the visualizations recorded.

1) Mass velocity G = 200 kg m^{-2} s^{-1}

Figure 4.19. Flow pattern during condensation of R134a at 40°C saturation temperature, mass velocity equal to 200 kg m^{-2} s^{-1} and vapor quality of 0.88
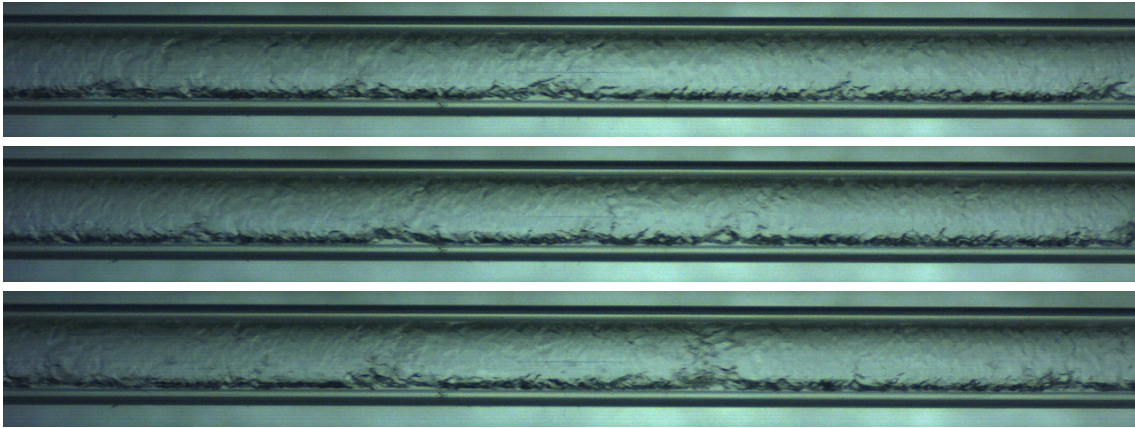
Figure 4.20. Flow pattern during condensation of R134a at 40°C saturation temperature, mass velocity equal to 200 kg m^{-2} s^{-1} and vapor quality of 0.79
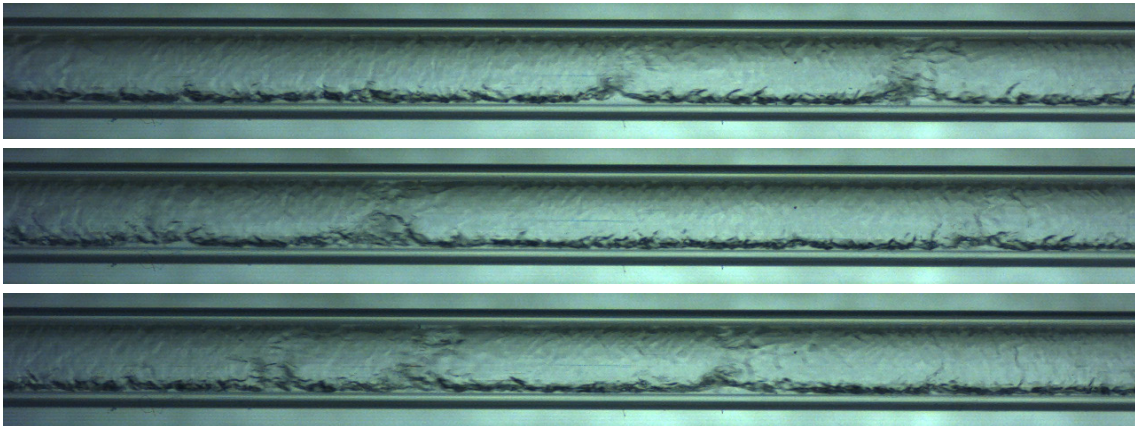
Figure 4.21. Flow pattern during condensation of R134a at 40°C saturation temperature, mass velocity equal to 200 kg m^{-2} s^{-1} and vapor quality of 0.69
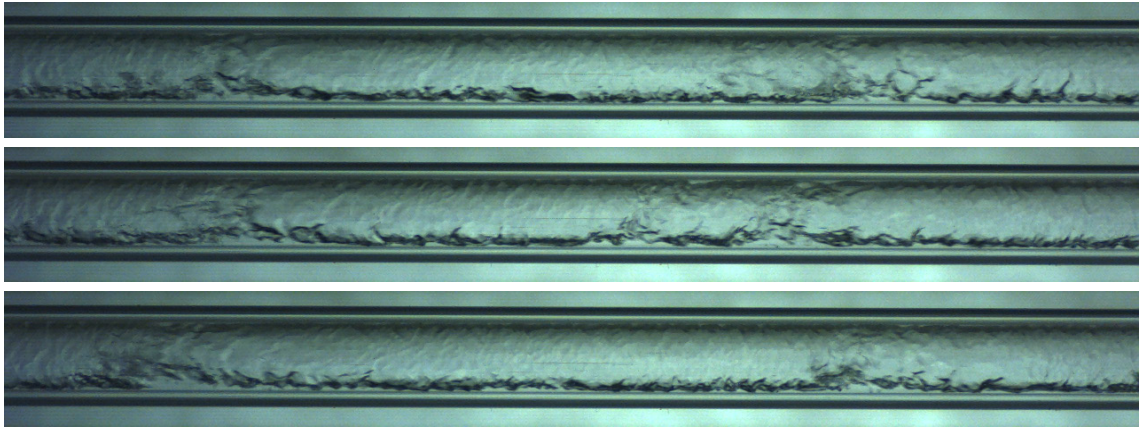
Figure 4.22. Flow pattern during condensation of R134a at 40°C saturation temperature, mass velocity equal to 200 kg m^{-2} s^{-1} and vapor quality of 0.60
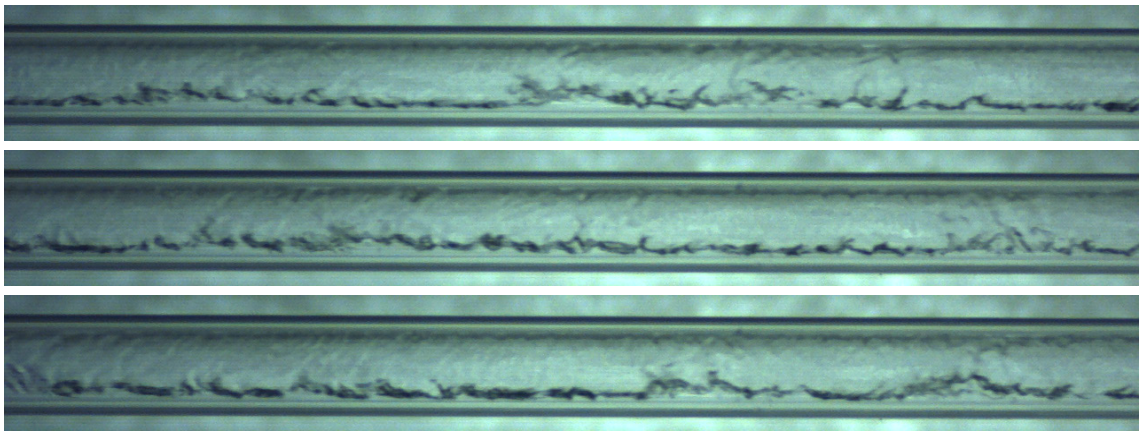
Figure 4.23. Flow pattern during condensation of R134a at 40°C saturation temperature, mass velocity equal to 200 kg m^{-2} s^{-1} and vapor quality of 0.52
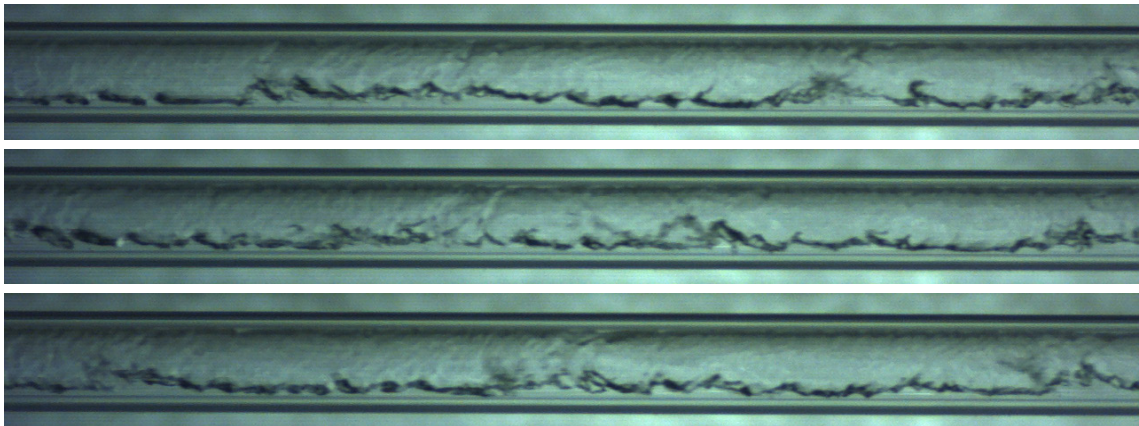
Figure 4.24. Flow pattern during condensation of R134a at 40°C saturation temperature, mass velocity equal to 200 kg m^{-2} s^{-1} and vapor quality of 0.44

2) Mass velocity G = 150 kg m^{-2} s^{-1}
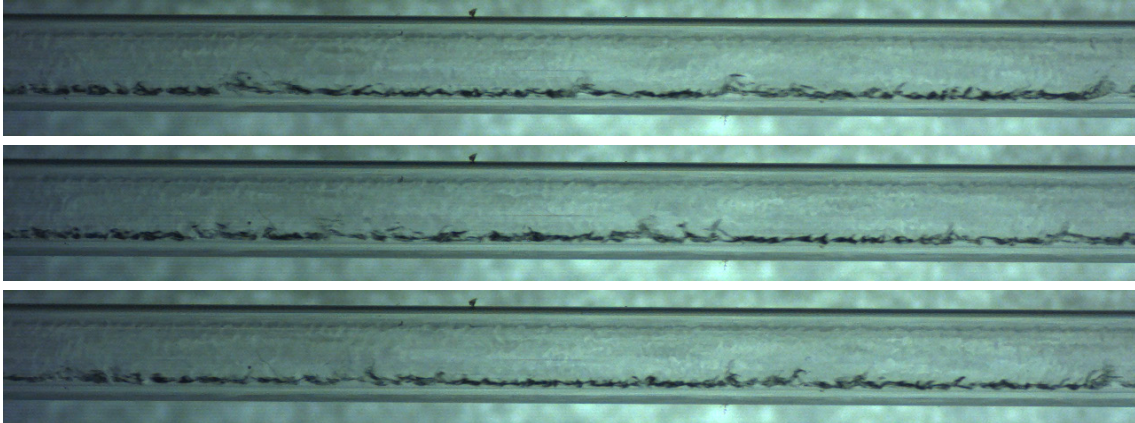
Figure 4.25. Flow pattern during condensation of R134a at 40°C saturation temperature, mass velocity equal to 150 kg m^{-2} s^{-1} and vapor quality of 0.81
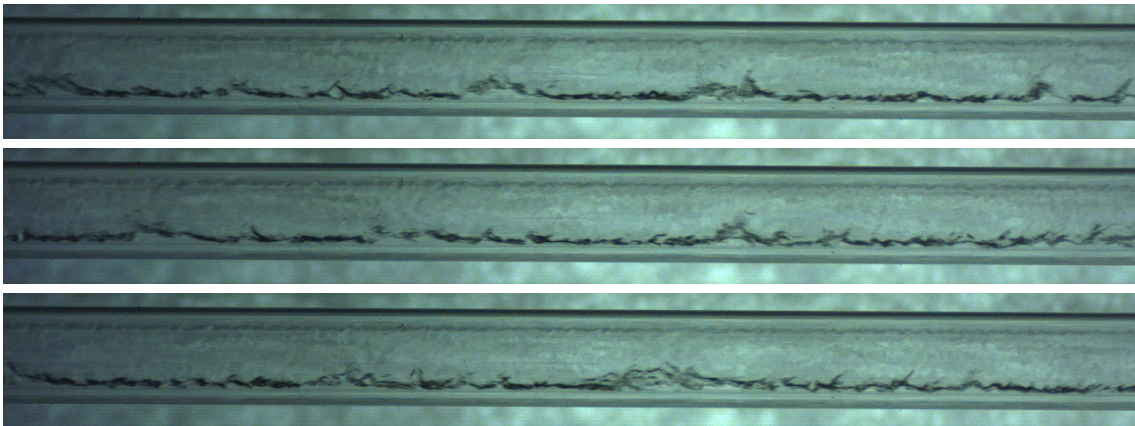
Figure 4.26. Flow pattern during condensation of R134a at 40°C saturation temperature, mass velocity equal to 150 kg m^{-2} s^{-1} and vapor quality of 0.69
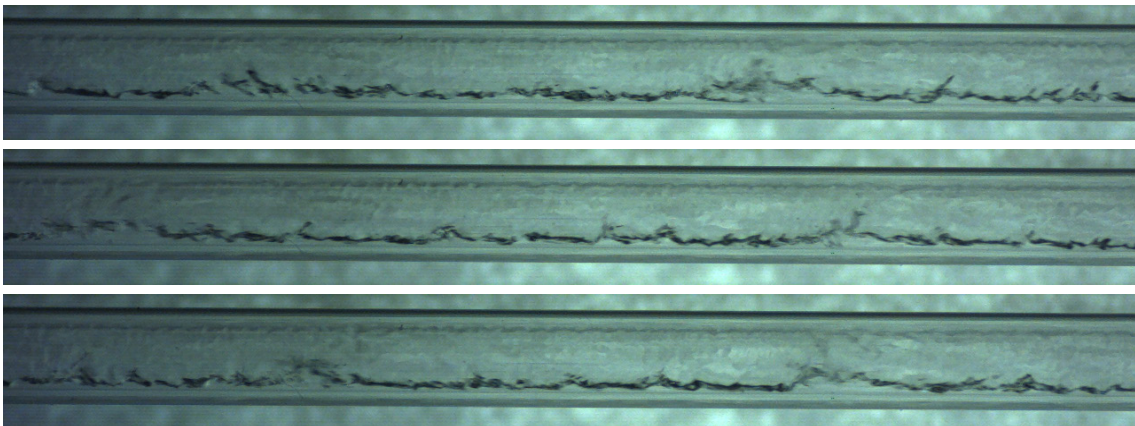
Figure 4.27. Flow pattern during condensation of R134a at 40°C saturation temperature, mass velocity equal to 150 kg m^{-2} s^{-1} and vapor quality of 0.58
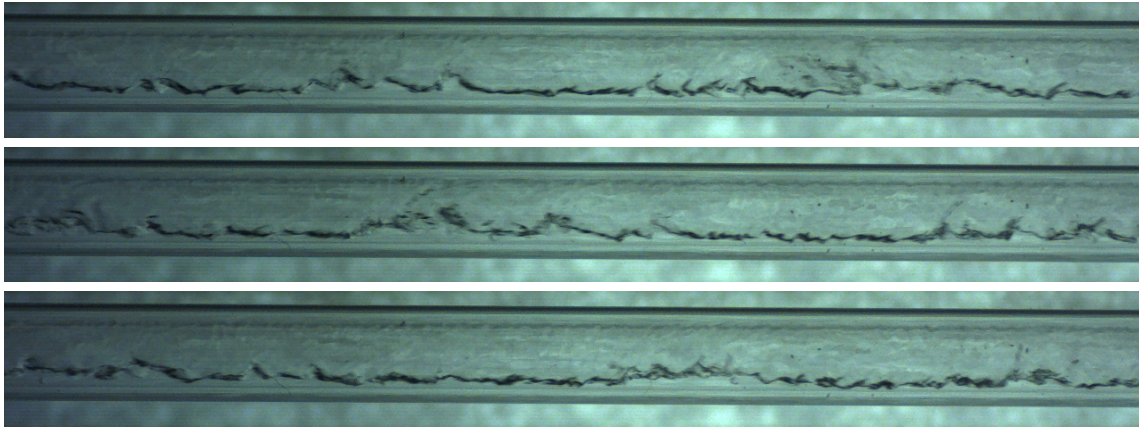
Figure 4.28. Flow pattern during condensation of R134a at 40°C saturation temperature, mass velocity equal to 150 kg m⁻² s⁻¹ and vapor quality of 0.52
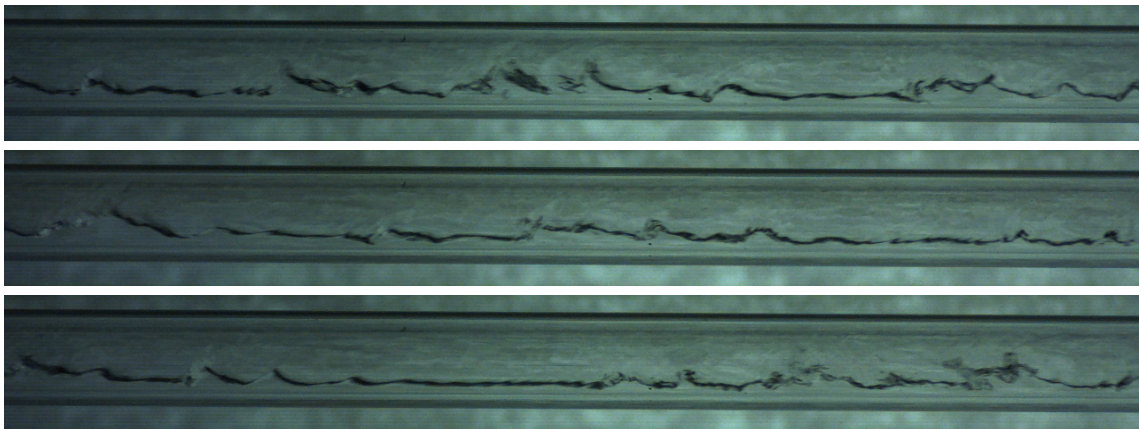
Figure 4.29. Flow pattern during condensation of R134a at 40°C saturation temperature, mass velocity equal to 150 kg m⁻² s⁻¹ and vapor quality of 0.41

3) Mass velocity G = 100 kg m⁻² s⁻¹
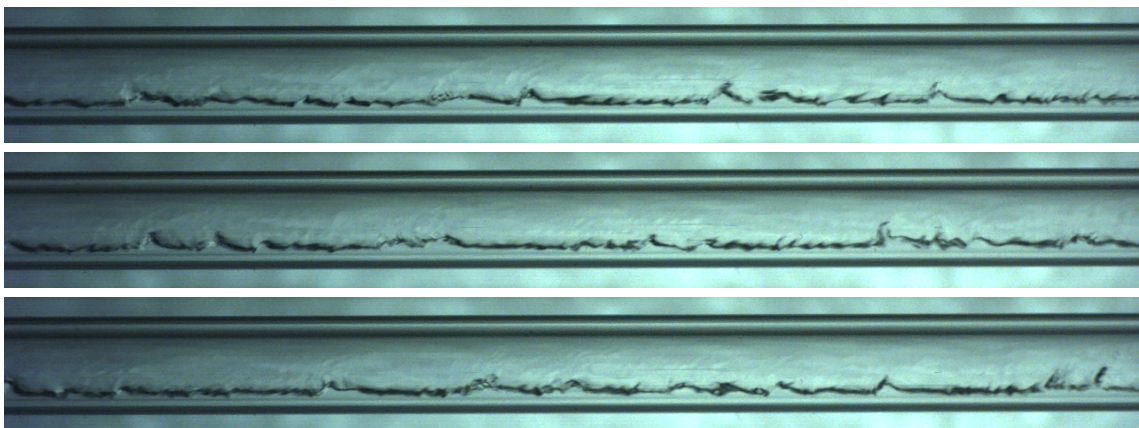
Figure 4.30. Flow pattern during condensation of R134a at 40°C saturation temperature, mass velocity equal to 100 kg m⁻² s⁻¹ and vapor quality of 0.81
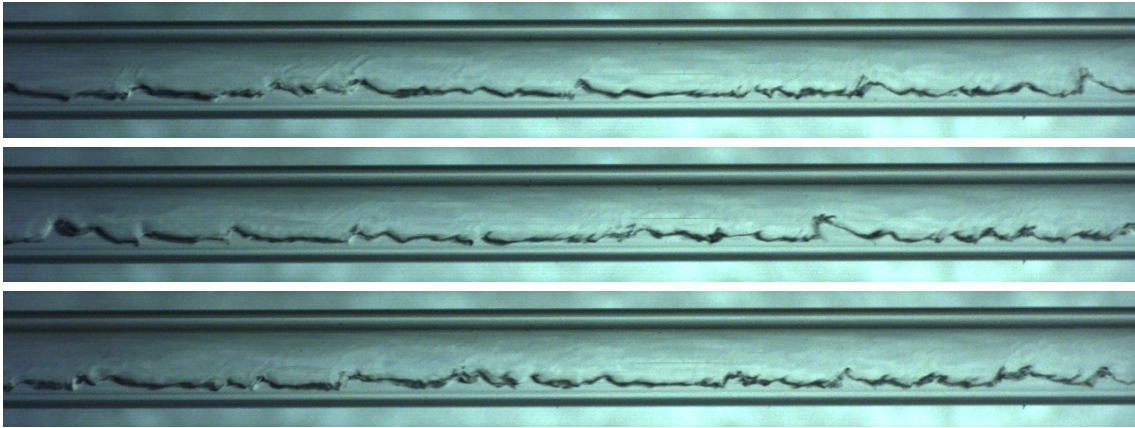
Figure 4.31. Flow pattern during condensation of R134a at 40°C saturation temperature, mass velocity equal to 100 kg m⁻² s⁻¹ and vapor quality of 0.68
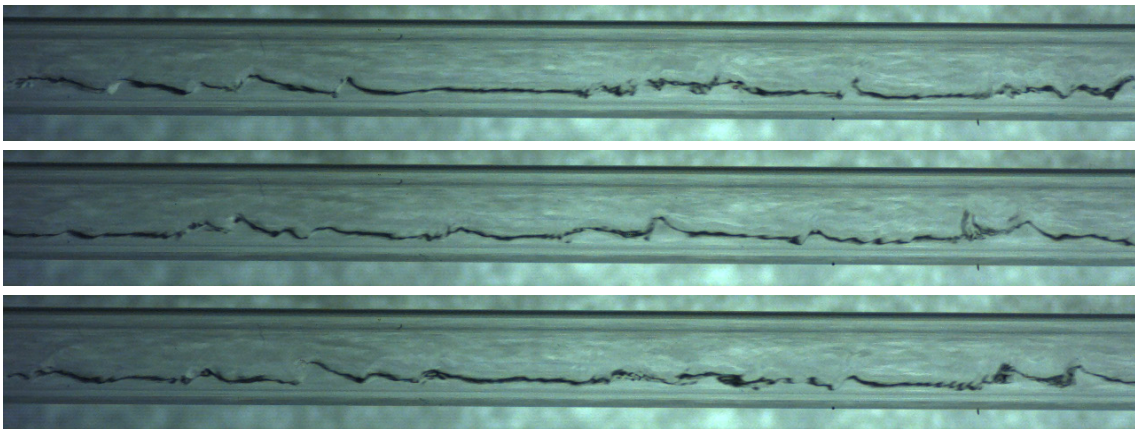
Figure 4.32. Flow pattern during condensation of R134a at 40°C saturation temperature, mass velocity equal to 100 kg m⁻² s⁻¹ and vapor quality of 0.59
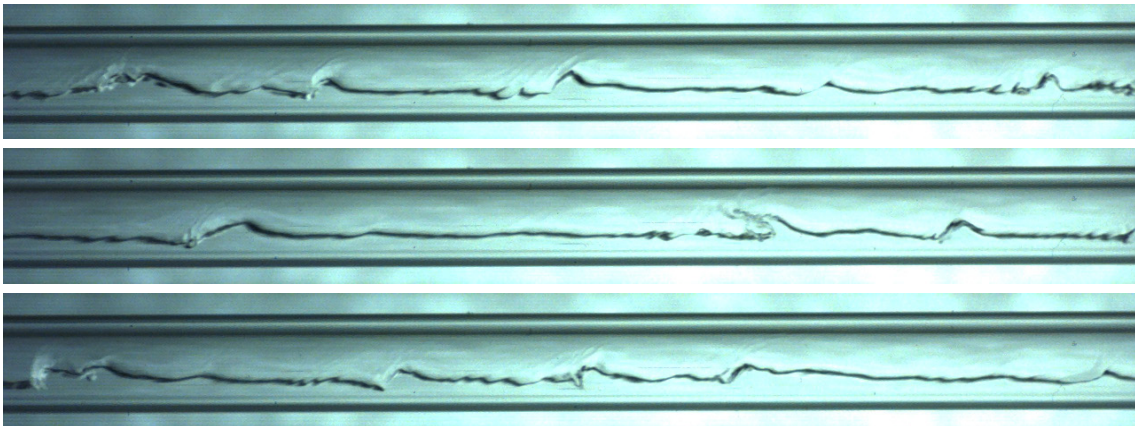
Figure 4.33. Flow pattern during condensation of R134a at 40°C saturation temperature, mass velocity equal to 100 kg m⁻² s⁻¹ and vapor quality of 0.46
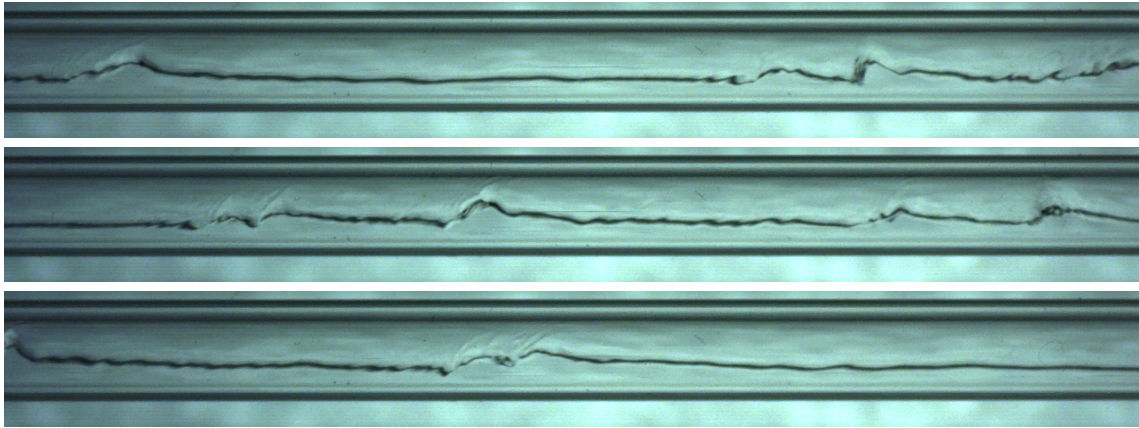
Figure 4.34. Flow pattern during condensation of R134a at 40°C saturation temperature, mass velocity equal to 100 kg m^{-2} s^{-1} and vapor quality of 0.41
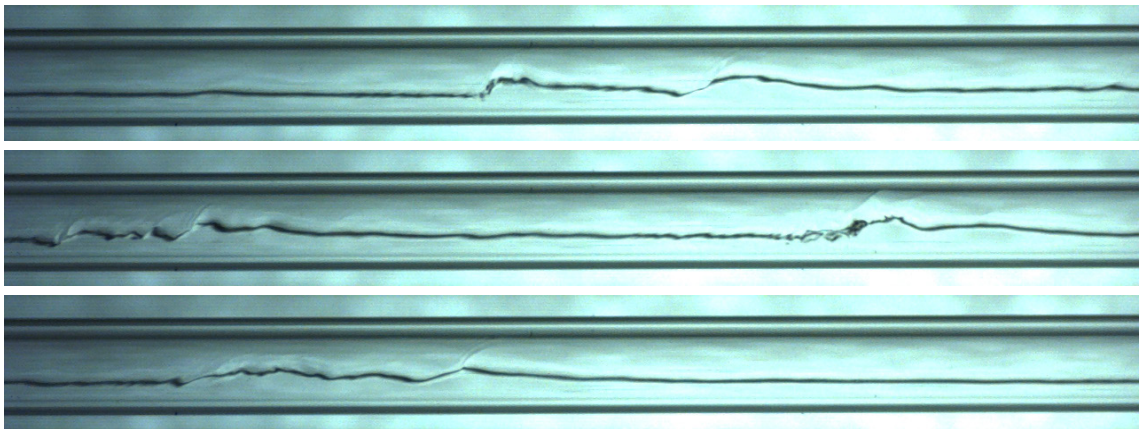
Figure 4.35. Flow pattern during condensation of R134a at 40°C saturation temperature, mass velocity equal to 100 kg m^{-2} s^{-1} and vapor quality of 0.37
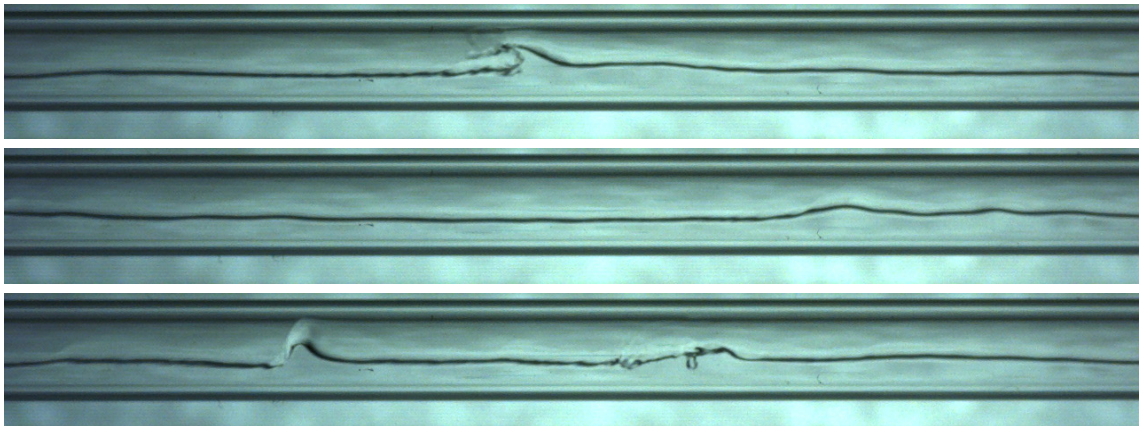
Figure 4.36. Flow pattern during condensation of R134a at 40°C saturation temperature, mass velocity equal to 100 kg m^{-2} s^{-1} and vapor quality of 0.27
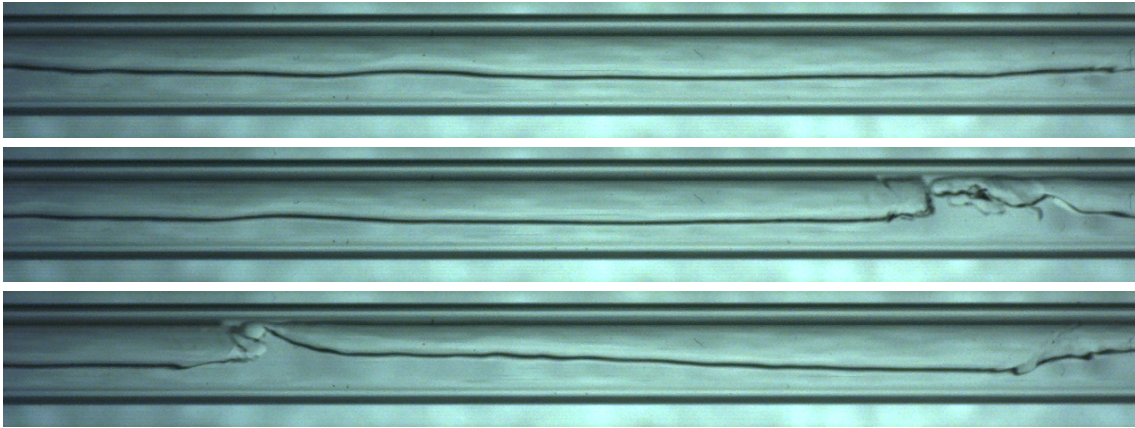
Figure 4.37. Flow pattern during condensation of R134a at 40°C saturation temperature, mass velocity equal to 100 kg m⁻² s⁻¹ and vapor quality of 0.21

4) Mass velocity G = 50 kg m⁻² s⁻¹
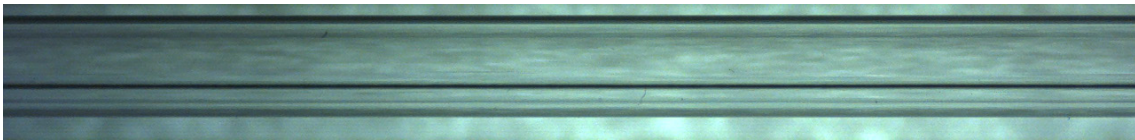
Figure 4.38. Flow pattern during condensation of R134a at 40°C saturation temperature, mass velocity equal to 50 kg m⁻² s⁻¹ and vapor quality of 0.81
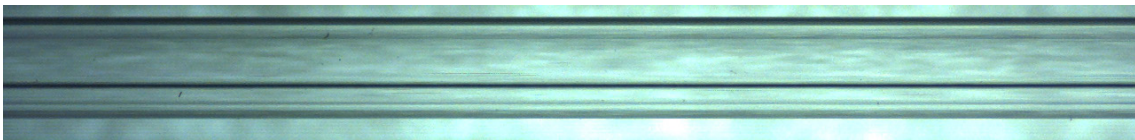
Figure 4.39. Flow pattern during condensation of R134a at 40°C saturation temperature, mass velocity equal to 50 kg m⁻² s⁻¹ and vapor quality of 0.73
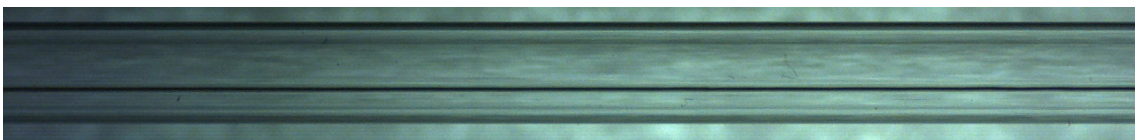
Figure 4.40. Flow pattern during condensation of R134a at 40°C saturation temperature, mass velocity equal to 50 kg m⁻² s⁻¹ and vapor quality of 0.65
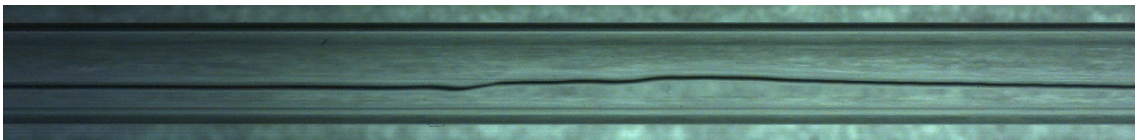
Figure 4.41. Flow pattern during condensation of R134a at 40°C saturation temperature, mass velocity equal to 50 kg m⁻² s⁻¹ and vapor quality of 0.58

Figure 4.42. Flow pattern during condensation of R134a at 40°C saturation temperature, mass velocity equal to 50 kg m⁻² s⁻¹ and vapor quality of 0.45
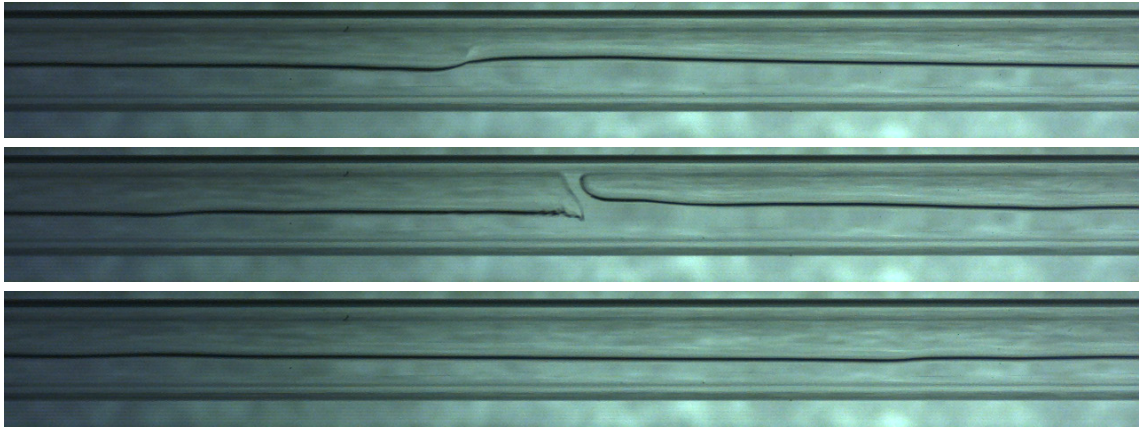
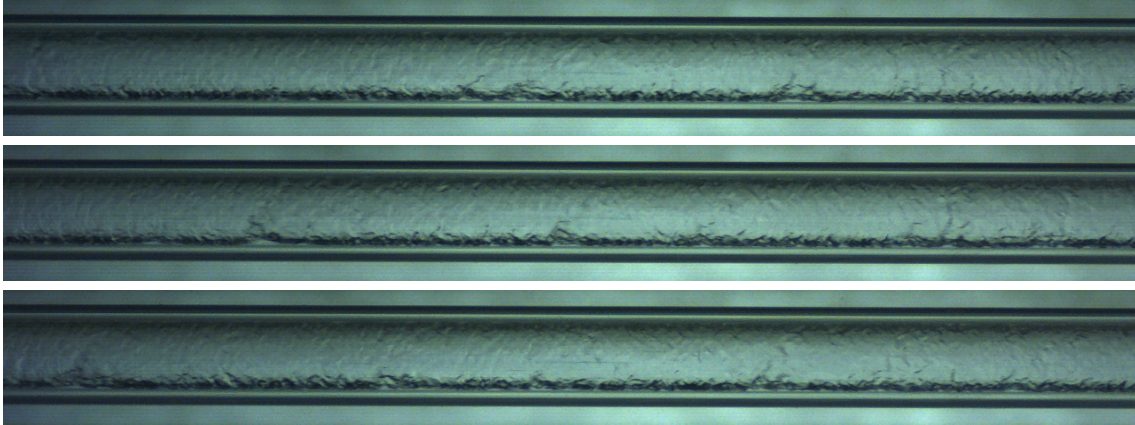**Figure 4.43. Flow pattern during condensation of R134a at 40°C saturation temperature, mass velocity equal to 50 kg m⁻² s⁻¹ and vapor quality of 0.37**
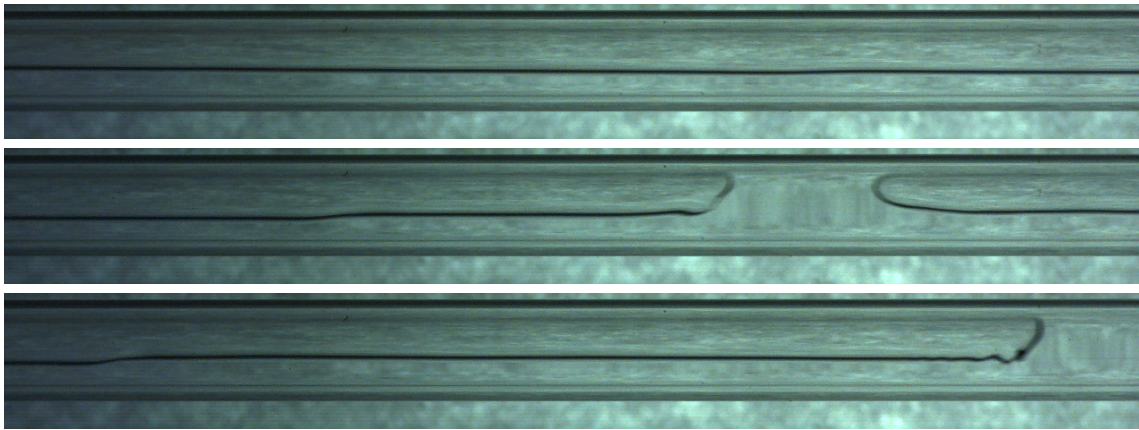
Figure 4.44. Flow pattern during condensation of R134a at 40°C saturation temperature, mass velocity equal to 50 kg m⁻² s⁻¹ and vapor quality of 0.26
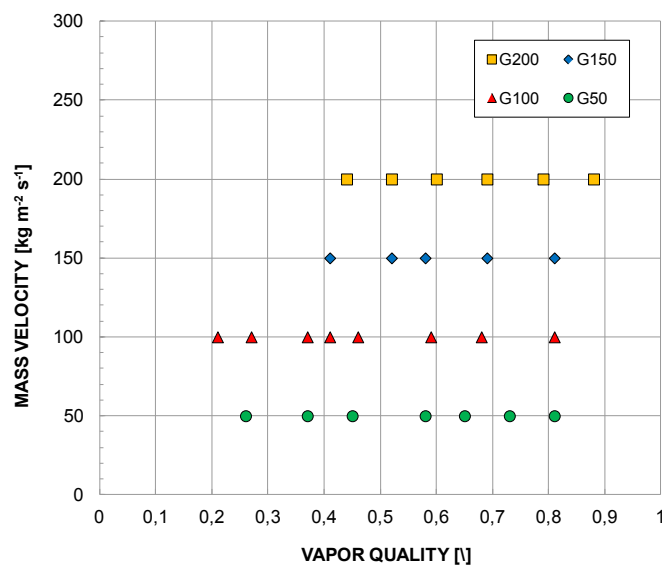

**Figure 4.45. Visualization performed during the condensation of R134a at 40°C saturation temperature in a circular minichannel with an inner diameter of 3.38 mm. Each point corresponds to a recorded flow pattern.**

4.2.7   *Comparison against correlations*

Experimental results, both heat transfer coefficient measurements and flow pattern visualizations, have been compared against three models and flow pattern maps available in the literature. The models are developed for heat transfer coefficient predictions inside macro-scale tubes and minichannels.

The Cavallini et al. [35] model can be used for condensation of halogenated refrigerants inside tubes with inside diameters between 3 and 21 mm, reduced pressure $p_R<0.75$ and density ratio $(\rho_L/\rho_G)>4$; it provides criteria for the definition of transition between different flow patterns. The flow patterns, occurring during the condensation process, considered are:

- Annular flow, for J_G greater than 2.5: it has been modeled starting from the simple equation proposed by Kosky and Staub [36] where the heat transfer coefficient is correlated to the frictional pressure gradient through the interfacial shear stress. For the evaluation of the frictional pressure gradient during annular flow, the authors suggested a correlation, based on the Friedel [37] parameters, but with modified numerical constants and exponents. This new equations have been obtained from a best-fitting of two databanks, Cavallini et al. [38] and Zhang [39], specifically calibrated for annular flow using data points relative to dimensionless vapor velocity J_G greater than 2.5.

- Annular-stratified flow transition and stratified flow, for $J_G<2.5$ and $X_{tt}<1.6$: in this region the heat transfer coefficient is calculated from a linear interpolation between the heat transfer coefficient for annular flow and the one for stratified flow. The heat transfer coefficient for annular flow is evaluated with the same equations used in the annular flow region but with the fictitious mass velocity G relative to J_G=2.5. The heat transfer coefficient for the stratified flow is expressed as the sum of two components: the first is relative to the upper part of the tube and it is calculated with a Nusselt-type equation; the second component is given as a convective term and refers to the lower part of the tube. The authors applied a best-fitting procedure to determine the constants and exponents of the heat transfer coefficient for the stratified flow equation. The fully stratified regime is located in this region but there is no criterion to distinguish it from the wavy-stratified flow regime.

- Stratified-slug transition and slug flow, for $J_G<2.5$ and $X_{tt}>1.6$: in this region the heat transfer coefficient can be computed as a linear interpolation from the coefficient calculated with the same equations used in the annular flow region but with the fictitious vapor quality x relative to X_{tt}=1.6 and the one for the liquid flowing with the entire flow rate. Although, as per authors note, this equation slightly overpredicts experimental data in the region of slug flow. Anyway, it can be noticed that this flow regime is less important than the annular-wavy transition in terms of thermal performance.

- Bubbly-Intermittent flow, $J_G>2.5$ and low vapor qualities: whatever the value of X_{tt} the authors suggested to use the equation of the annular flow regime.

The second model is the one by Cavallini et al. [18], which was developed to determine the condensation heat transfer coefficient of fluids flowing into horizontal smooth tubes with internal diameters higher than 3 mm. This correlation, slightly simplified the Cavallini et al.

[35] model and proposed two basic equation and account for the transition from ΔT-independent region and ΔT-dependent, where ΔT is the saturation minus wall temperature difference; the transition line is function of the fluid. The model included all possible flow regimes observed during the condensation process: annular flow, stratified-wavy flow, stratified-smooth flow and slug flow.

El Hajal et al. [40] in 2003 presented a new version of the two-phase flow pattern map for condensation inside horizontal plain tubes, originally developed by Kattan et al. [41] for flow boiling. Their flow pattern map considers the typical flow regime observed during condensation inside horizontal tubes: mist flow, annular, intermittent, stratified-wavy and fully stratified flow. To clarify the flow regime sub-division: the mist flow regime is typical of high mass velocities and vapor qualities; with intermittent they refer to the plug and slug flow regimes with the characteristic large amplitude waves washing the top of the tube. The flow pattern map incorporates the evaluation of a logarithmic mean void fraction obtained from the values calculated with the Rouhani-Axelsson (Steiner [42]) and the homogenous method, to span the range from low pressure up to pressures near the critical point. The flow pattern map is the milestone for the model presented in Thome et al. [43]. The authors compared the model against tests obtained in nine independent research laboratories with 15 different fluids (R-11, R-12, R-22, R-32, R-113, R-125, R-134a, R-236a, R-32/R-125, R-404A, R-410A, propane, n-butane, iso-butane, propylene). The test conditions varied between 24 to 1022 kg m^{-2} s^{-1} for the mass velocity, 0.03 to 0.97 for the vapor quality, 0.02 to 0.8 for the reduced pressure and from 3.1 to 21.4 mm for the tube internal diameter.

In Figure 4.46 the flow pattern map of Cavallini et al. [35] is overlaid on the El Hajal et al. [40] flow pattern map. As can be seen the two annular flow regions coincide and the slug flow of Cavallini et al. [35] is partially inside the intermittent region and the stratified-wavy region of El Hajal et al. [40]. The annular-wavy stratified flow transition + stratified flow of Cavallini et al. [35] falls mainly in 3 region of the El Hajal et al. [40] flow pattern map: the intermittent region, the stratified-wavy region and the stratified one; even if in the evaluation of the heat transfer coefficient of Cavallini et al. [35] they considered in the annular-wavy stratified flow transition + stratified flow a linear interpolation between the heat transfer coefficient for annular flow (calculated at the boundary condition of the region) and the heat transfer coefficient for stratified flow, the map does not account for a clear division between wavy-stratified and fully stratified zone.

In Figure 4.46 the experimental point of this work are also reported. Comparing the flow pattern maps of Cavallini et al. [35] and El Hajal et al. [40] with the flow visualizations reported in Section 4.2.6 it can be seen that:

- for G=200 kg m^{-2} s^{-1} the Cavallini et al. [35] predicts quite good the transition between the annular flow regime and the wavy flow, which from the visualization can be seen at vapor quality around 0.7-0.6. At this mass velocity the El Hajal et al. [40] map suggests annular flow and intermittent flow with the transition at x=0.45;

- from the visualization at G=150 kg m^{-2} s^{-1} for vapor quality x=0.81 the flow is annular, between 0.69 and 0.58 is in the transition between annular and stratified-wavy. The Cavallini et al. [35] map seems to well predict the transition between the annular and the

stratified-wavy regime; in the El Hajal et al. [40] map the transition between the annular and the stratified-wavy flow regime overlapped the experimental points;

- for G=100 kg m^{-2} s^{-1} both the flow pattern maps predicts a stratified-wavy flow regime as expected from the visualizations;

- as mentioned above in the Cavallini et al. [35] map there is no a clear boundary between the annular-wavy stratified flow transition + stratified flow region and the fully stratified flow region, so for G=50 kg m^{-2} s^{-1} the region is the same as G=100 kg m^{-2} s^{-1}. On the other hand the El Hajal et al. [40] map divides the fully and the wavy-stratified flow regions; however it slightly missed to predict that for G=50 kg m^{-2} s^{-1} greater than x=0.45 the flow is stratified smooth.
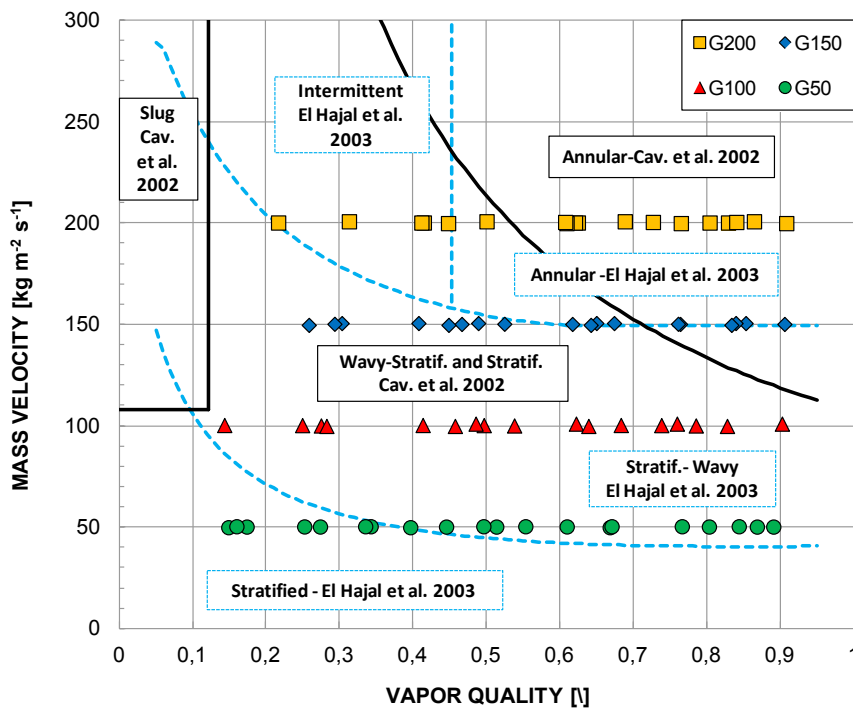
Figure 4.46. Comparison between the Cavallini et al. [35] (black lines) and the El Hajal et al. [40] (light blue lines) flow pattern maps, for R134a at 40°C saturation temperature in a 3.38 mm inner diameter channel.

In Figure 4.47 the Cavallini et al. [18] transition between the ΔT-dependent and the ΔT-independent flow regime is depicted and the transition curve from stratified-wavy flow to intermittent and annular flow of El Hajal et al. [40] has been converted to the J_g vs X_{tt} format to be displayed for comparison. The Cavallini et al. [18] map predicts quite well the transition between annular flow and stratified-wavy flow at G=200 kg m^{-2} s^{-1} and G=150 kg m^{-2} s^{-1}.
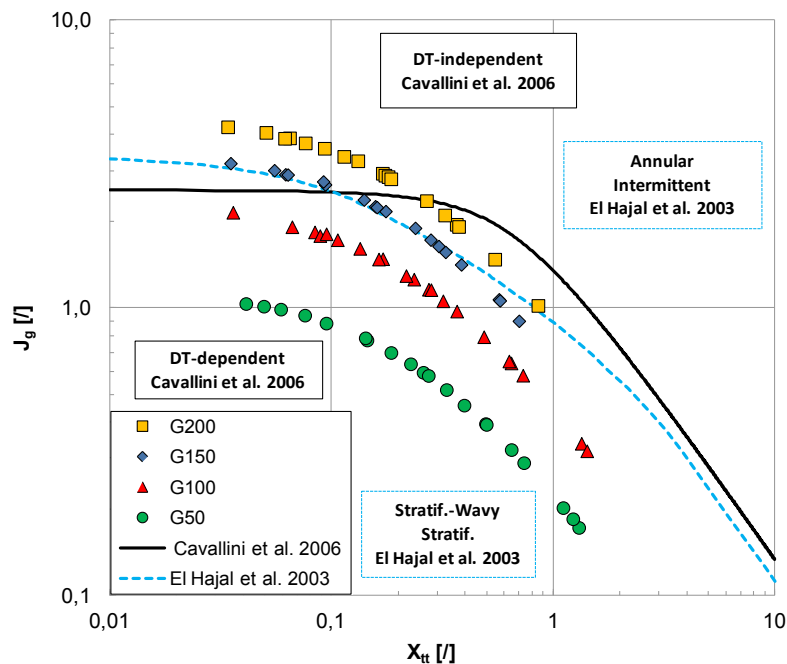
Figure 4.47. Comparison between the Cavallini et al. [18] (black line) and the El Hajal et al. [40] (light blue line) flow pattern maps, for R134a at 40°C saturation temperature in a 3.38 mm inner diameter channel.

Figure 4.48 reports the comparison between the experimental heat transfer coefficients and the predicted values using the correlation by Cavallini et al. [35]. The data at G=200 kg m^{-2} s^{-1} and G=150 kg m^{-2} s^{-1} are in good agreement with the experimental ones, showing that the experimental points in the annular flow regime close to the transition between annular and stratified-wavy flow regime are well predicted. Decreasing the mass velocity the correlation shows higher errors: a general underprediction for the data at G=100 kg m^{-2} s^{-1} and an high standard deviation for the data at 50 kg m^{-2} s^{-1}.

The comparison between the experimental data and predictions with the Cavallini et al. [18] model is reported in Figure 4.49. The model slightly underpredicts the experimental data with an e_{AB}=17.4 % and a σ_N=6.1 %.

In Figure 4.50 the comparison with the Thome et al. [43] is presented. Among the models tested until now is the one that predicted better the experimental data at G=50 kg m^{-2} s^{-1} with e_{AB} about 9 % and a σ_N about 9 %. Globally the model underestimates the database with e_{AB}=21.2 % and a σ_N=4.4 %. To avoid potential computational problems due to the fact that G=150 kg m^{-2} s^{-1} is over the transition between the annular flow region and the wavy-stratified flow region, the curve has been slightly moved, leaving the points in the annular flow zone; no significant results have been found. In the of Thome et al. [43] model some constants have been found statistically, as for example c, n and m in the equation of the convective condensation heat transfer coefficient (Eq. 4.30).

$$\alpha_c = c \cdot \text{Re}_L^n \cdot \text{Pr}_L^m \cdot \frac{\lambda_L}{\delta} f_i \qquad\qquad \textbf{4.30}$$

The database used was mainly formed with data coming from macro-tube (d_h>8 mm). As an exercise if the constant n is changed from 0.74 to 0.77 to better fit the present data, the absolute mean deviation of the model moves to 8.7 %. The new comparison is reported in Figure 4.51.

The results of the comparison between the experimental data and these three models, in their original version, are summarized in Table 4.5.
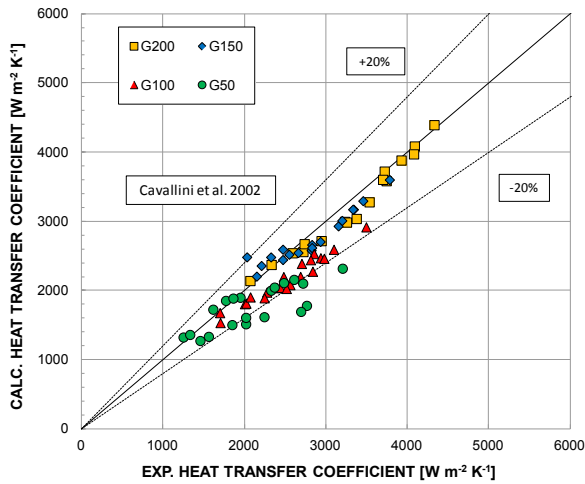
Figure 4.48. Comparison between measurements and calculated heat transfer coefficients by Cavallini et al. [35] during condensation of R134a at 40°C and different mass velocities G [kg m^{-2} s^{-1}]
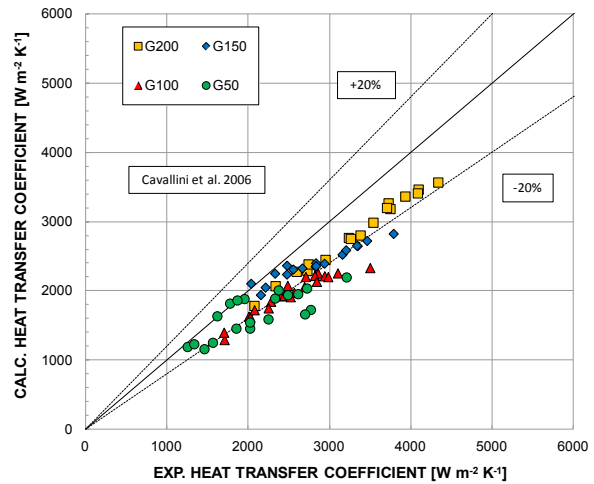
Figure 4.49. Comparison between measurements and calculated heat transfer coefficients by Cavallini et al. [18] during condensation of R134a at 40°C and different mass velocities G [kg m^{-2} s^{-1}]
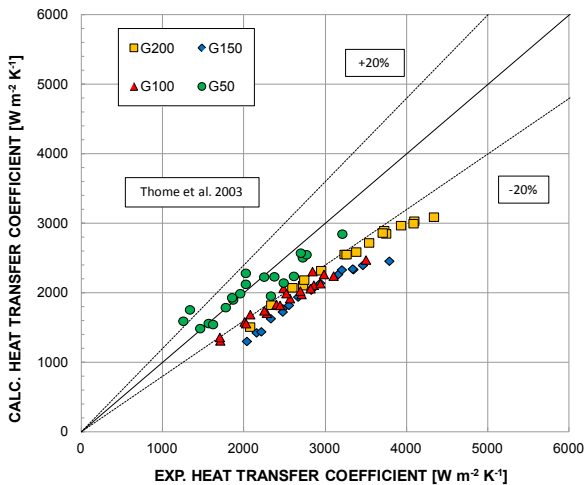
Figure 4.50. Comparison between measurements and calculated heat transfer coefficients by Thome et al. [43] during condensation of R134a at 40°C and different mass velocities G [kg m^{-2} s^{-1}]
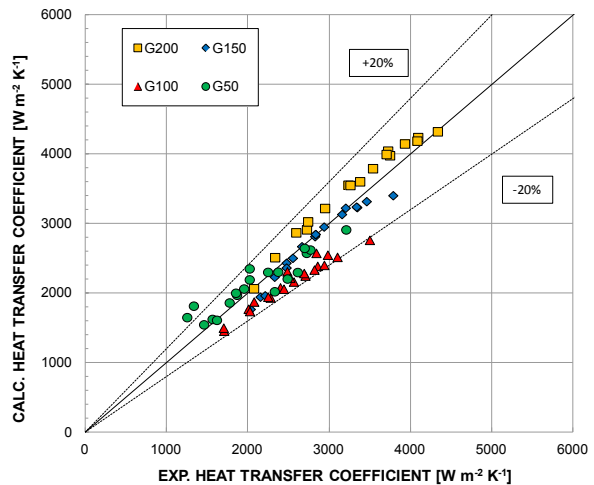
Figure 4.51. Comparison between measurements and calculated heat transfer coefficients by Thome et al. [43], with modified constants, during condensation of R134a at 40°C and different G [kg m^{-2} s^{-1}]

Table 4.5. Mean absolute deviations and standard deviation of the models. *G* is the mass velocity in [kg m⁻² s⁻¹]

Model	eAB [%]					σN [%]				
	G50	G100	G150	G200	Mean	G50	G100	G150	G200	Mean
Cavallini et al. [35]	16,3	13,9	6,2	4,3	**10,2**	10,7	4,5	4,5	3,2	**5,7**
Cavallini et al. [18]	18,7	22,1	14,1	14,7	**17,4**	11,9	4,0	6,8	1,7	**6,1**
Thome et al. [43]	8,8	23,4	29,7	23,0	**21,2**	8,7	3,3	3,0	2,4	**4,4**

4.3 Nomenclature

A	area	[m²]
c	specific heat	[J kg⁻¹ K⁻¹]
d, D_h	hydraulic diameter	[m]
f	friction factor	[/]
f_i	interfacial roughness factor	[/]
G	mass velocity	[kg m⁻² s⁻¹]
h	specific enthalpy	[J kg⁻¹]
L	length	[m]
$\dot{m}$	mass flow rate	[kg s⁻¹]
p	pressure	[Pa]
Pr	Prandtl number	[/]
q	heat flow rate	[W]
q'	heat flux	[W m⁻²]
R^2	R square coefficient of determination	[/]
R^2_{adj}	adjusted R square coefficient of determination	[/]
Ra	arithmetical mean deviation of the profile according to ISO 4297:1997	[μm]
Re	Reynolds number	[/]
T, t	temperature	[K]
u	uncertainty	
x	thermodynamic vapor quality	[/]
z	position	[m]

Greek symbols

α	heat transfer coefficient	[W m⁻² K⁻¹]
δ	liquid film thickness annular ring	[m]
Δh	enthalpy difference	[J kg⁻¹]
Δp	pressure difference	[Pa]
ΔT	temperature difference	[K]
λ	thermal conductivity	[W m⁻¹ K⁻¹]
μ	dynamic viscosity	[Pa s]
ρ	density	[kg m⁻³]
σ	surface tension	[N m⁻¹]

Subscripts

f	frictional
g,v,G	vapor
in	inlet
l,L	liquid
MS	measuring sector
out	outlet
PS	pre-conditioning sector
ref	refrigerant
sat	saturation
w	wall

5 CONDENSATION HEAT TRANSFER IN MICROGRAVITY CONDITIONS

5.1 Introduction

In the literature very few study deal with the effect of gravity during condensation. Some of these studies investigate the convective condensation at different inclination angles from vertical downward to vertical upward. Lips e Mayer [12] presented an experimental investigation of condensation of R134a inside a tube with an inner diameter of 8.38 mm at different inclinations. The mass velocity ranges between 200 to 600 kg m^{-2} s^{-1}. In their results, the heat transfer coefficient depends on the distribution of the two phases inside the tube and hence on the flow pattern, which results from the balance between gravitational force, shear stress and surface capillary force. The images collected using a high-speed camera display that at high vapor qualities and high mass fluxes, the flow becomes annular and is insensitive to the inclination angle. On the other hand, at low mass fluxes and vapor quality, the inclination strongly affects the flow pattern: stratified flow occurs at slightly downward orientations, intermittent flow is observed at higher angles, whatever the flow direction, and churn flow occurs both in vertical downflow and in vertical upflow. Under these conditions, the results show that for an inclination angle of 15° in downward flow, the maximum heat transfer coefficient is achieved. At high mass velocities, the shear stress is the dominant force and there is no effect of inclination on the heat transfer. According to the authors, it is necessary to develop new predictive flow pattern maps to study condensation in inclined tubes. A tube with the same diameter has been used by Mohseni et al. [44] to study the flow patter and the heat transfer during condensation of R134a. In this work the experiments have been conducted at 35°C saturation temperature, at mass flux spanning from 53 to 212 kg m^{-2} s^{-1}. In vertical downflow, the dominant flow pattern is annular, regardless of vapor quality and mass flux. At 60° and 30° downflow, similar flow regimes have been detected: in a wide range of vapor qualities and mass fluxes the flow pattern is annular or semi-annular while only at low vapor qualities, stratified flow occurs. When the tube is horizontal, changes from annular to wavy annular and finally to stratified-wavy have been observed when decreasing vapor quality. At 30° upflow, annular and wavy-annular (in some cases wavy-stratified) flow patterns occur, similarly to the case at 60° upflow, when slug flow pattern is also present at vapor quality lower than 0.1. Finally, in vertical upflow the following regimes have been noticed as condensation proceeds: annular, annular-wavy, churn and slug flow (only at the lowest mass velocities). In the range of low vapor qualities, the highest heat transfer coefficient occurs at 30° upwards. Lyulin et al. [45] investigated the heat transfer coefficient during convective condensation of pure ethanol vapor inside a circular smooth tube with an inner diameter of 4.8 mm and a length of 200 mm. During the tests mass velocity varied from 0.24 to 2.04 kg m^{-2} s^{-1} and the saturation temperature was fixed at 58°C. The study focused both on the difference between the wall to saturation temperature and the influence of inclination angle, that varied from 0° (horizontal) to 90° downflow. The results show that the heat

transfer coefficient reduces with the increase of the wall to saturation temperature difference; the dependency of the heat transfer coefficient on inclination has a maximum in the range from 15° to 35° downstream inclination due to the complex gravity drainage mechanism of the condensed liquid.

Regarding theoretical works, Wang and Rose [46] extended their model for condensation in minichannels to investigate the effect of channel inclination during condensation of R134a in square minichannels with side of 0.5, 1 and 3 mm. They treated the condensate film by taking into account the surface tension, the surface curvature and the Nusselt approximations of laminar flow, neglecting inertia and convection terms. Their work gives provisional results on the condensate film thickness, the mean heat flux and the mean heat transfer coefficient around the channel perimeter for a range of inclinations from vertical upflow to vertical downflow. Saffari and Naziri [47] presented a theoretical and numerical analysis of heat transfer during stratified condensation inside inclined tubes. The results are presented for the condensation of three different refrigerants: R141b, R11 and R134a inside a channel with an internal diameter equal to 14.3 mm. The inclination angle is shown to have a significant effect on condensation heat transfer coefficient and the optimum inclination angle was found to be in the range 30–50° from the horizontal position in upflow configuration. Both theoretical and experimental results were submitted by Wang and Du [48] for the condensation of water inside an inclined small diameter tube. They modeled and tested circular tubes with inner diameters ranging from 1.94 to 4.98 mm and for low mass fluxes (up to 100 kg m^{-2} s^{-1}) varying the orientation (horizontal and downward flow at 17°, 34° and 45°). They found that the effect of inclination on the heat transfer coefficient was poor for the smallest tubes and strong for the tube with bigger inner diameters. Da Riva and Del Col [2] simulated the condensation process inside a circular cross section minichannel (1 mm inner diameter) assuming horizontal orientation, vertical downflow orientation under normal gravity conditions and finally vertical orientation under zero-gravity conditions. In the simulations performed with the Volume of Fluid (VOF) method, R134a is the working refrigerant at 40°C saturation temperature and two mass velocities (G = 100 kg m^{-2} s^{-1} and G = 800 kg m^{-2} s^{-1}) are considered. The wall temperature has been assumed as constant and uniform all along the computational domain and the saturation to wall temperature difference has been fixed at a value of 10 K. At G = 100 kg m^{-2} s^{-1}, the liquid film flow has been assumed as laminar and higher heat transfer coefficients are obtained in the horizontal configuration as compared to the vertical one. In particular, at this low mass flux, in horizontal configuration, the gravity was found to have a key role: as condensation proceeds, the liquid films remains very thin in the upper part of the channel, while it gets thicker at the bottom. In vertical downflow at normal gravity, the problem was treated as axisymmetrical, because no difference is expected along the perimeter for a given channel cross section. At G = 800 kg m^{-2} s^{-1}, a computational approach based on the turbulent liquid film hypothesis has been considered and all the simulations display almost identical results and the shear stress is found to be the dominant force since the distribution of the local condensate thickness and local heat flux is axisymmetrical.

About convective condensation during microgravity conditions one work present in the literature is the one of Lee et al. [49]. They tested two different condensation modules using FC-72 as working fluid:

- the first one was dedicated to the evaluation of the heat transfer coefficient during in-tube convective condensation; the FC-72 flows in a stainless steel tube with an inner diameter of 7.12 mm and 0.41 mm wall thickness;

- the second was used for the visualization of the out-side tube condensation; the outer diameter of the tube is 5.99 mm.

Thus the evaluation of the heat transfer coefficient has been done during condensation inside tube and visualization of the flow pattern during condensation outside tube. The authors found that the condensation heat transfer coefficient is a strong function of the mass velocity of FC-72; for low FC-72 mass velocity the decrease of the heat transfer coefficient along the condensation length is monotonic; for high FC-72 mass velocities there is an enhancement due to both turbulence and increased waviness. They showed that the influence of gravity is very significant for low FC-72 mass velocities.

5.1.1 Platforms to simulate microgravity

Microgravity can be simulated on Earth in mainly three ways, with:

- drop tower: it is a long conduct in which microgravity is reach during free fall. With these systems the microgravity duration is quite short and for the operators is impossible to manually access to the experiment. The microgravity time depends on the length of the conduct, for example the 105 m German drop tower in Bremen (ZARM) gives the possibility to simulate the microgravity for 4.72 s;

- sounding rockets: like drop towers the experiments can be accessed manually by operators. They are sub-orbital carrier and they provide 180 to 780 s of reduce gravity;

- parabolic flights: they allow to achieve approximately 20 s of microgravity, preceded and followed by a period of hyper-gravity due to the parabola maneuver. During a flight several parabolas are performed and the possibility to access to the experiment is a significant advantage.

5.1.2 The present work

In this chapter, gravity effect on convective condensation inside a 3.38 mm circular channel is presented. Tests have been carried out on a wide range of mass velocity, including low values, down to 70 kg m^{-2} s^{-1}, during the 62nd ESA Parabolic Flight Campaign onboard the Novespace Airbus A-310.

Heat transfer coefficient measurements have been performed together with two-phase flow pattern visualizations during in-tube convective condensation of HFE-7000.

The objectives of this research are the following:

- measurements of the heat transfer coefficient during condensation in microgravity: obtain new reliable quasi-local heat transfer coefficient data to get a better understanding of the condensation phenomena in microgravity conditions. New unique data on the effects of shear stress and surface tension on heat transfer during condensation inside minichannels will be presented;

- perform visual observations: flow pattern and phase distribution will be characterized by direct visualization of the flow through a transparent section of the channel using a high-speed video camera. The effect of gravity/microgravity on the different flow regimes will then be analyzed.

- comparison with experiments at ground gravity conditions: the data obtained in microgravity will be compared with experimental data achieved at normal gravity to analyze the gravity effect on heat transfer coefficient, flow structures and regime transition.

It is also important to say here that this research activity has been carried out in collaboration with two other research groups:

- Microgravity Research Center, Université libre de Bruxelles;

- Laboratoire Plasma et Conversion d'Energie, Université Paul Sabatier, Toulouse.

5.2   Experimental apparatus

The experimental apparatus used in this study (Figure 5.1) has been designed to perform parabolic flight experiments and to provide detailed heat transfer measurements as to allow the simultaneous visualization of the flow pattern using an high speed camera. The experimental test section is described in Section 3.

The facility is composed of two main loops: the refrigerant loop and the coolant water loop. The working fluid exiting the fan coil as subcooled liquid is sent through a gear pump and in one of the two flowmeters, depending on the mass flow rate range. The M4 mass flow meter has an operation range between 0.75 to 15 mL/min and operates on a thermal, through-flow measuring principle; the M5 is a turbine mass flow meter and works on a higher range of mass flow rates, between 10 to 100 mL/min. Then the fluid is heated up in a stirrer evaporator and the exiting vapor is superheated before entering the condensation module using two electrical heaters H2 and H3. At the inlet of the test section the thermodynamic state of the superheated vapor is known from the local pressure and temperature measurements made using an absolute pressure transducer (range 0-2 bar) and a T-type thermocouple directly installed in the refrigerant flow. The superheated vapor is then partially or fully condensed inside the test section, which is described in details in Section 3.3, using water as secondary fluid. At the outlet of the measuring sector the pressure is measured using a differential pressure transducer (range 0-150 mbar) and the temperature is measured with a T-type thermocouple. After the condensation test module the refrigerant is completely condensed and, if necessary, subcooled in the post-condenser, which is a refrigerant-air fan-coils.

The water loop which is used to reject the heat from the refrigerant loop is composed of three sub-circuits in parallel. Each circuit consists of an air-cooled thermoelectric water-

cooling assembly (TEA), a turbine flowmeter and a regulating valve. The first branch is connected with the 1st subsector, the second branch is connected with the 2nd and 3rd sub-sectors, the third branch is connected with the 4th and 5th sub-sectors. The water and the refrigerant flows are in counter-current.

As the HFE-7000 is the working fluid it is critically important for the experiment that the refrigerant in the circuit is pure, free of any non-condensable gases. Therefore at the preliminary phase of the experiment the liquid is degassed thoroughly in an auxiliary system and after being charged it must always reside at pressure higher than the ambient one. During the experimental runs the pressure in the loop is kept 0.2-0.8 bar higher than the atmospheric one, but between the experiments or when the loop is switched off the pressure in the loop can be lower with the risk of leakages, or even worse some air can enter in the loop. Thus a damping accumulator is connected to the circuit and used to avoid gas entering the refrigerant circuit during unheated storage of the setup.

Since during the parabolic flight, the risk to release fluids should be minimized, the experimental rack is sealed towards the ambient, except the fans that should reject the heat to the environment.
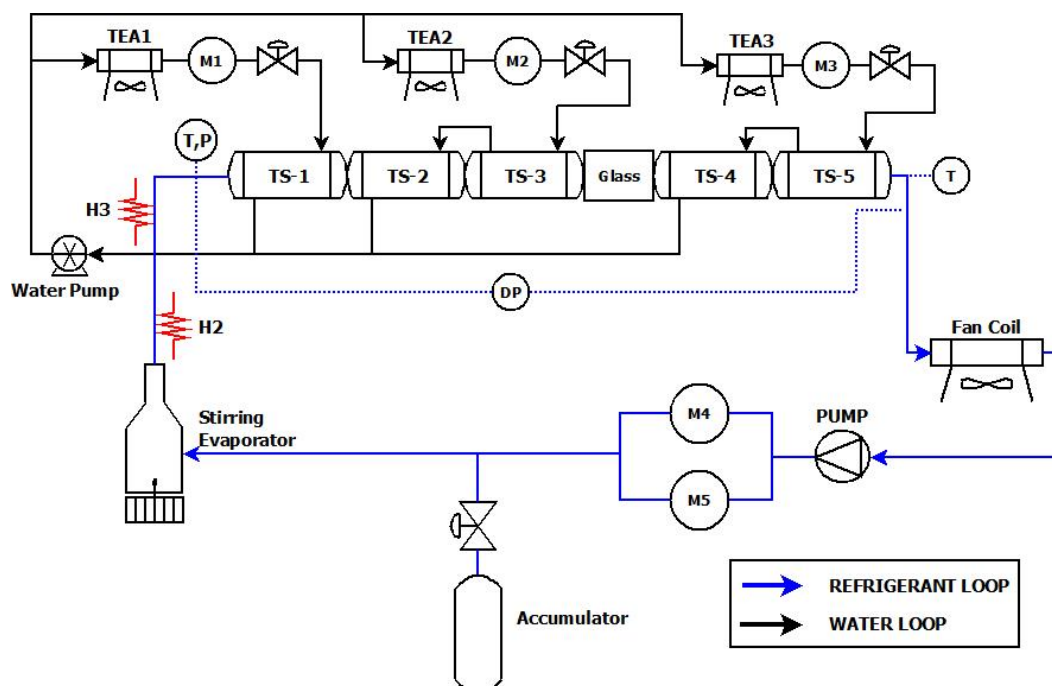
Figure 5.1. Layout of the experimental apparatus used for microgravity experiments

In correspondence of the glass tube the optical system is mounted on an optical table of 600 x 400 mm; it consists of a telecentric backlight, three LED light sources, a ground glass, two mirrors and a high speed camera with an objective. The system works in two different regimes:

- local visualization: the collimated light emitted by the telecentric backlight is directed towards the visualization section of the test cell by one mirror. The light transmitted through the test cell is redirect with another mirror and captured by the objective of the

camera which as a focal length of 100 mm and achieves a field of view of about 6.5 x 16.2 mm;

- global view: the light emitted by a LED sources passes through a ground glass to obtain a uniform distribution of the light and illuminates whole the transparent visualization window. Light passed through the cell is reflected from a mirror in the direction of the camera. The objective has a focal length of 35 mm and achieves a field of view of about 6.5 x 150 mm.

During a flight data are recorded continuously every 2.7 s.
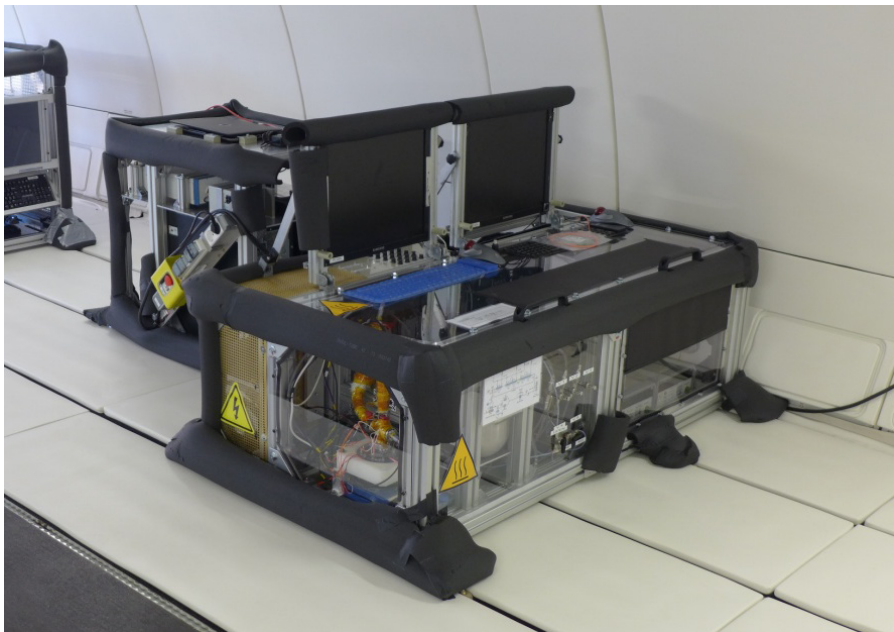
Figure 5.2. Experimental apparatus installed on the plane

Figure 5.3. Some team members during the parabolic flight campaign. © Copyright: Photo ESA/Anneke Le Floc'h

5.3 Experimental procedure

During condensation heat transfer tests the HFE-7000 enters the 3.38 mm inner diameter test section as superheated vapor; the pressure and the temperature of the refrigerant are measured in order to get the thermodynamic state. The test section is composed of two heat exchangers divided by the adiabatic glass tube for visualization purpose; the two heat exchangers are divided in 5 sub-sectors. In each sub-sector a quasi-local heat transfer coefficient can be evaluated using the thermocouples embedded on the wall and the heat flow rate measured on the water side. The flow pattern is also visualized using the glass tube. Then the fluid exiting the test section is subcooled in the post-condenser.

The HFE-7000 properties have been evaluated as reported in 4.1.3 and the data reduction to obtain the heat transfer coefficient and the vapor quality during condensation tests is described in 4.2.2.

A typical profile of refrigerant, wall and water temperatures during a condensation test with HFE-7000 at G=100 kg m^{-2} s^{-1} is reported in Figure 5.4. The refrigerant enters in the test section at about 60°C and it is cooled down to the saturation temperature at approximately 45°C. Along the test section, due to the pressure drop, the saturation temperature decreases from 46.2°C to 45.8°C. The water flows in counter-current in three circuits in parallel:

- in the first circuit it enters in the 1st sub-sector at 32.5°C;

- in the second circuit it enters in the 3rd sub-sector at about 30°C and exits from the 2nd one increasing its temperature of about 8 K

- in the third circuit it enters in the 5th sub-sector at 28.9°C and exits from the and 4th at 37.1°C

The measured wall temperature is between the water and the refrigerant temperature. From the Figure 5.4 it can be noticed that in the 4th sub-sector there is a big difference between the thermocouples place on the top and on the bottom in the first and last fin because they have been badly positioned as explained in 4.2.4.
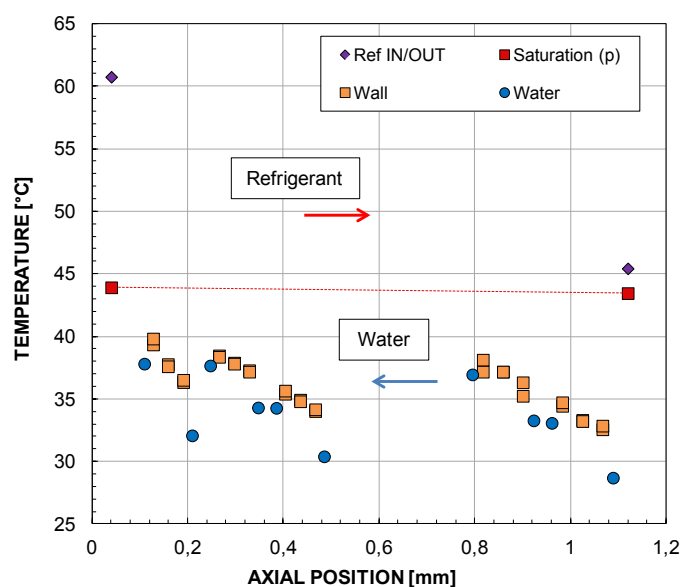
Figure 5.4. Measured wall, water and refrigerant temperature profiles during condensation of HFE-7000 in a 3.38 mm internal diameter minichannel at normal gravity conditions.

5.3.1 Steady-state conditions

In Figure 5.5 the temporal recording of saturation minus wall temperature difference in the five sub-sectors is reported. The wall temperature considered is the one measured by the two thermocouples placed in the middle fin of each sub-sector while the saturation temperature has been obtained from a linear interpolation of the measured pressure at the inlet and outlet of the test section. Similarly in Figure 5.6 the experimental heat transfer coefficient evaluated in the five sub-sectors during one parabola is reported. In both the figure, the temporal record of gravity is depicted.

A typical day of tests consists in a three hour flight during which 31 parabolic maneuvers are performed. Parabolas are usually divided in group of 5 and between each parabola of the same group there are 1 or 2 minutes break, instead between a group of parabolas and the following one the break is usually of 5-8 minutes.

Each parabola is composed of three phases:

- about 22 seconds of 1.8 g (hyper-g) 'pull-up';
- about 20 seconds of microgravity, 0±0.05 g, with a couple of seconds of transition between the hyper-g phase to the micro-g phase;
- about 22 seconds of 1.8 g (hyper-g) 'pull-out'.

Due to the low duration of the microgravity during a parabola there are some obvious concerns about the ability to reach steady state conditions. Therefore the construction of the experimental apparatus itself and of the test section has been done keeping in mind this problem. Anyway during parabolic flight tests, to minimize the response time, the refrigerant mass flow rate was kept constant during each group of parabolas and the water mass flow rates were set always at the maximum preferring to change the water temperature to vary the desire thermodynamic quality of the HFE-7000 in the visualization window when necessary. As one can seen from Figure 5.5 the transition from the 1.8 g phase to the 0 g phase introduces a sudden variation in the temperatures, which tend to a constant value just at the end of the microgravity phase. A similar behavior can be seen for the heat transfer coefficients in Figure 5.6.

In the end, the condensation heat transfer coefficients presented in the following sections are based on data measured during the last few (2 s) seconds of the microgravity phase. Unfortunately, some of the data collected during the three day of tests should be discarded due to instabilities or because the steady state was not reached.

What emerges is that steady state conditions are anyway difficult to reach in few seconds of microgravity and thus long duration experiments, like for example in the reduced gravity conditions ensured on the International Space Station, should be considered.
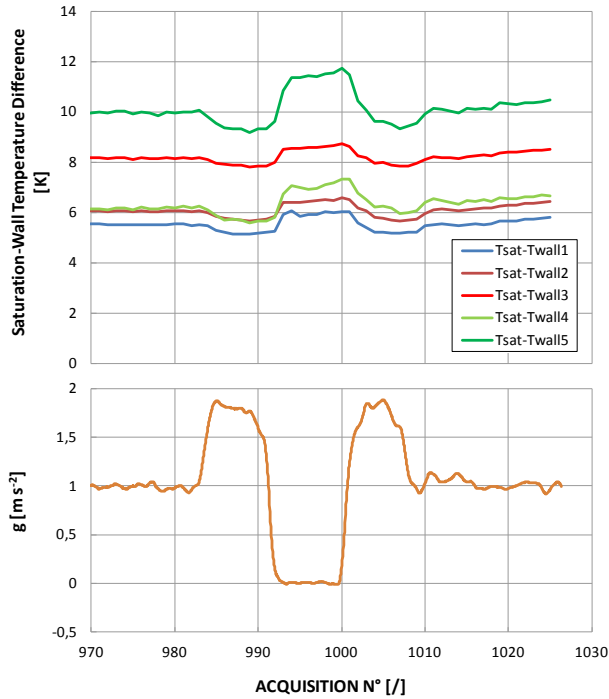
Figure 5.5. Temporal variation of the experimental saturation minus wall temperature difference for HFE-7000 at *G*=130 kg m⁻² s⁻¹. The saturation temperature is about 44.5 °C and the wall temperature is the one measured using the two thermocouples in the middle of each sub-sector. Temporal recorded gravity is reported below.
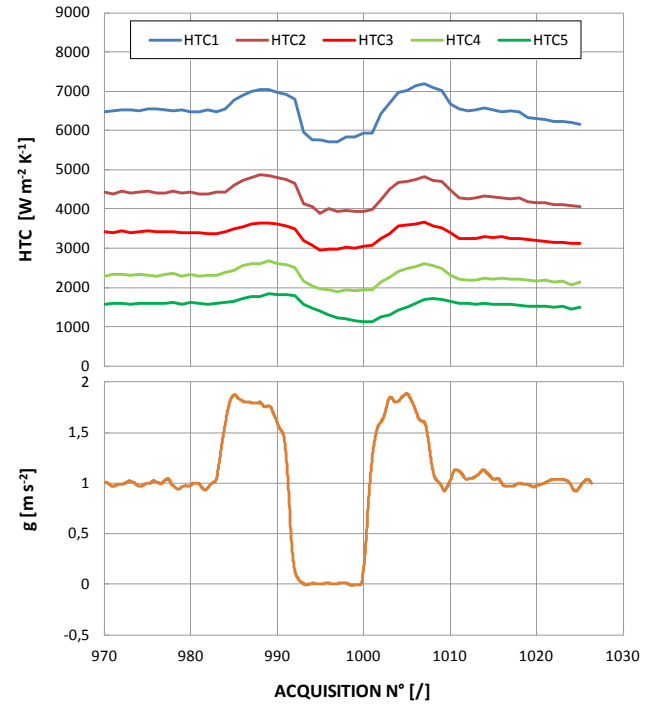
Figure 5.6. Temporal variation of the experimental heat transfer coefficient evaluated in the five sub-sectors for HFE-7000 at *G*=130 kg m⁻² s⁻¹. The saturation temperature is about 44.5 °C. Temporal recorded gravity is reported below.

5.4   Results during condensation tests in microgravity

The condensation heat transfer test runs are performed using HFE-7000 as working fluid, with mass velocity ranging from 70 to 130 kg m⁻² s⁻¹ and saturation temperature between 44.2°C and 47°C; a couple of tests have been performed at *G*=170 kg m⁻² s⁻¹. At the same working conditions tests have been repeated during different parabolas to achieve a kind of repeatability.

The data reduction is reported in Section 4.2.2.

The measured experimental condensation heat transfer coefficient in microgravity conditions is plotted against vapor quality in Figure 5.7. For the same mass velocity the heat transfer coefficient displays clearly a similar trend even if between one test and the other a small variation can be seen. For the whole range of mass velocities the heat transfer coefficient decreases with the vapor quality as excepted.
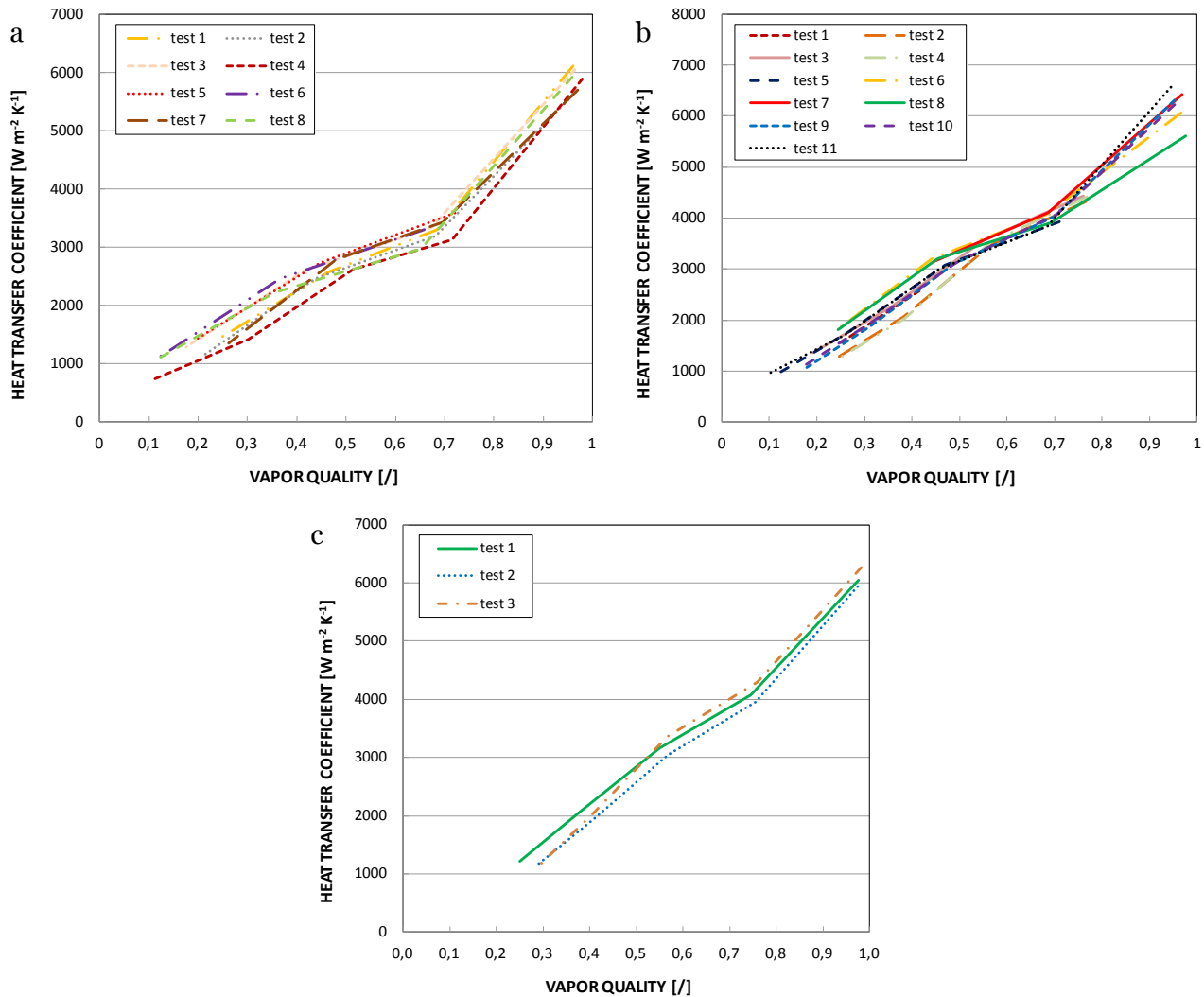
Figure 5.7. Quasi-local experimental heat transfer coefficients for HFE-7000 vs. vapor quality in microgravity conditions at different mass velocities. a) G=70 kg m⁻² s⁻¹, b) G=100 kg m⁻² s⁻¹, c) G=130 kg m⁻² s⁻¹.

What are the results if the heat transfer coefficients measured during microgravity are compare with those measured during normal gravity?

Data on normal gravity conditions have been taken with the same apparatus and in the same conditions of the parabolic flight campaign. Thus the condensation heat transfer coefficient presented hereafter in ground gravity conditions have been taken with the apparatus ready for the flight but still on ground or during the long breaks between a group of parabolas and the following one.

The answer to the above question can be seen in Figure 5.8 and Figure 5.9. Figure 5.8 shows the heat transfer coefficients for normal and microgravity conditions at 70 kg m⁻² s⁻¹; at this mass velocity there is a clear fall of the condensation heat transfer performance during microgravity. For the heat transfer coefficient during microgravity it is useful to clarify that a mean heat transfer coefficient has been calculated starting from those reported in Figure 5.7.
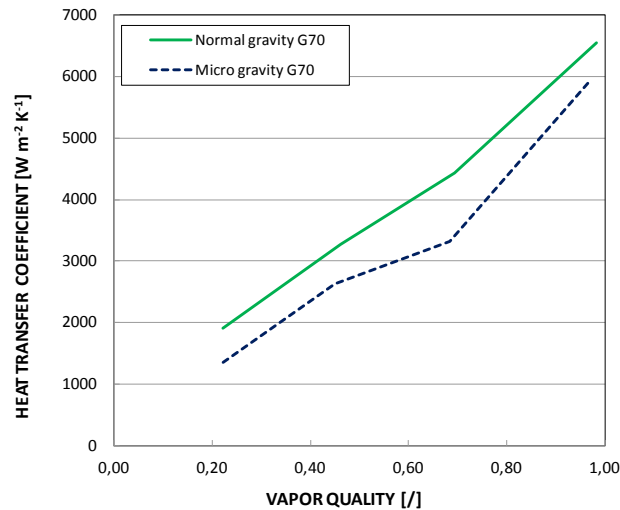
Figure 5.8. Quasi-local experimental heat transfer coefficients for HFE-7000 vs. vapor quality in normal and microgravity conditions at G=70 kg m^{-2} s^{-1}

It is interesting to notice that this decrease is function of the working conditions; Figure 5.9 reports the ratio between the mean experimental heat transfer coefficient in microgravity and in normal gravity conditions (a mean heat transfer coefficient has been calculated along the vapor quality range reported in Figure 5.7 and for $0.9<x<0.5$ at G=170 kg m^{-2} s^{-1}). The ratio is about 0.8 at G=70 kg m^{-2} s^{-1} and it increases with the mass velocity, approaching 1 at G=170 kg m^{-2} s^{-1}. This means that the effect of gravity depends on the working conditions as predicted by the criterion of Del Col et al. [5] and applied for this experimental test section in 3.2.1.

To clarify the deep connection between gravity effect and flow pattern the recorded images from the camera placed on the visualization window should be analyzed.
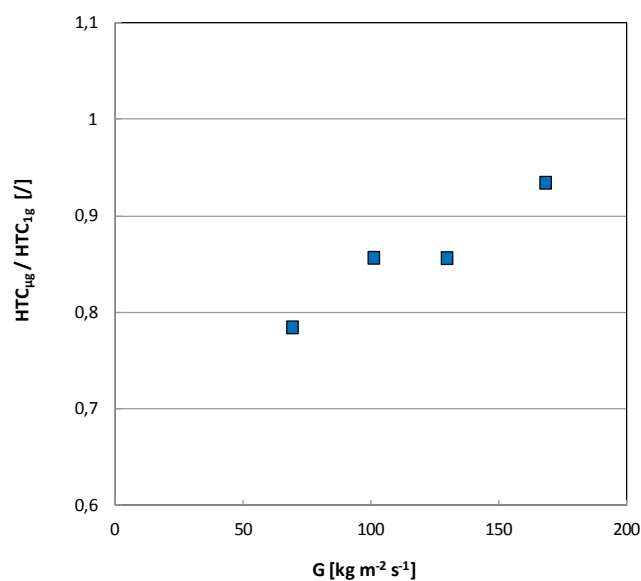
Figure 5.9. Ratio of the experimental heat transfer coefficient in microgravity and in normal gravity conditions for HFE-7000 at the different mass velocities (mean heat transfer coefficient calculated along the vapor quality range).

5.5   Flow visualization results

The figures below show sequential images of the condensing HFE-7000 during normal gravity and microgravity conditions in the adiabatic glass tube placed between the two heat exchangers of the test section. For each test condition, reported in Table 5.1, there are three images in normal gravity (1-2-3) and three in microgravity conditions (4-5-6); the images in normal gravity have been acquired before the pull-out phase of the parabola.

In Figure 5.10 the flow pattern for G=170 kg m^{-2} s^{-1} at x=0.64 is presented. During normal gravity, the liquid film appears slightly visible on the bottom of the tube and sometimes little waves can be seen also on the top of the tube; the flow pattern seems to be in the transition between annular and stratified wavy, even if it is not easy to give a clear definition. In microgravity conditions the flow pattern does not change significantly; the film on the top of the tube appears thicker although both, the liquid films on the bottom and on the top are difficult to be identified. It seems that the condensed liquid film is almost evenly distribute along the internal channel wall and keeping in mind the results in Figure 5.9 the shear stress plays an important role in the balance of forces.

Table 5.1. Summary of the test conditions, mass velocities and vapor qualities reported in the following figures

G [kg m^{-2} s^{-1}]	x 1-g[/]	x 0-g [/]
170	0,64	0,64
130	0,45	0,45
100	0,37	0,34
100	0,5	0,5
70	0,18	0,21
70	0,29	0,34
70	0,35	0,41

Normal gravity   Micro gravity

1

4

2

5

3

6
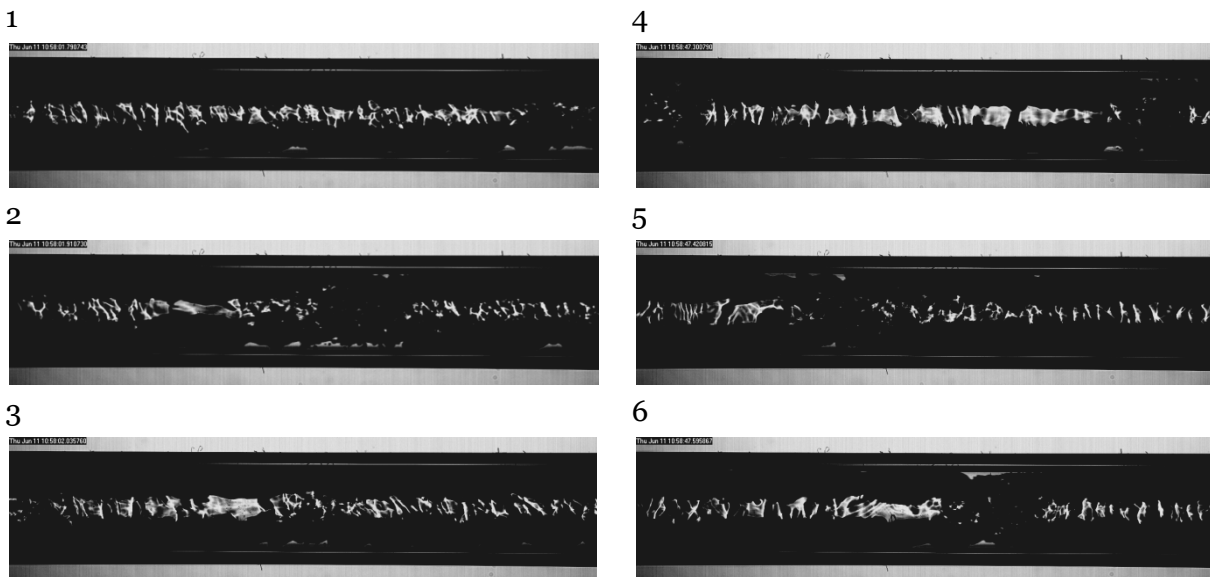
Figure 5.10. Flow pattern during condensation of HFE-7000 in normal and microgravity conditions at G=170 kg m^{-2} s^{-1} and x=0.64.

The recorded flow patterns for G=70 kg m^{-2} s^{-1} and vapor qualities ranging between 0.41 and 0.18 are presented from Figure 5.11 to Figure 5.13. These figures allow to appreciate the combined effect of gravity, surface tension and shear stress.

During normal gravity conditions the flow pattern is stratified wavy as can be seen in images 1-2-3 of each figure. The film is thicker on the bottom of the tube and not visible on the top; thus the gravity plays the important role to drain the condensed liquid on the lower part of the tube, creating a pool. In microgravity (images 4-5-6) the liquid, which was more present on the lower part, is free to spread along the internal circumference of the tube under the effect only of the surface tension and of the shear stress. The liquid film on the top is thicker and at a first sight comparable with the one on the lower part of the tube.

Keeping in mind that the heat transfer coefficient depends on the local condensate film thickness and considering a cross section of the channel: during normal gravity conditions the lower part of the tube has a low heat transfer coefficient, due to the presence of the liquid pool, but the upper part of the tube has an high heat transfer coefficient, resulting in a global higher heat transfer coefficient if compare to the microgravity conditions. In terms of heat transfer coefficient this result is reported in Figure 5.8 and Figure 5.9. The different distribution of the film thickness between normal and reduced gravity conditions can be seen not only from the images recorded in the glass window but also from the measured temperature in a sub-sector.

In particular Figure 5.14 shows the wall temperatures measured in 4 different positions on the 3rd sub-sector, which is immediately before the glass tube. The position of the thermocouple in each sub-sector is explained in Section 3.3.5 and depicted in Figure 3.14. Anyway it is useful to remember that on the inlet and on the outlet fins the thermocouples embedded on the wall are one on the top and one on the bottom.
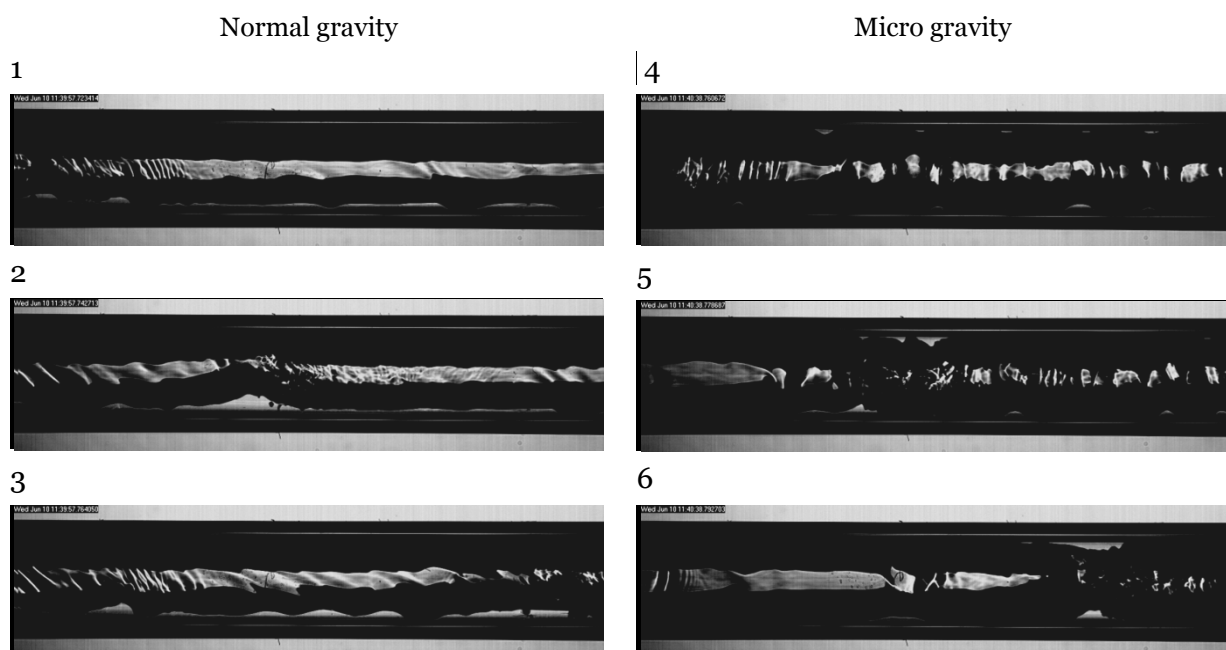
Figure 5.11. Flow pattern during condensation of HFE-7000 in normal and microgravity conditions at G=70 kg m^{-2} s^{-1}, x=0.35 (normal gravity) and x=0.41 (microgravity).

From the figure can be seen that during normal gravity there is a clear difference between the thermocouples placed on the opposite side of the same fin; the one on the top is at a higher temperature, which means that in a cross section at the same conditions the local heat transfer coefficient is higher on the upper part of the tube. This is a consequence of a thinner liquid film. It is also worth noting that, both on the inlet and outlet fin, the temperature difference between the thermocouple on the top and the one on the bottom decreases during microgravity conditions; this is due to the liquid film that in microgravity is almost evenly distribute on the tube wall while during normal gravity conditions is more thick on the bottom.

Normal gravity   Micro gravity
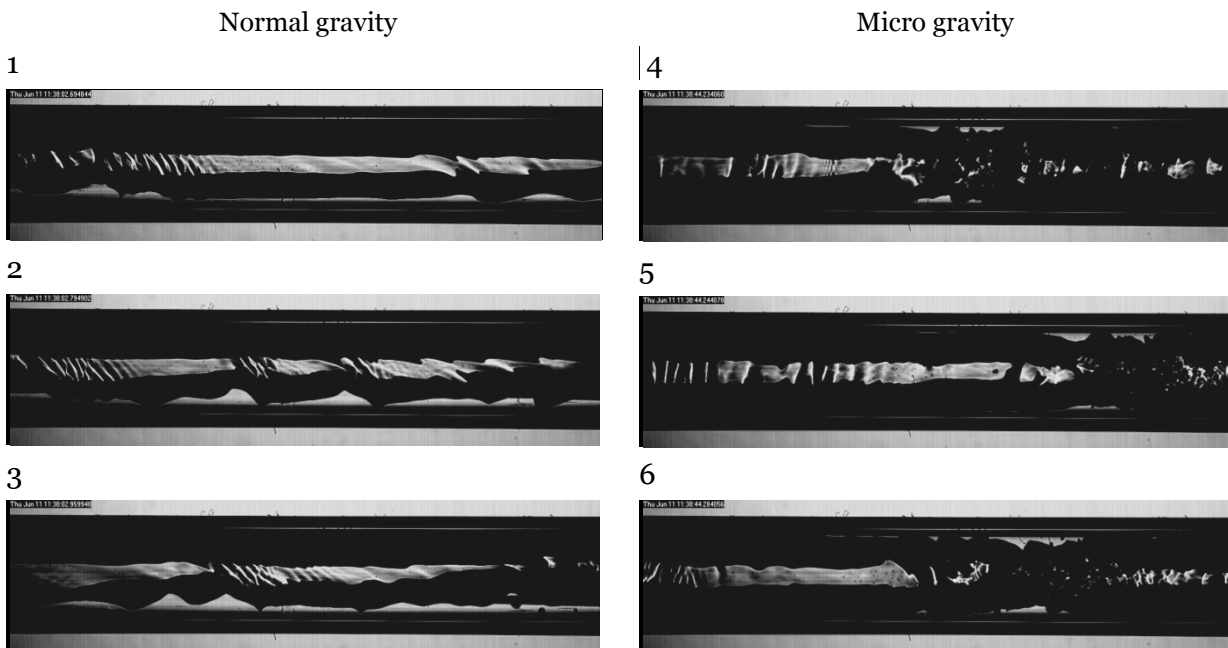
Figure 5.12. Flow pattern during condensation of HFE-7000 in normal and microgravity conditions at G=70 kg m^{-2} s^{-1}, x=0.29 (normal gravity) and x=0.34 (microgravity).

Normal gravity   Micro gravity
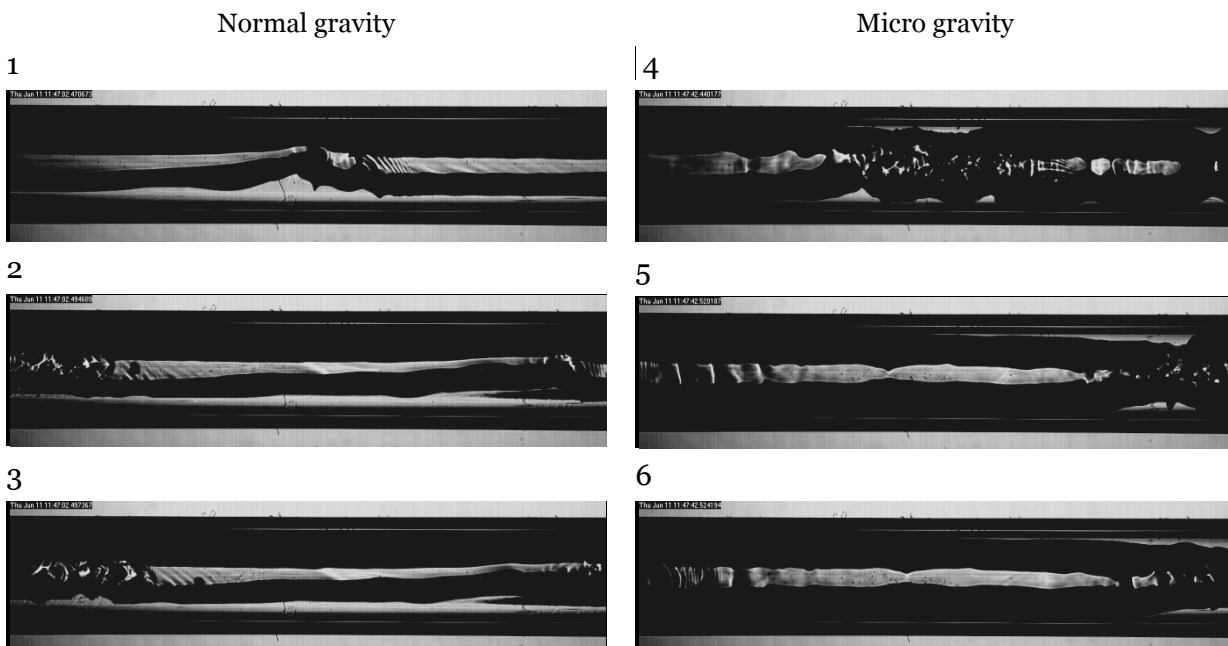
Figure 5.13. Flow pattern during condensation of HFE-7000 in normal and microgravity conditions at G=70 kg m^{-2} s^{-1}, x=0.18 (normal gravity) and x=0.21 (microgravity).
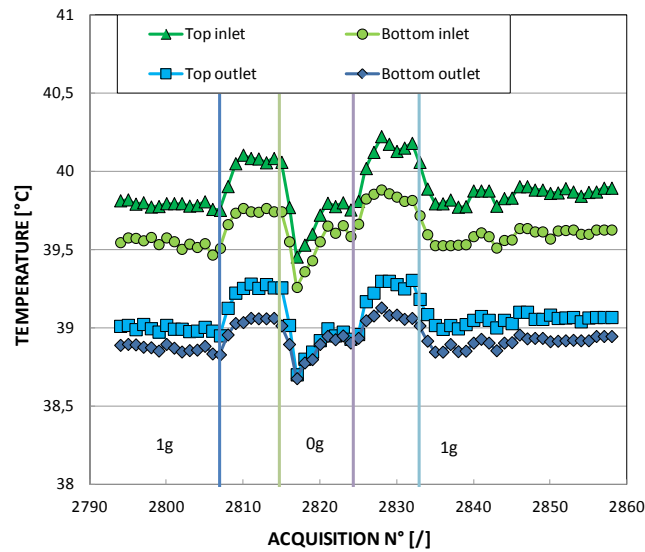
Figure 5.14. Temporal variation of the measured wall temperature in the inlet and outlet fins in the 3rd sub-sector during condensation of HFE-7000 at G=70 kg m^{-2} s^{-1}. The vertical lines give the transition between different gravity levels.

Figure 5.15 shows sequential images of the flow pattern for G=130 kg m^{-2} s^{-1} and x=0.45. All images depict a wavy interface with a clear liquid film on the bottom during normal gravity and a visible film also on the top during microgravity. Figure 5.16 and Figure 5.17 compare the images for the two different gravity levels for G=100 kg m^{-2} s^{-1} and different vapor qualities. The results are similar to the previous case. Anyhow for G=130 kg m^{-2} s^{-1} and G=100 kg m^{-2} s^{-1} the behavior of the liquid film and the interaction between the forces, gravity, shear stress and surface tension are in the middle between the two extreme cases here presented, G=170 kg m^{-2} s^{-1} and G=70 kg m^{-2} s^{-1}.
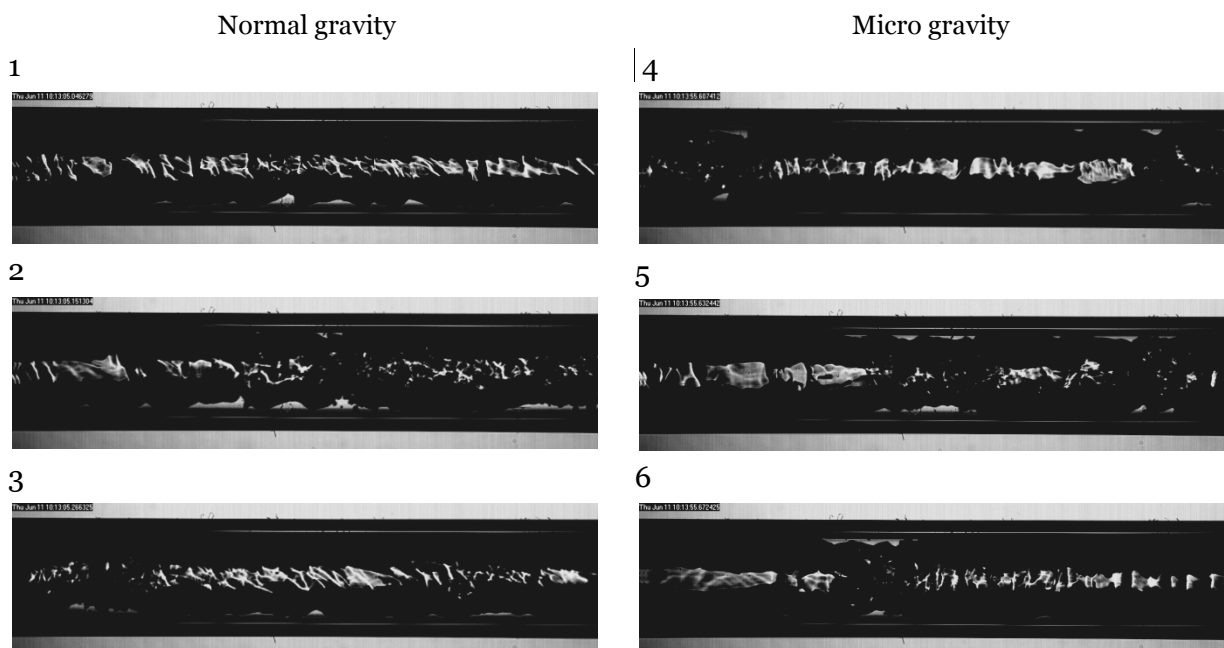
Figure 5.15. Flow pattern during condensation of HFE-7000 in normal and microgravity conditions at G=130 kg m^{-2} s^{-1} and x=0.45.

Normal gravity   Micro gravity

1

4

2

5

3

6
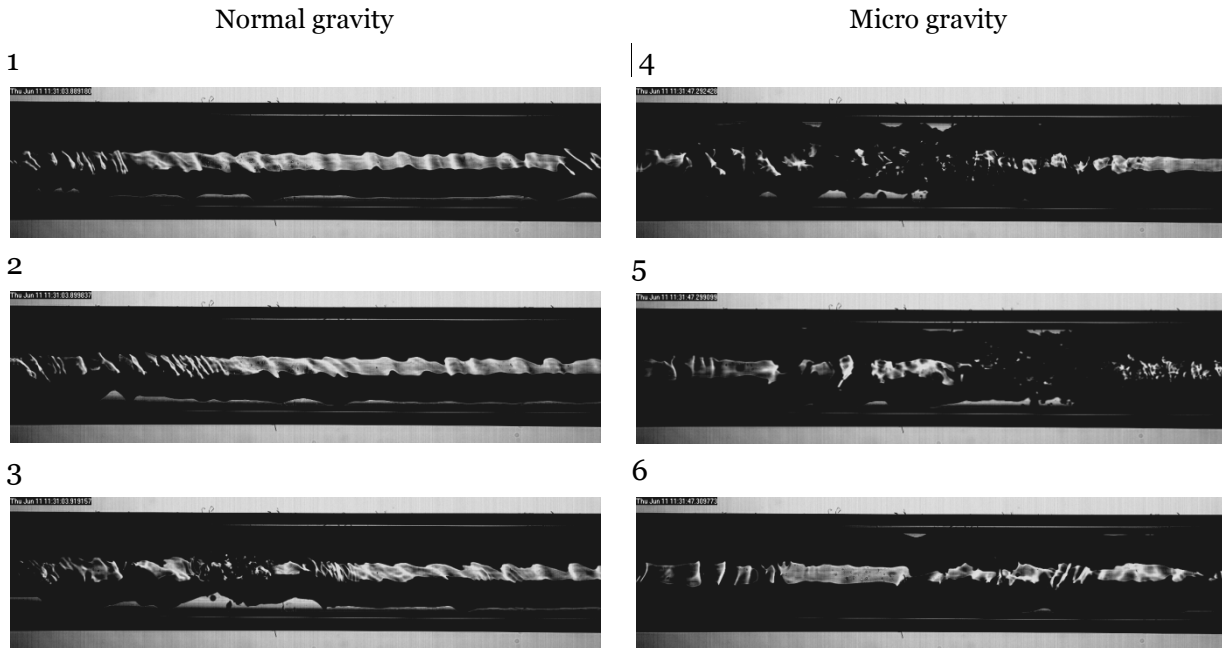
Figure 5.16. Flow pattern during condensation of HFE-7000 in normal and microgravity conditions at G=100 kg m^{-2} s^{-1}, x=0.37 (normal gravity) and x=0.34 (microgravity).

Micro gravity

4

5

6
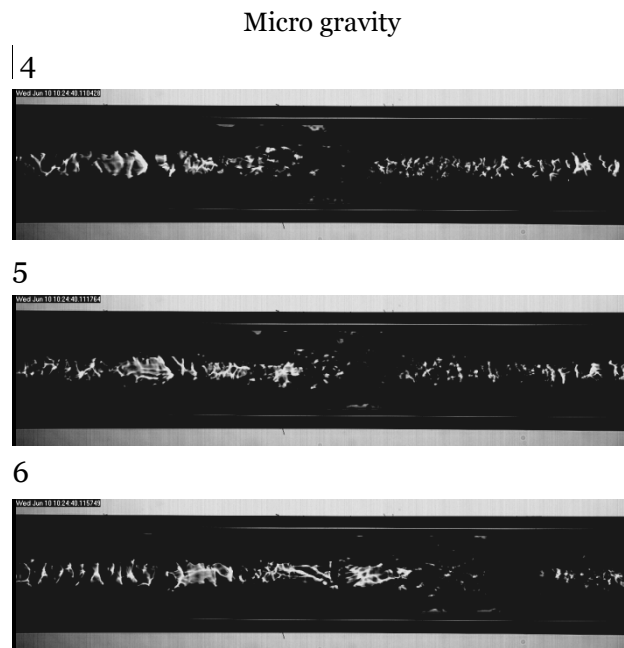
Figure 5.17. Flow pattern during condensation of HFE-7000 in normal and microgravity conditions at G=100 kg m^{-2} s^{-1} and x=0.5.

6 ADIABATIC TWO-PHASE FRICTIONAL PRESSURE DROP INSIDE A MINICHANNEL

Two-phase flow is widely encountered in minichannels heat exchangers such as air-cooled condensers and evaporators for automotive, compact devices for electronic cooling and aluminum condenser for air-conditioning applications. In the recent years much attention has been paid to the possible use of fluorinated propene isomers for the substitution of high global warming potential refrigerants. Among them, R1234ze(E) may be a substitute of R134a for refrigeration applications. R1234ze(E) has a GWP lower than 1 (considering a period time of 100 years), and it is receiving some attention also as a component of low global warming potential mixtures. In this and following Sections a mixture of R1234ze(E) and R32 at different mass compositions will be investigated with regard to the performance at the condenser and at the evaporator. Frictional pressure drop during adiabatic liquid-vapor flow will be firstly presented in this Section and compare with the results obtained for the pure R1234ze(E).

6.1 Introduction

Frictional pressure drop has a strong influence on two-phase heat transfer, mainly for three reasons. The first one is that pressure losses along the channel lead to a drop of the saturation temperature, which namely affects the driving temperature difference. The second issue refers to the higher energy consumption at the vapor-liquid interface. When the shear stress prevails over the surface tension and the gravity forces, the liquid film becomes turbulent and gets thinner, with possible liquid entrainment in the gas core. The thinner the liquid film, the lower the thermal resistance and thus a higher heat transfer coefficient is expected. However, the higher energy consumption is also related to the third issue, which is that higher shear stress leads to higher velocity gradient and thus higher temperature gradient in the thermal boundary layer. While the first issue, associated to the saturation temperature drop, penalizes the overall heat transfer rate, the other two issues enhance the condensation heat transfer coefficients. Because, as previously asserted, the two-phase heat transfer is strongly related to pressure drop, some predicting models (e.g. Moser et al. [50]; Bandhauer et al. [51]; Cavallini et al., [52]) require the evaluation of the shear stress (and thus pressure drop) for the estimation of the condensation heat transfer coefficient. In the open literature various pressure drop data are available for mini and microchannel taken with HFC and HCFC refrigerants. For example, Zhang and Webb [53] measured two-phase pressure drop during the adiabatic flow of R134a, R22 and R404A in a multiport extruded tube with an hydraulic diameter equal to 2.13 mm and in two copper channels with an internal diameter of 3.25 mm and 6.25 mm. Garimella et al. [54] performed pressure drop tests in tubes with hydraulic diameter from 0.42 to 0.84 and different shapes as circular, square, rectangular, triangular, barrel-shape, W-shape and N-shape using R134a. Cavallini et al. [55] used a multiport minichannel with a square cross

section and a hydraulic diameter of 1.4 mm to measure the pressure drop of R134a, R236fa and R410A. Two glass minichannels with hydraulic diameter of 0.509 mm and 0.790 mm have been used in the work of Revellin and Thome [56] to perform two-phase frictional pressure drop during adiabatic flow with R134a and R245fa. In the case halogenated olefins, such as R1234ze(E), most of the works available in the literature deals with macrochannels. Grauso et al. [57] performed pressure drop measurements during evaporation of R1234ze(E) and R134a inside a 6 mm internal diameter channel. Hossain et al. [58] investigated pressure drop of R1234ze(E), R32 and R410A in a copper tube with an internal diameter of 4.35 mm. With regard to propane, two-phase frictional pressure drop are reported in Field and Hrnjak [59] for a rectangular channel with a hydraulic diameter of 0.148 mm and in Choi et al. [60] for minichannels with diameter ranging between 1.5 mm and 3 mm. Two-phase pressure drop of propane inside a vertical circular minichannel with a inner diameter of 1.7 mm has been investigated by Maqbool et al. [61]. Considering HFO/HFC mixtures, very few data of two-phase pressure drop are available in the literature. For example, Kondou et al. [62] investigated flow boiling and pressure drop for the R32/R1234ze(E) mixture in a horizontal microfin tube with an inner diameter of 5.21 mm. In two-phase flow inside pipes, the pressure gradient is the sum of three components: frictional pressure gradient, pressure gradient due to momentum change, and hydrostatic pressure gradient. Since the last two components can be calculated from the estimation of void fraction, for a correct design of compact heat exchangers using minichannel technology, it is important to have reliable frictional pressure drop prediction methods covering a wide range of working fluids and operative conditions. Del Col et al. [19, 63] recently proposed a model for the prediction of frictional pressure drop during liquid-vapor flow inside channels with hydraulic diameter down to 500 μm, relative surface roughness lower than 0.007 and fluids with reduced pressure between 0.07 and 0.6. The authors verified the model against their two-phase frictional pressure drop experimental database, as well as against data from the scientific literature: it was shown that the new model displays higher accuracy with respect to other widely used correlations. The models tested by the authors were developed for macrochannels, as those proposed by Friedel [37, 64] and by Muller-Steinhagen and Heck [65], and for minichannels, as those proposed by Zhang and Webb [53] and by Cavallini et al. [26, 66].

.

6.2   Experimental apparatus and test section

The test section used for pressure drop measured is the one described in Section 2.2.2 During pressure drop tests the refrigerant enters the test section as superheated vapor to get experimental data in the 0.5 to 1.0 vapor quality range, while it enters as subcooled liquid to collect points with vapor quality below 0.5. The thermodynamic state of the refrigerant is determined from pressure and temperature measurements: pressure is gauged by a relative pressure transducer and temperature is measured by a T-type thermocouple. In both cases the refrigerant vapor quality at the inlet of the measuring sector is obtained from the energy balance in the pre-conditioning sector.

Since pressure drop tests have been run at about 40°C, the test section has been insulated in order to avoid heat losses to the external ambient.

6.3   Mixture preparation and property evaluation

In the present work, the R32/R1234ze(E) mixtures with three different compositions have been tested during adiabatic two-phase frictional pressure drop: 0.229/0.771, 0.505/0.495 and 0.748/0.252 by mass of R32 and R1234ze(E) (hereinafter, for the sake of simplicity, they will be referred to as 23/77%, 50/50% and 75/25%).

The two pure components are contained in two different high pressure tanks and during the mixture preparation process they are blended together inside the mixture reservoir.

The mixture preparation has been prepared at the Two-Phase Heat Transfer Lab adopting the following procedure:

- the mixture reservoir is connected to the fluid tank which has the lower saturation pressure (R1234ze(E) in the present case) and an alternative vacuum pump;

- the reservoir is placed on a balance with 0.001 kg sensitivity in order to constantly measure its weight and later the amount of fluid that will be charged;

- vacuum is applied in both the mixture reservoir and connection hose, then the vacuum pump is disconnected and the mixture reservoir is filled with the first refrigerant by opening the connection between it and the refrigerant tank;

- once the calculated amount of fluid is charged, the mixture reservoir valve is closed and the fluid tank disconnected;

- the mixture reservoir is connected to the second fluid tank (higher saturation pressure) and the procedure is repeated until the desired weight is reached.

Once the mixture is prepared, the test rig is filled with liquid phase to make sure that the mixture composition is as homogenous as possible.

During the preparation the weight, and so the composition, of the mixture is controlled using a balance with a high precision, anyway this is not enough to give a correct mixture mass composition. Thus, in the whole experimental campaign, the mass composition was checked using a gas chromatograph during test runs; the experimental uncertainty on the measured composition is ±0.001 by mass. Thermodynamic and transport properties of pure R32 and R1234ze(E) at 40°C saturation temperature are reported in Table 6.1. For the mixture R32/R1234ze(E), few experimental data are available and a limited number of publications have reported their properties. In particular, Akasaka [67] presented thermodynamic property models for mixture R32/R1234ze(E). The author emphasized that the property models proposed are designed for engineering use and are based on limited experimental data. For the R32/R1234ze(E) mixture, Akasaka [67] recommended the KW2 model with tuned parameters to better fit the experimental data. In the present article, the Akasaka [67] model is implemented in REFPROP 9.1 (Lemmon et al. [20]) to determine the mixture properties (Table 6.1). In particular the new coefficient suggest for the *Kunz and Wagner 2* mixing rule have been implemented in the *ASCII* file named *HMX.BNC* placed in the *Refprop\fluids* (Figure 6.1).

According with the UE Regulation N.517/2014 the GWP of a mixture is calculated as a weighted average, derived from the sum of the weight fractions of the individual substances multiplied by their GWP. So the GWP for the three mixtures considered are: 155, 337 and 506 respectively, increasing the mass fraction of R32.

Table 6.1: Properties of pure R32 and R1234ze(E) at 40°C saturation temperature; refrigerant mixture properties are reported at given mass composition; data from NIST Refprop 9.1 (Lemmon et al. [20])

Fluid	p_{sat} [bar]	ρ_l [kg m^{-3}]	ρ_g [kg m^{-3}]	μ_l [µPa s]	T_{dew} [°C]	T_{bub} °C]	Glide [K]
R32	24.8	893.0	73.3	95.0	/	/	/
R1234ze(E)	7.7	1111.3	40.6	167.0	/	/	/
23/77%	13.8	1066.7	59.6	140.1	47.6	36.8	10.8
50/50%	18	1008.3	65.5	119.2	43.7	36.3	7.4
75/25%	22	945.5	71.7	103.8	41.9	38.9	3

```
?R32/R1234ze            (R32/R1234ze)
?Kunz and Wagner (2007) manually inserted
75-10-5/29118-24-9      KW2   1.00343    0.977857    1.00586    0.982707    -0.265419  0.
                        TC1   0.         0.          0.         0.          0.         0.
                        VC1   0.         0.          0.         0.          0.         0.
!
```
Figure 6.1. Coefficient of the KW2 model in the HMX.BNC file

6.4   Experimental pressure drop tests

In this Section the experimental analysis of the adiabatic two-phase friction pressure drop is presented. In order to assess the present experimental technique, prior to perform two-phase pressure drop measurements, single phase pressure drop tests have been run.

6.4.1 Calibration and single phase pressure drop tests

Before performing any kind of test, thermal sensors and pressure transducers have been calibrated. Each T-type thermocouple has been calibrated at different water temperature using a calibration bore where a high precision four wire thermistor is installed. The thermistor is connected to a Hart Scientific Super Thermometer II. This measurement chain has a global accuracy of ±0.002 K. Comparing the readings of the thermistor with the acquire signal from each thermocouple a calibration curve can be derived.

For the triple junctions thermopile a similar procedure is followed using a Dewar vessel and a calibration bore. After the calibration, the Type B experimental uncertainty of the thermocouples is ±0.05 °C and that of the thermopile is ±0.03 °C, with a level of confidence of 95.45%.

A pressure calibrator has been used to assure the accuracy of the relative pressure transducers. The calibrator has a full scale value of 20 bar and an accuracy of ±0.025% of the reading between 3% and 100% of full scale and within ±0.15 mbar below 3% of full scale. The difference between the readings of the calibrator and those of the measure chain formed by the differential pressure transducer and the acquisition system was within the experimental uncertainty of the instrument

Due to the experimental technique, the desired inlet vapor quality is controlled using a pre-conditioning sector. Thus the accuracy of the thermal balance in the pre-conditioning sector is important; it has been checked comparing the heat balance on the water side to that on the refrigerant side during condensation from the superheated vapor to the subcooled liquid. The overall thermal balance was found to be within 4%.

Eventually the heat losses in the measuring sector have also been evaluated. It was found that this dissipation affect the vapor quality within ±0.01, so can be reasonably neglected compare to the uncertainty on the vapor quality.

The single phase friction factor f has been experimentally determined according to eq. 6.1 and its values are reported in Figure 6.2 against Reynolds number in the case of pure R1234ze(E) and the three R32/R1234ze(E) mixtures.

$$f = \frac{\rho \cdot D_h \cdot \Delta p}{2 \cdot G^2 \cdot L} \qquad\qquad \textbf{6.1}$$

As reported in Eq. 6.1, the evaluation of the friction factor requires the measurement of the pressure drop Δp along the channel length L and of the refrigerant mass flux G. Furthermore, the collected data are compared against the Churchill [16] correlation, which is valid for both laminar and turbulent flow and it accounts for the channel roughness. The relative roughness of the tube ε/d_h in the correlation by Churchill [16] is considered equal to $2Ra/d_h$. For all the tested fluids (pure refrigerants and mixtures) the deviation between experimental and calculated friction factor in laminar flow is below the experimental uncertainty. Blasius [28] equation developed for turbulent flow inside smooth tubes is also plotted in Figure 6.2 for comparison. For reader convenience, the Churchill [16] correlation is reported in Eqs. 6.2-6.4 and Blasius [28] equation is reported in Eq.6.5.

$$f = 2\left[\left(\frac{8}{Re}\right)^{12} + \frac{1}{(A+B)^{3/2}}\right]^{\frac{1}{12}} \qquad\qquad \textbf{6.2}$$

$$A = \left[2.457\ln\left(\frac{1}{(7/Re)^{0.9}} + \frac{0.54Ra}{d_h}\right)\right]^{16} \qquad\qquad \textbf{6.3}$$

$$B = \left(\frac{37530}{Re}\right)^{16} \qquad\qquad \textbf{6.4}$$

$$f = \frac{0.3164}{4} Re^{-\frac{1}{4}} \qquad\qquad \textbf{6.5}$$
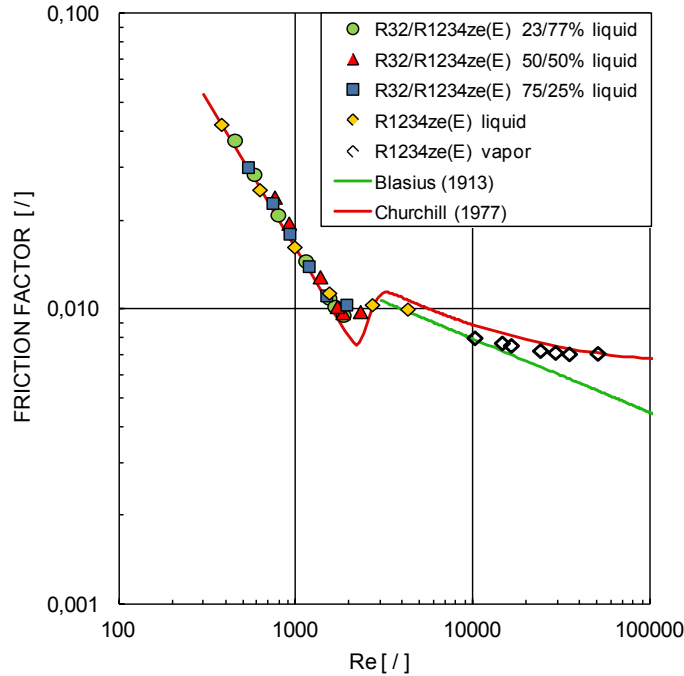
Figure 6.2: Experimental and calculated single phase friction factor versus Reynolds number

6.4.2 Two-phase pressure drop: data reduction and results

In case of pure fluids, the vapor quality at the inlet of the measuring sector is calculated using Eq. 6.6:

$$x = \frac{h_{in,MS} - h_L}{h_V - h_L} \qquad\qquad \textbf{6.6}$$

where h_L and h_V are the saturated liquid and saturated vapor specific enthalpies calculated at the measured absolute pressure and $h_{in,MS}$ is the refrigerant specific enthalpy at the inlet of the measuring sector resulting from the energy balance in the pre-conditioning sector, as reported in Eq. 6.7.

$$h_{in,MS} = h_{in,PS} - \frac{\dot{m}_{water} \cdot c_{water} \cdot \Delta T_{water,PS}}{\dot{m}_{ref}} \qquad\qquad \textbf{6.7}$$

The specific enthalpy of the refrigerant at the inlet of the pre-conditioning sector $h_{in,PS}$ derives from the measurement of the local temperature and pressure, while the specific

heat of the water c_{water} is referred to the mean water temperature in pre-conditioning sector.

For the refrigerant mixture 23/77% (by mass composition), two-phase frictional pressure drop tests have been carried out at 13.8 bar (corresponding to a dew temperature of 47.6°C and a bubble temperature of 36.8°C) and at a mass velocity of 400 kg m⁻² s⁻¹. For the mixture 50/50% (by mass composition) two-phase frictional pressure drop have been measured at a pressure of 18 bar (corresponding to a dew temperature of 43.7°C and a bubble temperature of 36.3°C) and mass velocity between 200 kg m⁻² s⁻¹ and 600 kg m⁻² s⁻¹. Finally, at 400 kg m⁻² s⁻¹ tests have been run for the 75/25% mixture at a working pressure of 22 bar which corresponds to a dew temperature of 41.9°C and a bubble temperature of 38.9°C. In the case of refrigerant mixtures, the vapor quality for each experimental point, assuming an equilibrium state, is calculated from the pressure, enthalpy and mixture composition as proposed in Kondou et al. [62]:

$$x = f\left(p, h_{in,MS}, Y_{R1234ze(E)}\right) \qquad \textbf{6.8}$$

where $Y_{R1234ze(E)}$ is the mass fraction of R1234ze(E) and $h_{in,MS}$ is the specific enthalpy of the refrigerant at the inlet of the measuring sector that results from the energy balance in the pre-conditioning sector according to Eq. 6.7. Test conditions are summarized in Table 6.2. For the mixture, the operative pressure has been chosen to obtain a mean refrigerant temperature, between bubble and dew temperatures, of about 40°C. In Figure 6.3, the experimental pressure gradient is reported for the refrigerant mixture 50/50% in the vapor quality range 0.1–0.95. As expected, the pressure gradient increases with mass velocity and vapor quality. The database reported in Table 6.2 includes also experimental two-phase frictional pressure drop of R1234ze(E) (Del Col et al. [6]) taken at mass velocities ranging from 200 kg m⁻² s⁻¹ to 800 kg m⁻² s⁻¹ and at saturation temperature of about 40°C. In Figure 6.4 the experimental frictional pressure gradient in case of pure R1234ze(E) and for three R32/R1234ze(E) mixtures is shown at mass velocity G=400 kg m⁻² s⁻¹. As it can be seen, at a fixed mass velocity, the frictional pressure gradient increases with vapor quality until the maximum value is reached (at about 0.8–0.9 vapor quality) and then it decreases to the value pertaining to single-phase vapor flow. A strong effect of the composition can be observed: adding a small quantity of R32, the pressure gradient is considerably reduced compared to the case of pure fluid. When the mass fraction of R32 is further increased the pressure gradient reduction is not so noticeable. For example, at given working conditions (G=400 kg m⁻² s⁻¹ and 0.6 vapor quality), the pressure gradient for the 50/50% mixture is equal to 41.6 kPa m⁻¹, while in the case of pure R1234ze(E) the measured pressure gradient is equal to 69.3 kPa m⁻¹, with about 40% reduction due to the different fluid properties.

The Type B standard uncertainty, for each measured quantity, is reported in Table 6.3. The expanded experimental uncertainty, corresponding to a level of confidence of about 95%, is evaluated as described in Section 11; maximum and minimum values for the pressure gradient uncertainty are reported in Table 6.2 (last column). The uncertainty related to vapor quality measurement is always lower than ±0.03.
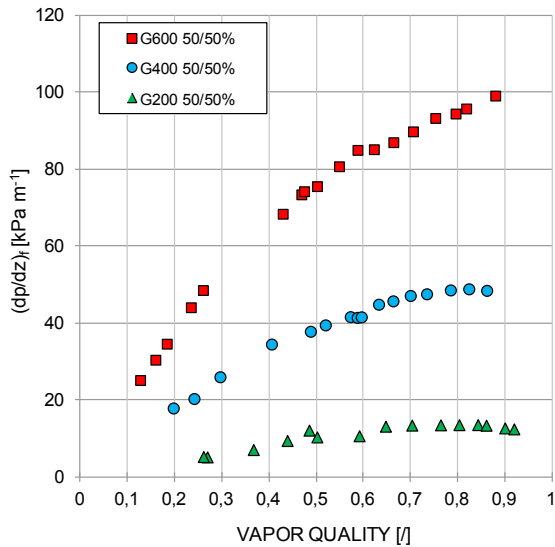
Figure 6.3: Experimental frictional pressure gradient versus vapor quality during two-phase adiabatic flow of the R32/R1234ze(E) mixture at 50/50% mass composition, 18 bar and different mass velocities, in a single minichannel with 0.96 mm inner diameter.
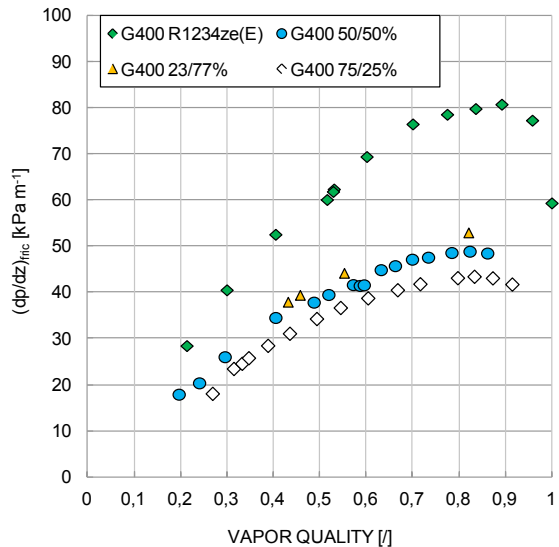
Figure 6.4: Experimental frictional pressure gradient versus vapor quality during two-phase adiabatic flow of pure R1234ze(E) and the mixture at three different composition at G=400 kg m⁻² s⁻¹, in a single minichannel with a inner diameter of 0.96 mm.

Table 6.2. Range of operative conditions during pressure drop tests.

Fluid	Mass velocity [kg m⁻² s⁻¹]	Pressure [bar]	Reduced pressure [/]	Bubble/Dew point temperature [°C]	Max/Min u_c(dp/dz) [kPa m⁻¹]
R1234ze(E)	200-400-600-800	7.7	0.21	40.1	1.3/0.4
0.23/0.77	400	13.8	0.28	36.7-47.6	2.4/1.8
0.5/0.5	200-400-600	18	0.32	36.3-43.7	4.7/0.4
0.75/0.25	400	22	0.38	38.9-41.9	2.0/0.9

Table 6.3. Type B experimental uncertainty of measured parameters

Temperature	±0.05°C
Temperature difference (with thermopile)	±0.03°C
Water flow rate in pre-conditioning sector	±0.2% at 10 kg h⁻¹
Refrigerant flow rate	±0.2% at 10 kg h⁻¹
Absolute pressure	±5 kPa (level of confidence: 99.7%)
Pressure difference (greater than 1 kPa)	±0.12 kPa (level of confidence: 99.7%)
Pressure difference (below 1 kPa)	±0.1% (level of confidence: 99.7%)

6.4.3 Comparison against correlations

The new mixture experimental data have been compared with four two-phase frictional pressure drop models.

One of the first correlations developed for two-phase frictional pressure drop is the one proposed by Friedel [37]. The model has been developed starting from a database of 25000 experimental points collected in both circular and rectangular tubes with hydraulic diameters from 1 mm up to 260 mm (it should be considered that most of the data have been taken in macrochannels). Horizontal flow, vertical upward flow and vertical downflow points were included in the database. Pure fluids and mixtures are included in the database; regarding the mixtures most of them are air-water or air-oil mixtures.

The second model is the one developed by Muller-Steinhagen and Heck [65]. They proposed a simple model, without using a two-phase multiplier, in which the resulting pressure drop is the combination of the single-phase vapor and liquid pressure drops. Their database includes 9300 data points for many fluids in horizontal flow, vertical upflow and vertical downflow. The range of the considered hydraulic diameters is from 4 mm to 392 mm.

The Zhang and Webb [53] correlation is based on a modification of the Friedel [37] correlation. Their database covers two-phase pressure drop for R134a, R22 and R404A inside channels with hydraulic diameters from 0.96 mm to 6.2 mm. They keep the form of the original correlation of Friedel [37] and adjusted the coefficient and exponents to obtain a best correlation for small diameter tubes. Moreover they suggested to replace the dimensionless group of density and viscosity with the reduced pressure and to neglect the Froude number and the Weber number.

The forth model for predicting frictional pressure gradient during two phase adiabatic flow inside minichannels is the one suggested by Cavallini et al. [26, 66] and later modified by Del Col et al. [19]. For annular and mist flow ($J_G > 2.5$) the equations are the following:

$$\left(\frac{\mathrm{d}p}{\mathrm{d}z}\right)_f = \phi_{LO}^2 \left(\frac{\mathrm{d}p}{\mathrm{d}z}\right)_{f,LO} \qquad\qquad \textbf{6.9}$$

$$\left(\frac{\mathrm{d}p}{\mathrm{d}z}\right)_{f,LO} = \frac{2 f_{LO} G^2}{D_h \rho_L} \qquad\qquad \textbf{6.10}$$

$$\left.\begin{aligned}
&\phi_{LO}^2 = Z + 3.595 \cdot F \cdot H \cdot (1-E)^W \\
&W = 1.398\, p_R \\
&Z = (1-x)^2 + x^2 \frac{\rho_L}{\rho_V}\left(\frac{\mu_V}{\mu_L}\right)^{0.2} \\
&F = x^{0.9525}(1-x)^{0.414} \\
&H = \left(\frac{\rho_L}{\rho_V}\right)^{1.132}\left(\frac{\mu_V}{\mu_L}\right)^{0.44}\left(1-\frac{\mu_V}{\mu_L}\right)^{3.542}
\end{aligned}\right\} \qquad \textbf{6.11}$$

In Eq. 6.10 f_{LO} is the liquid only friction factor, evaluated for any $Re_{LO} = (G\,d_h)/\mu_L$ as

$$f_{LO} = 0.046\left(Re_{LO}\right)^{-0.2} + 0.7RR \qquad\qquad \textbf{6.12}$$

The entrainment ratio E used in Eq. 6.11 has to be calculated as suggested by Paleev and Filippovich [68].

Cavallini et al. [26, 66] extended their model also to lower vapor qualities and mass velocities ($J_G<2.5$) proposing to select the higher value between $(dp/dz)_f$ evaluated through Eqs. 6.9-6.12 and the all liquid frictional pressure gradient $(dp/dz)_{f,LO}$. This is calculated through Eq. 6.10, by evaluating the liquid only friction factor as $f_{LO}=C/Re_{LO}$, with C equal to 16 for circular tubes and to 14.3 for square ones, when $Re_{LO}<2000$.

In Eq. 6.12 $RR=2Ra/d_h$ is the relative roughness of the tube, depending only on the tube characteristics, so the wall roughness has a constant effect on the friction factor, for all the values of Reynolds number Re_{LO}. However, the effects of the surface roughness on the frictional pressure losses in single phase flow may not be the same when varying Re_{LO}. These effects of the wall roughness on the fluid flow are expected to be smaller at lower mass velocity and higher liquid-phase viscosity μ_L. Thus they are smaller when the liquid-only Reynolds number is lower. This fact is shown in the Moody's chart (Moody and Princeton, [69]), where it is possible to see that, in the transition zone, the lower the Reynolds number, the lower the differences between the curve for smooth pipes and those for rough tubes. Moreover, in the laminar zone ($Re < 2100$) surface roughness has no effect on the frictional losses. In order to account for the effects of the pipe relative roughness on the frictional losses, Del Col et al. [19] modified Cavallini et al. [26, 66] equation for the evaluation of the liquid-only friction factor as follows:

$$f_{LO} = 0.046\left(Re_{LO}\right)^{-0.2} + 0.7RR \cdot X \qquad\qquad \textbf{6.13}$$

where X is a factor which relates the effects of the wall superficial roughness to the liquid-only Reynolds number

$$X = \begin{cases} 0 & \text{if} \quad Re_{LO} \leq Re_{LO}^{+} \\ 1 & \text{if} \quad Re_{LO} \geq 3500 \\ 1+\dfrac{A-0.046Re_{LO}^{-0.2}}{0.7 \cdot RR} & \text{if} \quad Re_{LO}^{+} < Re_{LO} < 3500 \end{cases} \qquad \textbf{6.14}$$

In Eq. 6.14 f^{+} is the smooth tube friction factor (evaluated as in Eq. 6.12 considering $RR=0$) at $Re_{LO} = 3500$ and Re_{LO}^{+} is the Reynolds number at which the smooth tubes friction factor (Eq. 6.12 with $RR=0$) is equal to the one for rough tubes (Eq. 6.12) evaluated at $Re_{LO}=3500$

$$f^+ = 0.046(3500)^{-0.2} \qquad\qquad \textbf{6.15}$$

$$Re_{LO}^+ = \left(\frac{f^+ + 0.7RR}{0.046}\right)^{-5} \qquad\qquad \textbf{6.16}$$

Eq. 6.13 interpolates the curve of Eq. 6.12, for rough channels, and the one for smooth tubes (Eq. 6.12 with RR=0), introducing two liquid-only Reynolds numbers regions; the first one ($Re_{LO} \le Re_{LO}^+$) is the region where RR has no effect on the pressure losses, the second one ($Re_{LO} \ge 3500$) is the region where the effects of RR are fully developed, so f_{LO} can be evaluated with Eq. 6.12. Between these two zones, the effects of RR are balanced by means of the coefficient X.

The new equation permits to link the effects of the tube relative roughness on the liquid-only friction factor to the mass velocity and to the properties of the fluid. If Re_{LO} is small RR does not affect the pressure losses, so f_{LO} is evaluated as in a smooth tube. If the liquid-only Reynolds number increases the relative roughness of the channel starts to influence the friction factor, until for $Re_{LO} \ge 3500$ f_{LO} tends to the one evaluated by Cavallini et al. [26, 66] for rough tubes.

The complete model is reported in Del Col et al. [19] and it has been verified for circular and noncircular minichannels having a hydraulic diameter bigger than 0.5 mm, a relative roughness smaller than 0.007 and for fluids with a reduced pressure ranging from 0.07 to 0.6. It is worth noting that it has not been tested for mixtures.

The comparison between the model and the new experimental data are reported in Figure 6.5-Figure 6.8. As shown in Figure 6.5, the correlation by Friedel [37] slightly underestimates the experimental data giving a e_R = -1.3% σ_N = 8.4% and e_{AB} = 7%. The results obtained with the Muller-Steinhagen and Heck [65] model are reported in Figure 6.6. The model is able to predict the 79% of data within ±20% (e_R = -11.7% σ_N = 9.9% and e_{AB} = 13.3%). Among the considered models the one proposed by Zhang and Webb [53] (Figure 6.7) presents the highest average deviations (e_R = -27.5% σ_N = 10% and e_{AB} = 27.7%).

Regarding the Del Col et al. [19] model (Figure 6.8), it well reproduces the experimental trend and, for the whole range of mass velocity and vapor quality, the 97% of the data points are within the ±20% error bands. Even if it was not developed for mixtures, the model is able to predict the data with an e_{AB} equal to 5.1%, σ_N of 7% and e_R = -0.4%, showing that a model developed for pure fluids can be successfully applied to these zeotropic mixtures without corrections but only substituting the pure fluid properties with those of the mixture. It should be noticed that, when the original correlation by Cavallini et al. [26, 66] (not accounting for the effects of roughness as a function of Re_{LO}) is compared with the present mixture data, the experimental frictional pressure gradient is predicted with less accuracy (absolute mean deviation e_{AB} equal to 7.1% and standard deviation σ_N of 9.8%).
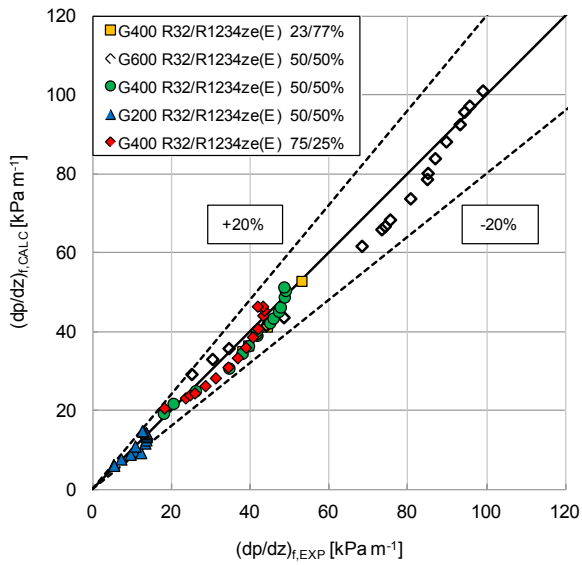
Figure 6.5: Prediction using the Friedel [37] model versus the experimental frictional pressure gradient during two-phase adiabatic flow of the R32/R1234ze(E) mixtures in a single minichannel with a inner diameter of 0.96 mm.
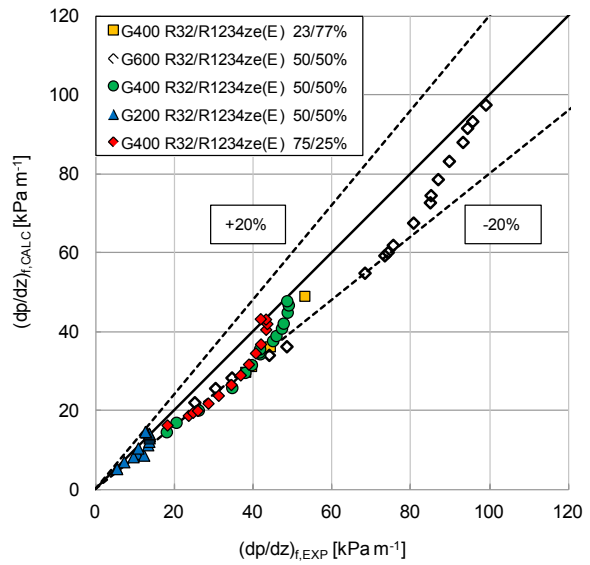
Figure 6.6: Prediction using the Muller-Steinhagen and Heck [65] model versus the experimental frictional pressure gradient during two-phase adiabatic flow of the R32/R1234ze(E) mixtures in a single minichannel with a inner diameter of 0.96 mm.
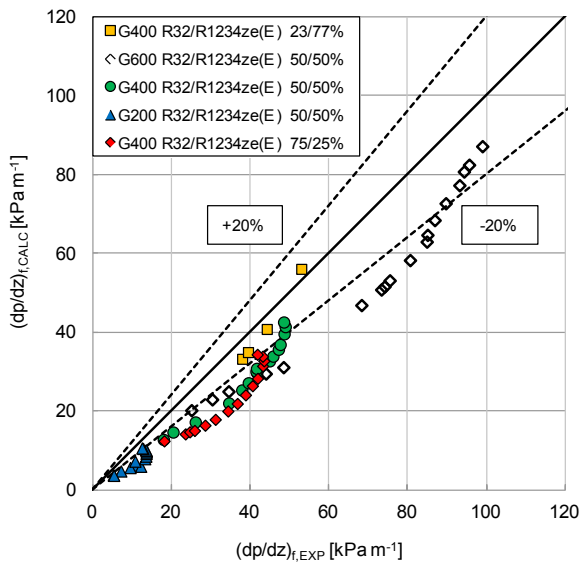
Figure 6.7: Prediction using the Zhang and Webb [53] model versus the experimental frictional pressure gradient during two-phase adiabatic flow of the R32/R1234ze(E) mixtures in a single minichannel with a inner diameter of 0.96 mm.
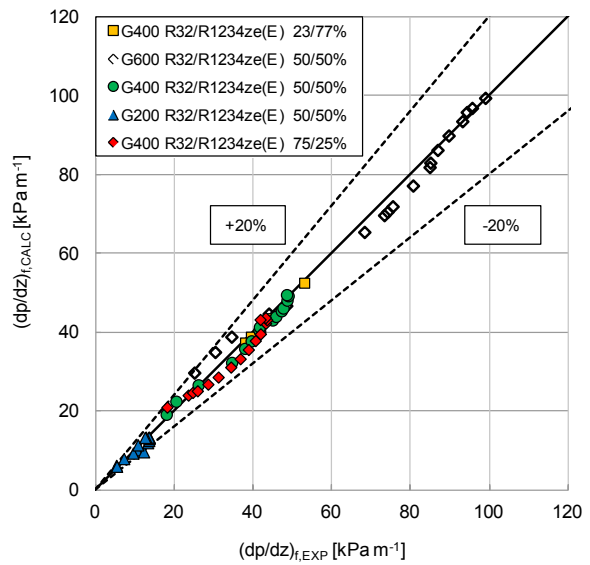
Figure 6.8: Prediction using the Del Col et al. [19] model versus the experimental frictional pressure gradient during two-phase adiabatic flow of the R32/R1234ze(E) mixtures in a single minichannel with a inner diameter of 0.96 mm.

6.5 Nomenclature

C	Hagen - Poiseuille constant	
c	specific heat	[J kg^{-1} K^{-1}]
D_h	hydraulic diameter	[m]
E	entrainment ratio	[/]
e	percent deviation $= \left[(\Delta p_{CALC} - \Delta p_{EXP}) / \Delta p_{EXP} \right] \cdot 100$	[%]
e_{AB}	absolute deviation $= \left(1/N_p \right) \sum \left[\lvert \Delta p_{CALC} - \Delta p_{EXP} \rvert / \Delta p_{EXP} \right] \cdot 100$	[%]
e_R	average deviation $= \left(1/N_p \right) \sum \left[(\Delta p_{CALC} - \Delta p_{EXP}) / \Delta p_{EXP} \right] \cdot 100$	[%]
f	friction factor	[/]
f^+	parameter in Eq. 6.15	[/]
F	parameter in Eq. 6.11	[/]
G	mass velocity	[kg m^{-2} s^{-1}]
g	gravitational acceleration	[m s^{-2}]
H	parameter in Eq. 6.11	[/]
h	enthalpy	[J kg^{-1}]
J_G	dimensionless gas velocity $= \dfrac{xG}{\left(gD_h\rho_V \left(\rho_L - \rho_V \right) \right)^{0.5}}$	[/]
L	channel length	[m]
$\dot{m}$	mass flow rate	[kg s^{-1}]
p	pressure	[Pa]
p_{CR}	critical pressure	[Pa]
p_R	reduced pressure $= p/p_{CR}$	[/]
Ra	arithmetical mean deviation of the assessed profile (according to ISO 4287:1997) [m]	
Re	Reynolds number $= (GD_h)/\mu$	[/]
Re$_{LO}$	liquid-only Reynolds number $= (GD_h)/\mu_L$	[/]
Re_{LO}^{+}	parameter in Eq. 6.14	[/]
RR	relative roughness of the channel $= 2Ra/D_h$	[/]
W	parameter in Eq. 6.11	[/]
x	thermodynamic vapor mass quality	[/]
X	corrective coefficient in Eq. 6.13	[/]
Y	mass fraction	[/]
z	axial coordinate oriented with the flow	[m]
Z	parameter in Eq. 6.11	[/]

Greek symbols

Δp	pressure difference	[Pa]
ΔT	temperature difference	[K]
ϕ_{LO}^{2}	$\left(\dfrac{dp}{dz} \right)_f \Big/ \left(\dfrac{dp}{dz} \right)_{f,LO}$	[/]
μ	dynamic viscosity	[Pa s]
ρ	density	[kg m^{-3}]
σ_N	standard deviation $= \left\{ \left[\sum (e - e_R)^2 \right] \Big/ \left(N_p - 1 \right) \right\}^{1/2}$	

Subscripts

CALC   calculated

EXP   experimental
f   frictional
in   inlet
L   liquid phase with its actual mass flow rate
LO   liquid phase with total mass flow rate
MS   measuring sector
PS   pre-conditioning sector
ref   refrigerant
V   vapor phase with its actual mass flow rate

7 CONDENSATION HEAT TRANSFER OF NON-AZEOTROPIC MIXTURES INSIDE A SINGLE CIRCULAR MINICHANNEL

7.1 Introduction

The worldwide alert about global warming has led to an increasing interest in new HVAC technologies with low environmental impact. When considering this impact, both an indirect effect due to the energy consumption—and the consequent carbon dioxide emissions caused by the electricity production process—and a direct effect due to leakages of refrigerant must be taken into account. The introduction of microchannels in the field of enhanced heat transfer and in refrigeration and air-conditioning applications is surely one attempt to respond to these needs. Microchannels allow the development of compact elements that work with reduced refrigerant charge, minimizing the problems of release of potentially hazardous fluids into the atmosphere and reaching high heat transfer performance. Beside achieving high heat transfer rates in compact heat exchangers, there is an increasing interest in refrigerants possessing low global warming potential (GWP). The Kyoto Protocol of the United Nations Framework Convention on Climate Change (1997) placed hydrofluorocarbons (HFCs) among the six categories of greenhouse gases because of their large values of GWP and called for their phase-out. Afterward, in 2014, the European Commission adopted a new regulation about F-gas (see Section 1). The search for alternatives primarily focuses on the use of natural refrigerants (hydrocarbons, ammonia, carbon dioxide) and new synthetic refrigerants having low GWP. However, natural refrigerants are often flammable or toxic, and few single-component low-GWP refrigerants are well developed so far. Hence, for most applications, an alternative to high-GWP synthetic refrigerants would rely on refrigerant mixtures. Koyama et al. [70] attempted to blend R1234ze(E) with R32 to investigate this mixture as a possible low-GWP substitute in vapor compression heat pump and refrigeration systems. As the result of their drop-in tests with R32/R1234ze(E) 0.5/0.5 by mass, they found that for the tested binary mixture, the coefficient of performance (COP) is slightly affected by the degree of subcooling at the condenser outlet, and it is only about 7.5% lower than that of R410A at the same heating load. They concluded that the mixtures of R32/R1234ze(E) can be considered to be applicable as low-GWP alternatives for R410A by adjusting the composition of the mixture and by reconsidering some design parameters of components of air-conditioning systems. For a cycle evolving between two temperatures (T_1 and T_2) with $T_1 > T_2$, the maximum COP is obtained by the Carnot cycle as in Eq. 7.1. In a cycle operating with a zeotropic mixture, the heat exchange at the evaporator and at the condenser will occur with gliding temperatures. Such cycles are sometimes called as Lorenz cycles. The COP for a Carnot cycle is still valid for reversible cycles with gliding temperatures, provided that T_1 and T_2 are properly evaluated. In this case, temperatures T_1 and T_2 can be replaced by the mean logarithmic absolute temperature of the working fluid (Eqs. 7.2-7.3). For example, in a refrigerating system, if the zeotropic mixture evolves in the condenser between temperatures T_{1in} and

T_{1out} due to the temperature glide, T_1 will be the mean logarithmic temperature, as reported in Equation 7.2:

$$COP = \frac{T_2}{T_1 - T_2} \qquad \textbf{7.1}$$

$$T_1 = \frac{T_{1in} - T_{1out}}{\ln\left(T_{1in}/T_{1out}\right)} \qquad \textbf{7.2}$$

$$T_2 = \frac{T_{2out} - T_{2in}}{\ln\left(T_{2out}/T_{2in}\right)} \qquad \textbf{7.3}$$

In the literature, a limited number of pressure drop and heat transfer data for mixtures of hydrofluoroolefins (HFOs) and HFCs in small-diameter channels (d_h<3 mm) is available. Regarding the vaporization of the mixture R1234ze(E)/R32, Kondou et al. [62] performed flow boiling tests in a horizontal microfin tube of 5.21 mm inner diameter at different mass compositions. The heat transfer coefficient and pressure drop are measured at a saturation temperature of 10°C, heat fluxes of 10 and 15 kW m^{-2}, and mass velocities from 150 to 400 kg m^{-2} s^{-1}. They found a significant decrease of the mixture heat transfer coefficient with respect to the pure components. Recently Miyara et al. [71] measured the heat transfer coefficient during condensation of the mixture R32/R1234ze(E) at 45/55% and 30/70% mass composition inside a 4.35 mm diameter tube. They showed that the mixture at these two different compositions displayed a lower heat transfer coefficient than the pure components; comparing the data with those of R410A, the heat transfer coefficients of the mixture result comparable. However, no data are available for microchannels. In this work the condensation heat transfer performance of the mixture R32/R1234ze(E) at two different compositions has been investigated inside a single circular cross section microchannel with an inner diameter of 0.96 mm. The experimental characterization of the R32/R1234ze(E) mixture includes the measurement of the frictional pressure drop during adiabatic two-phase flow in a dedicated test section.

7.2   Experimental apparatus

7.2.1   Test facility

The test section for heat transfer investigations is the one described in Section 2.2.1 and it is accommodated in the experimental apparatus presented in Section 2.2. For reader convenience, a brief description of the test facility is reported also in this section in order to better present the operative conditions during heat transfer test runs.
The test facility (Figure 4.5) consists of a primary refrigerant loop and three auxiliary water loops. The refrigerant loop underwent several washing cycles before filling it with the non-azeotropic mixture, to remove all possible contaminants. During test runs, in the primary loop, the subcooled refrigerant exiting the post-condenser is sent through a filter dryer by an independently controlled gear pump that is magnetically coupled to a variable-speed

electric motor. The gear pump is an oil-free system, thus no oil separator is required in the refrigerant loop. The mass flow rate is measured by a Coriolis-effect mass flow meter. Hence, the fluid passes through a mechanical filter, and using the hot water of the secondary loop, it can be vaporized and superheated in a tube-in-tube heat exchanger. Then the working fluid can be sent in different test sections. The 0.96 mm inner diameter heat transfer test section is composed of two counter-current heat exchangers. The first heat exchanger works as pre-conditioning sector and is used to reach the desired thermodynamic conditions at the inlet of the measuring sector. Both the sectors are served by the same thermal bath, using distilled water as secondary fluid. Each hydraulic loop is provided with a flow regulating valve and a Coriolis effect mass flow meter to set and measure the mass flow rate. When necessary the inlet water temperature in the inlet condition setter and the measuring section can be maintained at different values by using electrical heaters installed downstream of the thermal bath in each loop. In each sector the inlet and outlet water temperature is measured with a T-type thermocouple and the temperature difference is checked using a triple junction thermopile. In both the test sections (pressure drop and heat transfer test section), the operative pressure is measured at the inlet and outlet of the pre-conditioning sectors by means of two relative pressure transducers, whereas two differential pressure transducers with different operative ranges are employed to measure pressure drop along the measuring sectors. At the exits of the test sections the fluid is collected and sent to the post-condenser in which is subcooled using another thermal bath serving brine at 5°C. During the test runs, when the apparatus is working in steady-state conditions, measurements of pressure, temperature, and mass flow rate are recorded for 50 s and averaged.

7.3   Mixture composition and property evaluation

The halogenated olefin R1234ze(E) is regarded as a possible low-GWP substitute of R134a due to similar thermo-physical properties. The thermal performance of R1234ze(E) during condensation has been investigated recently by Del Col et al. [6] inside a circular microchannel with an internal diameter of 0.96 mm at 40°C saturation temperature and mass velocity ranging from 100 to 800 kg m^{-2} s^{-1}. The condensation heat transfer coefficients were compared against those of R32, R134a, and R1234yf taken in the same channel at the same operating conditions. At fixed mass flux and saturation temperature, the condensation heat transfer coefficients of R1234ze(E) result to be lower than those of R32, comparable with those of R134a and higher than those of R1234yf. Two-phase frictional pressure drop tests have also been carried out during adiabatic flow of R1234ze(E) inside the circular cross section microchannel at mass velocities ranging from 200 to 800 kg m^{-2} s^{-1} and at about a 40°C saturation temperature, because an analysis of the thermal performance during condensation can not disregard the pressure losses. With respect to R134a and R1234yf, R1234ze(E) displays the lowest reduced pressure and the highest frictional pressure gradient.

In the following Sections the results obtained with three R32/R1234ze(E) mixtures are presented. The compositions that have been tested during condensation are: 0.229/0.771, 0.457/0.543 and 0.748/0.252 (hereafter 23/77%, 46/54% and 75/25%). In the whole experimental campaign, the mass composition was checked using a gas chromatograph during test runs; the experimental uncertainty on the measured composition is ±0.001 by mass. Thermodynamic and transport properties of pure R32 and R1234ze(E) at a 40°C saturation temperature are reported in Table 7.1. For the mixture R32/R1234ze(E), few experimental data are available and a limited number of publications have reported their properties. In particular, Akasaka [67] presented thermodynamic property models for mixture R32/R1234ze(E). The author emphasized that the property models proposed are designed for engineering use and are based on limited experimental data. For the R32/R1234ze(E) mixture, Akasaka [67] recommended the KW2 model with tuned parameters to better fit the experimental data. In the present article, the Akasaka [67] model is implemented in REFPROP 9.1 (Lemmon et al. [20]) to determine the mixture properties (Table 7.1). According with the UE Regulation N.517/2014 the GWP of a mixture is calculated as a weighted average, derived from the sum of the weight fractions of the individual substances multiplied by their GWP. So the GWP for the three mixtures considered are: 155, 310 and 506 respectively, increasing the mass fraction of R32.

Figure 7.1 shows the temperature-composition diagram for the R32/R1234ze(E) mixture at 17.4 bar pressure, corresponding to a bubble point temperature of 36.2°C in the case of 46/54% mass composition. As it can be seen, the dew and bubble point lines divide the diagram in three parts: the upper area represents the superheated region, the area between the two lines is the two-phase zone, and the area below the bubble line is the subcooled liquid zone. During an isobaric condensation process, the mixture does not evolve at constant temperature, but its temperature changes between the dew and the bubble point temperature: this temperature difference is called glide. By looking at the phase diagram, it is clear that R32 is the more volatile fluid, and when the mass fraction of R32 is increased, the dew point temperature decreases. Considering a superheated vapor at point 1, heat is removed until point 2 (dew point temperature) is reached. In the two-phase region, the liquid and vapor concentrations change along the dew and bubble point lines. The first drop of condensate has a composition that is poorer of R32 (point 2'). As condensation proceeds, the refrigerant temperature decreases, and it reaches, for example, point 3'', where the equilibrium concentration of R32 in the vapor and in the liquid corresponds to points 3 and 3', respectively. When the condensation is completed, the mixture temperature is equal to the bubble temperature (point 4'). If more heat is removed, the mixture is subcooled (point 5). The chemical composition of both the liquid and vapor phases changes during the process and, as the heat is removed, the local concentration of the more volatile component increases in the vapor phase. This process creates a concentration gradient between the liquid–vapor interface and the vapor bulk; a similar concentration gradient is present in the liquid film. As the condensation proceeds, both the mixture components have to diffuse in the vapor and liquid phases: the mass transfer introduces a further resistance, which, from the heat transfer point of view, may be regarded as an additional thermal resistance.

Table 7.1. Properties of pure R32 and R1234ze(E) at 40°C saturation temperature; refrigerant mixture properties are reported at given mass composition and pressure; data from NIST Refprop 9.1 (Lemmon et al.[20])

Fluid	p_{sat} [bar]	ρ_l [kg m^{-3}]	ρ_g [kg m^{-3}]	μ_l [µPa s]	λ_l [W m^{-1} K^{-1}]	T_{dew} [°C]	T_{bub} [°C]	Glide [K]
R32	24.8	893.0	73.3	95.0	0.115	/	/	/
R1234ze(E)	7.7	1111.3	40.7	167.0	0.069	/	/	/
23/77%	13.1	1075.3	56.4	143.8	0.083	45.6	34.6	11
46/54%	17.4	1017.9	64.7	121.9	0.094	44.4	36.2	8.2
75/25%	22	945.5	71.7	103.8	0.106	41.9	38.9	3
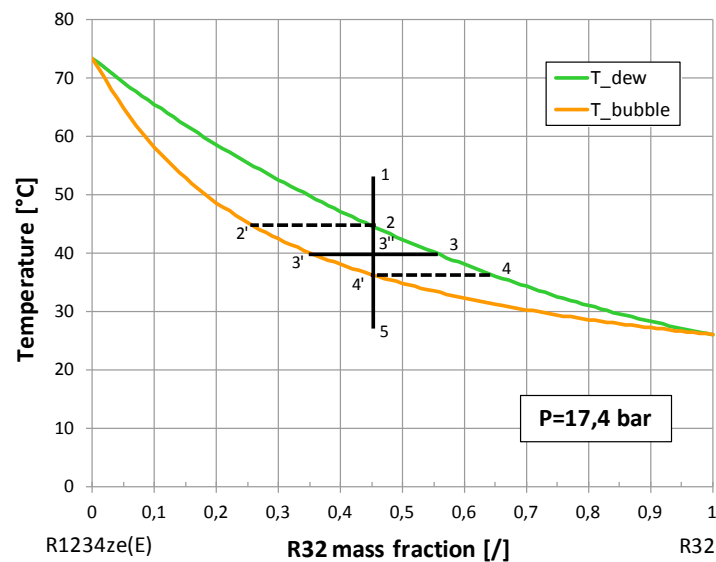
Figure 7.1. Temperature-composition diagram for the zeotropic R32/R1234ze(E) mixture at 17.4 bar constant pressure.

7.4 Data reduction and calibration tests

The data reduction procedure to evaluate the heat transfer coefficient in the 0.96 mm test section has been reported, for pure fluids, in Section 4.1.2. In the case of mixtures the procedure is similar but with few changes.

A typical temperatures profiles during a condensation test for the mixture 46/54 % by mass composition at *G*=400 kg m^{-2} s^{-1} is reported in Figure 7.2.
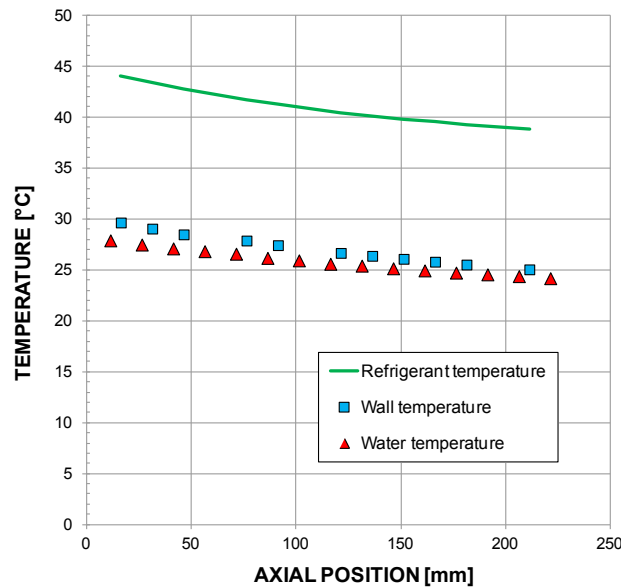
Figure 7.2. Refrigerant, wall and water temperatures along the measuring sector during a condensation test for the mixture 46/54, by mass composition, at *G*=400 kg m^{-2} s^{-1}.

In the determination of the local heat transfer coefficient, as reported in Eq. 7.4, three parameters are used.

$$\alpha(z) = \frac{q'(z)}{T_{ref}(z) - T_w(z)} \qquad \textbf{7.4}$$

Differently from Section 4.1.2 the saturation temperature has been replaced with the refrigerant temperature because during condensation of a non-azeotropic mixture it is not constant but, as seen, it changes from the dew point to the bubble point.

In the present case the local temperature of the refrigerant (Eq. 7.5) is calculated from the local pressure, local enthalpy and mixture composition, assuming an equilibrium state and using the thermodynamic properties of the refrigerant. The local pressure and enthalpy in Eq. 7.5 are evaluated in the same way as reported in Section 4.1.2.

$$T_{ref}(z) = f\left(p(z), h(z), X_{R1234ze}\right) \qquad \textbf{7.5}$$

As for the refrigerant temperature, the vapor quality along the test section is evaluated using Eq. 7.6:

$$x(z) = f\left(p(z), h(z), X_{R1234ze}\right) \qquad \textbf{7.6}$$

Besides the on-site calibration of thermocouples, thermopiles and pressure transducers, some preliminary tests on the heat transfer test section have been made before starting the experimental campaign. The energy balance in the test section was controlled for each mixture composition, comparing the water side heat transfer rate with the refrigerant one when superheated vapor enters the test section and subcooled liquid exits. The agreement between the two was found to be within 4% in any case.

7.5   Experimental data: results and discussion

Condensation tests have been performed with mass velocity ranging from 150 to 800 kg m^{-2} s^{-1} at a pressure of about 13.1, 17.4 and 22 bar, respectively, for the 23/77%, 46/54% and 75/25% mixtures over the entire range of vapor quality.

For a better comprehension, the local heat transfer coefficients for the R32/R1234ze(E) mixture at 23/77% and 46/54% compositions are reported in Figure 7.3 and the local heat transfer coefficients for the mixture 46/54% and 75/25% are reported in Figure 7.4.

As expected for forced convective condensation inside conventional pipes, the heat transfer coefficient increases mass velocity. This behaviour can be justified by the fact that, at higher mass velocities, the condensation process is dominated by the shear stress at the liquid-vapor interface, while gravity and surface tension play a marginal role. In this case the condensation process takes place with annular flow regime, characterized by a liquid film uniformly distributed on the inner channel perimeter. At lower mass velocities, the influence of gravity and surface tension increases as the vapor is unable to sustain the annular liquid film and the shear stress decreases; this lead the liquid film to become thicker on the lower side of the channel leading to a non uniform distribution. The decreasing trend of the heat transfer coefficient with the vapor quality is due to the fact that, during the condensation, the forming liquid film introduces a further thermal resistance. As the condensation proceeds, the liquid film becomes thicker and the relative thermal resistance rises up.

Looking at the data in Figure 7.3 and Figure 7.4 it is worth noting that, for given values of mass velocity and vapor quality, the heat transfer coefficient increases as the R32 mass fraction in the mixture increases. When the mass fraction of R32 is increased from 23% to 46%, the heat transfer coefficient increases on average of 7% at $G = 800$ kg m^{-2}s^{-1} and $G = 400$ kg m^{-2} s^{-1}, and by 10% at $G = 200$ kg m^{-2} s^{-1}. If the 75/25% mixture is compare with the 23/77% and the 46/54% mixtures, the heat transfer coefficient increases averagely of about 28% and 18% respectively. This is due to the thermodynamic characteristics of the R32, which offers higher performances than R1234ze(E) at the same operative conditions. By looking at Table 7.1 can be noticed that pure R32 has larger latent heat (about 1.53 times) and higher liquid thermal conductivity (about 1.66 times) if compared with pure R1234ze(E) at a saturation temperature of 40°C.

In Table 7.2, the heat transfer coefficient percentage increase achieved by increasing the concentration of R32 at each mass velocity is reported.

Table 7.2. Heat transfer coefficient percentage increase at each mass velocity

Mass composition	46/54%	75/25%	
Mass composition considered for comparison	23/77%	23/77%	46/54%
G=800 kg m^{-2}s^{-1}	7,4	25,3	16,6
G=600 kg m^{-2}s^{-1}	9,2	24,8	14,3
G=400 kg m^{-2}s^{-1}	7,2	26,7	18,3
G=200 kg m^{-2}s^{-1}	10,4	34,1	21,5
Average difference	**8,6**	**27,7**	**17,7**
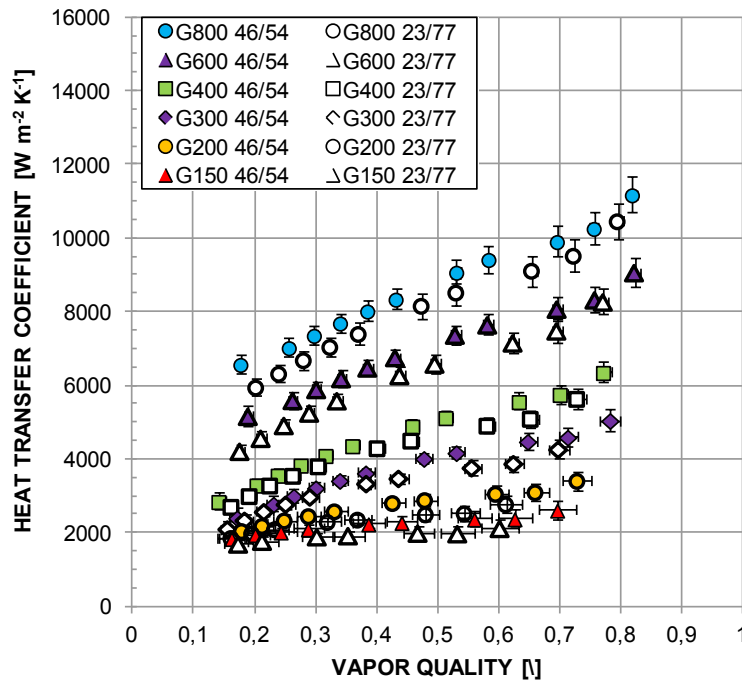
Figure 7.3. Experimental local condensation heat transfer coefficient versus vapor quality for the R32/R1234ze(E) mixture at 46/54% and 23/77% by mass composition, at mass velocity *G* ranging from 150 to 800 kg m⁻² s⁻¹. Each point is reported with the corresponding error bands on the heat transfer coefficient and on the vapor quality.
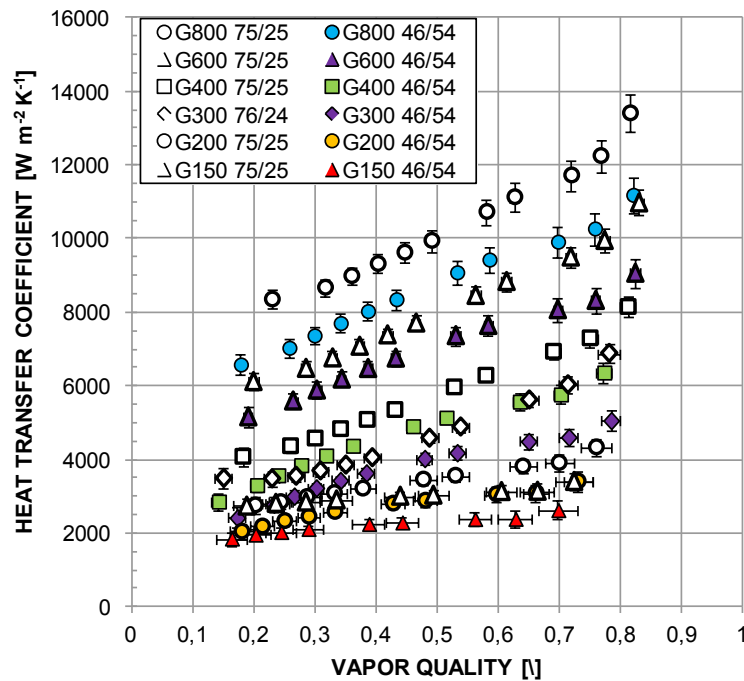
Figure 7.4. Experimental local condensation heat transfer coefficient versus vapor quality for the R32/R1234ze(E) mixture at 75/25% and 46/54% by mass composition, at mass velocity *G* ranging from 150 to 800 kg m⁻² s⁻¹. Each point is reported with the corresponding error bands on the heat transfer coefficient and on the vapor quality.

A further comparison can be made by plotting the heat transfer coefficient against the vapor quality for both pure fluids and mixtures, as shown in Figure 7.5; data of the pure fluids have been taken in the same microchannels [6]. Both R32 and R1234ze(E) display similar trends with mass velocity and vapor quality, but the heat transfer coefficient for R32 is about 30%, 35%, 29%, and 18% higher at 800, 600, 400, and 200 kg m^{-2} s^{-1}, respectively. It is also possible to see how the 23/77% and 46/54% mixtures achieve lower, or at least equal, heat transfer coefficients if compared with the pure R1234ze(E), for all the mass velocities reported; for low vapor qualities these two mixtures are very close to pure R1234ze(E). On average the 23/77% mixture shows a decrease around 11% with respect to pure R1234ze(E) while the mixture 46/54% assumes a comparable value with respect to the same fluid (only 4% lower). Only mixture 75/25% shows an improvement on the heat transfer coefficient of about 13% if compared with pure R1234ze(E). All the mixtures show a decrease with respect to pure R32 around 31%, 25% and 12% for mixtures 23/77%, 46/54% and 75/25% respectively. The mean values resulting from the comparison of the heat transfer coefficient of the mixture and the pure fluids at each mass flow rate and for different vapor qualities is reported in Table 7.3.

Table 7.3. Heat transfer coefficient percentage difference between the experimental values of the mixture and those of the pure components at the same operating conditions.

	23/77%	46/54%	75/25%	23/77%	46/54%	75/25%
	R32			R1234ze(E)		
G=800 kg m^{-2}s^{-1}	-29,5	-24,2	-11,7	-8,6	-1,8	14,5
G=600 kg m^{-2}s^{-1}	-31,7	-25,5	-14,9	-7,7	0,9	15,2
G=400 kg m^{-2}s^{-1}	-29,6	-24,6	-10,9	-9,4	-3,0	14,6
G=200 kg m^{-2}s^{-1}	-31,4	-25,8	-9,9	-18,9	-12,3	6,4
Average difference	**-30,6**	**-25,0**	**-11,9**	**-11,1**	**-4,0**	**12,7**

a)

b)

c)
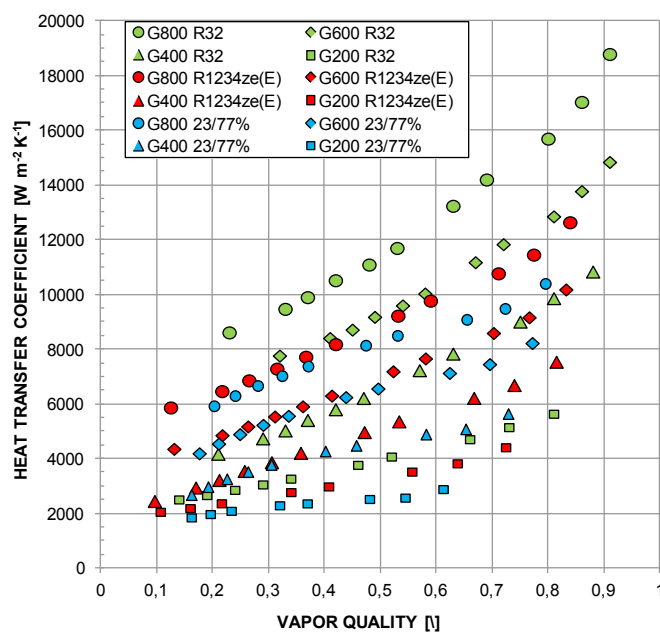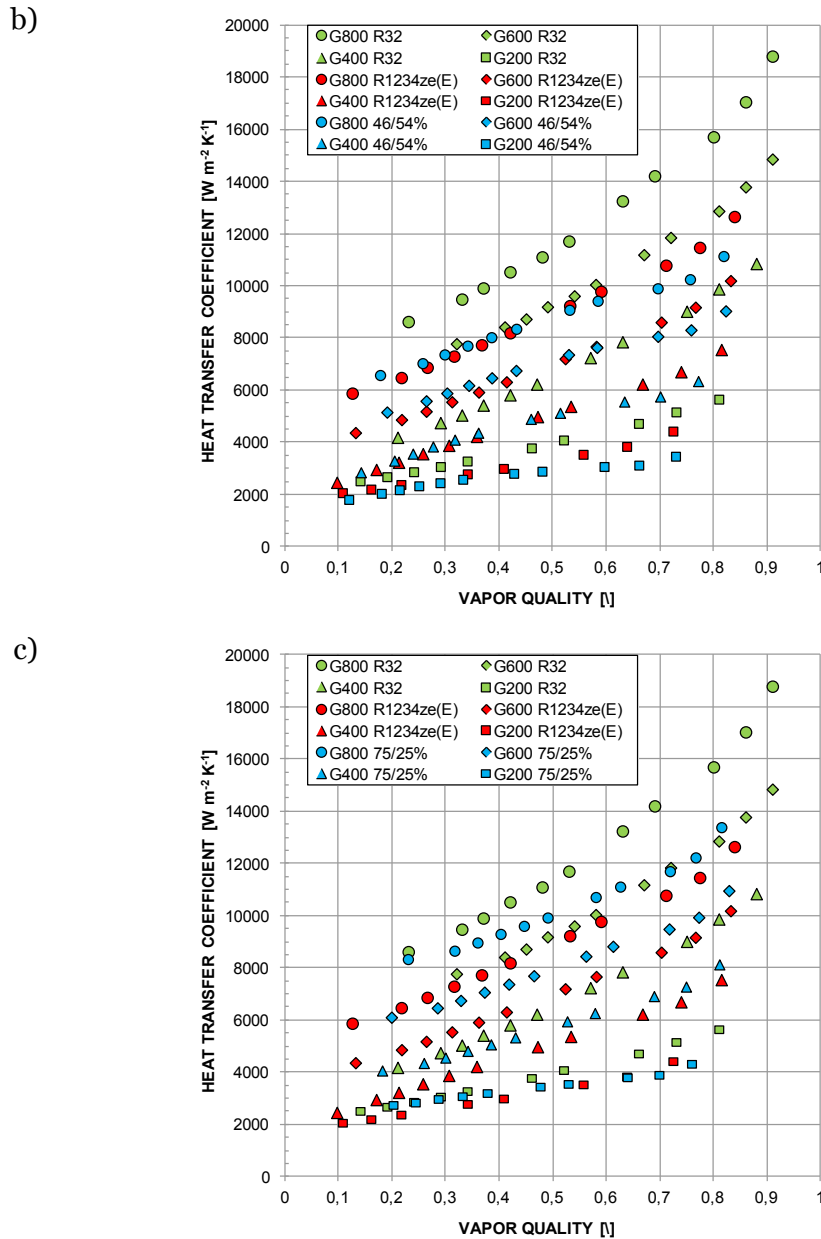
Figure 7.5. Experimental local heat transfer coefficient versus vapor quality for pure R32, pure R1234ze(E) and the R32/R1234ze(E) mixture at different mass velocity *G* [kg m⁻² s⁻¹]; a) comparison with the mixture 23/77% by mass composition, b) comparison with the mixture 46/54% by mass composition, comparison with the mixture 75/25% by mass composition

7.6   Uncertainty analysis

The uncertainty on the heat transfer coefficient and vapor quality has been evaluated as described in Section 11. Results are hereafter reported.

The expanded percentage uncertainty, considering a coverage factor equal to 2 (level of confidence of 95.45%), for the heat transfer coefficient is reported in Table 7.4. On average the percentage uncertainty is 5.3% (about 87% of data points inside the 8%); the maximum of 16.6% has been found at G=300 kg m⁻² s⁻¹ and x=0.15 for the mass composition 75/25%.

Regarding the vapor quality, the average expanded (coverage factor equal to 2 - level of confidence of 95.45%) uncertainty is about ±0.014.

Table 7.4. Expanded uncertainty for the experimental heat transfer coefficient. The coverage factor is equal to 2. Maximum, minimum and mean values are reported in the table.

Mass composition	G [kg m^{-2} s^{-1}]	Max u(α) [%]	Min u(α) [%]	Mean u(α) [%]
23/77%	800	4,8	3,7	4,2
	600	4,4	3,5	3,9
	400	6,7	3,5	4,5
	300	9,0	3,9	5,4
	200	8,7	5,3	7,0
	150	10,5	6,0	8,0
46/54%	800	4,4	3,3	3,7
	600	5,2	3,2	3,8
	400	8,1	3,1	4,4
	300	11,4	3,5	5,5
	200	10,3	4,2	6,5
	150	9,9	4,9	7,5
75/25%	800	4,8	3,1	3,7
	600	4,4	3,0	3,6
	400	6,0	3,1	4,3
	300	16,6	4,5	7,5
	200	8,8	3,9	6,4
	150	12,1	4,6	8,1

Table 7.5. Expanded uncertainty for the experimental vapor quality. The coverage factor is equal to 2. Maximum, minimum and mean values are reported in the table.

Mass composition	G [kg m^{-2} s^{-1}]	Max u(x) [/]	Min u(x) [/]	Mean u(x) [/]
23/77%	800	0,008	0,006	0,007
	600	0,009	0,007	0,008
	400	0,013	0,010	0,011
	300	0,017	0,013	0,014
	200	0,026	0,020	0,022
	150	0,030	0,022	0,025
46/54%	800	0,007	0,006	0,006
	600	0,009	0,007	0,007
	400	0,012	0,010	0,010
	300	0,016	0,013	0,014
	200	0,023	0,018	0,020
	150	0,031	0,024	0,026
75/25%	800	0,006	0,005	0,006
	600	0,009	0,007	0,008
	400	0,013	0,011	0,011
	300	0,020	0,018	0,018
	200	0,024	0,020	0,021
	150	0,032	0,027	0,028

For a better understanding, Figure 7.6 shows the contributions of the different parameters to the global heat transfer coefficient uncertainty. The figure shows the percent uncertainty values against vapor quality for the mixture at 46/54% mass composition during a condensation test at G=400 kg m^{-2}s^{-1}.

As can be seen, the inner perimeter uncertainty and the saturation minus wall temperature uncertainty remain rather constant during the condensation process along the duct. The water temperature gradient uncertainty varies with the position along the measuring section and presents a near-parabolic trend with the minimum value located near the middle of the section. This trend is strongly dependent on the water temperature profile interpolation: the polynomial function well fits the points in the middle of the section but commits a bigger error at the ends.
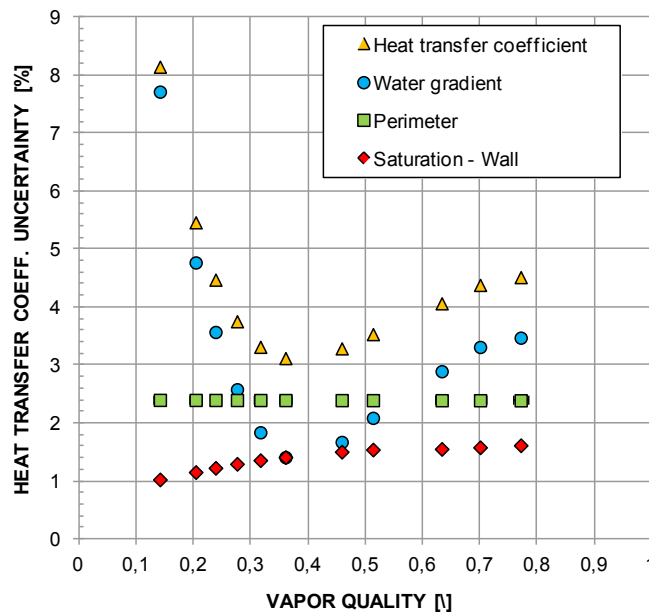
Figure 7.6. Total experimental percentage uncertainties of the heat transfer coefficient and its components. The values are referred to condensation test of 46/54% by mass of R32/R1234ze(E) at G=400 kg m^{-2} s^{-1}.

7.7 Penalization due to the mass transfer resistance during condensation

In Figure 7.7 the heat transfer coefficients for pure R1234ze(E), pure R32 and for the mixture at the three compositions are reported at four mass velocities and vapor qualities. The figure shows that the heat transfer coefficients of the mixtures are always lower than the values calculated by an ideal linear behavior between the values pertaining to the pure components at the same operating conditions. The deviation from the ideal behaviour could be explained by the mass transfer resistance introduction: during the condensation process, both liquid and vapor phases show a change in composition (see Section 7.3); the diffusion of both the mixture components through the liquid/vapor interface introduces a further

resistance that penalizes the heat exchange. The penalization due to the additional mass transfer resistance at different operating conditions is reported in Table 7.6. For all the three investigated vapor qualities, the higher penalization is shown by mixture 23/77% while mixture 46/54% and 76/24% show lower penalizations. This can be explained by the fact that by increasing the R32 mass fraction the glide magnitude decrease as well as the differential latent heat.

Table 7.6. Heat transfer coefficient penalization; an ideal linear behavior between the values pertaining to the two pure components is assumed as reference

G [kg m^{-2} s^{-1}]	x [/]	Penalization at different composition		
		23/77%	46/54%	75/25%
800	**0,7**	-18,2	-18,5	-12,0
600	**0,7**	-18,2	-18,0	-12,1
400	**0,7**	-21,9	-21,1	-12,1
200	**0,6**	-27,1	-24,3	-13,3
800	**0,4**	-10,4	-10,3	-4,3
600	**0,4**	-10,2	-8,9	-7,2
400	**0,4**	-10,2	-8,5	-3,8
200	**0,4**	-22,2	-15,0	-3,7
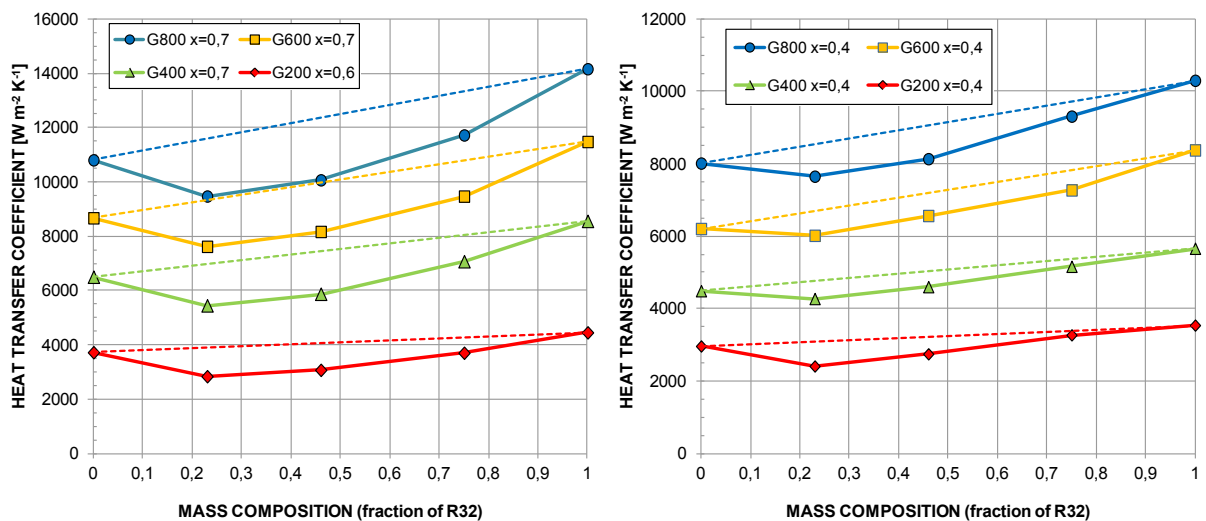
Figure 7.7. Experimental local heat transfer coefficients for the refrigerant mixture R32/R1234ze(E) and its pure components. Dashed lines refer to an ideal linear behavior. A mass composition equal to 0 corresponds to pure R1234ze(E). *G* is mass velocity in [kg m^{-2} s^{-1}] and *x* is vapor quality.

7.8   Prediction of the condensation heat transfer coefficient

Cavallini et al. [18] proposed a method to predict condensation heat transfer coefficients inside horizontal smooth tubes with an internal diameter greater than 3 mm. The model, developed for pure fluids, was validated against data for hydrochlorofluorocarbons

(HCFCs), HFCs, hydrocarbons (HCs), carbon dioxide, ammonia, and water. The authors considered in this model two categories: a ΔT-dependent flow regime and a ΔT-independent flow regime, requiring only one transition criterion. The criterion adopted to find the transition curve between the two regimes involves mainly two parameters: the dimensionless gas velocity J_G and the Martinelli parameter X_{tt}. In the definition of the transition line a parameter that accounts if the fluid is a hydrocarbon or another refrigerant is adopted. As stated by the authors, all possible flow regimes observed during the condensation process are included in the model.

As reported in Matkovic et al. [17] and Del Col et al. [6], the present model was in good agreement with experimental data for the pure components of the refrigerant blend.

The experimental points available for the comparison for the whole mass velocity range of the refrigerant blend are: 55 points for mixture 23/77%, 62 points for mixture 46/54% and 63 points for mixture 75/25% leading to a database of 180 points. The comparison between experimental data and calculations by Cavallini et al. [18] model is reported in Figure 7.8. It can be noticed that, in general, the correlation slightly overpredicts the heat transfer coefficient values. The model gives an absolute mean deviation (e_{AB}) of 10.1% for mixture 23/77% while for mixtures 46/54% and 75/25% the e_{AB} is respectively 11.6% and 10%. This correlation seems to well predict the mixture heat transfer coefficients as 96% of the experimental points fall within ±20% error bands with low values of standard deviation (σ_N): for mixture 23/77% the σ_N is 5.8%, 6.0% for mixture 46/54% and 7.0% for mixture 75/25%.

Figure 7.8. Comparison between the experimental heat transfer coefficient of the mixture R32/R1234ze(E) at the three different compositions and corresponding values calculated with the model by Cavallini et al. [18] for pure fluids.

As reported in Del Col et al. [72], during condensation of zeotropic mixtures, the heat transfer mechanisms are the same that occur during condensation of a pure fluid, convective condensation, and film condensation. However, due to the zeotropic characteristic of the mixture, the condensation process is non-isothermal (see Section 7.3), and there is sensible heat to be removed both in the liquid and vapor phases. This contribution may be significant, depending on the heat transfer coefficient associated with the removal of the sensible heat from the vapor. In addition, as previously stated, the composition in both phases is continuously changing during the condensation process, and an additional diffusion mass transfer resistance must be considered. The key point for calculations is the mass transfer resistance in the vapor phase. Models developed for pure vapor condensation can in principle be applied to mixtures when complete mixing, both in the liquid and in the vapor phase, is reached and overall equilibrium is maintained, provided that the additional resistance due to the mass transfer is properly accounted for. Hence, a model for pure fluids can be applied to the zeotropic mixture using the Bell and Ghaly [73] and the Silver [74] corrections. According to this correction, the additional mass transfer resistance is proportional to the sensible heat transfer resistance in the vapor phase. In this procedure, the heat transfer coefficient of the mixture is calculated as a function of the heat transfer coefficient of the condensate, the heat transfer coefficient of the vapor phase flowing alone in the duct α_g (calculated with the Dittus–Boelter equation), and the ratio between the sensible heat duty removed by cooling the vapor and the total transferred heat flow rate $\partial q_{sg}/\partial q_t$, as reported in Eq. 7.7:

$$\alpha_m = \left(\frac{1}{\alpha} + \frac{\partial q_{sg}/\partial q_t}{\alpha_g} \right)^{-1} \qquad \text{7.7}$$

The ratio of the sensible to total heat duty can be expressed with good approximation as reported in Eq. 7.8:

$$\frac{\partial q_{sg}}{\partial q_t} \approx x c_{pg} \left(\frac{\mathrm{d}T}{\mathrm{d}h} \right) \qquad \text{7.8}$$

If the ratio of dT/dh remains approximately constant during the condensation process, it can be rewritten as:

$$\frac{\mathrm{d}T}{\mathrm{d}h} \approx \frac{\Delta T_{GL}}{\Delta h_m} \qquad \text{7.9}$$

where Δh_m is the isobaric change in enthalpy of the mixture. The comparison between the experimental data and the model by Cavallini et al. [18] applied with the Silver–Bell–Ghaly correction is reported in Figure 7.9. With this correction the model better predicts the

experimental data giving an e_{AB} of 8.1% for the mixture 23/77%, 6.9% and 6.3% respectively for the 46/54% and the 75/25% mixtures. Considering the whole database the mean relative deviation is about -5% and the standard deviation of about 5.4%.

The results obtained with the model are summarized in Table 7.7.

Table 7.7. Mean relative deviation (e_R), mean absolute deviation (e_{AB}) and standard deviation (σ_N) obtained comparing the Cavallini et al. [18] model and the Cavallini et al. [18] model with the Silver−Bell−Ghaly correction with the present refrigerant blend database.

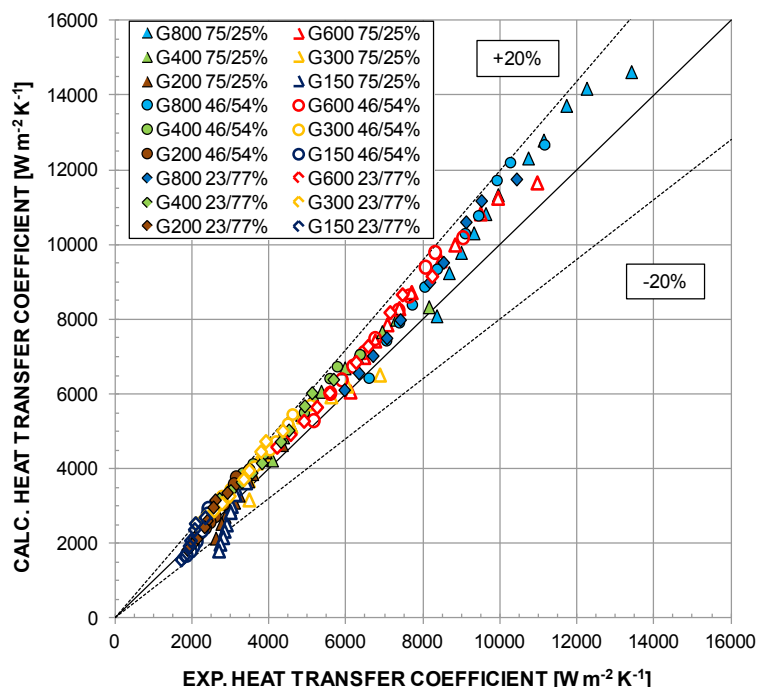| Composition R32/R1234ze(E)	Cavallini et al. [18]			Cavallini et al. [18] with the Silver−Bell−Ghaly correction		
	e_R	e_{AB}	σ_N	e_R	e_{AB}	σ_N
23/77%	9,3	10,1	5,8	-7,0	8,1	5,4
46/54%	10,6	11,6	6,0	-5,5	6,9	4,9
75/25%	5,2	10,0	7,0	-2,4	6,3	5,9
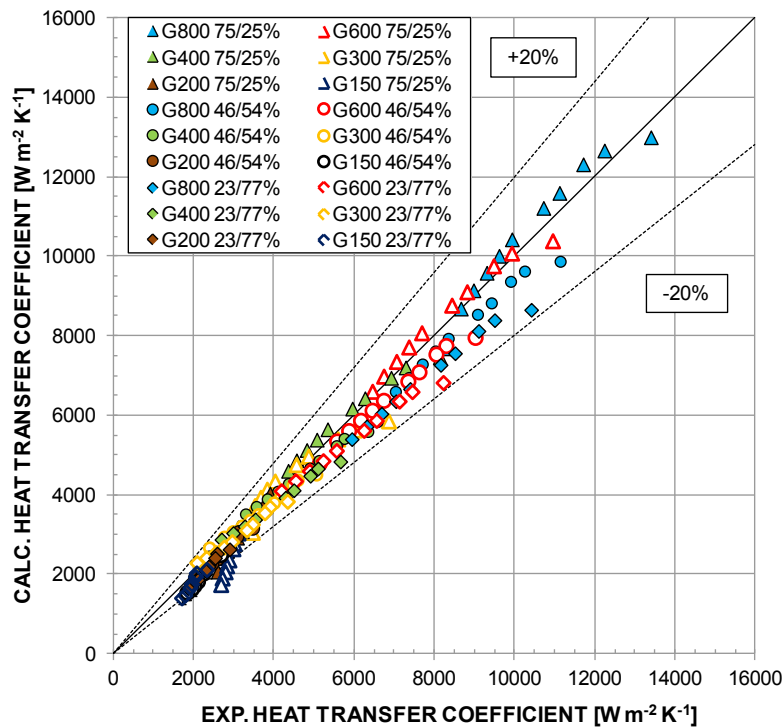
Figure 7.9. Comparison between the experimental heat transfer coefficients for the mixture R32/R1234ze(E) at the three compositions and the corresponding values calculated with the Cavallini et al. [18] model and the Silver−Bell−Ghaly correction.

7.9   Performance in condensation considering both heat transfer and pressure drop: Penalty Factor

A complete comparison between different refrigerants during convective condensation should account not only for the heat transfer coefficient but also for the pressure drop. To allow the performance analysis of refrigerants for condenser applications based on their heat transfer potential, a Performance Evaluation Criterion (PEC) is now adopted, referring to the analysis conducted by Cavallini et al. [75].

During condensation a larger saturation temperature drop implies that an additional compressor work will be needed in a refrigeration or air conditioning equipment to maintain a suitable value of the driving temperature difference. Thus, the local saturation temperature drop with respect to the vapor quality can be expressed as:

$$\frac{\mathrm{d}T_{sat}}{\mathrm{d}x} = \frac{\mathrm{d}T_{sat}}{\mathrm{d}p_f} \cdot \frac{\mathrm{d}p_f}{\mathrm{d}z} \cdot \frac{\mathrm{d}z}{\mathrm{d}x} \qquad\qquad \textbf{7.10}$$

where $\mathrm{d}p_f/\mathrm{d}z$ is the frictional pressure drop along the tube length.

The first term on the right-side can be rewritten reminding the Clausius-Clapeyron equation:

$$\frac{\mathrm{d}p_{sat}}{\mathrm{d}T_{sat}} = \frac{h_{LV}}{T_{sat}\left(\dfrac{1}{\rho_L} - \dfrac{1}{\rho_V}\right)} \qquad\qquad \textbf{7.11}$$

Applying an energy balance for an elementary length $\mathrm{d}z$ of a tube undergoing condensation from saturated vapor to saturated liquid, Eq. 7.10 can be rewritten as:

$$\frac{\mathrm{d}T_{sat}}{\mathrm{d}x} = \frac{G \cdot d \cdot T_{sat}}{4 \cdot \alpha \cdot \Delta T_{dr}} \cdot \left(\frac{1}{\rho_L} - \frac{1}{\rho_V}\right) \cdot \frac{\mathrm{d}p_f}{\mathrm{d}z} \qquad\qquad \textbf{7.12}$$

Eq. (7.12) contains two energy penalization terms: the first one is $\mathrm{d}T_{sat}/\mathrm{d}x$ which is associated with the frictional pressure drop of the condensing refrigerant, the second being $\Delta T_{dr}=T_{sat}-T_w$ which is associated with the driving temperature difference for the heat transfer process; both the terms adversely affect the compressor power consumption as their increase implies an increase in the compression ratio.

For a specified refrigerant, geometry and working conditions Cavallini et al. [75] reported that the product of the two penalization components can be expressed only as a function of α, at least in shear dominated condensation where both α and $\mathrm{d}p_f/\mathrm{d}z$ can be considered independent of the local heat flux. This product was dubbed penalty factor (*PF*, Eq. 7.13) of the condensation process:

$$PF = \left(\frac{\mathrm{d}T_{sat}}{\mathrm{d}x}\right)\Delta T_{dr} = \left(\Delta T_{sat}\right) \cdot \left(\Delta T_{dr}\right) \qquad\qquad \textbf{7.13}$$

where ΔT_{sat} is the saturation temperature decrease associate with the frictional pressure drop.

By combining Eqs. 7.12 and 7.13 the penalty factor can be rewritten as:

$$PF = \frac{G \cdot d \cdot T_{sat}}{4 \cdot \alpha} \cdot \left(\frac{1}{\rho_L} - \frac{1}{\rho_V} \right) \cdot \frac{\mathrm{d}p_f}{\mathrm{d}z} \qquad\qquad \textbf{7.14}$$

Looking at Eq. 7.14 it is clear that the application of this methodology requires that both the heat transfer coefficient and the frictional pressure gradient have to be known at given operating conditions; it means that accurate models for the heat transfer coefficient and frictional pressure drop are essentials.

It can be noticed that when the penalty factor is computed at the same value of condensation heat transfer coefficient for a given tube geometry, it can be directly used as a quantitative criterion to rank the heat transfer performance of different refrigerants: the smaller the PF, the better is the potential performance of the refrigerant.

Cavallini et al. [75] showed that when the Penalty Factor is plotted against the heat transfer coefficient in a graph that uses logarithmic scales for both the axes, the data for various refrigerants with the same geometry and in the same test conditions lied along nearly parallel straight lines as long as shear dominated condensation occurs. Therefore, they found that in annular flow condensation, the penalty factor can be represented in general form as:

$$PF = C_{ref} \cdot \alpha^{\varepsilon} \qquad\qquad \textbf{7.15}$$

where C_{ref} and ε depend on the channel geometry, vapor quality and refrigerant properties.

7.9.1 *Comparative analysis between the pure components and the mixture*

This method has been applied to the pure fluids R32, R1234ze(E) and the mixture in order to compare them in terms of heat transfer performances. In the present work, the model by Cavallini et al. [18], corrected for mixtures, is used for the prediction of the heat transfer coefficient, and the model by Del Col et al. [63] is used for the pressure drop. The accuracy of these models in the case of pure fluids and for the present mixture has been proven in previous sections. Anyway the trends of models are hereafter reported for the convenience of the reader. Figure 7.10 displays the condensation heat transfer coefficient calculated using the Cavallini et al. [18] model at 40°C saturation temperature (or mean refrigerant temperature for the mixture), inside the 0.96 mm minichannel (described in Section 4.1) at 400 kg m-2 s-1; the correction for mixture is applied when necessary. In the graphs, the vapor quality ranges between 0.1 and 0.9 and all the predicted points are within the ΔT-independent flow region, where the condensation process can be considered dominated by shear stress. Figure 7.11 displays the frictional pressure gradient versus vapor quality

during two-phase adiabatic flow calculated using the Del Col et al. [63] model for all the tested refrigerants in the circular minichannel (described in Section 2.2.2) at 400 kg m⁻² s⁻¹ and at 40°C saturation temperature (or mean refrigerant temperature for the mixture). In the plot, the vapor quality ranges between 0.1 and 0.9.
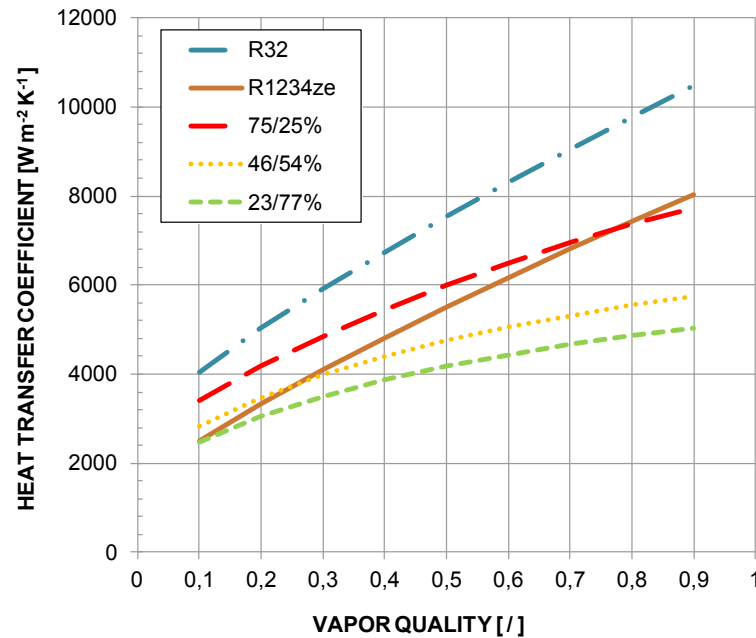
Figure 7.10. Predicted heat transfer coefficient during condensation at 40°C saturation temperature (or mean refrigerant temperature for the mixture) and at *G*=400 kg m⁻² s⁻¹ mass velocities inside the tested minichannel using the model by Cavallini et al. [18] for the pure fluids and the Cavallini et al. [18] model corrected for mixture in the case of the blend.
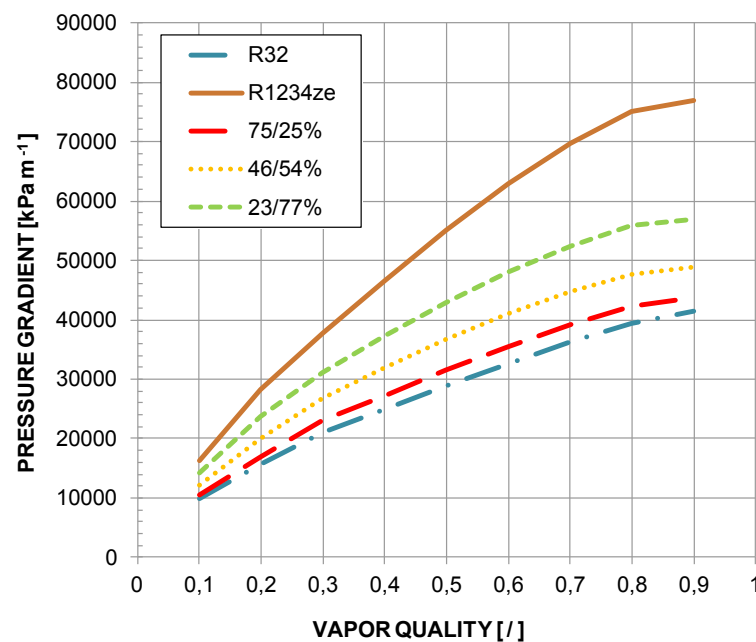

Figure 7.11. Predicted frictional pressure gradient during two-phase adiabatic flow at 40°C saturation temperature (or mean refrigerant temperature for the mixture) and at *G*=400 kg m⁻² s⁻¹ mass velocities inside the tested minichannel using the model by Del Col et al. [63] for all the considered fluids.

The penalty factor has been evaluated for the different refrigerants considering:
- a minichannel with an hydraulic diameter equal to 0.96 mm;
- an average roughness of the internal wall equal to 1. 3 μm;
- a mass velocity of 400 kg m^{-2} s^{-1};
- a saturation temperature 40°C for the pure fluids and 40°C as mean refrigerant temperature for the mixtures;
- the wall temperature is kept 10 K lower than the saturation temperature (or the refrigerant mean temperature).

It can be noticed (Figure 7.12) that the low-GWP refrigerant R1234ze(E) shows the highest PF in the whole vapor quality range, while R32 shows the lowest (PF = 1.4 K^2 at x = 0.5). This can be expected considering the properties of the two fluids at the same saturation temperature, as reported in Table 7.1 and the experimental data reported in previous sections. The two mixtures present PF curves lying between the pure fluids; as the R32 mass fraction increases, the PF decreases.

Now, by looking at the PF definition, if the same operative conditions are realized in terms of PF a different value of the mass velocity for each fluid can be calculated. To do this, the PF has been fixed at 5 K^2 at a vapor quality of 0.5 (Figure 7.13). The fixed value of the Penalty factor has been chosen in such a way that the mass velocity resulting for each considered refrigerant is within the range of working conditions for shear stress dominated condensation. According to the model by Cavallini et al. [18], this means that all the working conditions defined from the fixed value of Penalty Factor have to lie in the ΔT-independent flow region. Once the mass velocities at the same PF are identified, condensation heat transfer coefficients can be calculated and compared. These particular mass velocities are the ones that lead the fluids to show the same energy penalizations during a condensation process.

From Figure 7.13 one can see that for pure R32 the mass velocity is the highest, G=815 kg m^{-2} s^{-1} and for pure R1234ze(E) is the lowest G=337 kg m^{-2} s^{-1}. As expected, the three mixtures show mass velocities between the ones of the pure fluids. The mixtures mass velocities are G = 387 kg m^{-2} s^{-1} for mixture 23/77%, G = 497 kg m^{-2} s^{-1} for mixture 46/54% and G = 662 kg m^{-2} s^{-1} for mixture 75/25%.

A further comparison is made by plotting the predicted heat transfer coefficient using the correlation by Cavallini et al [18], with the correction for mixture when necessary, versus vapor quality for the particular mass velocities of the considered fluids; results are shown in Figure 7.14. It is evident that pure R32 confirms its high performance and reaches the highest heat transfer coefficients, while pure R1234ze(E) shows the lowest ones. The three mixtures show intermediate values, increasing with the R32 mass fraction. The mixture with the mass composition 23/77% is very close to pure R1234ze(E) in terms of heat transfer coefficient for the same value of PF at x = 0.5; on average it is 13% lower that the value of the pure R1234ze(E). Regarding the 46/54% mass composition, the mean heat transfer coefficients increase compare to the values of the pure R1234ze(E) is about 21%; anyway they are 57.8% lower than that of R32. According to this approach, the

condensation heat transfer coefficient for the 75/25% mixture is on average 91.9% higher than that of pure R1234ze(E) and 32.8% lower than that of R32.

It is interesting to notice that in the case of the present mixtures, with this analysis, the heat transfer degradation due to the additional mass transfer resistance is mitigated when accounting for the pressure drop characteristics. For example, if experimental data are compared as reported in Section 7.5, the heat transfer coefficients for the 46/54% mixture are on average lower of 4% than those of pure R1234ze(E); according to this analysis the condensation heat transfer coefficient is found to be 21% higher.
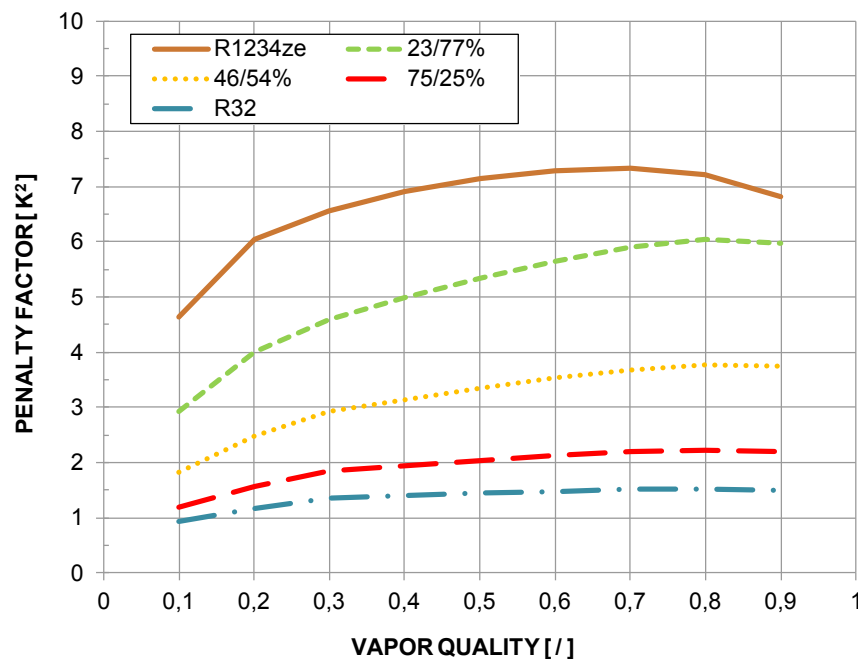
Figure 7.12. Penalty Factor versus vapor quality for each fluid considering at G=400 kg m^{-2} s^{-1}, T_{sat} = 40°C, T_{sat}-T_w=10°C (for the mixture is considered a mean refrigerant temperature of 40°C). PF has been calculated using the Del Col et al. [63] correlation for the two-phase pressure drop gradient and the Cavallini et al. [18] model for the condensation heat transfer coefficient, corrected for mixtures when necessary.
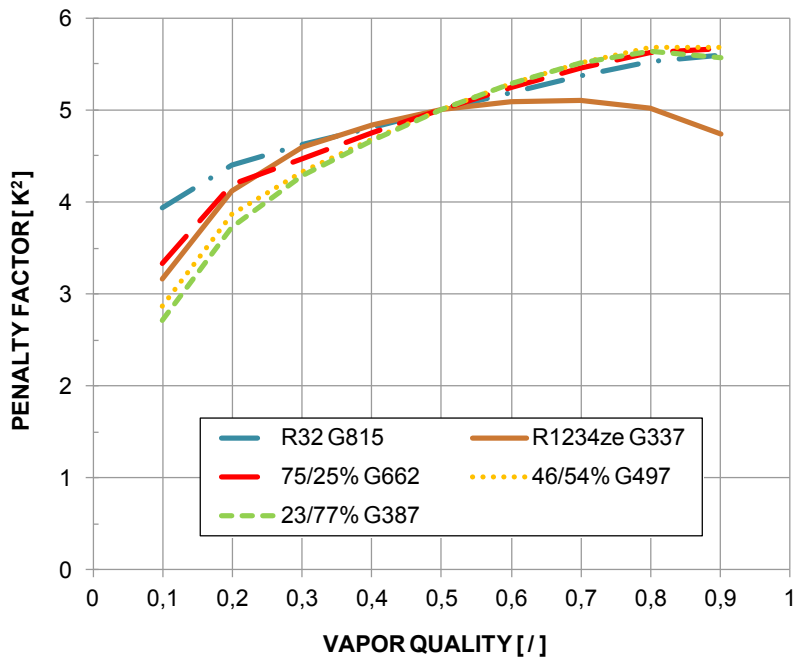
Figure 7.13. Penalty Factor versus vapor quality considering the specific mass velocity for each fluid in order to obtain PF = 5 K² at *x* = 0.5 and *T*_{sat} = 40°C (for the mixture is considered a mean refrigerant temperature of 40°C). PF has been calculated using the Del Col et al. [63] correlation for the two-phase pressure drop gradient and the Cavallini et al. [18] model for the condensation heat transfer coefficient, corrected for mixtures when necessary.
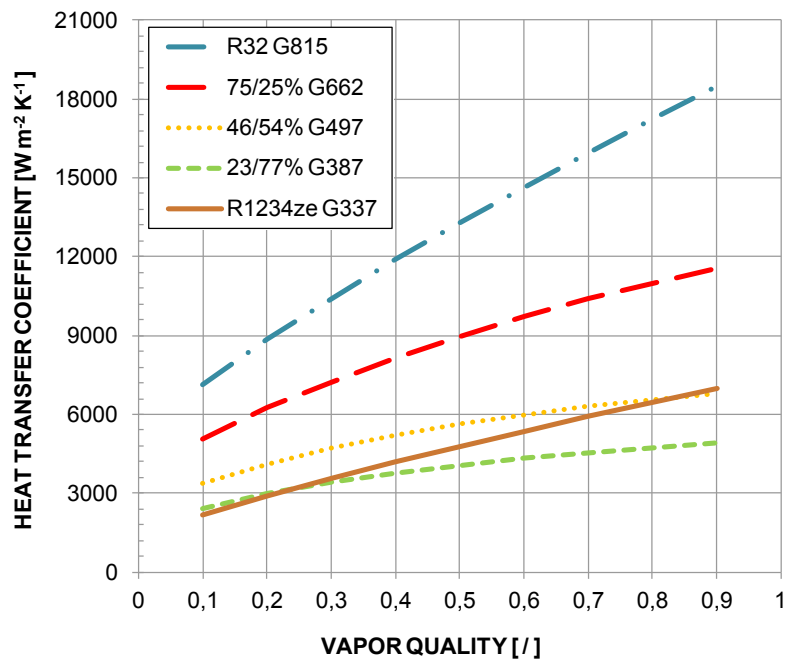
Figure 7.14. Predicted condensation heat transfer coefficient versus vapor quality at a specific mass velocity for each considered fluids giving PF = 5 K² at *x* = 0.5 and *T*_{sat} = 40°C (for the mixture is considered a mean refrigerant temperature of 40°C). The model employed is the one by Cavallini et al. [18] for the condensation heat transfer coefficient, corrected for mixtures when necessary.

7.10 Nomenclature

c	specific heat	[J kg^{-1} K^{-1}]
CF	coverage factor	[-]
COP	coefficient of performance	[-]
d	hydraulic diameter	[m]
f	friction factor	[-]
G	mass velocity	[kg m^{-2} s^{-1}]
h	specific enthalpy	[J kg^{-1}]
L	length	[m]
$\dot{m}$	mass flow rate	[kg s^{-1}]
p	pressure	[Pa]
PF	penalty factor	[K^2]
q	heat flow rate	[W]
q'	heat flux	[W m^{-2}]
Ra	arithmetical mean deviation of the profile according to ISO 4297:1997	[µm]
Re	Reynolds number	[-]
T, t	temperature	[K]
u	uncertainty	
x	thermodynamic vapor quality	[-]
X	mass fraction	[-]
z	position	[m]

Greek symbols

α	heat transfer coefficient	[W m^{-2} K^{-1}]
Δh	enthalpy difference	[J kg^{-1}]
Δp	pressure difference	[Pa]
ΔT	temperature difference	[K]
λ	thermal conductivity	[W m^{-1} K^{-1}]
μ	dynamic viscosity	[µPa s]
ρ	density	[kg m^{-3}]

Subscripts

bub	bubble
c	combined
dr	driving
f	frictional
g	vapor
GL	glide
in	inlet
l	liquid
m	mixture
MS	measuring sector
out	outlet
PS	pre-conditioning sector
ref	refrigerant
s	sensible
sr, sat	saturation
t	total
w	wall

8 FLOW BOILING OF A NON-AZEOTROPIC MIXTURE INSIDE A SINGLE CIRCULAR MINICHANNEL

8.1 Introduction

A brief state of the art regarding flow boiling of R1234ze(E) and mixture of HFC and HFO is hereafter exposed.

8.1.1 Studies of flow boiling of R1234ze(E)

Tibiriçá et al. [76] obtained flow boiling experimental data for the refrigerant R1234ze(E) in two horizontal stainless steel circular channels with diameter of 1.0 and 2.2 mm. The experimental campaign includes mass velocities ranging from 50 to 1500 kg m^{-2} s^{-1}, heat fluxes from 10 to 300 kW m^{-2} and saturation temperature of 25°C, 31°C and 35°C. R1234ze(E) demonstrated similar thermal performance with respect to R134a when running at similar conditions. With regard to the heat transfer, they found that an increase in mass velocity or in vapor quality causes an increase in heat transfer coefficient at constant heat flux. Vakili-Farahani et al. [77] carried out upward flow boiling experiments in a flat aluminum extruded multiport tube, which is composed of 7 parallel rectangular channels (1.1 mm x 2.1 mm) with hydraulic diameter of 1.4 mm. Two refrigerants, R245fa and R1234ze(E) were tested. Once saturated boiling begins, the heat transfer coefficient profile remains either rather flat with vapor quality. Moreover, the heat transfer coefficient increases with increase of saturation temperature, heat flux and mass flux. In air-cooled condensers of domestic air conditioning units and heat pumps, fin-and-tube heat exchanger is the usual geometry (tube diameter ranging between 6 and 10 mm) but the utilization of small channels is expected to increase being the refrigerant charge reduction a central issue in such equipments. Diani et al. [78] studied R1234ze(E) flow boiling inside a 3.4 mm ID microfin tube. The mass velocity was varied between G = 190 kg m^{-2} s^{-1} and G = 940 kg m^{-2} s^{-1}, the vapour quality from 0.2 to 0.99, and three heat fluxes were imposed: 10, 25, and 50 kW m^{-2}. The low-GWP refrigerant shows lower, at least similar, values of heat transfer coefficient measured for R134a, while its frictional pressure gradients are higher than those obtained for the traditional refrigerant. Recently Bortolin and Del Col [79] performed an experimental investigation of heat transfer during flow boiling of R1234ze(E) in a horizontally-assembled square cross section microchannel having an hydraulic diameter of 1.23 mm are presented. The test runs have been performed at around 30°C saturation temperature, correspondent to 5.8 bar, with mass flux ranging between 300 and 500 kg m^{-2} s^{-1}. The experimental heat transfer coefficient is found to be highly dependent on the heat flux; instead mass velocity and vapor quality seem to have a negligible effect on the heat transfer coefficient.

8.1.2 Studies of HFO/HFC mixtures

As previously asserted, the currently available HFOs cannot replace all the high GWP hydrofluorocarbons employed in cooling, heat pump and refrigeration systems. A solution can be found in refrigerants blend, for example by mixing HFOs and HFCs in order to mitigate the GWP of the last ones. For example, Koyama et al. [70] attempted to blend R1234ze(E) with another refrigerant, R32, to investigate this mixture as a possible low GWP substitute in vapor compression heat pump and refrigeration systems. As the result of their drop-in tests with R32/R1234ze(E) 0.5/0.5 by mass, they found that, for the tested binary mixture, the COP is slightly affected by the degree of subcooling at the condenser outlet and it is only about 7.5% lower than that of R410A at the same heating load. They conclude that the mixtures of R32/R1234ze(E) can be considered to be applicable as low-GWP alternatives for R410A by adjusting the composition of the mixture and by reconsidering some design parameters of components of air-conditioning system. Wang and Amrane [80] presented the results of the Low Global Warming Potential Alternative Refrigerants Evaluation Program (Low-GWP AREP) performed by the Air-Conditioning, Heating, and Refrigeration Institute (AHRI). The intent of the program is to help industry select promising low-GWP alternative refrigerants for major air conditioning and refrigeration products. Thirty-eight refrigerant candidates were tested by twenty one international manufacturers and laboratories and, among the tested refrigerant, a considerable part consists of HFOs/HFCs mixtures. Results were obtained from drop-in and soft-optimized tests performed on equipment designed for the baseline refrigerants and not for the low-GWP alternatives. They showed that here are several alternative candidates with comparable performance than the baseline refrigerants they intend to replace. However, it appears unlikely that a single refrigerant will replace R-22, R-134a, R-404A, and R-410A. More probably, mixtures can be used instead of pure fluids, because the required overall properties could be obtained more easily by mixing two or more components. One of the characteristics of non-azeotropic mixtures is the variable temperature during phase change at constant pressure. This phenomenon can be utilized to reduce the thermodynamic irreversibility in counter-current heat exchangers resulting in an increase in heat exchanger efficiency. In addition, mixtures offer numerous other advantages such as capacity control and lower pressure ratios across the compressor. In spite of these advantages, however, the use of refrigerant zeotropic mixtures has not yet been popular due in part to the inconveniences in handling the mixture and running the systems (variable saturation temperature, change in composition due to leakages, ...) but also due to the lack of such information as heat transfer coefficients. An efficient use of the zeotropic mixtures requires a proper design of the heat exchangers and experimental data in different conditions are needed to compare performance with those of the pure fluids and to assess the possible design correlations. With zeotropic mixtures, boiling heat transfer is more complicated. The flow boiling of mixtures has been studied for a long time [81-83], but regarding the vaporization of HFOs/HFCs very few studies are available in the literature, especially in mini/microchannels.

Kondou et al. [62] performed flow boiling tests in a horizontal microfin tube of 5.21 mm inner diameter with a R32/R1234ze(E) mixture at two mass compositions, 0.2/0.8 and 0.5/0.5. The heat transfer coefficient and pressure drop are measured at a saturation temperature of 10°C, heat fluxes of 10 and 15 kW m^{-2}, and mass velocities from 150 to 400 kg m^{-2} s^{-1}. When comparing the HTCs of the two mixtures, they found that in the vapor quality range from 0 to 0.4 the heat transfer coefficient is higher for the 0.5/0.5 mixture while for the quality above 0.4 the heat transfer coefficient for the 0.5/0.5 mixture is slightly lower than that of the 0.2/0.8. They also tested both the pure components in the same test section; the mixture heat transfer coefficient is always lower than that of the pure fluids due to the mass transfer resistance. Hossain et al. [84] measured the heat transfer coefficient of the mixture at 45/55% mass composition (R32/R1234ze(E)) inside a 4.35 mm smooth copper tube. The arithmetic mean roughness is 0.666 μm, the total length of the test section is 6.59 m with an effective heat transfer length of 3.6 m. From the study emerged that the measured heat transfer coefficient was lower than that of R32 and R410A for the whole quality range and higher than that of pure R1234ze(E) only in the low vapor quality region.

So far the R32/R1234ze(E) mixture has not been studied in microchannels. Furthermore, very limited data are available in the literature regarding flow boiling of zeotropic mixtures in microchannels. Differently from single-phase flow heat transfer, the current knowledge of flow boiling heat transfer in macroscale cannot be extended without modifications to microscale, where bubble confinement plays a more relevant role with the decreasing of the channel size. In two-phase microchannel flow, capillary (surface tension) forces become predominant over gravity force, thus impeding stratification of liquid. As reported by Thome et al. [85], bubble flow, slug flow, annular flow and mist flow are the primary flow regimes observed in microchannels. For evaporating flow, the zone with bubbles smaller than channel diameter is very short as bubbles grow to the channel size very quickly. In spite of the large number of papers published in the flow boiling area, many aspects still need to be better explained in order to provide a full understanding of local two-phase flow boiling characteristics in microchannels and to develop more reliable prediction methods for the design of new microchannel evaporators. Some recent studies have put some light on the main heat transfer mechanism. However, additional innovative studies are necessary to investigate local phenomena (Tibiriçá and Ribatski [86]).

The first work dealing with mixtures flow boiling inside microchannels is the one by Peng et al. [87]. They investigated the flow boiling of subcooled binary mixtures of methanol and water flowing through 12 kinds of multiport microchannels with hydraulic diameters ranging between 0.133 and 0.343 mm. The measured heat transfer are presented and compared to identify the flow boiling characteristics and the effect of parameters such as liquid flow velocity, concentration, heat flux, wall superheat, and microchannel geometric configuration. Lin et al. [88] experimentally studied the flow boiling of methanol-water mixtures in a diverging microchannel. The test section was a silicon strip prepared by microfabrication via silicon dry etching, laser direct writing for micromachining of through holes and artificial cavities, and anodic bonding with Pyrex for flow visualization. The

microchannel has a 150 μm hydraulic diameter, a divergence angle and 24 laser-drilled cavities distributed along the bottom wall. The concentration was varied over the full range of molar fraction. Flow visualizations of bubble nucleation and two-phase flow patterns were performed. Few data on the heat transfer coefficient were reported. More recently the same research group, [89] performed visualization of flow boiling of methanol–water and ethanol–water mixtures in the same microchannel. Four boiling regimes were observed and identified: bubbly-elongated slug flow, annular flow, liquid film breakup, and dryout. Liquid film breakup persisted up to the highest heat flux at molar fractions of 0.3 and 0.1 for the methanol–water and ethanol– water mixtures, respectively. This is because the Marangoni effect was most significant at these particular molar fractions. Recently, Li et al. [90] investigated the heat transfer performance during vaporization of the mixture R1234yf/R32 at two mass compositions, 80/20% and 50/50%. The test section was a horizontal stainless steel tube with an inner diameter of 2 mm and using electrical heating as source for the required vaporization power. In their tests the mass flux ranged from 100 to 400 kg m^{-2} s^{-1} and the heat flux from 6 to 24 kW m^{-2}. They found that the heat transfer coefficient for the 80/20% mixture was lower than that of pure R1234yf and higher for the 50% mass fraction at large heat and mass fluxes; the R32 outperformed the mixture data in all the tested conditions.

8.2   Experimental apparatus and mixture composition

The test facility and the heat transfer test section are the same used for the condensation tests and described in Section 2.2 and 2.2.1. During flow boiling tests the fluid is slightly heated up in the pre-conditioning sector to reach the desired subcooling and then it enters the measuring sector (described in details in Section 3.2) in which it is vaporized.

The composition of the R32/R1234ze(E) mixture tested in the present study is 0.505/0.495 and it has been measured using a gas-chromatograph with an experimental uncertainty of ±0.001 by mass. The mixture thermodynamic properties as described in Section 7.3 have been evaluated using REFPROP 9.1 (Lemmon et al., [20]) with the model suggested by Akasaka [67].

8.3   Test procedure and data reduction

The measured temperature taken during blow boiling tests of R32/R1234ze(E) at G = 400 kg m^{-2} s^{-1} are shown in Figure 7.10. On the left side of Figure 7.10, the refrigerant enters the test channel with 3.6 K subcooling at 14 bar pressure, which corresponds to 26.2°C bubble temperature. At the exit, the refrigerant temperature is increased by 5.2 K because evaporation of a two components mixture is a non-isothermal process and the refrigerant temperature evolves from bubble to dew temperature. The water flows in counter flow entering at 38.5°C and its temperature decreases because the heat is rejected to the boiling refrigerant. As it can be seen, the refrigerant and the water temperature profiles are well
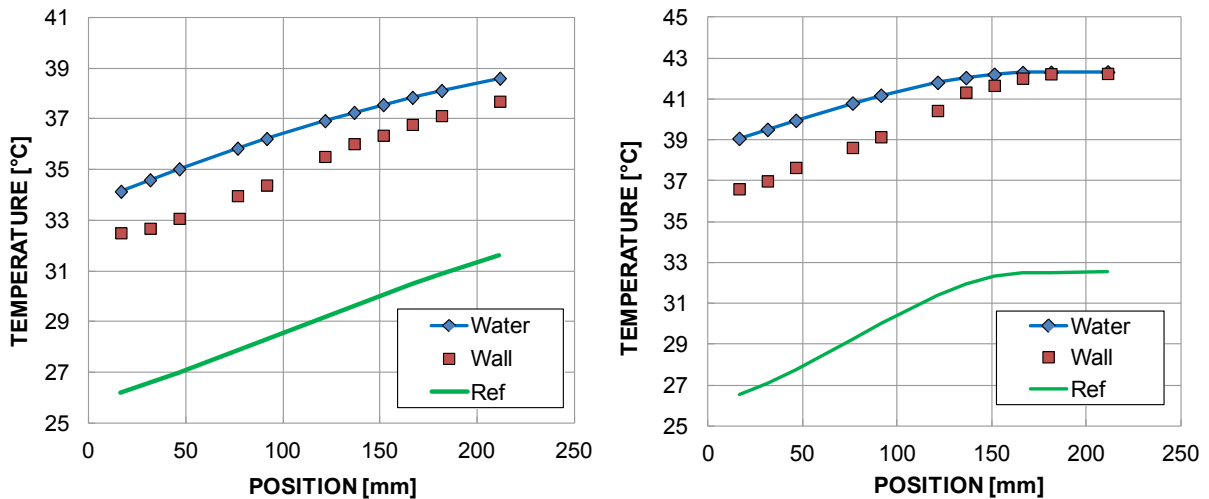
Figure 8.1. Temperature profiles of water, wall and refrigerant along the axial coordinate during flow boiling of R32/R1234ze(E) at 50/50% by mass composition and mass velocity of 400 kg m⁻² s⁻¹. Left: temperature profiles before the onset of dryout; Right: temperature profiles with part of the measuring sector in dryout condition

coupled (the water-to-refrigerant temperature difference is pretty constant, 7.6 K) leading to a reduction of the exergy losses associated with the heat transfer process. On the right side of Figure 7.10 the water and wall temperature profiles increase linearly up to the position of 130 mm, hence the water temperature profile becomes flat and the wall to water temperature difference approaches zero. This behaviour is due to the onset of dryout which is responsible for reducing abruptly the heat transfer coefficient inside the channel. A more detailed description of the dryout phenomena with pure fluids in microchannels can be found in Del Col and Bortolin [91]. It is worth noting that only the data points characterized by vaporization in the channel length prior to onset of dryout are considered in the present work.

The heat flux is obtained from the slope of the secondary fluid temperature profile:

$$q' = \dot{m}_{water} \cdot c_{water} \cdot \frac{1}{\pi d}\frac{\mathrm{d}T_{water}}{\mathrm{d}z} \qquad\qquad \textbf{8.1}$$

where z is the axial coordinate along the tube and $\mathrm{d}T_{water}/\mathrm{d}z$ is the derivative of the measured water temperature along z. In the calculation, a polynomial function is used to interpolate the water temperature along the channel. Two different independent procedures have been adopted for the determination of the fitting polynomial degree of the water temperature and thus for the calculation of the heat flux. According to the first criterion (named as physical), the deviation between the water temperatures calculated by the polynomial interpolation and the experimental values should be below always ± 0.06 K. The second criterion consists of a statistical method based on the choice of the simplest fitting polynomial. This statistic approach uses the R square (R^2) statistic parameter and adjusted R square (R^2_{adj}) to assess the goodness of the fitting method. The coefficient R^2_{adj}, unlike R^2, increases with the number of parameters of the fitting equation only if the new

term improves significantly the fitting correlation. If two polynomial functions are considered, increasing the degree from y_1 to y_2, the function with the lower polynomial degree will be chosen if:

$$\left| R^2_{adj}(y_1) - R^2_{adj}(y_2) \right| < 0.0035 \qquad \textbf{8.2}$$

The two criteria are applied for each test run and in most cases they give the same interpolation polynomial equation. If not, the test run is disregarded when the results from the two methods are in disagreement by more than 10%.

Once the heat flux is determined, the local heat transfer coefficient inside the microchannel is obtained as the ratio of heat flux to temperature difference:

$$\alpha(z) = \frac{q(z)'}{\left(T_{wall}(z) - T_{ref}(z) \right)} \qquad \textbf{8.3}$$

where the wall temperature is directly measured by the thermocouples embedded in the wall and the local refrigerant temperature along the channel, assuming thermodynamic equilibrium, is calculated from the pressure, enthalpy and mixture composition using REFPROP 9.1 (Lemmon et al. [20]):

$$T_{ref}(z) = f\left(p(z), h(z), X_{R1234ze(E)} \right) \qquad \textbf{8.4}$$

The refrigerant pressure is measured at the inlet and outlet of the measuring sector and a non-linear pressure profile along the channel is calculated from a model by matching the measured values at inlet and outlet of the test section. As reported in Section 6.4.3, the Del Col et al. [92] model can be successfully applied to predict frictional pressure drop during two-phase flow of mixtures in microchannels. Furthermore, the equation by Churchill [16] is used to calculate the pressure drop of the subcooled liquid at the inlet of the microchannel under laminar or turbulent flow condition; the formulae reported in Idelchik [25] are used for the pressure drop across the inlet expansion; the Rouhani and Axelsson [93] model for the void fraction is used to compute the pressure variation due to momentum in the boiling region and the Paliwoda [24] equation for the pressure drop across the outlet contraction under two-phase flow conditions. The refrigerant enthalpy at a given position z along the channel of the i-th wall thermocouple is obtained from the thermal balance between the water and the refrigerant mixture that flows in counter-flow as reported in Eq. 8.5; the enthalpy of the subcooled refrigerant is determined from the measured inlet pressure and temperature.

$$h(z) = h_{sub} + \frac{\dot{m}_{water}}{\dot{m}_{ref}} c_{water} \left(T_{water}(z) - T_{water,out} \right) \qquad \textbf{8.5}$$

Once the pressure profile and the enthalpy along the channel are known, the local refrigerant temperature can be determined using Eq. 8.4. Similarly to the refrigerant temperature, the vapor quality along the test section is evaluated using Eq. 8.6.

$$x(z) = f\left(p(z), h(z), X_{R1234ze(E)} \right) \qquad \textbf{8.6}$$

The uncertainty analysis has been carried in the same way as for condensation tests (Section 11). The expanded uncertainty depicted in the following graphs is obtained considering a coverage factor CF=2 and thus a level of confidence of approximately 95%. The mean experimental uncertainty of the heat transfer coefficient is about 9% and for the mean value for the vapor quality is ±0.02.

8.4   Experimental data: results and discussion

In the test section the heat flux is not imposed, the heat is transferred to the refrigerant mixture using water as a secondary fluid and thus during flow boiling tests only the mass flow rates and the inlet temperatures of the two fluids can be set. The local heat flux is the result of such boundary conditions and it varies along the channel. This configuration is interesting because the conditions are close to those encountered in water-to-refrigerant evaporators but, since the heat flux cannot be directly controlled, this complicates the comparison of the present data to the ones obtained with electrical heating and it requires a further processing of the data [27]. Several tests were made by varying the inlet conditions of the secondary fluid and keeping constant mass flow rate and temperature of the mixture in order to explore the effects of the heat flux and vapor quality on the heat transfer coefficient. Flow boiling tests have been performed with mass velocity ranging between 300 and 600 kg m^{-2} s^{-1} at about 14 bar working pressure. More than 300 experimental data have been collected and the complete tests conditions are reported in Table 8.1. The experimental data maps are plotted in Figure 8.2. The graph on the left shows the mean operating conditions of the test runs: heat flux, mass flux and vapor quality. The graph on the right shows the effect of these operating parameters on the heat transfer coefficient. As a mean trend, the heat transfer coefficient increases with heat flux but the large scatter at given heat flux suggest that mass flux and vapor quality also affect the heat transfer coefficient. In order to investigate the effect of heat flux, vapor quality and mass velocity on the heat transfer coefficient a further data processing is then required.

Table 8.1. Experimental test conditions during flow boiling of the R32/R1234ze(E) at 50/50% by mass composition

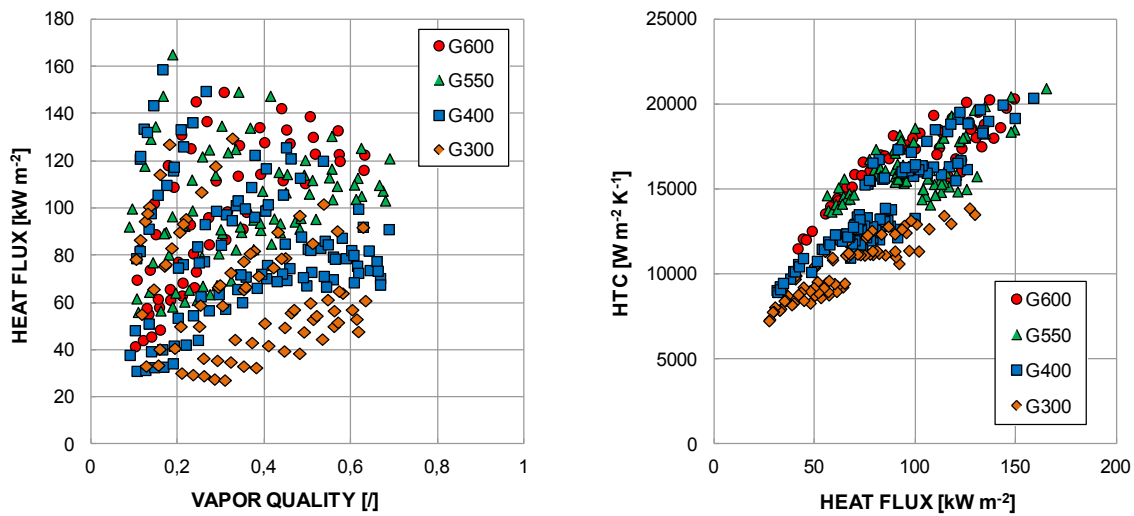| Mass flux [kg m^{-2} s^{-1}]	Heat flux [kW m^{-2}]	Vapor quality [/]	Pressure [bar]
300 ± 1 %	27 - 129	0.1 - 0.65	13.8 - 14
400 ± 1 %	31 - 159	0.1 - 0.7	13.8 - 14
550 ± 1 %	56 - 165	0.1 - 0.7	13.6 - 14
600 ± 0.5 %	41 - 149	0.1 - 0.63	13.5 - 13.9

Figure 8.2. Experimental flow pattern maps of the data collected during flow boiling of the mixture R32/R1234ze(E) at the mass composition of 50/50%: on the left the measured local heat flux is reported versus the vapor quality; on the right the heat transfer coefficient is reported versus the heat flux.

8.4.1 Effect of heat flux, mass flux and quality

The effect of heat flux on the heat transfer coefficient can be better understood by filtering the data in Figure 8.2 (Right) at constant mass velocity and vapor quality, as depicted in Figure 8.3 for x = 0.2 and 0.3. At constant quality, the heat transfer coefficient increases with heat flux; this is consistent with other authors' findings for pure fluids in microchannel saturated flow boiling [94-96]. However, in the case of the present mixture, a peculiar behavior was observed: because the slope of the heat transfer coefficient versus heat flux varies and the heat transfer coefficients seems to be less dependent on the heat flux. This is clearer in Figure 8.4 where the data points of the mixture are compared with those of pure components and R134a taken in the same test section and in similar conditions. In Figure 8.4 it can be seen the dependence of the heat transfer coefficient on the heat flux for the three fluids and the mixture varying the mass velocity. In Figure 8.5 the heat transfer coefficient of the pure R1234ze(E) and R134a are compared with the present mixture at G = 400 kg m^{-2} s^{-1}. It can be seen that for the pure fluids the heat transfer coefficients are proportional to the heat flux with a power law close to 0.67 (coefficient of determination obtained with a linear regression of about 0.98). The mixture heat transfer coefficients display a different behaviour, especially at the highest values of heat flux, with a much lower value of the exponent, close to 0.53. In the end for the mixture the heat transfer coefficient rises with the heat flux but to a lower extent.

The mass velocity seems also to have an effect on the heat transfer coefficient: at fixed vapor quality and heat flux, the higher the mass velocity the higher the heat transfer coefficient. Such behaviour is confirmed in Figure 8.6 where heat transfer coefficients are plotted against vapor quality at varying mass velocity and two different values of heat flux.

By processing data at constant heat flux, it is possible to get information on the influence of vapor quality. From Figure 8.6 it is evident that the heat transfer coefficient decreases with vapor quality for all the tested conditions. Finally, in Figure 8.7, the heat transfer coefficient is reported against vapor quality at a constant mass velocity.

Hence, the experimental results can be summarized as follows:

- the heat flux has an important effect on the heat transfer coefficient but the power law does not follow the exponent of the pure fluids;

- the heat transfer coefficient is found to decrease with vapor quality;

- an increase in mass velocity leads to an enhancement of the heat transfer coefficient, especially at the lowest G.
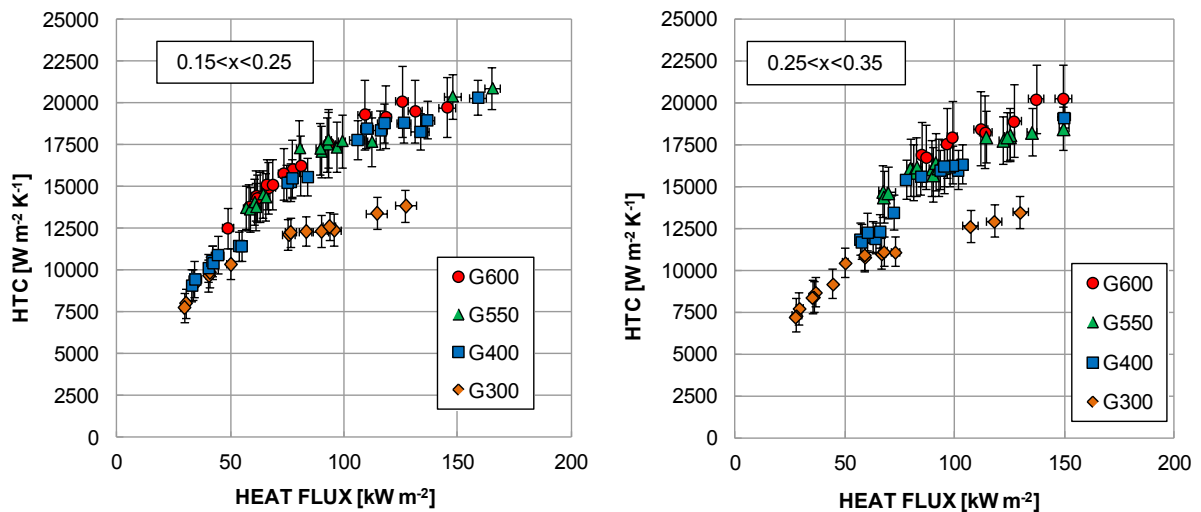
Figure 8.3. Experimental local heat transfer coefficient for the R32/R1234ze(E) mixture at 50/50% by mass composition versus heat flux for different mass velocities at two vapor qualities: x=0.2±0.05 (left) and x=0.3±0.05 (right)

Figure 8.4. Experimental local heat transfer coefficient versus heat flux for the mixture R32/R1234ze(E) at 50/50% mass composition, the pure components and for pure R134a during flow boiling in the circular minichannel with 0.96 mm inside diameter at x=0.2

Figure 8.5. Experimental local heat transfer coefficient versus heat flux for the mixture R32/R1234ze(E) at 50/50% mass composition, pure R1234ze(E) and R134a during flow boiling in the circular minichannel with 0.96 mm inside diameter for *G*=400 kg m⁻² s⁻¹ and x=0.2

Figure 8.6. Experimental local heat transfer coefficient versus vapor quality for the mixture R32/R1234ze(E) at 50/50% mass composition: left, heat flux of about 65 kW m⁻²; right, heat flux of about 125 kW m⁻²
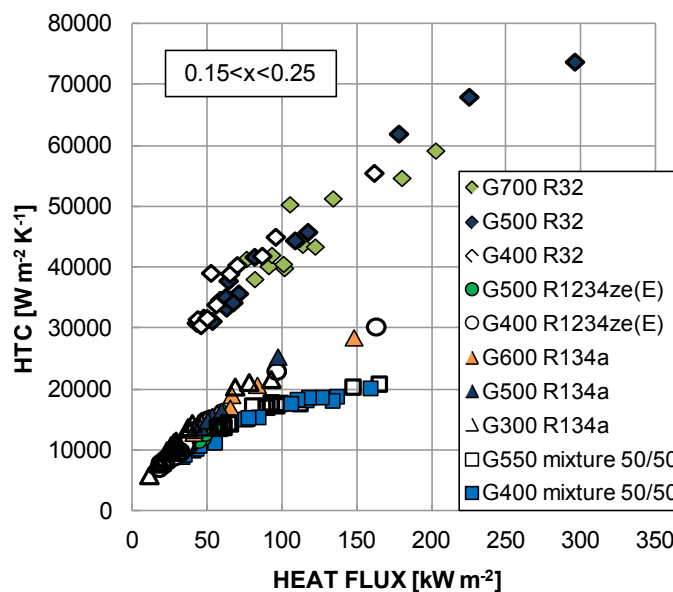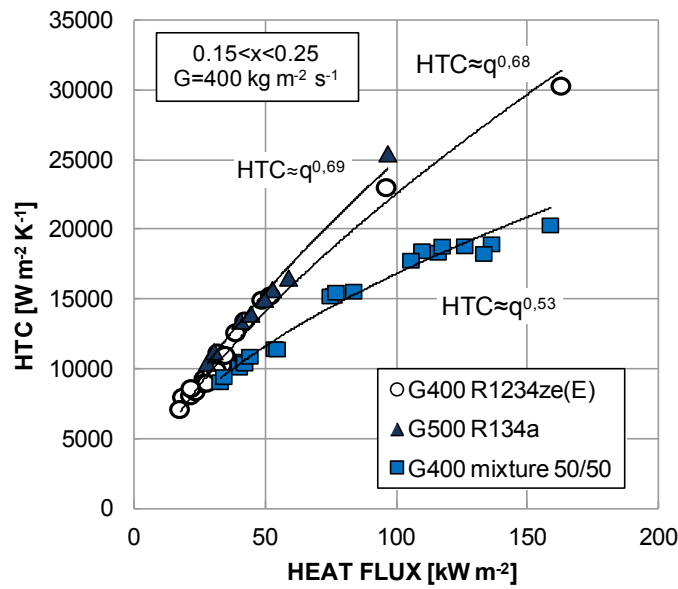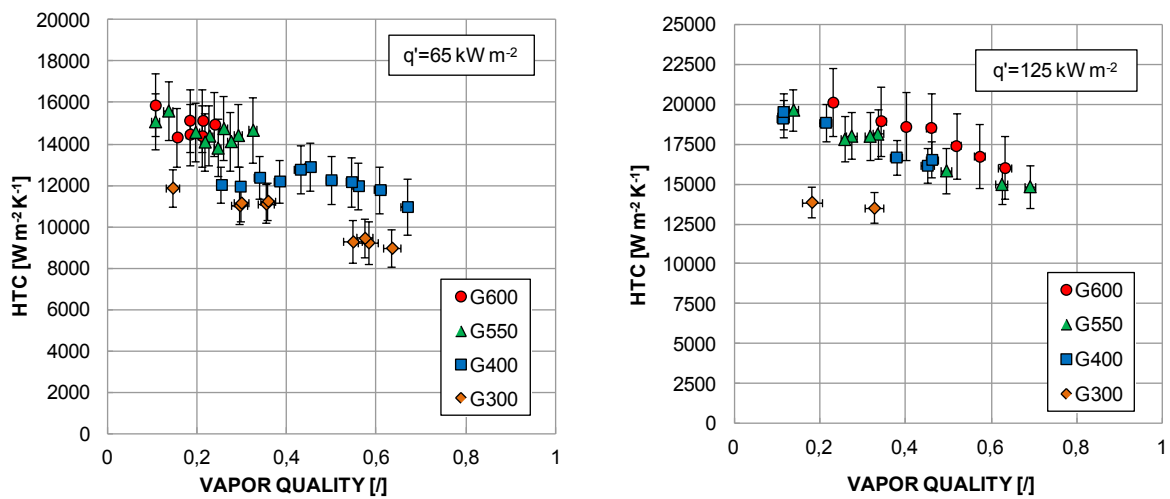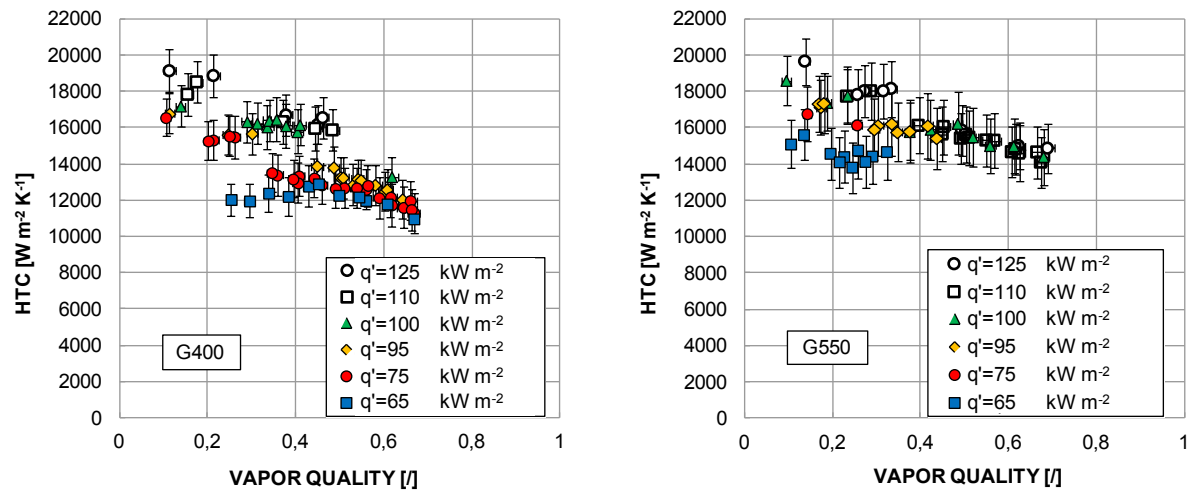
Figure 8.7. Experimental local heat transfer coefficient versus vapor quality for the mixture R32/R1234ze(E) at 50/50% mass composition: left, mass velocity of 400 kg m^{-2} s^{-1}; right, mass velocity of 550 kg m^{-2} s^{-1}

8.4.2 Discussion of results and comparison with pure fluids

In some previous studies, Del Col and coworkers [27, 97] performed flow boiling tests inside the same 0.96 mm inner diameter circular channel with pure R1234ze(E) and R32. They found that the heat transfer coefficient always increases with heat flux, it is independent on mass velocity and it decreases when increasing vapor quality. Comparing the results obtained with the mixture and the two pure fluids, some similarities can be found. First of all, in both cases the heat transfer coefficient decreases with vapor quality. This decrease is found in other experimental studies inside microchannels with pure fluids and it is also in agreement with the behaviour predicted by model such as the one of Dupont et al. [98]. Instead the effect of heat flux and mass velocity in the case of mixtures deserve further discussion.

From the most recent studies available in the literature, it can be inferred that during saturated flow boiling in microchannels there are three main regions, each characterized by different heat transfer mechanisms: the initial part of the channel (low vapor quality) where bubbles nucleate and grow rapidly filling all the channel; the zone characterized by elongated bubbles with evaporation occurring at the thin liquid film surrounding the bubble; an annular zone before the dryout region. In a recent work, Tibiriçá and Ribatski [99] observed bubble active sites for all flow patterns, also in the slug flow regime. They found that, increasing the heat flux level over the tube surface, the number of nucleation sites increases and for high heat flux multiple nucleation sites become active. With pure fluids, as reported in Del Col et al. [27], there is a clear heat transfer coefficient increase with the heat flux. Such behaviour can be explained considering the presence of active nucleation sites in the microchannel. However, as reported in Dupont et al. [98], the heat flux effect can be explained and predicted by the thin-film evaporation process occurring around elongated bubbles in the slug flow regime, without any nucleation sites in the

elongated bubble region. Their model shows that the heat flux dependency comes mainly through its effect on the bubble frequency and the thin film evaporation process. Starting from that background, an attempt to give a physical explanation of the results obtained with the zeotropic mixture is here provided.

In the case of the present mixture, when a bubble grows at the heated wall, the vapor fraction of the more volatile component (R32) is higher than in the surrounding bulk liquid. When evaporation proceeds, more R32 in the liquid must evaporate to provide the additional fraction of the volatile component in the bubble. This process causes a reduction of R32 composition in the liquid surrounding the bubble, leading to a concentration gradient that drives the mass diffusion of R32 to the bubble interface. A similar phenomenon is also expected with an evaporating liquid film.

The heat flux is an important parameter when studying microchannel flow boiling both for pure fluids and mixtures. But in case of the mixture, the reduced heat flux dependence observed when increasing the q' can be due to the mass diffusion resistance. In fact, when the heat flux is increased, the frequency of the bubble at the inlet of the channel is expected to increase (according to Tibiriçá and Ribatski [99] more nucleation sites may also become active in the channel) and this explains the rise of the heat transfer coefficient with the heat flux. At high heat flux, the mass diffusion is not longer capable of sustaining the bubbles grow and the heat transfer coefficient increases less with heat flux. Regarding the effect of mass velocity, when the mass velocity is increased, the velocity gradient and the turbulence inside the liquid are higher and thus the mass diffusion resistance is reduced leading to higher heat transfer coefficients.

8.4.3 Degradation of the heat transfer coefficient

As reported in Figure 8.8, the present refrigerant mixture displays lower heat transfer coefficients as compared to the pure components R1234ze(E) and R32. The heat transfer degradation from a linear law between the values pertaining to the pure fluids is about 50% for all the three operating conditions reported on the graph. This degradation is partially caused by the bubble point temperature increase at the liquid-vapor interface due to the mole fraction gradient at the interface, created by the volatility difference of the two pure components. During the evaporation process the liquid becomes richer in R1234ze(E) (less volatile component) and the vapor becomes richer in R32 (more volatile component). Part of the heat transfer coefficient reduction is caused by the diffusion of the more volatile component to the interface and the concentration of the least volatile component at the heated surface is not favorable to the vaporization process. Beside this, some additional heat flow rate is needed to heat the liquid and the vapor to the boiling temperature, constantly increasing along the tube.
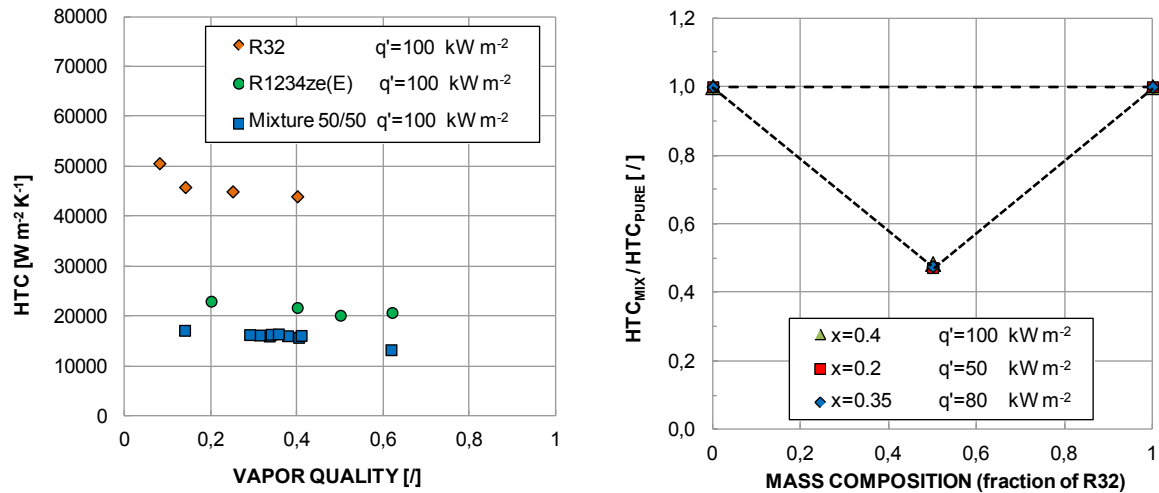
Figure 8.8. Degradation of the local heat transfer coefficients for the mixture R32/R1234ze(E) due to the additional mass transfer resistance at G = 400 kg m^{-2} s^{-1}. Left, local heat transfer coefficient versus vapor quality for the pure components and the mixture at G = 400 kg m^{-2} s^{-1} and q' = 100 ± 5 kW m^{-2}; Right, ratio of mixture heat transfer coefficient to the one considering a linear trend between the values pertaining to the pure fluids at G = 400 kg m^{-2} s^{-1} .

8.5   Prediction of the flow boiling heat transfer coefficient

The experimental data acquired and presented previously have been compared with five correlations available in the scientific literature that use different approaches to predict flow boiling heat transfer coefficients. Some correlations express the heat transfer coefficient as a function of liquid Reynolds number and boiling number; other models calculate the heat transfer coefficient from a convective term and a nucleate boiling term. Hereinafter each model is presented with its equations and its range of applicability. As a first step, the models developed for pure fluids are applied to the present experimental database without any correction for mixtures. The following comparison provides some assessment of the predicting accuracy of the models for application in microchannel heat exchangers when the working fluid is a refrigerants mixture and it provides some clue on the importance of the mass transfer resistance in the process.

The first correlation here considered is the one proposed by Lazarek and Black [100]. This was specifically developed for small diameter channels. The authors developed their heat transfer correlation starting from a study of saturated boiling of R113 in a smooth stainless steel round tube with an inner diameter of 3.15 mm. They observed that the saturated boiling heat transfer was strongly dependent on the heat flux, while vapor quality had a negligible effect. In the Lazarek and Black correlation (Eq. 8.7) no dependence of the heat transfer coefficient on the local vapor quality is reported: the heat transfer coefficient is a function only of the liquid Reynolds number and of the boiling number.

$$\alpha = 30 \cdot \mathrm{Re}_{lo}^{0.857} \cdot \mathrm{Bo}^{0.714} \cdot \frac{\lambda_l}{D}$$

8.7

The comparison of the experimental data against the predicted values by Lazarek and Black [100] is shown in Figure 8.9 (left). The model overestimates the experimental heat transfer coefficient with e_R =+44% and σ_N = 17%.

Recently, Sun and Mishima [101], in agreement with Lazarek and Black [100] observations, assumed that the nucleate boiling was the dominant mechanism, and perceived that the heat transfer coefficient was dependent on the Weber number. So the Lazarek and Black [100] correlation was modified by Sun and Mishima [101] introducing the Weber number for liquid phase (Eq. 8.8). The authors, to derive and test their correlation, considered a wide heat transfer coefficient database: more than 2500 data with 11 fluids in channels with diameter ranging from 0.21 mm to 6.5 mm. In their database six halogenated pure fluids, three halogenated mixtures (R404A, R407C and R410A), carbon dioxide and water were included; the mass flux ranged between 44 and 1500 kg m^{-2} s^{-1} and the heat flux between 5 to 109 kW m^{-2}.

$$\alpha = \frac{6\,Re_{lo}^{1.05}\,Bo^{0.54}}{We_{lo}^{0.191}\left(\dfrac{\rho_l}{\rho_g}\right)^{0.142}}\frac{\lambda_l}{D} \qquad\qquad \textbf{8.8}$$

As reported in Figure 8.9 (right), the Sun and Mishima [101] correlation overpredicts the present mixture experimental data giving an average deviation e_R = +64% and a standard deviation σ_N = 15%.

It is also worth noting that, although the heat flux is the most important term, none of the two previous correlations accounts for the effect of microchannel internal surface roughness.
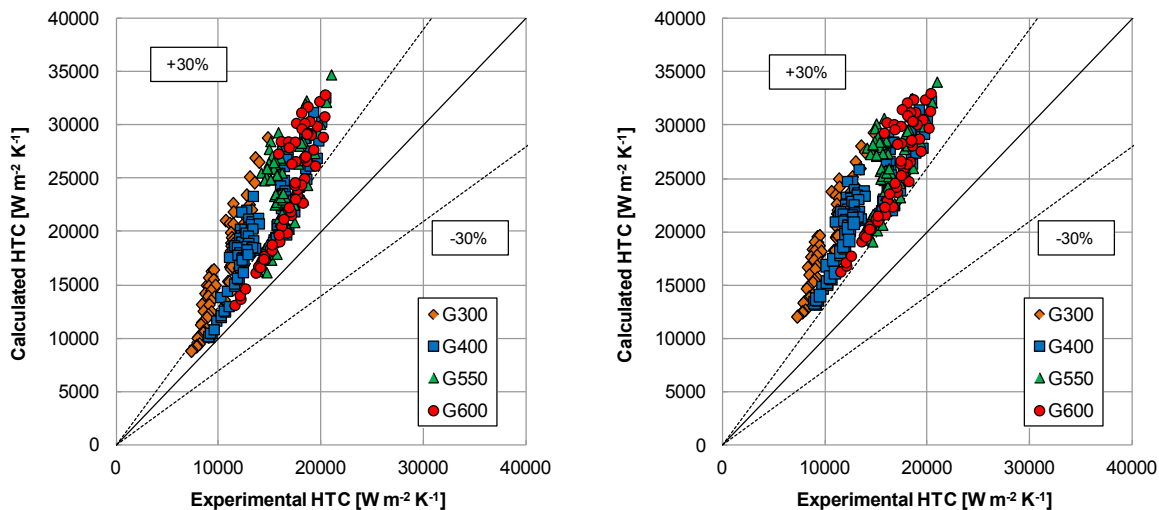

Figure 8.9. Experimental local heat transfer coefficient of the R32/R1234ze(E) at 50/50% mass composition compared with the model of Lazarek and Black [100] (left) and Sun and Mishima [101] (right).

Gungor and Winterton [102] developed a general correlation for forced convection boiling using a database with over 4300 data points, covering water, refrigerants and ethylene glycol, mostly for saturated boiling in vertical and horizontal tubes with diameters ranging from 2.95 to 32 mm. The correlation proposed is in the form of the Chen [103] equation. The α_l given by the Dittus-Boelter equation for liquid only flowing in the duct (Eq. 8.10) is increased by an enhancement factor E (Eq. 8.11). The pool boiling term α_{nb} calculated with the Cooper [104] correlation, Eq. 8.12, is multiplied by a suppression factor S, as reported in Eq. 8.13.

$$\alpha = \alpha_{nb}S + \alpha_l E \qquad \qquad \textbf{8.9}$$

$$\alpha_l = 0.023\,\mathrm{Re}_l^{0.8}\,\mathrm{Pr}_l^{0.4}\,\frac{\lambda_l}{D} \qquad \qquad \textbf{8.10}$$

$$E = 1 + 24000\,\mathrm{Bo}^{1.16} + 1.37\left(1 - X_{tt}\right)^{0.86} \qquad \qquad \textbf{8.11}$$

$$\alpha_{nb} = C\left(\frac{p}{p_{crit}}\right)^{0.12 - 0.2\log R_p}\left(-\log\frac{p}{p_{crit}}\right)^{-0.55} M^{-0.5}q^{0.67} \qquad \qquad \textbf{8.12}$$

$$S = \frac{1}{1 + 1.15\cdot 10^{-6}\,E^2\,\mathrm{Re}_l^{1.17}} \qquad \qquad \textbf{8.13}$$

If the Froude number is lower than 0.05 and the tube is in horizontal position then E should be $E = Fr^{(0.1 - 2\cdot Fr)}$ and S should be $S = \sqrt{Fr}$. The model by Gungor and Winterton [102] strongly overpredicts all the experimental data as shown in Figure 8.10 (left): the average deviation e_R is +139%.

Another Chen type correlation (Eq. 8.14) is the one developed by Bertsch et al. [105]. It is derived from a wide database covering saturated flow boiling studies on 12 fluids, hydraulic diameter from 0.16 mm to 2.92 mm with corresponding confinement numbers of 0.3 to 4, mass flux from 20 to 3000 kg m^{-2} s^{-1}, heat flux from 4 kW m^{-2} to 1150 kW m^{-2}. Data covers vertical and horizontal flow, single and multiple parallel channel arrangements. In their correlation the pool boiling term (Eq. 8.15) is calculated with the Cooper [104] correlation multiplied by the suppression factor S to account for partial dryout as the vapor quality increases. The factor S in Eq. 8.16, suggests a linear decrease of the nucleate boiling heat transfer coefficient with increasing vapor quality. The convective heat transfer coefficient (Eq. 8.17) is calculated as the sum of the convective heat transfer coefficient pertaining to pure liquid (Eq. 8.18) and pure vapor (Eq. 8.19) with a linear dependence on the vapor quality. The enhancement factor F, in Eq. 8.20, is a function of the confinement number Co and of the vapor quality; it reduces to 1 for pure liquid and pure vapor and it is greater than 1 within the two-phase region. The present heat transfer coefficients are overestimated by the Bertsch et al. [105] model, as illustrated in Figure 8.10 (right), with e_R = +47% and σ_N = 19%.

$$\alpha = \alpha_{nb} S + \alpha_{cb} F \qquad \textbf{8.14}$$

$$\alpha_{nb} = C \left(\frac{p}{p_{crit}} \right)^{0.12 - 0.2 \log R_p} \left(-\log \frac{p}{p_{crit}} \right)^{-0.55} M^{-0.5} q^{0.67} \qquad \textbf{8.15}$$

$$S = 1 - x \qquad \textbf{8.16}$$

$$\alpha_{cb} = \alpha_{cb,l} (1 - x) + \alpha_{cb,g} x \qquad \textbf{8.17}$$

$$\alpha_{cb,l} = \left(3.66 + \frac{0.668 \dfrac{D}{L} \mathrm{Re}_l \, \mathrm{Pr}_l}{1 + 0.04 \left(\dfrac{D_h}{L} \mathrm{Re}_l \, \mathrm{Pr}_l \right)^{2/3}} \right) \frac{\lambda_l}{D} \qquad \textbf{8.18}$$

$$\alpha_{cb,g} = \left(3.66 + \frac{0.668 \dfrac{D}{L} \mathrm{Re}_g \, \mathrm{Pr}_g}{1 + 0.04 \left(\dfrac{D_h}{L} \mathrm{Re}_g \, \mathrm{Pr}_g \right)^{2/3}} \right) \frac{\lambda_g}{D} \qquad \textbf{8.19}$$

$$F = 1 + 80 e^{-0.6 Co} (x^2 - x^6) \qquad \textbf{8.20}$$
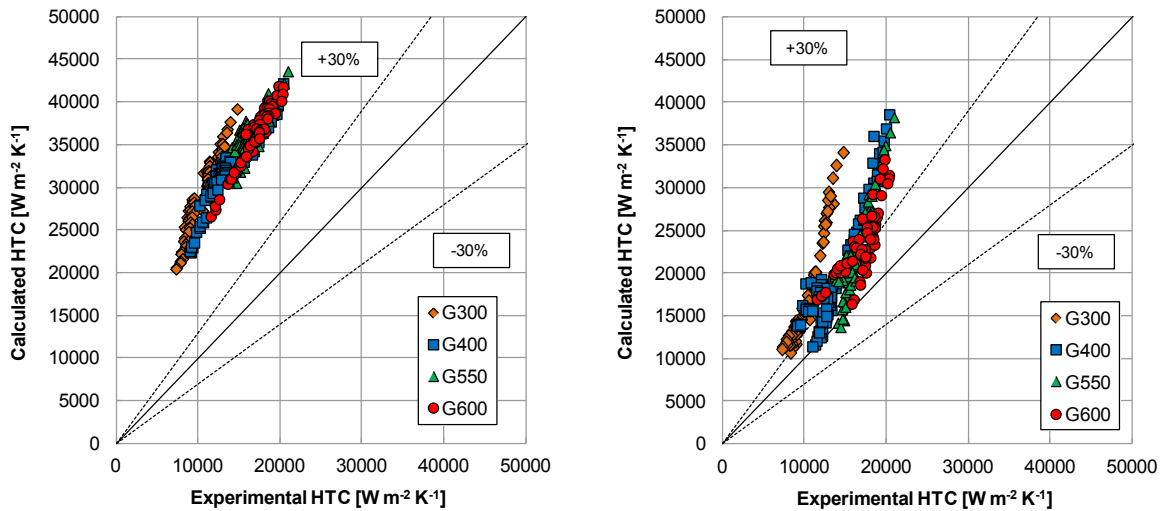
Figure 8.10. Experimental local heat transfer coefficient of the R32/R1234ze(E) at 50/50% mass composition compared with the model of Gungor and Winterton [102] **(left) and Bertsch et al.** [105] **(right).**

Among the considered correlations, the Thome et al. [106] model is based on a different physical description of the phenomenon, stressing the importance of film evaporation. A three-zone flow boiling model is proposed by the authors to describe the evaporation of elongated bubbles in microchannels. The model has been developed considering that at a fixed location the process proceeds as follows: passage of a liquid slug, passage of an elongated bubble, passage of a vapor slug if the evaporating film of the bubble dries out. The local time-averaged heat transfer coefficient of a pair or triplet passing by a location z is reported in Eq. 8.21.

$$\alpha = \frac{t_l}{\tau}\alpha_l(z) + \frac{t_{film}}{\tau}\alpha_{film}(z) + \frac{t_{dry}}{\tau}\alpha_g(z)$$

8.21

The authors emphasise the dependency of heat transfer on the bubble frequency, the minimum liquid film thickness at dryout and the liquid film formation thickness: the importance of the cyclic variation in the heat transfer coefficient due to the process is also underlined. In Dupont et al. [98] the model has been tested against a database covering R11, R12, R113, R123, R134a, R141b and carbon dioxide data, tube diameters from 0.77 mm to 3.1 mm, mass velocities between 50 kg m^{-2} s^{-1} and 564 kg m^{-2} s^{-1}, heat fluxes between 5 kW m^{-2} and 178 kW m^{-2} and vapor qualities from 0.01 to 0.99. In their model, three parameters have been derived from a parametric study of the initial database. The three parameters are the following.

- Minimum film thickness of the liquid film at dryout δ_{min}. It is related to the roughness of the surface and the thermo-physical properties of the fluid. Dupont et al. [98] highlighted that the minimum film thickness has a strong impact on the mean heat transfer coefficient in the film; thus in order to reduce the model sensitivity they proposed another equation to evaluate the mean heat transfer coefficient in the film to replace the one in Thome et al.[106]. They suggested that the choice of a constant value for δ_{min} is reasonable, and considering their database they proposed $\delta_{min} = 0.3 \cdot 10^{-6}$ m.

- Correction factor on the initial thickness of the liquid film $C_{\delta o}$. The authors proposed to use in the model a constant value of $C_{\delta o} = 0.29$ for the entire database, because no relationship to dimensionless numbers or other study parameters could be found. The authors emphasised also the lack of data with good accuracy on the film formation thickness in microchannels.

- Pair frequency f which involves the bubble formation process. The optimal pair (or triplete) frequency, which is mainly dependent on the heat flux, is reported in Eq. 8.22

$$f_{opt} = \left(\frac{q}{q_{ref}}\right)^{n_f}$$

8.22

where q_{ref} (Eq. 8.23) was expressed as a function of the reduced pressure as proposed by Cooper [104] in his pool boiling correlation.

$$q_{ref} = \alpha_q \left(\frac{p}{p_{crit}}\right)^{n_q}$$

8.23

Dupont et al. [98] fitted the data from different works and proposed specific values for each study and also suggested a set of parameter values to be used in the model (α_q=3328 W m^{-2}, n_q = -0.5, n_f = 1.74).

The whole experimental database used in the present work is overpredicted by the Dupont et al. [98] model, as illustrated in Figure 8.11. The average deviation e_R is equal to +111%

while the standard deviation σ_N is 22%. In more recent papers [96, 107] the original dryout film thickness of 300 nm has been replaced with the measured roughness of the tube obtaining better results. Following such results, calculations have been performed using the present database but no significant improvements have been found when the minimum film thickness is set equal to the channel roughness.
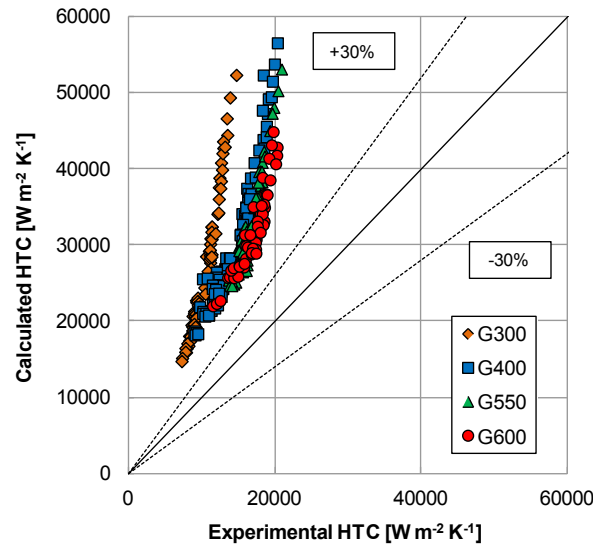

Figure 8.11. Experimental local heat transfer coefficient of the R32/R1234ze(E) at 50/50% mass composition compared with the model of Thome et al. [106].

8.5.1 Extension of models to zeotropic mixtures

In the previous section, correlations originally developed for pure fluids were applied in the case of a zeotropic mixture by employing the thermodynamic and transport properties of the mixture and neglecting the additional mass diffusion resistance. As shown, this leads to a general overestimation of the heat transfer coefficient. This is somehow expected because the heat transfer coefficient of the mixture is significantly lower than the ones of the pure fluids at the same operating conditions (Figure 8.8). It can be seen that the need for a correction is evident also in Figure 8.5 where the data points for the mixture are compared with those of pure R1234ze(E) at constant vapor quality. R1234ze(E) has comparable trends and their heat transfer coefficients are proportional to the heat flux with a power law close to 0.67, while the mixture heat transfer coefficients display a different behavior, especially at the highest values of heat flux, with lower value of the exponent.

The degradation of the heat transfer coefficient is related to the mass diffusion of the more volatile component to the bubble interface or to the vapor liquid-interface, causing an increase of the bubble point temperature at the interface and a reduction of the temperature driving force. Beside this, during flow boiling of a zeotropic mixture, the saturation temperature increases with the vapor quality and an additional amount of heat is needed to heat the liquid and the vapor to the boiling temperature, as stated by Stephan [108]. To account for the sensible heating and for the additional thermal resistance at the

liquid-vapor interface, as reported by Cavallini et al. [109], the heat transfer coefficient of the mixture can be properly calculated using the correction by Bell and Ghaly [73] as reported in Eqs. 7.7-7.9 for condensation.

The heat transfer coefficient α_f can be calculated with a flow boiling correlation developed for pure fluids, using the physical properties of the mixture and correcting the nucleate boiling component for mass diffusion effect as suggested by Thome [110]. The correction factor F_c (Eq. 8.24) was analytically developed by Thome [83]:

$$F_c = \left[1 + \left(\frac{\alpha_{fb,id}\,\Delta T_{GL}}{q'} \right) \left(1 - e^{-\left(\frac{B\,q}{\rho_l \Delta h_m \beta_l} \right)} \right) \right]^{-1} \qquad \textbf{8.24}$$

where $\alpha_{fb,id}$ is the heat transfer coefficient calculated with a correlation for pure fluids, B is a scaling factor assumed to be equal to 1, β_l is the liquid phase mass transfer coefficient that is considered to be 0.0003 m s^{-1}. The term q should be the local nucleate boiling heat flux but, for small boiling ranges, as an approximation it can be taken equal to the total heat flux.

In the case of Lazarek and Black [100] type correlations, the mixture correction factor F_c by Thome multiplies the Boiling number as reported in Eq. 8.25. Instead, for Chen [103] type correlations, F_c is applied to the nucleate boiling contribution (Eq. 8.26).

$$\alpha_f = \gamma\, \mathrm{Re}_{lo}^{\omega} (\mathrm{Bo} \cdot F_c)^{\psi}\, \frac{\lambda_l}{D} \qquad \textbf{8.25}$$

$$\alpha_f = \alpha_{nb}\, F_c + \alpha_{cb} \qquad \textbf{8.26}$$

As a guideline, the following steps are proposed to extend a flow boiling correlation developed for pure fluids to the case of zeotropic mixtures:

1) calculate the heat transfer coefficient applying a model for pure fluids with the mixture thermophysical properties;

2) evaluate the correction factor F_c;

3) estimate α_f correcting the heat transfer coefficient for pure fluids with F_c;

4) evaluate the convective heat transfer coefficient of the vapor phase and the ratio of the vapor sensible heat flow rate to the total heat flow rate;

5) calculate the heat transfer coefficient for the mixture with Eq. 7.7.

The comparison with the Lazarek and Black [100] model corrected following steps 1 to 5 is presented in Figure 8.12. The model underpredicts the experimental heat transfer coefficients with e_R =-37%, σ_N = 4% and is not able to predict the vapor quality effect. A similar behavior for boiling data of pure R32 is reported in Del Col et al. [27] where the experimental trend with vapor quality is not predicted by the model. This was somehow expected because the model does not consider any dependence of the heat transfer coefficient on vapor quality while experimental data show a variation of the heat transfer coefficient with vapor quality.
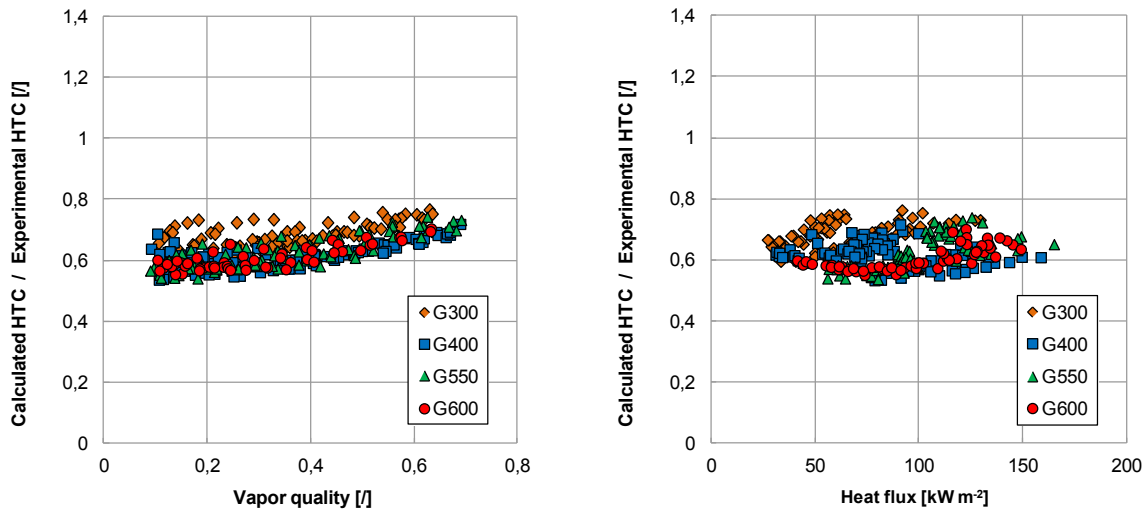
Figure 8.12. Lazarek and Black [100] **model corrected for mixture. Ratio of the calculated heat transfer coefficient to the experimental local heat transfer coefficient of the R32/R1234ze(E) at 50/50% mass composition versus vapor quality (left) and heat flux (right).**

The present heat transfer coefficients are compared with the predicted values of the Sun and Mishima [101] correlation when the correction for mixtures is applied (Figure 8.13). As compared to the Lazarek and Black [100] model, an improvement in the prediction accuracy has been found (e_R =-23%, σ_N = 4%); nevertheless the effect of the heat flux and vapor quality is not captured by the model.

Figure 8.13. Sun and Mishima [101] **model corrected for mixture. Ratio of the calculated heat transfer coefficient to the experimental local heat transfer coefficient of the R32/R1234ze(E) at 50/50% mass composition versus vapor quality (left) and heat flux (right).**

The comparison with the Chen type correlation of Gungor and Winterton [102], corrected for mixtures, is reported in Figure 8.14. The correlation predicts 99% of data points within ±30%, leading to e_R = +1.3%, σ_N = 4% with a strong accuracy improvement with respect to the original correlation. Since in the Gungor and Winterton model the suppression term is a

function of vapor quality, the nucleate boiling term is reduced when quality increases and the model is able to predict the experimental trend of the heat transfer coefficient decreasing with vapor quality at fixed heat flux and mass velocity.
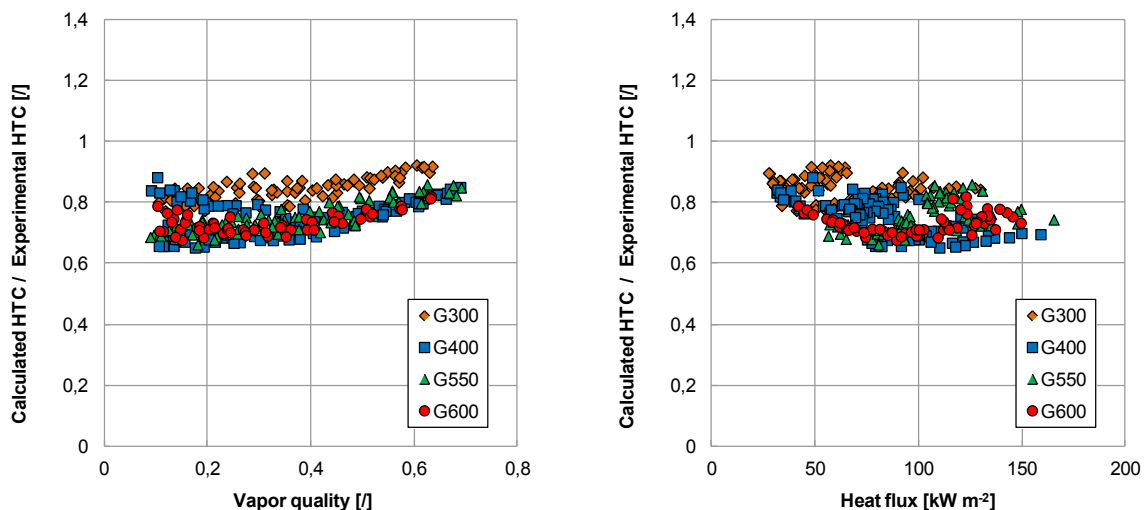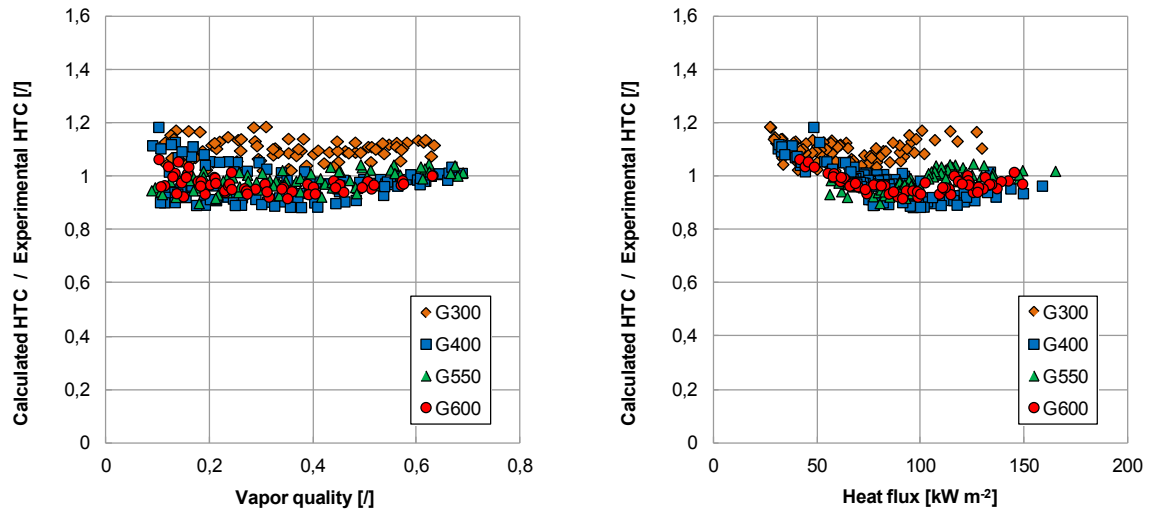

Figure 8.14. Gungor and Winterton [102] **model corrected for mixture. Ratio of the calculated heat transfer coefficient to the experimental local heat transfer coefficient of the R32/R1234ze(E) at 50/50% mass composition versus vapor quality (left) and heat flux (right).**

In Figure 8.15 the present database is compared against the predictions by the Bertsch et al. [105] model. The model underpredicts all the experimental data, even if it is able to catch the experimental trend versus vapor quality and heat flux. This model, previously compared by Del Col et al. [27] with experimental heat transfer coefficients of pure R32, provided a similar underprediction of pure fluid data. The authors explained this behavior reminding that the database used for the model development mainly refers to low pressure fluids. In fact, in a recent, paper by Bortolin et al. [111], they found that the Bertsch et al. [105] model provides an accurate prediction of their data using the low pressure refrigerant R245fa.

Figure 8.15. Bertsch et al. [105] **model corrected for mixture. Ratio of the calculated heat transfer coefficient to the experimental local heat transfer coefficient of the R32/R1234ze(E) at 50/50% mass composition versus vapor quality (left) and heat flux (right).**

When applying the correction for mixtures to the Thome et al. [106] three-zone model, only steps 4 and 5 are applied. A correction factor to the nucleate boiling component cannot be directly applied to the model, being the pair frequency determined with an empirical method. The model is able to predict the experimental data with an e_R = +28% and σ_N = 9% (Figure 8.16) and, despite the general overestimation, it is able to catch the effect of vapor quality above 0.3. When reducing the vapor quality, the disagreement between model predictions and experimental results becomes more significant; this can be ascribed to the fact that the pair frequency is obtained with a different database and the effect of the mass diffusion during the bubble formation is not considered. The adjustable parameters used are those proposed for the general model, a_q = 3328 W m^{-2}, n_q = -0.5, n_f = 1.74, $C_{\delta o}$ = 0.29, δ_{min} = 300 nm. The database used by Dupont et al. [98] does not include data for mixtures and a better prediction could be obtained by properly adjusting the empirical parameters to this particular mixture.
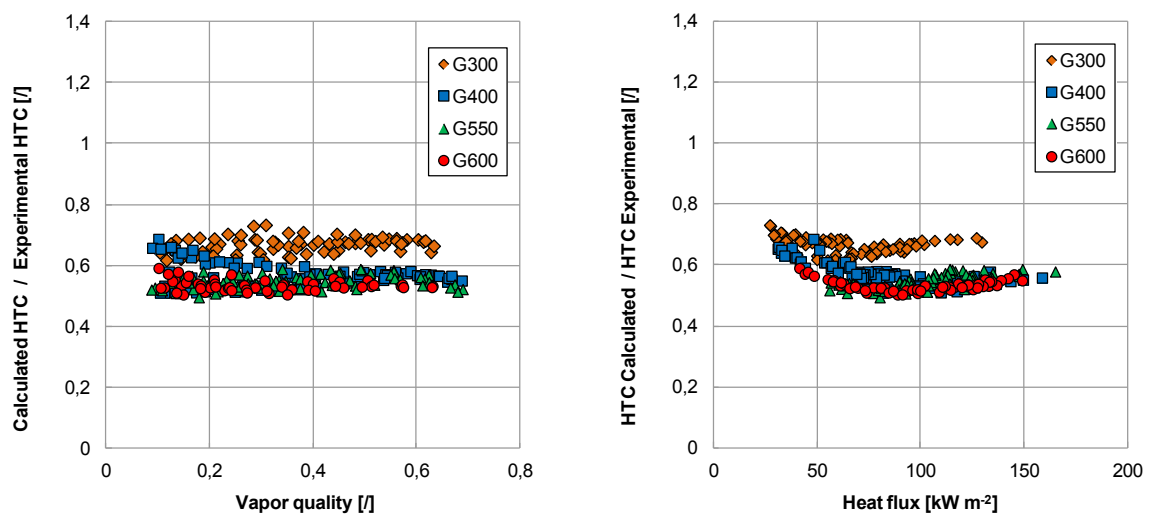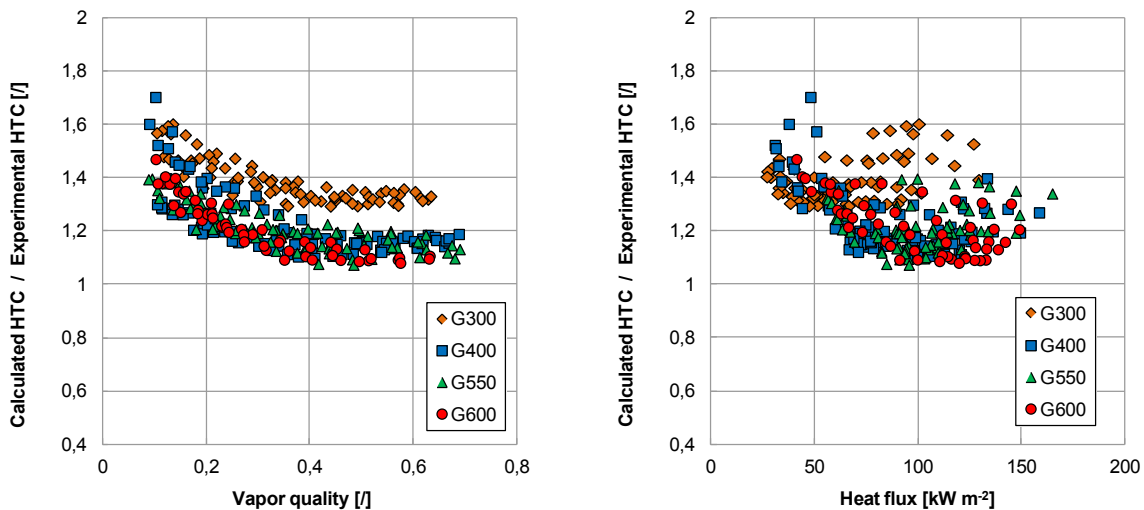

Figure 8.16. Thome et al. [106] **model corrected for mixture. Ratio of the calculated heat transfer coefficient to the experimental local heat transfer coefficient of the R32/R1234ze(E) at 50/50% mass composition versus vapor quality (left) and heat flux (right).**

8.6 Nomenclature

$a_0,...,$	coefficients of the water temperature fitting equation
Bo	Boiling number
CF	coverage factor to obtain the total (expanded) uncertainty [/]
c	specific heat [J kg^{-1} K^{-1}]
C	parameter in the Cooper [104] correlation
Co	confinement number
$C_{\delta o}$	parameter in the Thome et al. [106] correlation
d, D	inner diameter [m]
dp/dz	pressure drop gradient [Pa m^{-1}]
E	enhancement factor in Gungor and Winterton [102] correlation

e_P percentage deviation = $100 \ (HTC_{CALC}\text{-}HTC_{EXP}) \ / \ HTC_{EXP}$

e_R average mean deviation = $(1/N_P) \ \Sigma e_P$

F enhancement factor in Bertsch et al. [105] correlation

f pair frequency [Hz]

F_c mixture correction factor [/]

Fr   Froude number [/]

G mass velocity [kg m^{-2} s^{-1}]

h specific enthalpy [J kg^{-1}]

HTC   heat transfer coefficient [W m^{-2} K^{-1}]

L_{MS} length of the measuring sector [m]

M molar mass [kg kmol^{-1}]

$\dot{m}$ mass flow rate [kg s^{-1}]

N_P number of data points [/]

n_q parameter in the Thome et al. [106] correlation [/]

n_f parameter in the Thome et al. [106] correlation [/]

nTC   number of water thermocouples considered for data reduction [/]

p pressure [Pa]

q' local heat flux [W m^{-2}]

R^2 R square coefficient of determination [/]

R^2_{adj} adjusted R square coefficient of determination [/]

Ra arithmetic mean deviation of the assessed profile [μm]according to EN ISO 4287:1998/A1

R_p roughness in the Cooper [104] correlation [μm]

S suppression factor [/]

T temperature [K]

u_A type A uncertainty

u_B type B uncertainty

u_C combined experimental uncertainty

We Weber number [/]

X mass fraction [/]

X_{tt} Martinelli parameter [/]

x thermodynamic vapour quality [/]

y Fitting function for water temperature as a function of z

z axial position [m]

Greek symbols

α heat transfer coefficient   [W m^{-2} K^{-1}]

α_q parameter in the Thome et al. [106] correlation   [W m^{-2}]

δ liquid film thickness   [m]

γ generic parameter   [-]

Δh enthalpy difference   [J kg^{-1}]

ΔT temperature difference   [K]

λ thermal conductivity   [W m^{-1} K^{-1}]

μ dynamic viscosity   [Pa s]

ρ	density	[kg m^{-3}]
σ_N	standard deviation $= [\Sigma\,(e_p - e_R)^2/(N_P - 1)]^{1/2}$	
τ	pair period	[s]
ψ	generic parameter	[-]
ω	generic parameter	[-]

Subscripts

cb	convective boiling
crit	critical
dry	dryout zone
f	film
fb	flow boiling
film	liquid film between the bubble and the wall
g,v	vapor
GL	glide
in	inlet
l	liquid
lo	liquid only
m	mixture
min	minimum
nb	nucleate boiling
opt	optimal
out	outlet
ref	reference
s	sensible
sub	subcooled
t	total
w	wall
z	local

9 Conclusions

In this thesis four main activities have been performed:

1) Design and the realization of a new test section to measure condensation heat transfer coefficients and to perform visual observations of the flow patterns in a 3.38 mm circular channel has been presented. Experimental tests have been conducted during condensation of R134a;

2) Study of the effect of gravity during in-tube condensation. Experimental tests in microgravity conditions have been conducted during the 62nd ESA Parabolic Flight Campaign;

3) Experimental investigation of the thermal performance of the R32/R1234ze(E) non-azeotropic mixture: condensation heat transfer coefficients and two-phase frictional pressure drop have been measured in a 0.96 mm internal diameter single round channel.

4) Experimental investigation of flow boiling heat transfer of the R32/R1234ze(E) non-azeotropic mixture in a 0.96 mm internal diameter minichannel.

1) The design and the realization of a new test section for the measurement of heat transfer coefficients and flow visualizations have been presented. After the design process a prototype has been realized and then the final test section. The new test section is composed of two heat exchangers divided in five sub-sectors; the refrigerant flows in the internal circular copper channel of 3.38 mm and the water flows in counter-current in a specific design path. The two heat exchangers are divided by a glass tube, with the same internal diameter, to visualize the flow patterns in adiabatic conditions.

After the installation in the experimental rig, the new test section has been calibrated and preliminary tests performed. Single phase pressure drop has been measured to characterize the test channel and liquid phase heat transfer tests have been done to check the experimental procedure. The condensation quasi-local heat transfer coefficients of R134a at mass velocity between 200 and 50 kg m^{-2} s^{-1} have been presented in Section 4. For the present operating conditions the heat transfer coefficient presents a dependence on the saturation to wall temperature difference only at G=50 kg m^{-2} s^{-1}; at the other mass velocities it increases with vapor quality and mass flow rates. The flow pattern in the visualization window has also been recorded at the different mass velocities and vapor qualities. For mass velocities between 200 and 100 kg m^{-2} s^{-1} annular, stratified-wavy and slug flow have been visualized. For the lowest mass flow rate, smooth stratified and slug/plug flow have been recorded. The flow patterns visualized have been compared with two flow pattern maps available in the literature: the one by Cavallini et al. [35] and the one by El Hajal et al. [40]. The two flow pattern maps seem to predict quite well the transition between the flow regimes. The experimental heat transfer coefficient data were then compared against different models for condensation. Among them, as shown by the comparisons, the best agreement was found using the model by Cavallini et al. [35] developed for condensation of halogenated refrigerants inside tubes with diameters between 3 and 21 mm.

In parallel to the design and realization of the new test section some condensation heat transfer tests in a 0.96 mm inner diameter minichannel have been performed with HFE-7000, which is also the fluid used for the condensation tests in microgravity conditions.

2) The new test section has been used to study the gravity effect on convective condensation during the 62nd ESA Parabolic Flight Campaign. This has been one of the first attempts to perform heat transfer coefficients measurements and flow pattern visualizations on normal gravity and microgravity conditions. From the experimental tests it is clear that the effect of gravity depends on the working conditions and in the present case the mean decrease of performance during microgravity at G=70 kg m^{-2} s^{-1} is approximately about 20 %. The difference between the heat transfer coefficient measured in microgravity conditions and in normal gravity is negligible at G=170 kg m^{-2} s^{-1}. The deep connection between gravity effect and flow pattern has been shown in the images recorded during microgravity. When the condensation process is shear stress dominated the flow pattern visualized in normal gravity is quite similar to the one in microgravity. At the lowest mass flow rate and 1 g, the gravity plays the important role to drain the condensed liquid on the lower part of the tube leaving a thinner film on the upper part. In microgravity conditions the liquid film is free to spread along the circumference giving as a result a globally lower heat transfer coefficient.

3) Frictional pressure drop during adiabatic liquid-vapor flow has been experimentally investigated inside a 0.96 mm diameter minichannel. Tests have been run with the mixture R32/R1234ze(E) at three different mass compositions (23/77%, 50/50% and 75/25%) and mass flux ranging between 200 and 800 kg m^{-2} s^{-1}. Single-phase pressure drop has been measured for the assessment of the experimental technique. During two-phase tests, a strong effect of the composition has been detected for the R1234ze(E)/R32 mixture: adding a small quantity of R32 the pressure gradient is considerably reduced compared to the pure R1234ze(E). The new experimental data have been compared with several models available in the literature: the correlation by Friedel [37], the Muller-Steinhagen and Heck [65] model, the model proposed by Zhang and Webb [53] the Del Col et al. [19] model. Among them the Del Col et al. [19] model well reproduces the experimental trend showing that a model developed for pure fluids can be successfully applied to these zeotropic mixtures without corrections.

The thermal performance during condensation of the mixture R32/R1234ze(E) at three mass compositions 23/77%, 46/54% and 75/25% inside a 0.96 mm diameter microchannel has been investigated in Section 7. Depending on the mass composition these zeotropic mixtures display GWPs of 155, 310 and 506 and temperature glides of about 11, 8 and 3 K, respectively. From this Section the following conclusions can be drawn:

- During condensation tests, data have been collected at pressures of 13.7, 17.7 and 22 bar respectively, with mass velocity ranging between 150 and 800 kg m^{-2} s^{-1}. When the mass fraction of R32 is increased from 23% to 46%, the heat transfer coefficient increases by 7.4% at G = 800 kg m^{-2} s^{-1}, by 7.2% at G = 400 kg m^{-2} s^{-1}, and by 10.4% at G = 200 kg m^{-2} s^{-1}. From the mass fraction 46/54% to the 75/25%, the heat transfer coefficient increases by 16.6% at G = 800 kg m^{-2} s^{-1}, by 14.3% at G = 400 kg m^{-2} s^{-1}, and by 18.3% at G = 200 kg m^{-2} s^{-1}. Comparing the heat transfer coefficient of the

mixture with those of the pure R1234ze(E) on average the 23/77% mixture shows a decrease around 11%, the mixture 46/54% assumes values 4% lower while only the 75/25% mixture shows an improvement on the heat transfer coefficient of about 13%. Respect to pure R32 all the mixtures show lower heat transfer coefficients around 31%, 25% and 12%.

- The penalization of the heat transfer coefficient due to the additional mass transfer resistance can be estimated by comparing the measured heat transfer coefficients versus an ideal linear behavior of the mixture between the values pertaining to the pure components at the same operating conditions. At $G = 400$ kg m^{-2} s^{-1} and $x = 0.7$, such penalization is about 22%, 21% and 12% for the three mixtures in the order of increasing R32 mass fraction, while at 400 kg m^{-2} s^{-1} and $x = 0.4$, it is equal to 10%, 8,5% and 4% respectively.

- The present experimental heat transfer coefficients have been compared with those predicted by the Cavallini et al. [18] model coupled with the Silver–Bell–Ghaly correction to account for the additional mass transfer resistance. This model predicts the experimental data with good accuracy, displaying a relative deviation of -5%.

- Using the parameter PF as a performance evaluation criterion, a comparative analysis that accounts for both the heat transfer coefficient and the pressure drop has been performed. At the same PF and 0.5 vapor quality, the mass velocity that leads to the same energy penalization during condensation varies with the fluid, and thus, the optimal operating conditions depend on the refrigerant. From this analysis, it was shown that in the case of the present mixtures, the performance degradation due to the additional mass transfer resistance is mitigated when also accounting for the pressure drop effect. According to this approach, the heat transfer coefficients for the 46/54% mixture are on average higher of 21% than those of pure R1234ze(E) and for the 75/25% they are on average 91.9% higher.

4) Flow boiling heat transfer has also been investigated inside the 0.96 mm diameter circular minichannel with the mixture at 0.5/0.5 by mass composition.

Experimental local heat transfer coefficients have been measured at mass flow rate between 300 and 600 kg m^{-2} s^{-1}, pressure of 14 bar (bubble temperature 26.3°C) and heat flux from 27 to 165 kW m^{-2}. The boiling process is promoted by a secondary fluid (water) instead of fixing the heat flux by electric heating. From Section 7 the following conclusions can be drawn:

- The heat transfer coefficient measured during flow boiling was found to be dependent on the heat flux. However, when increasing the heat flux the heat transfer coefficient is less dependent on the heat flux as compared to the case of pure fluids. As observed in the case of flow boiling of pure fluids in microchannels, the heat transfer coefficient decreases with vapor quality in the whole quality range. An increase of the mass velocity leads to an increase of the heat transfer coefficient. This trend is more enhanced moving from the lowest values of mass flux.

- Mixture heat transfer coefficients have been compared against flow boiling data taken by Del Col and coworkers [27, 97] inside the same 0.96 mm channel. The present

refrigerant mixture displays lower heat transfer coefficients than those of the pure fluids. The heat transfer degradation from a linear behaviour is about 50 % for all the tested conditions due to the additional mass transfer resistance typical of the zeotropic mixture.

- The new experimental heat transfer coefficient data have been compared with several correlations available in the literature developed for pure fluids. All the models were found to overpredict the measured heat transfer coefficients when no correction is applied. Such large overestimation was expected because the correlations do not account for the penalization due to the additional mass transfer resistance.

- A correction is needed in the case of mixtures. The Thome [83] correction factor F_c is applied to correct the nucleate boiling component in some available correlations. A correction to account for the additional mass transfer resistance, as reported by Cavallini et al. [109], is also introduced. From the comparison with the correlations corrected for zeotropic mixtures, it can be seen that all the models display better accuracy. In particular, the Gungor and Winterton [102] correlation is the one that best predicts the present database. Good results are also obtained with the Thome et al. [106] model and further improvements could be achieved if the present database is used to calculate the optimum model parameters. The Bertsch et al. [105] model, developed from a low reduce pressure fluids database, is able to catch the experimental trend of heat transfer coefficient versus vapor quality and heat flux, but it strongly underpredicts experimental values.

10 ANNEX A: DETAILS OF THE NEW MINICHANNEL TEST SECTION

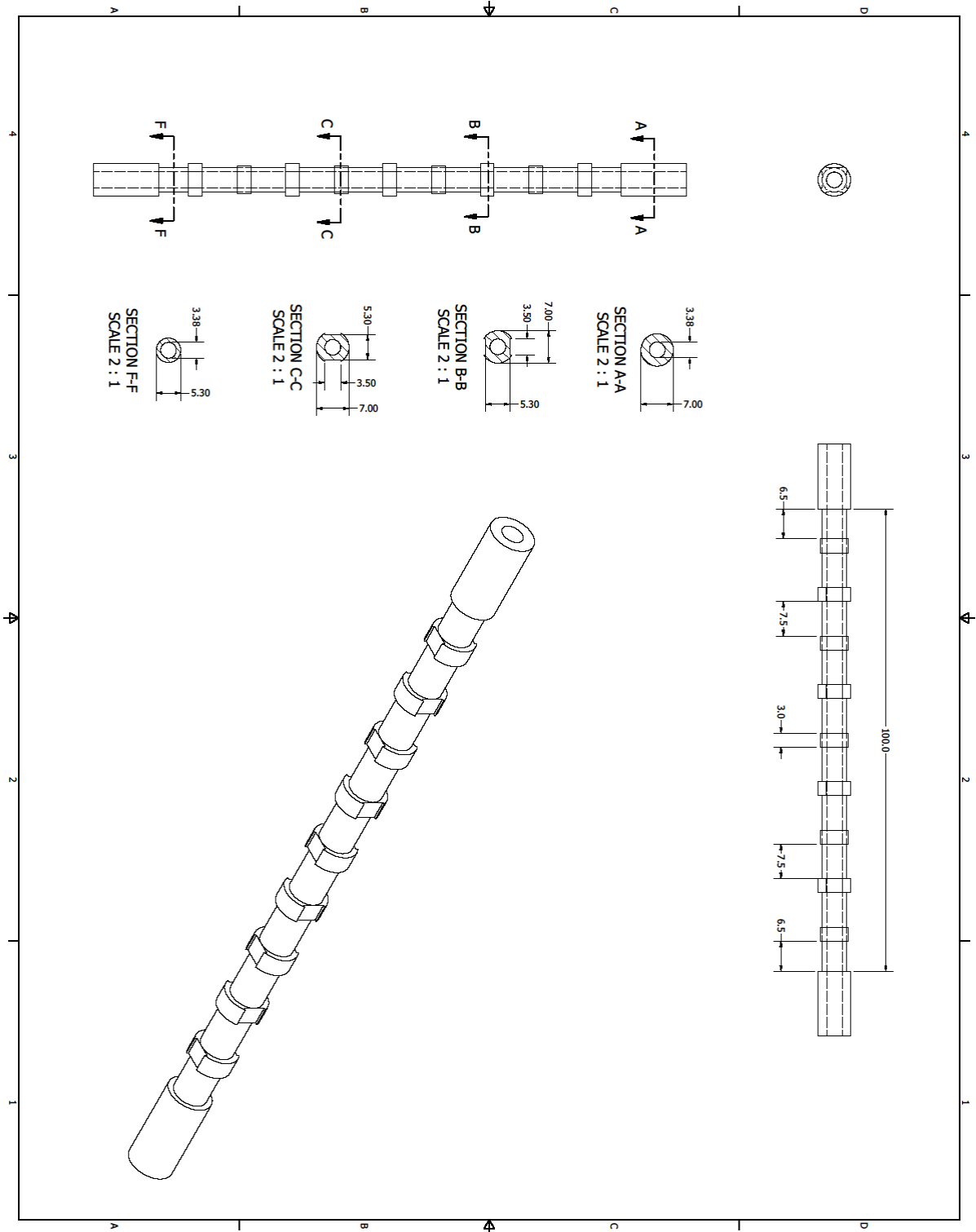The technical drawings of the test section described in Section 3 are reported hereafter.

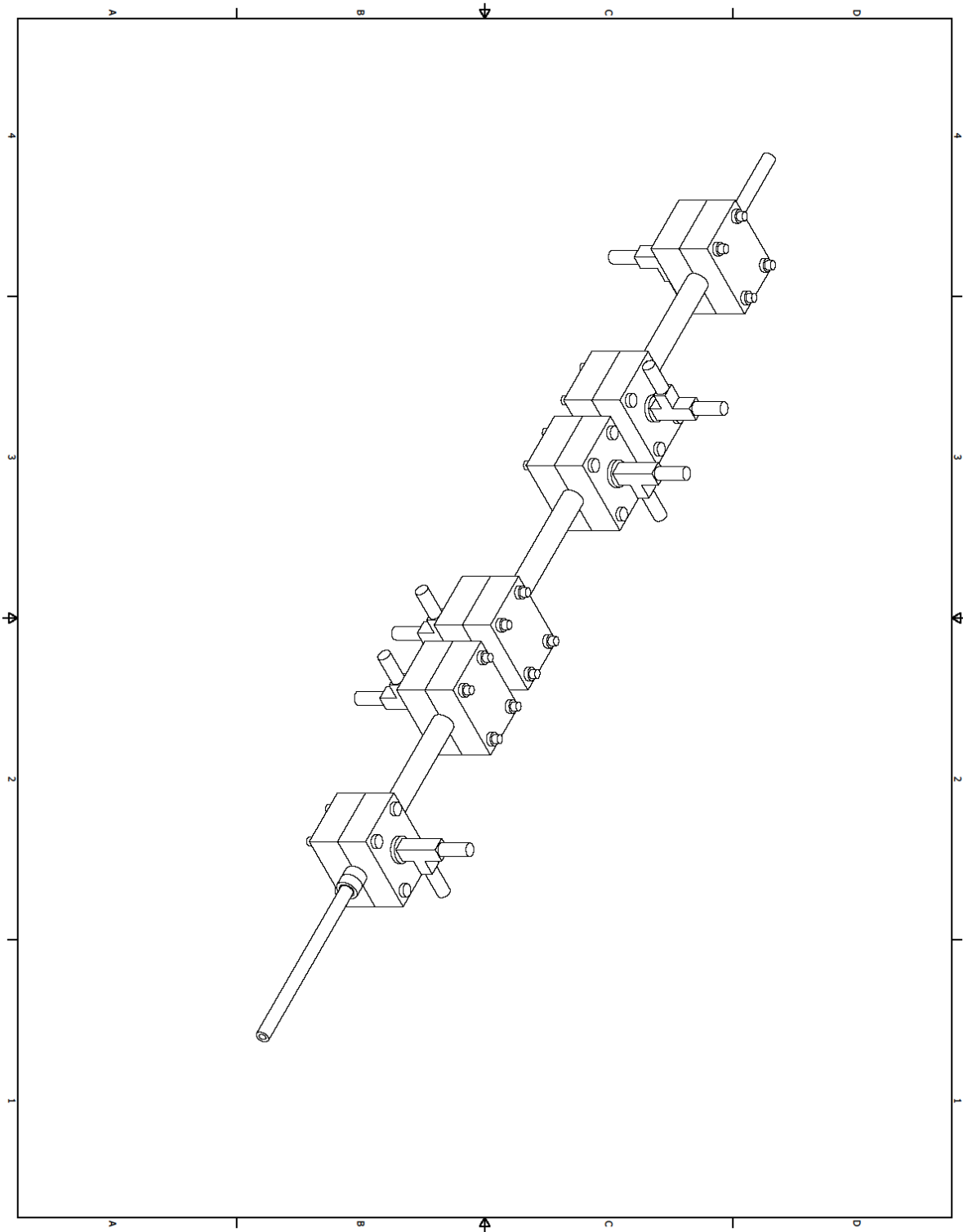**Figure 10.1. Technical drawings of a sub-sector in the first heat exchanger.**

Figure 10.2. Complete layout of the first heat exchangers with the three sub-sectors
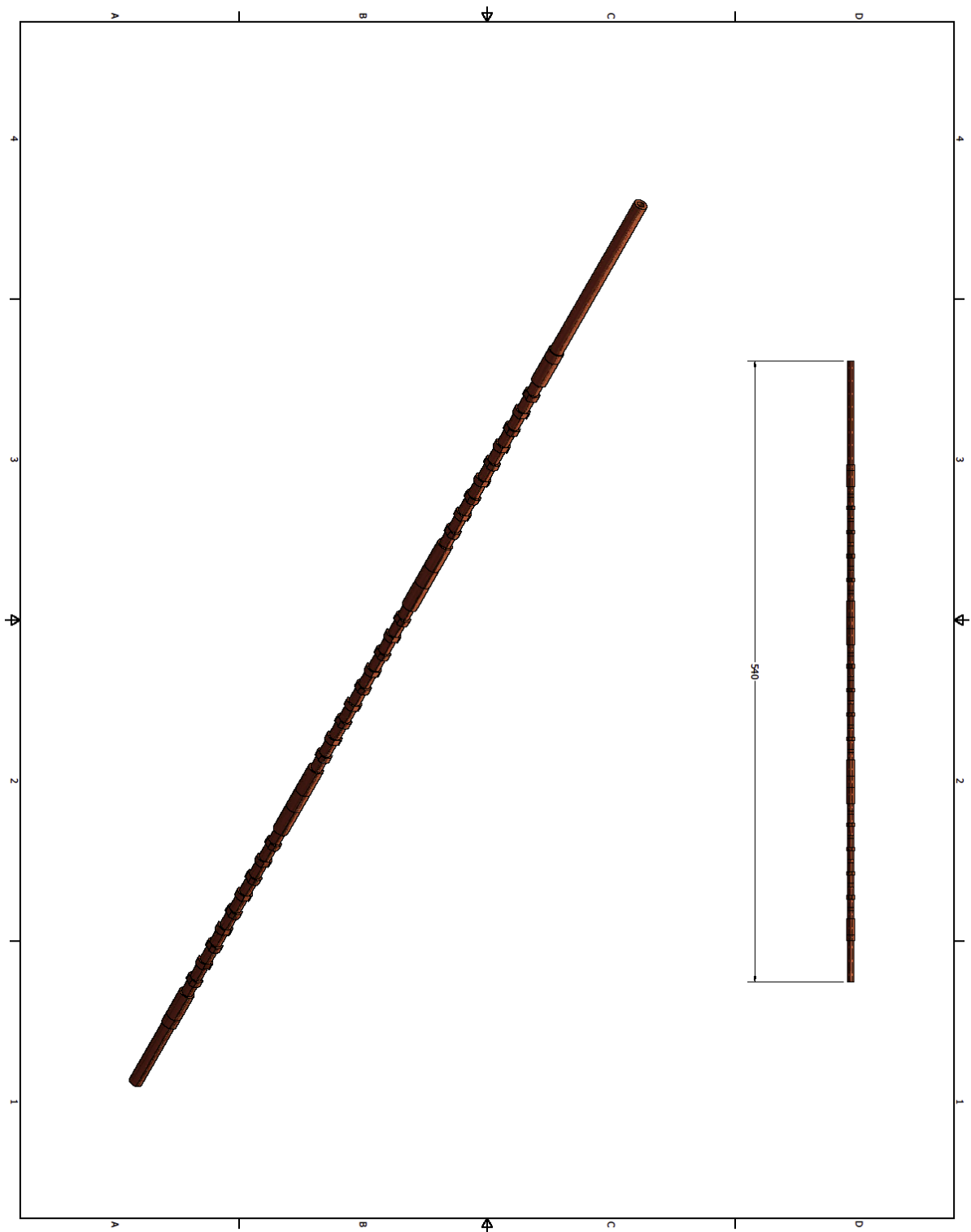
Figure 10.3. Technical drawing of the copper tube of the first heat exchanger. The total length of the heat exchanger is about 540 mm.
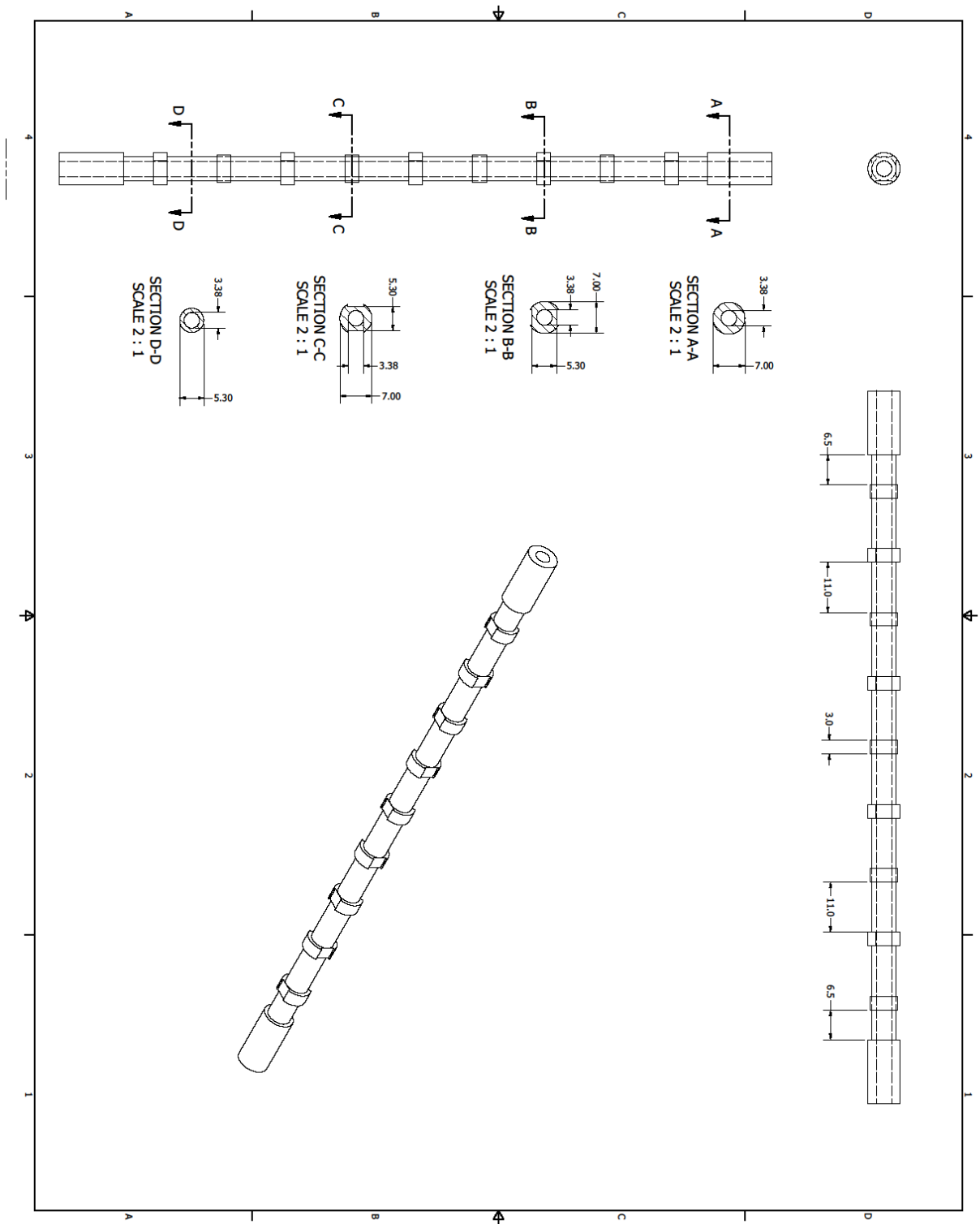
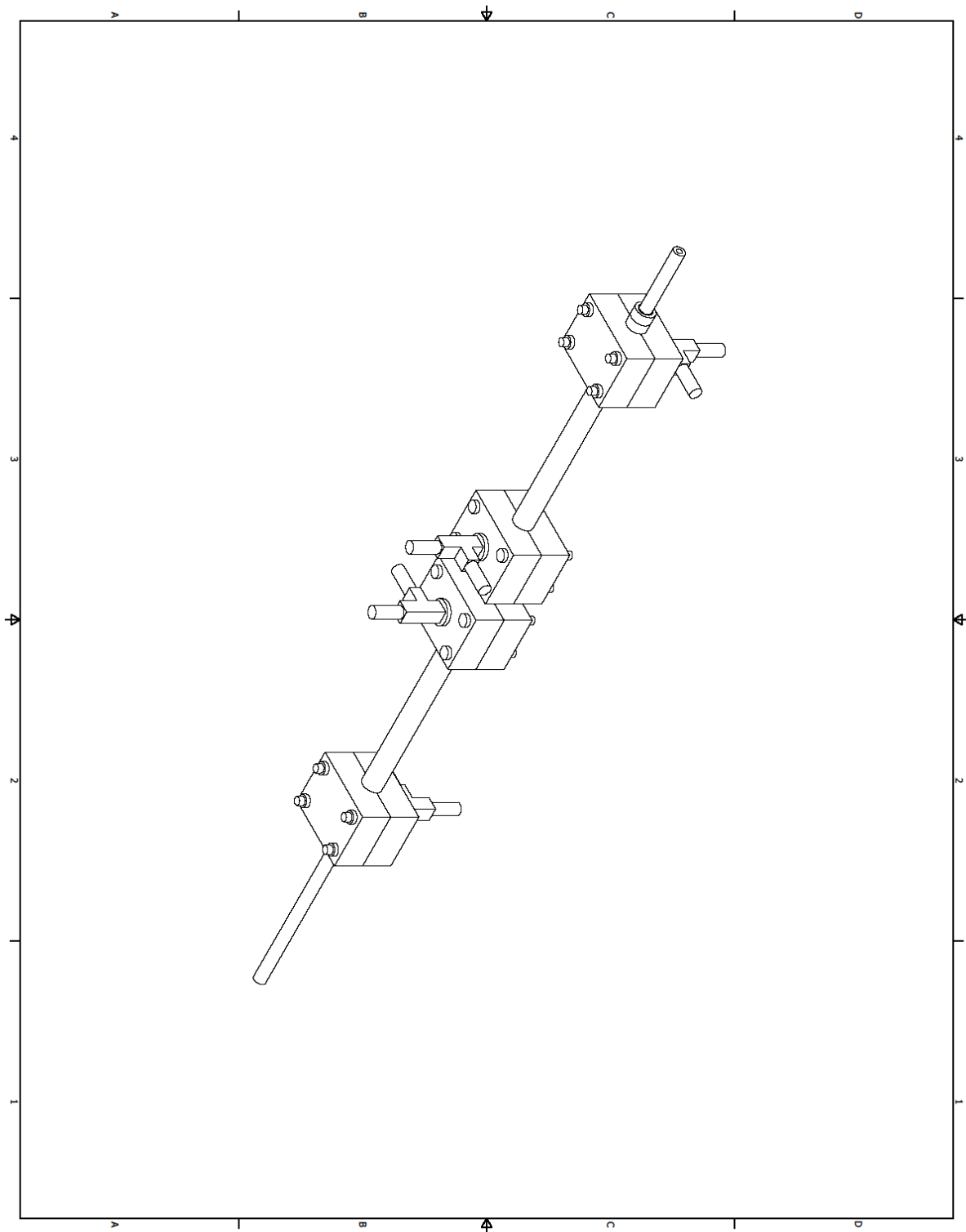**Figure 10.4 Technical drawings of a sub-sector of the second heat exchanger**

Figure 10.5. Complete layout of the second heat exchangers with two sub-sectors
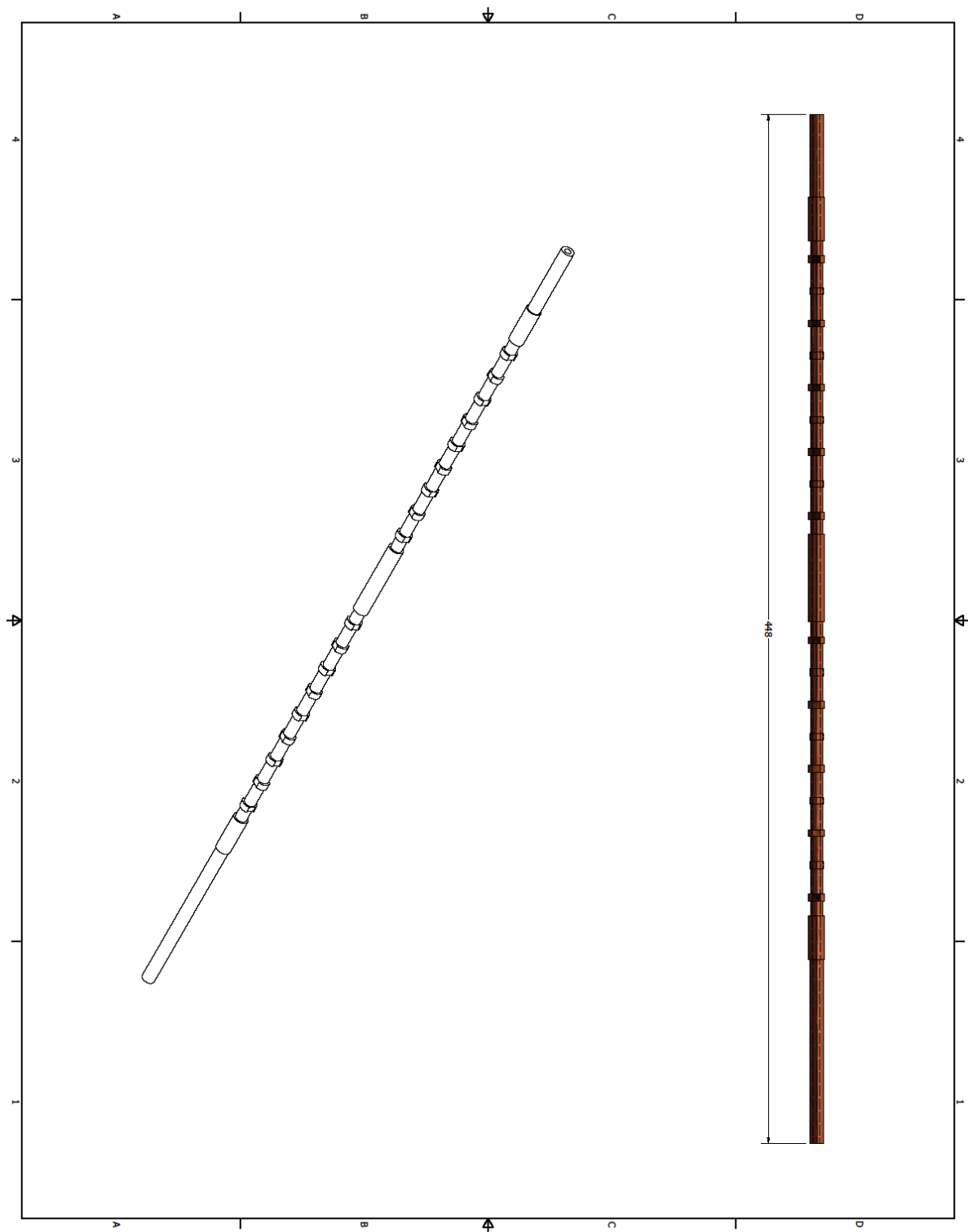
Figure 10.6. Technical drawing of the copper tube of the second heat exchanger. The total length of the heat exchanger is about 448 mm
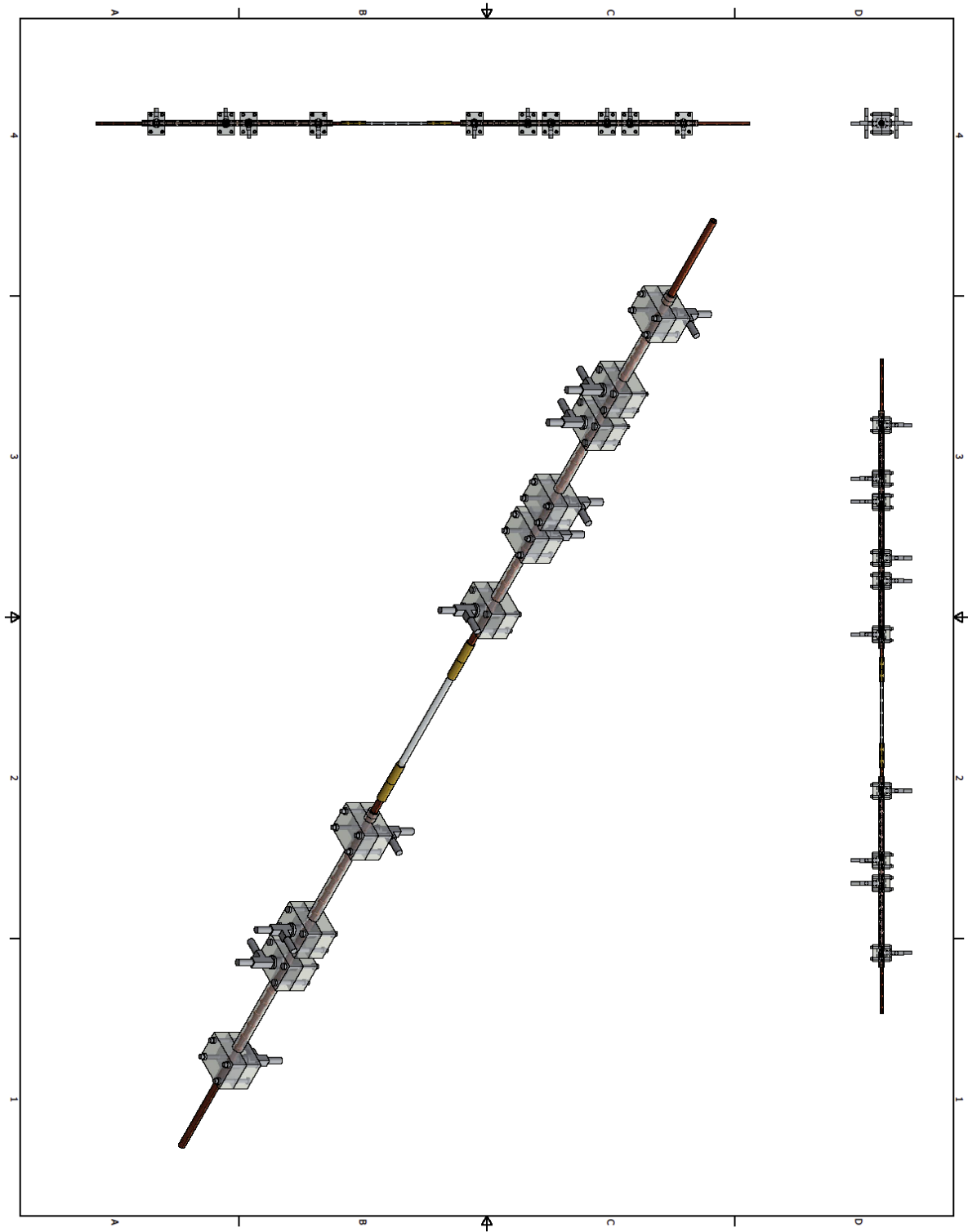
Figure 10.7. Complete test section

11 ANNEX B: UNCERTAINTY ANALYSIS FOR HEAT TRANSFER COEFFICIENTS AND PRESSURE DROP IN THE TWO TEST SECTIONS OF DIAMETER 0.96 mm

The combined standard uncertainty u_C of a measured parameter θ result from the Type A and Type B components according to Eq. 11.1. The type B components for the different parameters are reported in Table 11.1.

$$u_C(\theta) = \sqrt{u_A(\theta)^2 + u_B(\theta)^2}$$ **11.1**

Table 11.1. Type B experimental uncertainty of measured parameters

Temperature	$\pm$ 0.05 °C
Temperature difference (with thermopile)	$\pm$ 0.03 °C
Water flow rate in measuring sector	$\pm$ 0.14 % at 10 kg h^{-1}
Refrigerant flow rate	$\pm$ 0.2 % at 2 kg h^{-1}
Absolute pressure	$\pm$ 5 kPa (level of confidence: 99.7%)
Pressure difference (greater than 1 kPa)	$\pm$ 0.12 kPa (level of confidence: 99.7%)
Pressure difference (below 1 kPa)	$\pm$ 0.1% (level con confidence 99.7%)

When a searched parameter ξ is not directly measured but it can be expressed as a function F of uncorrelated input quantities $\theta_1, \theta_2, ..., \theta_N$, as in the case of heat transfer coefficient or thermodynamic vapour quality, its combined standard uncertainty is determined from Eq. 11.2.

$$u_C(\xi) = \sqrt{\sum_{i=1}^{N} \left(\frac{\delta F}{\delta \theta_i} \right)^2 u_C(\theta_i)^2}$$ **11.2**

According to Eq. 11.3, the local heat transfer coefficient is function of (water mass flow rate, water temperature gradient, refrigerant and wall temperature, internal diameter):

$$\alpha(z) = F\left(\dot{m}_{water}, \frac{dT_{water}}{dz}, T_{ref}, T_w, d \right)$$ **11.3**

In the present technique, because of the geometry of the water channel, the dominant thermal resistance during condensation and evaporation is on the refrigerant side. This aspect is favorable to the reduction of the experimental uncertainty associated to the determination of the heat transfer coefficient.

The procedure that has been implemented for determining the uncertainty related to the water temperature gradient is the weighted least square (WLS) regression method (Press et al. [112]). For each test run, a function of the axial position z has been determined to fit the water temperature. The fitting function has been chosen among a several polynomial functions as reported in Section 7.4. Whatever the fitting function y(z), its $M+1$ coefficients $a_0, ..., a_M$ are defined in order to minimize the merit figure χ^2. In Eq. 11.4, $T_{water,i}$ is the water

temperature measured at the *i-th* axial location, identified by the axial coordinate z_i (i ranges between 1 and the number of water thermocouples *nTC* considered for the data reduction).

$$\chi^2 = \sum_{i=1}^{nTC} \left[\frac{T_{water,i} - y(z_i)}{u_C\left(T_{water,i}\right)} \right]^2$$

11.4

The minimum of the merit figure occurs where its derivative with respect to all parameters a_o, ...,a_M is equal to zero. This condition yields the following matrix equation:

$$\left(\mathbf{A}^T \times \mathbf{A}\right) \times \mathbf{a} = \mathbf{A}^T \times \mathbf{b}$$

11.5

where **A** is a *nTC* x *M+1* matrix whose elements are obtain as reported in Eq. 11.6

$$A_{ij} = \left(\frac{\dfrac{\partial y}{\partial a_{j-1}}}{u_C\left(t_{w,i}\right)} \right)$$

11.6

b is a vector of *nTC* constant terms defined as the ratio between the water temperature measured at the *i-th* location and the correspondent uncertainty:

$$b_i = \left(\frac{t_{w,i}}{u_C\left(t_{w,i}\right)} \right)$$

11.7

and finally **a** is the vector of the *M+1* coefficients of the fitting equation.

The covariance matrix **C**, defined according to Eq. 11.8, is closely related to the standard uncertainty of the estimated parameters a_i: the diagonal elements C_{jj} are the square uncertainties of the fitted parameters a_i, while the off-diagonal elements C_{jk} are the covariances between the estimated coefficients a_j and a_k, dubbed *cov(a_j, a_k)*.

$$\mathbf{C} = \left(\mathbf{A}^T \times \mathbf{A}\right)^{-1}$$

11.8

The elements of the covariance matrix **C** are useful to calculate the uncertainty related to the temperature gradient by applying the law of propagation of uncertainty for correlated input quantities (Eq. 11.9). In this calculation, the coefficient a_o is not present, as it is a constant term in the water temperature fitting function *y(z)*.

$$u_C\left(\frac{dt_{water}}{dz}\right) = \sqrt{ \sum_{j=1}^{M} \left(\frac{\partial\left(\frac{dy}{dz}\right)}{\partial a_j} \right)^2 (u^2(a_j)) + 2\sum_{j=1}^{M-1}\sum_{k=j+1}^{M} \left(\frac{\partial\left(\frac{dy}{dz}\right)}{\partial a_j} \right)\left(\frac{\partial\left(\frac{dy}{dz}\right)}{\partial a_k} \right) cov(a_j, a_k) }$$

11.9

As reported in Del Col et al. [1], the effect of the uncertainty in the thermocouple location has also been checked and it was found to be negligible as compared to the uncertainty due to the temperature readings. The uncertainty of the latent heat of condensation as well as the uncertainty of the water isobaric specific heat is neglected.

In the case of pure fluids, as described in the data reduction procedure, the local saturation temperature is estimated by an iterative procedure which implements several models in order to account for the pressure drop. Consequently, the experimental combined uncertainty for the local saturation temperature is calculated from a linear combination of the experimental combined uncertainty of the inlet and outlet saturation temperature, derived from the pressure measurements. The uncertainty for a saturation temperature derived from a pressure measurements is determined by the difference between the value of the saturation temperature at the measured pressure and the value pertaining at that pressure with its uncertainty (Eq. 11.10 and 11.11).

$$u_c\left(T_{sat,in,MS}\right) = T_{sat,in,MS}\left(p_{in,MS}\right) - T_{sat,in,MS}\left(p_{in,MS} + u_c\left(p_{in,MS}\right)\right) \qquad \textbf{11.10}$$

$$u_c\left(T_{sat,out,MS}\right) = T_{sat,out,MS}\left(p_{out,MS}\right) - T_{sat,out,MS}\left(p_{out,MS} + u_c\left(p_{out,MS}\right)\right) \qquad \textbf{11.11}$$

The local saturation temperature uncertainty is calculated as a combination of the two previous values

$$u_c\left(T_{sat}(z)\right) = \sqrt{\left(1 - \frac{z}{L_{MS}}\right)^2 \left(u_c\left(T_{sat,in,MS}\right)\right)^2 + \left(\frac{z}{L_{MS}}\right)^2 \left(u_c\left(T_{sat,out,MS}\right)\right)^2} \qquad \textbf{11.12}$$

where z is the axial position and L_{MS} the length of the measuring sector.
As it was done for the heat transfer coefficient, the experimental uncertainty for the vapor quality along the measuring sector, can be calculated as a combination of (Eq. 11.13): inlet enthalpy, water mass flow rate, water specific heat, water temperatures, refrigerant mass flow rate, latent heat).

$$x(z) = F\left(h_{in,MS}, \dot{m}_{water,MS}, c_{water}, T_{water,out,ms}, T_{water}(z), \dot{m}_{ref}, h_{LV}\right) \qquad \textbf{11.13}$$

In the case of the non-azeotropic mixture the local refrigerant temperature, as reported in Eq. 7.5, is evaluated using the pressure, enthalpy and mass composition. The local pressure is not simply estimated assuming a linear pressure profile between the measured values at inlet and outlet but, to catch the real pressure profile, an iterative procedure, which implements several models in order to account for the pressure drop due to friction, abrupt geometry change and momentum variation is applied. The local refrigerant enthalpy is evaluated using Eq. 4.11 where the mass composition has been measured using a gas-chromatograph as reported in Section 7.3. The single contribution of the pressure, enthalpy and mass composition in the determination of the uncertainty of the refrigerant temperature at the inlet of the measuring section is evaluated as follow:

$$T_{ref,in,u(p)} = f\left(p_{in} + u_c(p_{in}), h_{in}, X_{R1234ze(E)}\right) \qquad \textbf{11.14}$$

$$T_{ref,in,u(h)} = f\left(p_{in}, h_{in} + u_c(h_{in}), X_{R1234ze(E)}\right) \qquad \textbf{11.15}$$

$$T_{ref,in,u(X)} = f\left(p_{in}, h_{in}, X_{R1234ze(E)} + u_c(X_{R1234ze(E)})\right) \qquad \textbf{11.16}$$

Hence, the combined uncertainty for the refrigerant temperature at the inlet of the measuring section is calculated with Eq. 11.2, using the contributions in Eqs. 11.14-11.16. In these equations: the combine uncertainty for the pressure at the inlet of the measuring sector comes from the uncertainty of the pressure transducer and the standard deviation of the readings; the combined uncertainty of the enthalpy at the inlet of the measuring sector is evaluated applying the law of propagation (Eq. 11.2) for the heat balance in the pre-conditioning sector using the uncertainty of the thermopile and the ones of mass flow rates. The same procedure is used to the calculation of the uncertainty for the refrigerant temperature at the outlet and along the test section, using the corresponding local pressure and enthalpies. The uncertainty related to vapor quality is evaluated in the same way to that of the refrigerant temperature.

For the pressure drop test section the experimental pressure gradient uncertainty is calculated as reported in Eq. 11.17, applying the law of propagation.

$$u_C\left(\frac{dp}{dz}\right) = \sqrt{\left(\frac{\partial\left(\frac{dp}{dz}\right)}{\partial \Delta p}\right)^2 u_c(\Delta p)^2 + \left(\frac{\partial\left(\frac{dp}{dz}\right)}{\partial L_{MS}}\right)^2 u_c(L_{MS})^2}$$

11.17

where Δp is the pressure difference and L_{MS} the distance between the two pressure ports.

REFERENCES

[1] D. Del Col, S. Bortolin, A. Cavallini and M. Matkovic, *Effect of Cross Sectional Shape during Condensation in a Single Square Minichannel*, Int.J.Heat Mass Transfer. 54 (2011), pp. 3909-3920.

[2] E. Da Riva and D. Del Col, *Effect of Gravity during Condensation of R134a in a Circular Minichannel: VOF Simulation of Annular Condensation*, Microgravity Sci Technol. 23 (2011), pp. S87-S97.

[3] N. Liu, J.M. Li, J. Sun and H.S. Wang, *Heat Transfer and Pressure Drop during Condensation of R152a in Circular and Square Microchannels*, Exp.Therm.Fluid Sci. 47 (2013), pp. 60-67.

[4] I. Marchuk, Y. Lyulin and O. Kabov, *Theoretical and Experimental Study of Convective Condensation Inside a Circular Tube*, Interfacial Phenomena and Heat Transfer. 1 (2013), pp. 153-171.

[5] D. Del Col, M. Bortolato, M. Azzolin and S. Bortolin, *Effect of Inclination during Condensation Inside a Square Cross Section Minichannel*, Int.J.Heat Mass Transfer. 78 (2014), pp. 760-777.

[6] D. Del Col, M. Bortolato, M. Azzolin and S. Bortolin, *Condensation Heat Transfer and Two-Phase Frictional Pressure Drop in a Single Minichannel with R1234ze(E) and Other Refrigerants*, Int.J.Refrig. 50 (2015), pp. 87-103.

[7] S. Garimella, B.M. Fronk, J.A. Milkie and B. Keinath, *Versatile Models for Condensation of Fluids with Widely Varying Properties from the Micro to Macroscale*, 2014.

[8] European Parliament and Council, *REGULATION (EU) no 517/2014*, Official Journal of the European Union. L 150/195 (2014).

[9] International Standard Organization, *EN ISO 4287:1998/A1, Geometrical Product Specifications (GPS) - Surface Texture: Profile Method- Terms, Definitions and Surface Texture Parameters* (1998).

[10] M. Matkovic, *Experimental Condensation Inside Minichannels*, University of Padova, 2006.

[11] D. Torresin, *Experimental Study of Two Phase Flow and Heat Transfer during Vaporization, Filmwise and Dropwise Condensation of Refrigerants and Steam Inside Small Diameters Channels*, Università degli Studi di Padova, 2012.

[12] S. Lips and J.P. Meyer, *Experimental Study of Convective Condensation in an Inclined Smooth Tube. Part I: Inclination Effect on Flow Pattern and Heat Transfer Coefficient*, Int.J.Heat Mass Transfer. 55 (2012), pp. 395-404.

[13] B. Mederic, M. Miscevic, V. Platel, P. Lavieille and J. Joly, *Experimental Study of Flow Characteristics during Condensation in Narrow Channels: The Influence of the Diameter Channel on Structure Patterns*, Eurotherm 75: Microscale Heat Transfer 2, July 8, 2003 - July 10, 2004.

[14] B. Mederic, P. Lavieille and M. Miscevic, *Heat Transfer Analysis According to Condensation Flow Structures in a Minichannel*, Exp.Therm.Fluid Sci. 30 (2006), pp. 785-793.

[15] Y. Taitel and A.E. Dukler, *MODEL FOR PREDICTING FLOW REGIME TRANSITIONS IN HORIZONTAL AND NEAR HORIZONTAL GAS-LIQUID FLOW*, AIChE J. 22 (1976), pp. 47-55.

[16] S.W. Churchill, *Friction-Factor Equation Spans all Fluid-Flow Regimes*, Chemical Engineering (New York). 84 (1977), pp. 91-92.

[17] M. Matkovic, A. Cavallini, D. Del Col and L. Rossetto, *Experimental Study on Condensation Heat Transfer Inside a Single Circular Minichannel*, Int.J.Heat Mass Transfer. 52 (2009), pp. 2311-2323.

[18] A. Cavallini, D. Del Col, L. Doretti, M. Matkovic, L. Rossetto, C. Zilio and G. Censi, *Condensation in Horizontal Smooth Tubes: A New Heat Transfer Model for Heat Exchanger Design*, 2006.

[19] D. Del Col, A. Bisetto, M. Bortolato, D. Torresin and L. Rossetto, *Experiments and Updated Model for Two Phase Frictional Pressure Drop Inside Minichannels*, Int.J.Heat Mass Transfer. 67 (2013), pp. 326-337.

[20] E.W. Lemmon, M.L. Huber and M.O. McLinden, *NIST Standard Reference Database 23: Reference Fluid Thermodynamic and Transport Properties-REFPROP, Version 9.1, National Institute of Standards and Technology, Standard Reference Data Program, Gaithersburg* (2013).

[21] J. Klomfar, M. Souckova and J. Patek, *Surface Tension and $p{-}\rho{-}T$ Data for 1,1,1,3,3-Pentafluorobutane (HFC-365mfc) and 1,1,1,2,2,3,3-Heptafluoro-3-Methoxy-Propane (HFE-347mcc)*, Journal of Chemical & Engineering data. 58 (2013), pp. 2316-2325.

[22] J.O. Rawlings, S.G. Pantula and D.A. Dickey, *Applied Regression Analysis*, Springer, New York, 1998.

[23] M. Bortolato, *Two-Phase Heat Transfer Inside Minichannels: Fundamentals and Applications in Refrigeration and Solar Technology*, University of Padova, 2014.

[24] A. Paliwoda, *Generalized Method of Pressure Drop and Tube Length Calculation with Boiling and Condensing Refrigerants within the Entire Zone of Saturation*, Int.J.Refrig. 12 (1989), pp. 314-322.

[25] I.E. Idelchik, *Handbook of Hydraulic Resistance*, 3 ed., , Begell House, New York, 1996.

[26] A. Cavallini, D. Del Col, M. Matkovic and L. Rossetto, *Frictional Pressure Drop during Vapour-Liquid Flow in Minichannels: Modelling and Experimental Evaluation*, Int J Heat Fluid Flow. 30 (2009), pp. 131-139.

[27] D. Del Col, S. Bortolin and L. Rossetto, *Convective Boiling Inside a Single Circular Microchannel*, Int.J.Heat Mass Transfer. 67 (2013), pp. 1231-1245.

[28] H. Blasius, *Das Ahnlichkeitsgesetz Bei Reibungsvorgangen in Flussigkeiten*, Forschg. Arb, Ing.-Wes. 131 (1913).

[29] VDI Heat Atlas/ed. Verein Deutscher Ingenieure, *VDI-Gesellschaft Verfahrenstechnik Und Chemieingenieurwesen (GVC)*, Second Edition ed., , Springer-Verlag, 2010.

[30] International Standard Organization, *Guide to the Expression of Uncertainty in Measurements*, 1995.

[31] G. Nema, S. Garimella and B.M. Fronk, *Flow Regime Transitions during Condensation in Microchannels*, Int.J.Refrig. 40 (2014), pp. 227-240.

[32] J.W. Coleman and S. Garimella, *Visualization of Refrigerant Two-Phase Flow during Condensation*, Pittsburgh, Pennsylvania, 2000.

[33] Coleman J.W. and Garimella S., *Two-Phase Flow Regime Transitions in Microchannel Tubes: The Effect of Hydraulic Diameter*, ASME Heat Transfer Div.Publ.HTD. 366 (2000), pp. 71-83.

[34] Coleman J.W. and Garimella S., *Two-Phase Flow Regimes in Round, Square and Rectangular Tubes during Condensation of Refrigerant R 134a*, Int.J.Refrig. 26 (2003), pp. 117-128.

[35] A. Cavallini, G. Censi, D. Del Col, L. Doretti, G.A. Longo and L. Rossetto, *Condensation of Halogenated Refrigerants Inside Smooth Tubes*, HVAC&R Research. 8 (2002), pp. 429-451.

[36] P.G. Kosky and F.W. Staub, *Local Condensing Heat Transfer Coefficients in the Annular Flow Regime*, AIChE J. 17 (1971), pp. 1037-1043.

[37] L. Friedel, *Improved Friction Pressure Drop Correlations for Horizontal and Vertical Two Phase Flow, Paper E2*, Ispra, Italy, 1979.

[38] A. Cavallini, G. Censi, D. Del Col, L. Doretti, G.A. Longo and L. Rossetto, *Experimental Investigation on Condensation Heat Transfer and Pressure Drop of New HFC Refrigerants (R134a, R125, R32, R410A, R236ea) in a Horizontal Smooth Tube*, Int.J.Refrig. 24 (2001), pp. 73-87.

[39] M. Zhang, *A New Equivalent Reynolds Number Model for Vapor Shear-Controlled Condensation Inside Smooth and Micro-Fin Tubes*, The Pennsylvania State University, 1998.

[40] J. El Hajal, J.R. Thome and A. Cavallini, *Condensation in Horizontal Tubes, Part 1: Two-Phase Flow Pattern Map*, Int.J.Heat Mass Transfer. 46 (2003), pp. 3349-3363.

[41] N. Kattan, J.R. Thome and D. Favrat, *Flow Boiling in Horizontal Tubes: Part 1 - Development of a Diabatic Two-Phase Flow Pattern Map*, Journal of Heat Transfer. 120 (1998), pp. 140-147.

[42] D. Steiner, *Heat Transfer to Boiling Saturated Liquids*, in *VDI Heat Atlas*, Anonymous , Dusseldorf, 1993, pp. Chapter Hbb.

[43] J.R. Thome, J. El Hajal and A. Cavallini, *Condensation in Horizontal Tubes, Part 2: New Heat Transfer Model Based on Flow Regimes*, Int.J.Heat Mass Transfer. 46 (2003), pp. 3365-3387.

[44] S.G. Mohseni, M.A. Akhavan-Behabadi and M. Saeedinia, *Flow Pattern Visualization and Heat Transfer Characteristics of R-134a during Condensation Inside a Smooth Tube with Different Tube Inclinations*, Int.J.Heat Mass Transfer. 60 (2013), pp. 598-602.

[45] Y. Lyulin, I. Marchuk, S. Chikov and O. Kabov, *Experimental Study of Laminar Convective Condensation of Pure Vapor Inside an Inclined Circular Tube*, Microgravity Sci Technol. 23 (2011), pp. 439-445.

[46] H.S. Wang and J.W. Rose, *Film Condensation in Microchannels: Effect of Tube Inclination*, Limerick, Ireland, 2006.

[47] H. Saffari and V. Naziri, *Theoretical Modeling and Numerical Solution of Stratified Condensation in Inclined Tubes*, Journal of Mechanical Science and Technology. 24 (2010), pp. 2587-2596.

[48] B. Wang and X. Du, *Study on Laminar Film-Wise Condensation for Vapor Flow in an Inclined small/mini-Diameter Tube*, Int.J.Heat Mass Transfer. 43 (2000), pp. 1859-1868.

[49] H. Lee, I. Mudawar and M.M. Hasan, *Experimental and Theoretical Investigation of Annular Flow Condensation in Microgravity*, Int.J.Heat Mass Transfer. 61 (2013), pp. 293-309.

[50] K.W. Moser, R.L. Webb and B. Na, *A New Equivalent Reynolds Number Model for Condensation in Smooth Tubes*, Journal of Heat Transfer. 120 (1998), pp. 410-417.

[51] T.M. Bandhauer, A. Agarwal and S. Garimella, *Measurement and Modeling of Condensation Heat Transfer Coefficients in Circular Microchannels*, Journal of Heat Transfer. 128 (2006), pp. 1050-1059.

[52] A. Cavallini, G. Censi, D. Del Col, L. Doretti, G.A. Longo, L. Rossetto and C. Zilio, *Condensation Inside and Outside Smooth and Enhanced Tubes -a Review of Recent Research*, Int.J.Refrig. 26 (2003), pp. 373-392.

[53] M. Zhang and R.L. Webb, *Correlation of Two-Phase Friction for Refrigerants in Small-Diameter Tubes*, Exp.Therm.Fluid Sci. 25 (2001), pp. 131-139.

[54] S. Garimella, J.D. Killion and J.W. Coleman, *An Expermentally Validated Model for Two-Phase Pressure Drop in the Intermittent Flow Regime for Noncircular Microchannels*, J Fluids Eng Trans ASME. 125 (2003), pp. 887-894.

[55] A. Cavallini, D. Del Col, L. Doretti, M. Matkovic, L. Rossetto and C. Zilio, *Two-Phase Frictional Pressure Gradient of R236ea, R134a and R410A Inside Multi-Port Mini-Channels*, 2005.

[56] R. Revellin and J.R. Thome, *Adiabatic Two-Phase Frictional Pressure Drops in Microchannels*, Exp.Therm.Fluid Sci. 31 (2007), pp. 673-685.

[57] S. Grauso, R. Mastrullo, A.W. Mauro, J.R. Thome and G.P. Vanoli, *Flow Pattern Map, Heat Transfer and Pressure Drops during Evaporation of R-1234ze(E) and R134a in a*

Horizontal, Circular Smooth Tube: Experiments and Assessment of Predictive Methods, Int.J.Refrig. 36 (2013), pp. 478-491.

[58] M.A. Hossain, Y. Onaka and A. Miyara, *Experimental Study on Condensation Heat Transfer and Pressure Drop in Horizontal Smooth Tube for R1234ze(E), R32 and R410A*, 2012.

[59] B.S. Field and P. Hrnjak, *Adiabatic Two-Phase Pressure Drop of Refrigerants in Small Channels*, 4th International Conference on Nanochannels, Microchannels and Minichannels, ICNMM2006, June 19, 2006 - June 21, 2006.

[60] K. Choi, A.S. Pamitran, J. Oh and K. Saito, *Pressure Drop and Heat Transfer during Two-Phase Flow Vaporization of Propane in Horizontal Smooth Minichannels*, Int.J.Refrig. 32 (2009), pp. 837-845.

[61] M.H. Maqbool, B. Palm and R. Khodabandeh, *Investigation of Two Phase Heat Transfer and Pressure Drop of Propane in a Vertical Circular Minichannel*, Exp.Therm.Fluid Sci. 46 (2013), pp. 120-130.

[62] C. Kondou, D. Baba, F. Mishima and S. Koyama, *Flow Boiling of Non-Azeotropic Mixture R32/R1234ze(E) in Horizontal Microfin Tubes*, Int.J.Refrig. 36 (2013), pp. 2366-2378.

[63] D. Del Col, M. Azzolin, A. Bisetto and S. Bortolin, *A Prediction Method of Frictional Pressure Drop during Two-Phase Flow in Small Diameter Channels*, Proc. of 13th International Conference on Multiphase Flow in Industrial Plants, Sestri Levante, Genova, Italy, 2014.

[64] L. Friedel, *PRESSURE DROP DURING GAS/VAPOR-LIQUID FLOW IN PIPES*, Int.Chem.Eng. 20 (1980), pp. 352-367.

[65] H. Mueller-Steinhagen and K. Heck, *SIMPLE FRICTION PRESSURE DROP CORRELATION FOR TWO-PHASE FLOW IN PIPES*, Chem.Eng.Process. 20 (1986), pp. 297-308.

[66] A. Cavallini, D. Del Col, M. Matkovic and L. Rossetto, *Pressure Drop during Two-Phase Flow of R134a and R32 in a Single Minichannel*, Journal of Heat Transfer. 131 (2009), pp. 1-8.

[67] R. Akasaka, *Thermodynamic Property Models for the Difluoromethane (R-32)+trans-1,3,3,3-Tetrafluoropropene (R-1234ze(E)) and difluoromethane+2,3,3,3-Tetrafluoropropene (R-1234yf) Mixtures*, Fluid Phase Equilib. 358 (2013), pp. 98-104.

[68] I.I. Paleev and B.S. Filippovich, *Phenomena of Liquid Transfer in Two-Phase Dispersed Annular Flow*, International Journal of Heat and Mass Transfer. 9 (1966), pp. 1089-1093.

[69] L.F. Moody and N.J. Princeton, *Friction Factors for Pipe Flow*, Transactions of the ASME. 11 (1944), pp. 671-684.

[70] S. Koyama, N. Takata and S. Fukuda, *Drop-in Experiments on Heat Pump Cycle using HFO-1234ze(E) and its Mixtures with HFC-32*, Proc. Int. Refrigeration and Air Conditioning Conf., Purdue, West Lafayette, IN, 2010.

[71] A. Miyara, H.M.M. Afroz and M.A. Hossain, *In-Tube Condensation of Low GWP Mixture Refrigerants R1234ze(E)/R32*, Kyoto, Japan, 2014.

[72] D. Del Col, A. Cavallini and J.R. Thome, *Condensation of Zeotropic Mixtures in Horizontal Tubes: New Simplified Heat Transfer Model Based on Flow Regimes*, Journal of Heat Transfer. 127 (2005), pp. 221-230.

[73] K.J. Bell and M.A. Ghaly, *APPROXIMATE GENERALIZED DESIGN METHOD FOR MULTICOMPONENT/PARTIAL CONDENSERS*, American Institute of Chemical Engineers, Papers (1972).

[74] L. Silver, *Gas Cooling with Aqueous Condensation*, Transactions of the Institute of Chemical Engineers. 25 (1947), pp. 30-42.

[75] A. Cavallini, J.S. Brown, D. Del Col and C. Zilio, *In-Tube Condensation Performance of Refrigerants Considering Penalization Terms (Exergy Losses) for Heat Transfer and Pressure Drop*, Int.J.Heat Mass Transfer. 53 (2010), pp. 2885-2896.

[76] C.B. Tibircia, G. Ribatski and J.R. Thome, *Flow Boiling Characteristics for R1234ze(E) in 1.0 and 2.2 mm Circular Channels*, Journal of Heat Transfer. 134 (2012).

[77] F. Vakili-Farahani, B. Agostini and J.R. Thome, *Experimental Study on Flow Boiling Heat Transfer of Multiport Tubes with R245fa and R1234ze(E)*, 2013.

[78] A. Diani, S. Mancin and L. Rossetto, *R1234ze(E) Flow Boiling Inside a 3.4 mm ID Microfin Tube*, Int.J.Refrig. 47 (2014), pp. 105-119.

[79] S. Bortolin and D. Del Col, *Flow Boiling of a New Low-GWP Refrigerant Inside a Single Square Cross Section Microchannel*, Journal of Physics: Conference Series. 547 (2014).

[80] X. Wang and K. Amrane, *AHRI Low Global Warming Potential Alternative Refrigerants Evaluation Program (Low-GWP AREP) – Summary of Phase I Testing Results*, Proc. Int. Refrigeration and Air Conditioning Conf., Purdue, West Lafayette, IN, 2014.

[81] G.P. Celata, M. Cumo and T. Setaro, *Forced Convective Boiling in Binary Mixtures*, Int.J.Heat Mass Transfer. 36 (1993), pp. 3299-3309.

[82] G.P. Celata, M. Cumo and T. Setaro, *Review of Pool and Forced Convective Boiling of Binary Mixtures*, Exp.Therm.Fluid Sci. 9 (1994), pp. 367-381.

[83] J.R. Thome, *Prediction of the Mixture Effect on Boiling in Vertical Thermosyphon Reboilers*, Heat Transfer Eng. 10 (1989), pp. 29-38.

[84] M. Anowar Hossain, Y. Onaka, H.M.M. Afroz and A. Miyara, *Heat Transfer during Evaporation of R1234ze(E), R32, R410A and a Mixture of R1234ze(E) and R32 Inside a Horizontal Smooth Tube*, 2013.

[85] J.R. Thome, A. Bar-Cohen, R. Revellin and I. Zun, *Unified Mechanistic Multiscale Mapping of Two-Phase Flow Patterns in Microchannels*, Exp.Therm.Fluid Sci. 44 (2013), pp. 1-22.

[86] C.B. Tibirica and G. Ribatski, *Flow Boiling in Micro-Scale Channels-Synthesized Literature Review*, 2013.

[87] X.F. Peng, G.P. Peterson and B.X. Wang, *Flow Boiling of Binary Mixtures in Microchanneled Plates*, Int.J.Heat Mass Transfer. 39 (1996), pp. 1257-1264.

[88] P.H. Lin, B.R. Fu and C. Pan, *Critical Heat Flux on Flow Boiling of Methanol-Water Mixtures in a Diverging Microchannel with Artificial Cavities*, Int.J.Heat Mass Transfer. 54 (2011), pp. 3156-3166.

[89] B.R. Fu, P.H. Lin, M.S. Tsou and C. Pan, *Flow Pattern Maps and Transition Criteria for Flow Boiling of Binary Mixtures in a Diverging Microchannel*, Int.J.Heat Mass Transfer. 55 (2012), pp. 1754-1763.

[90] M. Li, C. Dang and E. Hihara, *Flow Boiling Heat Transfer of HFO1234yf and R32 Refrigerant Mixtures in a Smooth Horizontal Tube: Part I. Experimental Investigation*, Int.J.Heat Mass Transfer. 55 (2012), pp. 3437-3446.

[91] D. Del Col and S. Bortolin, *Investigation of Dryout during Flow Boiling in a Single Microchannel Under Non-Uniform Axial Heat Flux*, International Journal of Thermal Sciences. 57 (2012), pp. 25-36.

[92] D. Del Col, M. Azzolin, A. Bisetto and S. Bortolin, *Frictional Pressure Drop during Two-Phase Flow of Pure Fluids and Mixtures in Small Diameter Channels*, Int. J. Chem. React. Eng. (2015).

[93] Z. Rouhani and E. Axelsson, *Calculation of the Void Volume Fraction in the Subcooled and Quality Boiling Region*, Int. J. Heat Mass Transfer. 13 (1970), pp. 383-393.

[94] R. Ali, B. Palm and M.H. Maqbool, *Flow Boiling Heat Transfer of Refrigerants R134A and R245fA in a Horizontal Micro-Channel*, Exp.Heat Transfer. 25 (2012), pp. 181-196.

[95] T.G. Karayiannis, D. Shiferaw, D.B.R. Kenning and V.V. Wadekar, *Flow Patterns and Heat Transfer for Flow Boiling in Small to Micro Diameter Tubes*, Heat Transfer Eng. 31 (2010), pp. 257-275.

[96] C.L. Ong and J.R. Thome, *Macro-to-Microchannel Transition in Two-Phase Flow: Part 1 - Two-Phase Flow Patterns and Film Thickness Measurements*, Exp.Therm.Fluid Sci. 35 (2011), pp. 37-47.

[97] D. Del Col, M. Bortolato and S. Bortolin, *Measurements of Heat Transfer Coefficient during Flow Boiling of Two HFOs Inside a Circular Minichannel*, Proc. 8th World Conference on Experimental Heat Transfer, Fluid Mechanics, and Thermodynamic, Lisbon, June 16-20 2013.

[98] V. Dupont, J.R. Thome and A.M. Jacobi, *Heat Transfer Model for Evaporation in Microchannels. Part II: Comparison with the Database*, Int.J.Heat Mass Transfer. 47 (2004), pp. 3387-3401.

[99] C.B. Tibiria and G. Ribatski, *Flow Patterns and Bubble Departure Fundamental Characteristics during Flow Boiling in Microscale Channels*, Exp.Therm.Fluid Sci. 59 (2014), pp. 152-165.

[100] G.M. Lazarek and S.H. Black, *EVAPORATIVE HEAT TRANSFER, PRESSURE DROP AND CRITICAL HEAT FLUX IN A SMALL VERTICAL TUBE WITH R-113*, Int.J.Heat Mass Transfer. 25 (1982), pp. 945-960.

[101] L. Sun and K. Mishima, *An Evaluation of Prediction Methods for Saturated Flow Boiling Heat Transfer in Mini-Channels*, Int.J.Heat Mass Transfer. 52 (2009), pp. 5323-5329.

[102] K.E. Gungor and R.H.S. Winterton, *GENERAL CORRELATION FOR FLOW BOILING IN TUBES AND ANNULI*, Int.J.Heat Mass Transfer. 29 (1986), pp. 351-358.

[103] J.C. Chen, *A Correlation for Boiling Heat Transfer to Saturated Fluids in Convective Flow*, Industrial & Engineering Chemistry Process Design and Development. 5 (1966), pp. 322-329.

[104] M.G. Cooper, *HEAT FLOW RATES IN SATURATED NUCLEATE POOL BOILING - A WIDE-RANGING EXAMINATION USING REDUCED PROPERTIES*, Advances in Heat Transfer. 16 (1984), pp. 157-239.

[105] S.S. Bertsch, E.A. Groll and S.V. Garimella, *A Composite Heat Transfer Correlation for Saturated Flow Boiling in Small Channels*, Int.J.Heat Mass Transfer. 52 (2009), pp. 2110-2118.

[106] J.R. Thome, V. Dupont and A.M. Jacobi, *Heat Transfer Model for Evaporation in Microchannels. Part I: Presentation of the Model*, Int.J.Heat Mass Transfer. 47 (2004), pp. 3375-3385.

[107] B. Agostini, J.R. Thome, M. Fabbri, B. Michel, D. Calmi and U. Kloter, *High Heat Flux Flow Boiling in Silicon Multi-Microchannels - Part II: Heat Transfer Characteristics of Refrigerant R245fa*, Int.J.Heat Mass Transfer. 51 (2008), pp. 5415-5425.

[108] K. Stephan, *Heat Transfer in Condensation and Boiling*, Springer-Verlag, Berlin.

[109] A. Cavallini, D. Del Col, L. Doretti, G.A. Longo and L. Rossetto, *Refrigerant Vaporization Inside Enhanced Tubes: A Heat Transfer Model*, Heat Technol. 17 (1999), pp. 29-36.

[110] J.R. Thome, *Boiling of New Refrigerants: A State-of-the-Art Review*, Int.J.Refrig. 19 (1996), pp. 435-457.

[111] S. Bortolin, D. Del Col and L. Rossetto, *Flow Boiling of R245fa in a Single Circular Microchannel*, Heat Transfer Eng. 32 (2011), pp. 1160-1172.

[112] W.H. Press, B.P. Flannery, S.A. Teukolsky and W.T. Vetterling, *Numerical Recipes*, Cambridge University Press, New York, 2007.

PUBLICATIONS

In International Journals

Del Col D., Bortolato M., Azzolin M., Bortolin S., (2014), Effect of inclination during condensation inside a square cross section minichannel, INTERNATIONAL JOURNAL OF HEAT AND MASS TRANSFER, 78, 760–777

Del Col D., Bortolato M., Azzolin M., Bortolin S., (2015), Condensation heat transfer and two-phase frictional pressure drop in a single minichannel with R1234ze(E) and other refrigerants. INTERNATIONAL JOURNAL OF REFRIGERATION, 50, 87-103

Del Col D., Azzolin M., Benassi G., Mantovan M., (2015), Energy efficiency in a ground source heat pump with variable speed drives. ENERGY AND BUILDINGS, 91, 105-114

Del Col D., Azzolin M., Bisetto A., Bortolin S., (2015), Frictional Pressure Drop during Two-Phase Flow of Pure Fluids and Mixtures in Small Diameter Channels. INTERNATIONAL JOURNAL OF CHEMICAL REACTOR ENGINEERING, doi: 10.1515/ijcre-2014-0180

Del Col D., Azzolin M., Bortolin S., Zilio C., (2015), Two-phase pressure drop and condensation heat transfer of R32/R1234ze(E) non-azeotropic mixtures inside a single microchannel. SCIENCE AND TECHNOLOGY FOR THE BUILT ENVIRONMENT, 21, 595-606

Azzolin M., Bortolin S., Del Col D., in press, Predicting methods for flow boiling heat transfer of a non-azeotropic mixture inside a single microchannel, HEAT TRANSFER ENGINEERING

In International Conference Proceedings

Del Col D., Benassi G., Mantovan M., Azzolin M., (2012), Energy Efficiency in a Ground Source Heat Pump with Variable Speed Drives. In: International Refrigeration and Air Conditioning Conference at Purdue. Purdue, West Lafayette, USA, July 16-19, 2012

Del Col D., Bortolato M., Bortolin S., Azzolin M., (2012), Minichannel condensation in downward, upward and horizontal configuration. In: Journal of Physics: Conference Series. JOURNAL OF PHYSICS. CONFERENCE SERIES, vol. 395, IOP PUBLISHING LTD, ENGLAND, ISSN: 1742-6596, doi: 10.1088/1742-6596/395/1/012092

Del Col D., Azzolin M., Bortolato M., Bortolin S., (2013), Condensation heat transfer and pressure drop in a single minichannel with R1234ze(E) and other refrigerants. In: 4th IIR Conference on Thermophysical Properties and Transfer Processes of Refrigerants. Carlos Infante Ferreira, Delft University of Technology, ISBN: 9782913149991, Delft, The Netherlands

Del Col D., Azzolin M., Benassi G., Mantovan M., (2014), Experimental analysis of optimal operation mode of a ground source heat pump system. In: Energy Procedia. ENERGY

PROCEDIA, vol. 45, p. 1354-1363, ISSN: 1876-6102, Bologna, 11-13 September 2013, doi: 10.1016/j.egypro.2014.01.142

Del Col D., Azzolin M., Bortolin S., Zilio C., (2014), Condensation heat transfer of a non-azeotropic mixture in a single minichannel. In: Proceedings of the 15th International Heat Transfer Conference. ISBN: 9781567004212, Kyoto, Japan, August 10-15, 2014

Del Col D., Azzolin M., Bortolin S., (2014), Condensation heat transfer and pressure drop of R32/R1234ze(E) mixture inside a single circular microchannel. In: Proceedings of the 9th two-phase systems for ground and space applications. Baltimore, MD, USA, September 22-26, 2014

Del Col D., Azzolin M., Bisetto A., Bortolin S., (2014), A prediction method of frictional pressure drop during two-phase flow in small diameter channels. In: 13th International Conference on Multiphase Flow in Industrial Plants. Sestri Levante (Genova), 17-19 Settembre 2014

Del Col D., Azzolin M., Bortolin S., (2014), Flow boiling heat transfer of a non-azeotropic mixture inside a single microchannel. In: 4th Micro and Nano Flows Conference. ISBN: 9781908549167, UCL, London, UK, 7-10 September 2014

Del Col D., Azzolin M., Bortolin S., (2014), Two-Phase Flow and Heat Transfer of a Non-Azeotropic Mixture inside a Single Microchannel. In: 15th International Refrigeration and Air Conditioning Conference at Purdue. West Lafayette, Indiana (USA), July 14-17

Azzolin M., Bortolin S., Le Nguyen L.P, Del Col D., (2015), A New Test Section for Investigation of Convective Condensation: Calibration and Preliminary Results. In: 10th International Conference on TWO-PHASE SYSTEMS FOR GROUND AND SPACE APPLICATIONS

In National Conference Proceddings

Azzolin M., Benassi G., Del Col D., Mantovan M., (2013), Methods to increase energy efficiency in a ground source heat pump system with variable speed drives. In: INNOVAZIONE E TENDENZE NELLA TECNOLOGIA E NELLE APPLICAZIONI DELLE POMPE DI CALORE. AICARR, ISBN: 9788895620152

Submitted to International Journals

Azzolin M., Bortolin S., Del Col D., Flow boiling heat transfer of a non-azeotropic binary mixture of new refrigerants inside a single microchannel, Submitted to International Journal of Thermal Sciences

ACKNOWLEDGEMENTS